DYNAMICAL MODELS FOR THE EARTH'S GEOID

Thesis by

Mark Alan Richards

In Partial Fulfillment of the Requirements

for the Degree of

Doctor of Philosophy

California Institute of Technology

Pasadena, California

1986

(Submitted February 24th, 1986)

To my parents,

Jim and Dorothy Richards.

Acknowledgments

Undoubtedly the most pleasant part of writing this thesis is the opportunity to recognize those who have helped me along the way. Brad Hager has been tireless in his efforts to teach me how to turn ideas into science, and he unselfishly turned over to me an outstanding geophysical problem. For five years as my thesis research advisor, Brad has been supportive in every way possible and has been a good friend. Academic advisor and committee chairman Tom Ahrens has graciously allowed me to take my own course, contributing wit and wisdom at times. Don Anderson provided many stimulating ideas and criticisms, and is especially appreciated for his role in creating the excellent research environment at the Seismo Lab -- I have never known a better place to work.

Rob Clayton was particularly generous with his computer, his programs, and his tomography results. Dave Stevenson's constant interest in the geoid problem has kept us on our toes, and his doubts helped inspire Chapter 3. Norm Sleep contributed many clever ideas and keen insight which led to the collaborative work on hotspots in the final chapter. The numerical results in Chapters 3 and 4 were obtained using codes developed mainly by Arthur Raefsky. A special note of thanks goes to Barclay Kamb, whose support for my work on The Glacier greatly enriched my experience at Caltech. Support from the staff in our Division has been unfailing, and thanks are due to Nancy Durland, Dorothy Coy, and particularly Laszlo Lenches, who prepared most of the more professionally drafted figures in this thesis.

Officemates Tom Hearn, Ronan Lebras, Doug Schmitt, Oli Gundmundsson, and John Louie were always tolerant and sometimes hilarious. Thanks, John, for rescuing me from the VAX. Fellow students Gene Humphreys, Bob Svendsen, and Lucianna Astiz have been especially good friends, and Darby Dyar has made these last few

hectic months much easier and even fun. Since arriving at Caltech I have been blessed with many dear friends on "the outside" who have made my life warmer and happier. Thanks to Marvin and Rebecca, Jean-Francois, Zofia, Pamela, and especially to Lyndi and Brother Don for helping me maintain some sense of balance.

Mrs. J : I just cannot get your three-year-old son to go out and play with the other children.

Mrs. R : That is because you are playing Bach on the phonograph.

Mrs. J : What?!

Mrs. R : Mark is waiting for the music to finish. Then he will go out and play.

Abstract

The Earth's largest geoid anomalies occur at the lowest spherical harmonic degrees, or longest wavelengths, and are primarily the result of mantle convection. Thermal density contrasts due to convection are partially compensated by boundary deformations due to viscous flow whose effects must be included in order to obtain a dynamically consistent model for the geoid. These deformations occur rapidly with respect to the timescale for convection, and we have analytically calculated geoid response kernels for steady-state, viscous, incompressible, self-gravitating, layered-Earth models which include the deformation of boundaries due to internal loads. Both the sign and magnitude of geoid anomalies depend strongly upon the viscosity structure of the mantle as well as the possible presence of chemical layering.

Correlations of various global geophysical data sets with the observed geoid can be used to construct theoretical geoid models which constrain the dynamics of mantle convection. Surface features such as topography and plate velocities are not obviously related to the low-degree geoid, with the exception of subduction zones which are characterized by geoid highs (degrees 4-9). Recent models for seismic heterogeneity in the mantle provide additional constraints, and much of the low-degree (2-3) geoid can be attributed to seismically inferred density anomalies in the lower mantle. The Earth's largest geoid highs are underlain by low density material in the lower mantle, thus requiring compensating deformations of the Earth's surface. A dynamical model for whole mantle convection with a low viscosity upper mantle can explain these observations and successfully predicts more than 80% of the observed geoid variance.

Temperature variations associated with density anomalies in the mantle cause lateral viscosity variations whose effects are not included in the analytical models.

However, perturbation theory and numerical tests show that broad-scale lateral viscosity variations are much less important than radial variations; in this respect, geoid models, which depend upon steady-state surface deformations, may provide more reliable constraints on mantle structure than inferences from transient phenomena such as postglacial rebound. Stronger, smaller-scale viscosity variations associated with mantle plumes and subducting slabs may be more important. On the basis of numerical modelling of low viscosity plumes, we conclude that the global association of geoid highs (after slab effects are removed) with hotspots and, perhaps, mantle plumes, is the result of hot, upwelling material in the lower mantle; this conclusion does not depend strongly upon plume rheology. The global distribution of hotspots and the dominant, low-degree geoid highs may correspond to a dominant mode of convection stabilized by the ancient Pangean continental assemblage.

Table of Contents

Introductory Remarks

The shape of the Earth's long-wavelength gravitational potential field, or geoid, became known from studies of satellite orbit perturbations just after plate tectonic and sea floor spreading concepts achieved widespread acceptance among geologists and geophysicists. However, a direct correspondence between plate motions and convection cells in the mantle was not verified by the gravity data. The largest geoid anomalies are apparently unrelated to the current configuration of plates, and this has remained a difficult problem for geodynamicists. This situation has improved in the last several years, largely as a result of recent models of seismic heterogeneity in the mantle. I was fortunate to have been working simultaneously on theoretical models for geoid anomalies caused by lateral density contrasts due to convection.

The inherently non-unique relationship between the geoid and internal density contrasts does not allow for independent inversion of the geoid data alone. My initial investigations showed (as had earlier researchers) that the deformation of the Earth in response to convecting density contrasts had a substantial effect upon the geoid. This effect was found to depend strongly upon the viscosity structure of the mantle and the depth of convection, neither of which was well constrained at the time. Having begun with some pessimism, this theoretical work had made a difficult problem seem even more intractable. However, with the new seismic data in hand to constrain *a priori* the internal density structure, it has become possible not only to model most of the observed long-wavelength geoid but also to derive new constraints on the

dynamics and viscosity structure of the mantle. These constraints are consistent with postglacial rebound and other transient loading phenomena. In addition, what has been assumed by most researchers for almost two decades can now be stated with more confidence: the lack of a strong correspondence between plate tectonics and the geoid is due to the relatively weak coupling of plates, outside of subduction zones, to the large-scale mantle flow.

These remarks are included to give some flavor for the evolution of my thinking since I began working on the geoid problem. The four chapters of this thesis, all of which deal with some aspect of geoid modelling and interpretation, were written to be published independently and, for the most part, contain their own introductory material. Much repetition of the basic concepts of dynamic compensation will be found from chapter to chapter, because these ideas are non-intuitive and are not familiar to many geophysicists. The first chapter, which was published some time ago, has been kept more or less in its original form. It may be interesting to contrast some of the ideas in that earlier paper to the more current conclusions of Chapters 2, 3, and 4. I hope and expect that continuing advances in geodynamics will, within a few years, make some of these recent efforts seem equally naive.

Chapter 1

Geoid Anomalies in a Dynamic Earth

INTRODUCTION

The relationship between large-scale geoid anomalies and thermally driven flow in the Earth's mantle was discussed almost 50 years ago by Pekeris (1935). He showed that the gravitational effect of the surface deformation caused by the flow is opposite in sign and comparable in magnitude to that of the driving density contrast. Consequently, in a viscous Earth, the net gravity or geoid anomaly is also dependent in both sign and magnitude upon the dynamics of the mantle. This represents a complete departure from the result for a rigid or elastic Earth in which positive internal density contrasts are always associated with positive gravitational anomalies.

Studies of postglacial rebound (e.g., Haskell, 1935; Cathles, 1975), as well as the very existence of plate motions, show that the mantle responds to stresses applied over geologic timescales by slow creeping flow. Therefore, any interpretation of long-wavelength geoid anomalies should include the dynamical effects first described by Pekeris. These effects, particularly boundary deformation caused by flow, have been investigated by Morgan (1965), McKenzie (1977), and Parsons and Daly (1983) for intermediate wavelength features using two-dimensional models with uniform mantle viscosity. Runcorn (1964, 1967) addressed the relationship between long-wavelength gravity anomalies and the flow field in a self-gravitating, uniform viscous sphere. Each of these studies showed that the deformation of boundaries, especially the upper surface, has a major effect upon the net gravity or geoid anomaly arising from a

density contrast at depth. Moreover, the effects of viscosity stratification and layered convection in the mantle can significantly alter the calculated relationship between geoid elevations and driving density contrasts (Richards and Hager, 1981; Ricard, Fleitout, and Froidevaux, 1984).

In this chapter, we develop and discuss several dynamical models and their implications for geoid interpretation. The aim is to provide quantitative relationships between density contrasts within the Earth and other geophysical observables, including boundary topography, as well as the geoid. At the present time we cannot solve the full problem of thermal convection for a given model to determine these dynamical relationships for the whole system (see McKenzie, 1977, for two-dimensional numerical examples). Since both the temperature structure of the mantle and the temperature dependence of the density and viscosity of mantle minerals are unknown, and since even the geometry of the convective circulation is not known (i.e., whole mantle vs. layered convection), a simpler and more direct approach is desirable. If the thermal density anomaly is treated simply as a "load", the resulting surface deformation and geoid anomaly can be determined by solving only the equilibrium equations for a viscous Earth.

The standard characterization of the Earth's response to tidal loading in terms of Love numbers (Love, 1911; Munk and MacDonald, 1960) suggests a useful way to characterize dynamic response functions. Love numbers for *internal* loading of the Earth are obtained by normalizing residual geoid anomalies and boundary deformations by the gravitational potential of the driving load. We obtain these quantities as functions of the depth and harmonic degree of the load, thus yielding Love numbers that are equivalent to Green functions.

A major question currently is whether chemical stratification of the mantle, associated with the 670 km seismic discontinuity, presents a barrier to vertical flow and divides the mantle into separately convecting layers. In order to address this issue, our flow models include not only radial viscosity variations but also the possibility of either mantle-wide or chemically stratified flow in the mantle as illustrated in Figure 1. Both the geoid and boundary deformation response functions (Love numbers) show a strong model dependence. For example, for mantle-wide flow, positive driving density contrasts cause net negative geoid anomalies for uniform mantle viscosity, since the negative anomaly caused by upper surface deformation overwhelms the geoid anomaly due to the density contrast itself. However, net positive geoid anomalies are obtained for a channel of sufficiently low viscosity in the upper mantle. This occurs because low upper mantle viscosity reduces the deformation of the upper surface. The core-mantle boundary deformation increases but has less effect upon the geoid because of its great depth. As shown in Figure 1(b), the layered flow case introduces much more complicated behavior. It is precisely this strong model dependence that makes these models useful in geodynamics. The *observed* spectral and loading-depth dependence of these response functions can be used to discriminate among various proposed models for mantle structure and rheology.

Although observations of satellite orbits provided the means for determining the lower order harmonics of the geopotential over two decades ago (Kaula, 1963a; Guier, 1963), subsequent efforts to interpret the long-wavelength geoid have been largely unsuccessful. Some correlations with tectonic features have been suggested (e.g., Kaula, 1972), notably a general correspondence between subduction zones and geoid highs. Chase (1979) and Crough and Jurdy (1980) demonstrated a remarkable

correlation between the spatial distribution of hot spots and the nonhydrostatic second harmonic geoid. Hager (1984) has shown that the fourth through ninth geoid harmonics are strongly correlated with the seismicity-inferred presence of subducting slabs, thus yielding quantitative estimates over a definite spectral range for the dynamic response functions which are the subject of this chapter. Additionally, recent seismological determinations of lateral variations in seismic velocities (e.g., Nakanishi and Anderson, 1982; Dziewonski, 1984; Clayton and Comer, 1983) provide another powerful constraint on geoid interpretation, and a large amount of information on crustal thickness, topography, and density has yet to be considered in relation to the geoid. It is therefore reasonable to expect increasingly accurate and useful observations of the Earth's density anomalies and effective boundary deformations. Cast in the form of dynamic response functions as discussed in this chapter, these data provide means for discriminating among various dynamic models for the mantle.

MODELLING CONSIDERATIONS

Quantitative models for the geoid derive from constitutive laws, equations of motion and material continuity, and boundary conditions. It is impossible at the present time to specify fully the Earth's rheology or to solve all these equations exactly. We must make various approximations and assumptions in developing mathematical models; in doing so we try to include the important physical effects while avoiding unnecessary complication in the method of solution. In this section we discuss our assumptions concerning mantle rheology and flow, boundary conditions, and the thermal driving forces involved. Boundary deformation is afforded a detailed treatment in a separate section.

Rheology and Flow

The selection of appropriate models for the mechanical behavior of the lithosphere, mantle, and core depends upon both the time and length scales involved. Here we are interested in length scales for which lithospheric strength is negligible, roughly defining what is meant by "long-wavelength" geoid anomalies, and time scales of the order of those required for substantial changes in the convective flow pattern in the mantle. As we show below, this implies harmonic degrees l less than 40 (wavelengths greater than 1000 km). If mantle flow is reflected in plate motions, the mantle flow pattern is stable for times far in excess of 1 Myr, which we take as a characteristic timescale. The core is inviscid for the timescales of interest here; it may also be assumed to be in a state of hydrostatic equilibrium.

The lithosphere presents several problems, including those of finite elastic strength and of lateral variations in rheological properties, density, and thickness. For loads of wavelength greater than about 1000 km the elastic strength of the lithosphere is negligible (McKenzie and Bowin, 1976; Watts, 1978), so that surface loads are supported by buoyancy and the resulting flow in the mantle. The lithosphere is essentially transparent to long-wavelength normal tractions from flow in the mantle.

Lateral variations in rheological properties of the lithosphere are responsible for the plate tectonic style of convection in the Earth's mantle. The plates move as distinct units with respect to each other and effectively form a rigid lid for any sublithospheric small-scale convection which may exist. Plate boundaries, on the other hand, are relatively weak, allowing the plates themselves to participate in mantle convection (Hager and O'Connell, 1981). This lateral heterogeneity of the effective viscosity of the lithosphere allows density contrasts in the interior to excite significant

toroidal flow (Hager and O'Connell, 1978), not just the poloidal flow which would result from a mantle with spherically symmetric viscosity structure.

The choice of boundary conditions at the surface is not obvious, and the analytical technique we use here does not account for lateral viscosity variations. We argue that the mechanical effect of the lithosphere on small-scale flow beneath plate interiors can be represented by a no-slip boundary condition at the Earth's surface. Flow involving the plates themselves is probably best approximated by a free-slip boundary condition. We present calculations for both cases and find that the results are similar. This suggests that a more complicated boundary condition that would better represent the effects of lithospheric plates would also be similar.

The effect on the geoid of lateral variations in lithospheric thickness and density have been discussed by Chase and McNutt (1982) and Hager (1983). These variations are primarily the result of variations in crustal thickness and in the age of the lithosphere. Since they are close to the surface, they are generally well compensated, and their effect on the geoid is small (less than 20 m out of a total geoid variation of greater than 200 m). However, their effect on topography is large. If surface deformation and the geoid are to be used concurrently to obtain sublithospheric density contrasts as discussed below, corrections must be made to compensate for the topographic effects of large density contrasts within the lithosphere.

The appropriate constitutive law (or laws) for modelling flow in the mantle cannot be determined with certainty at the present time. Possible creep mechanisms for deformation of mantle minerals include dislocation climb (Weertman, 1968), which implies a non-linear rheology, and grain boundary diffusion or superplasticity (Twiss, 1976; Ashby and Verrall, 1977; Berckhemer, Auer, and Drisler, 1979), which at low

stress levels might result in a linear relationship between shear stress and strain rate. Mathematical tractability has led most researchers to employ linear rheology, either Maxwellian or Newtonian, in modelling flow in the mantle. Furthermore, for some surface loading problems in which the magnitude of shear stress decays with depth, non-linear rheology might not be distinguishable from layered linear rheology; the lower stress levels found at depth would correspond to higher apparent viscosity. Estimates for effective mantle viscosity have been obtained for a variety of loading problems. Values given for average mantle viscosity have generally been on the order of 10^{21} Pa-sec (10^{22} Poise) (O'Connell, 1971; Cathles, 1975; Peltier, 1976; Yuen, Sabadini, and Boschi, 1982) although estimates as small as 10^{18} Pa-sec have been obtained for the upper mantle or asthenosphere for loads of smaller scale (Passey, 1981). Although viscoelastic models have found application to shorter term problems such as glacial loading and unloading (Clark, Farrell, and Peltier, 1978; Wu and Peltier, 1982), the timescales of 1 Myr or greater of interest here are in excess of Maxwell times for the mantle, so we ignore elastic effects. For the purpose of exploring the basic physics of internal loading problems and for mathematical simplicity, we employ Newtonian models in which viscosity is dependent on depth only, although, when this theory is applied to actual data, the results suggest that lateral variations in effective viscosity may be important.

Boundary Conditions

Three possible boundaries are considered in our spherically symmetric, layered Earth models: (1) the core-mantle boundary; (2) the upper surface; (3) a change in composition and/or viscosity across the 670 km seismic discontinuity.

We model the core-mantle boundary as one at which there is no shear traction and no steady-state vertical transport. As discussed above, the mantle-lithosphere boundary is more complicated. We have investigated both no-slip and free-slip conditions and have included both types in the results presented here, although, as we noted above, the difference between the two is not profound.

Chemical stratification and multi-layer convection have been suggested (e.g., Anderson, 1979) to explain the major seismic discontinuity at 670 km. Geochemical budget models as well as the lack of seismicity below 670 km are thought by some to suggest that upper mantle flow does not penetrate this level (Jacobsen and Wasserburg, 1980; Richter and McKenzie, 1981). We include the effect of such a boundary in our investigation in order to understand how geoid and geodetic data might be used to test the chemical layer hypothesis. A chemical discontinuity is modelled by setting the (steady-state) vertical velocity to zero at the boundary; horizontal velocities and normal and shear tractions are continuous. This results in a two-layer, shear-coupled, antisymmetric flow system as illustrated in Figure 1(b). Another possibility associated with both the 400 km and 670 km discontinuities is that of an abrupt phase change within the mantle, which in the simplest case might be modelled as a spike in the compressibility curve for the mantle, assuming that the transition is adiabatic and ignoring thermal effects. We have not treated this case since compressibility introduces nonlinearity into the field equations and makes solutions much more difficult to obtain.

Driving Forces and Loads

The relationships among loading, gravity, and deformation can be obtained without solving for the thermodynamics. This is accomplished by calculating the flow driven by arbitrary density contrasts at any given depth. Kernels (Love numbers) representing the viscous response functions so obtained can then be integrated over depth in accordance with any prescribed distribution of thermal density anomalies; the linearity of the problem (with the caveat of linear, spherically symmetric viscosity) allows for superposition of solutions. Our method is to solve for loading due to a surface density contrast at a given depth and spherical harmonic degree, thereby characterizing the response as a function of spatial wavelength and depth in the mantle. In this way we can isolate the relationships desired for geophysical observables from the thermal part of the convection problem.

The Field Equations

With the above qualifications and simplifications we can specify tractable field equations to investigate the loading problem for a variety of rheological and structural configurations in the mantle. The mantle will be assumed to behave as a self-gravitating, spherically symmetric, incompressible, Newtonian viscous fluid. Since the Reynold's number is very large owing to the mantle's high viscosity, inertial or time-dependent terms are omitted from the equations of motion. The only time dependence is introduced by changes in position with time of the driving density contrasts and relaxation of the boundaries to a steady-state condition of deformation. We address the relaxation problem in detail in Appendix 2, the result being that boundary deformations decay rapidly compared to the timescale of flow in the interior.

The equations of motion can be written:

$$\nabla \cdot \underline{\tau} + \rho \mathbf{g} = 0 \tag{1}$$

where $\underline{\tau}$ is the stress tensor, ρ the density and $\mathbf{g}$ the gravitational acceleration. The mantle will be assumed to be incompressible throughout; although radial density layering can be arbitrarily imposed in our method of solution, allowance for finite fluid compressibility is mathematically difficult and is generally ignored by most authors (Cathles, 1975; Peltier, 1981) since the dynamic effect is probably small (Jarvis and McKenzie, 1980). Ricard et al. (1984) have shown that the effect of compression from lateral gravity variations is negligible. The incompressible continuity equation is:

$$\nabla \cdot \mathbf{v} = 0 \tag{2}$$

where $\mathbf{v}$ is the velocity vector. The Newtonian constitutive relation is:

$$\underline{\tau} = -p\,\underline{\mathbf{I}} + 2\eta\underline{\epsilon} \tag{3}$$

where p is the pressure, $\underline{\mathbf{I}}$ the identity matrix, η the viscosity, and $\underline{\epsilon}$ the strain rate tensor.

For global scale loading problems, self-gravitation effects cannot be ignored (Love, 1911; Clark et. al., 1978). The gravitational effects of deformed boundaries must be included in any self-consistent model. The gravitational potential V must satisfy

$$\nabla^2 V = 4\pi G\,\rho \tag{4}$$

where we have chosen the sign convention such that $\mathbf{g} = -\nabla V$. These equations are linear in all the variables and can be straightforwardly solved by either propagator

matrix (Hager and O'Connell, 1981) or numerical techniques. Before proceeding to a fully three-dimensional (spherical) solution, we present some useful results from the simple two-dimensional half space problem. Results from the viscous relaxation problem that justify the hypothesis of steady-state flow are given in Appendix 2.

ANALYTICAL TREATMENT OF BOUNDARY DEFORMATION

Loading of the Earth by gravitational potential (e.g., tidal loading), by external loads (e.g., glacial loading), or internal density contrasts (e.g., thermal convection), will produce deformations of both the surface and any internal boundaries. In this section we analytically treat boundary deformation to first-order accuracy and derive some useful results for the two-dimensional problem. Figure 2 illustrates the warping of a material boundary relative to its deformed or reference state, with densities ρ_1 and ρ_2 above and below the boundary, respectively. The velocity and stress fields must be continuous at the deformed boundary. However, our solution technique requires that we propagate solution vectors from one horizontal boundary to the next, so we require expressions for the velocity and stress fields at the reference (undeformed) boundaries. If the magnitude of deformation, δz, is sufficiently small compared to the thickness of either of the adjacent layers and the spatial wavelength, λ, of interest (as in this study), any variable, u^i in medium i, may be continued, to first-order accuracy, from the deformed boundary to the reference level by:

$$u^i_{ref} = u^i_{def} - \frac{\partial u^i}{\partial z}\delta z \tag{5}$$

Since flow-induced stresses are always much smaller (first-order) than the lithostatic stress level in the mantle (zeroth order), flow and stress variables are first-order also;

their derivatives behave like the product of first-order terms and the approximate spatial wavenumber. The only first-order correction due to deformation is the hydrostatic correction to the normal stress:

$$\tau^i_{zz_{ref}} = \tau^i_{zz_{def}} - \rho_i\, g\, \delta z \tag{6}$$

In passing from the *reference* boundary as seen in medium 2 to that seen in medium 1, we get an apparent jump in normal stress:

$$\Delta\tau^{12}_{zz_{ref}} = \tau^1_{zz_{def}} - \tau^2_{zz_{def}} - \Delta\rho_{12} g\, \delta z \tag{7}$$

where $\Delta\rho_{12} = \rho_1 - \rho_2$. By continuity of stress at the deformed boundary:

$$\Delta\tau^{12}_{zz_{ref}} = -\Delta\rho_{12} g\, \delta z \tag{8}$$

(A similar argument will imply an effective jump in the gravitational acceleration at the reference boundary in the fully self-gravitating spherical case.)

This result can be readily applied to a simple half space problem. Figure 3 illustrates a surface density contrast (i.e., a thermal density anomaly), $\sigma_d(k)\cos(kx)$, at depth d, exciting flow in a viscous half space of viscosity η and density ρ, with a traction free surface at the top. For simplicity we will first assume that the density contrast is not advected with the resulting flow so that it remains fixed in space (this could be done experimentally using a heat pump, for example). We will then show that the density contrast would not be advected a significant distance in the time it takes for the boundary deformation to reach equilibrium. Solving equations (1)-(3) using the two-dimensional propagator (Hager and O'Connell, 1981), we find that the boundary displacement δz evolves from its initial undeformed position as

$$\delta z = -\frac{\sigma_d(k)\cos(kx)}{\rho}(1+kd)\exp(-kd)(1-e^{-t/\tau}) \tag{9}$$

The boundary relaxes with time exponentially toward a steady state of deformation with time constant

$$\tau = 2\eta k / \rho g \tag{10}$$

This is the same time as that derived for the surface loading or unloading problem, e.g., postglacial rebound (Haskell, 1935; Cathles, 1975). For example, with $\eta = 10^{21}$ Pa-sec, $\lambda = 2\pi/k \geq 1000$ km, $\rho = 3.5$ Mg/m^3, $g = 9.8$ m/sec^2, we obtain $\tau \leq 11{,}000$ yr. Assuming velocities in the mantle of the order of 100 mm/yr or less, we see that mantle transport of at most a few kilometers (much less than the depth scale of mantle convection) occurs before the free surface is completely relaxed.

Alternatively, we can assume that boundary deformation is rapid and calculate flow velocities under the assumption that vertical flow at the deformed surface vanishes (i.e., boundary deformation is complete). In this case,

$$v_z(d) = \frac{g\,\sigma_d(k)\cos(kx)}{4\eta k}\,[(1+2kd)\exp(-2kd)-1] \tag{11}$$

Comparing this to the characteristic surface velocity obtained by differentiating (9), we find that:

$$\frac{\delta\dot{z}}{v_z(d)} = \frac{2(1+kd)e^{-t/\tau}}{\exp(kd)-(1+2kd)\exp(-kd)} \tag{12}$$

Once again, we see that long-wavelength boundary deformation is rapid compared to changes in the convective flow pattern *independent* of $\sigma_d(k)$. Note that this result holds even for "thin" layers which are normally associated with long relaxation times. In Appendix 2 we show that viscous relaxation occurs on a timescale much shorter than that for mantle convection by calculating relaxation times for several spherical Earth models.

The long time limit of equation (9) shows that the effective mass deficit associated with the surface deformation, $\sigma_{eff} = \rho\delta z$, is of opposite sign and of the same order of magnitude as σ_d. It is now evident for at least two reasons that the assumption that δz is sufficiently small for the application of a linear continuation of the boundary condition is probably justified: (1)Thermal density contrasts in the Earth, with the possible exception of subducted slabs, are probably not large enough to cause gross deformation of either internal or external boundaries. (2) The Earth's topography *a priori* precludes lithospheric deformations greater than 10 km while seismic data do not suggest large deformations of the core-mantle boundary (Dziewonski and Haddon, 1974) or the 670 km discontinuity, although coverage is limited, especially in subduction zones where deformation is expected to be the largest (Hager, 1984).

From equation (7) we can obtain the relationship between the observed gravitational potential and the load as well as the relationship between topography and geoid due to $\sigma_d(k)$. The residual potential calculated at the reference surface contains contributions from both σ_d and σ_{eff} :

$$\delta V^{res}(z=0) = \delta V^{eff} + \delta V^{\sigma_d} = \frac{2\pi G \cos(kx)}{k}[-(1+kd)+1]exp(-kd)\sigma_d(k)$$

or

$$\frac{\delta V^{res}(0)}{\delta V^{\sigma_d}(0)} = -kd \tag{13}$$

This means that, for a uniform half space, a positive density contrast at depth results in a negative geoid anomaly. The geoid anomaly goes to zero as the density contrast approaches the surface. Furthermore, for depths greater than the wavelength, the

geoid can be much larger in magnitude than that obtained for a rigid half space for which there would be no boundary deformation. This occurs because the stress that causes boundary deformation falls off less rapidly with the depth of loading than the potential from the load itself.

For spherical models in general, the normalized potential

$$K_l(r) = \frac{\delta V_l^{res}}{\delta V_l^{\sigma}} \tag{14}$$

is the Green function for the Earth's surface potential per unit loading at radius r and spherical harmonic degree l. This quantity is a function of the Earth model in general and is related to Kaula's (1963b) elastic internal loading potential Love number, k_l'', by

$$K_l(r) = 1 + k_l'' \tag{15}$$

This response function is measurable if the driving density contrasts within the Earth are known *a priori*. Hager (1984) has used this in his discussion of geoid anomalies from subducted slabs, where density contrasts can be estimated. Another application is in comparing seismic velocity heterogeneities to the geoid (Hager et. al., 1985). By assuming a relation between seismic velocity and density the long-wavelength geoid coefficients are obtained from the integral:

$$\delta V_l^{geoid} = \frac{4\pi G a}{2l+1} \int_{r=0}^{r=a} K_l(r)(r/a)^{l+2} \delta\rho_l(r)\, dr \tag{16}$$

where a is the radius of the Earth, $\delta\rho_l(r)$ is the lth harmonic density contrast at radius r,and G is the gravitational constant.

The other observable we can calculate is a dimensionless "impedance", defined as the ratio of geoid elevation to boundary deformation:

$$Z_l(r) = \frac{\delta V_l^{geoid}}{g\,\delta r_l} \tag{17}$$

where δr_l is the lth harmonic deformation of the surface, and g is the gravitational acceleration. (Note that this is not a true impedance since it involves the observed potential δV_l^{geoid} instead of the driving potential δV^{σ_l} .) Defining a surface deformation Love number $h_l{}'{}'$ (e.g., Munk and MacDonald, 1960), we have

$$Z_l(r) = 1 + \frac{k_l{}'{}'}{h_l{}'{}'}$$

This quantity could be estimated for the surface by taking the ratio of harmonic geoid coefficients to topographic coefficients with the effects of crustal thickness variations removed. To estimate $Z_l(r)$ for a given density distribution and Earth model, the numerator and denominator of (17) must be integrated separately.

We have now defined two observables relating the geoid directly to internal loading and Earth structure for a density contrast at a given depth. Also, equation (16) shows how to interpret these quantities for models with distributed density contrasts. We have not yet introduced the gravitational interaction between the load and the mass anomalies due to boundary deformation.

SPHERICAL EARTH MODELS

Formal Solution

Analytical solutions to field equations (1) through (4) with radial variations in viscosity and density and for arbitrary, laterally varying internal loading are found in Hager and O'Connell (1981). Internal density contrasts drive poloidal flow fields for which the relevant stress, flow, and gravitational potential variables can be propagated from one radial layer to another according to:

$$\mathbf{u}(r) = \underline{\mathbf{P}}(r, r_0)\mathbf{u}(r_0) + \int_{r_0}^{r} \underline{\mathbf{P}}(r, \xi)\mathbf{b}(\xi) d\xi \tag{18}$$

where $\mathbf{u}$ is the six-vector given by

$$\mathbf{u}(r) = \left[v_r \ , \ v_\theta \ , \ r\tau_{rr}/\eta_0 \ , \ r\tau_{r\theta}/\eta_0 \ , \ \rho_0 r \delta V/\eta_0 \ , \ \frac{\rho_0 r^2}{\eta_0} \frac{\partial \delta V}{\partial r} \right]^T \tag{19}$$

with radial and tangential velocities v_r and v_θ, normal radial and shear deviatoric stresses τ_{rr} and $\tau_{r\theta}$, perturbed potential δV, and reference density and viscosity ρ_0 and η_0. In these expressions and for the remainder of this chapter all dynamical variables contain an implicit spherical harmonic dependence which has been suppressed for simplicity. The 6x6 matrix $\underline{\mathbf{P}}(r, r_0)$ can be expressed analytically (Gantmacher, 1960) as a function of r/r_0, normalized layer density $\rho^* = \rho/\rho_0$, normalized layer viscosity $\eta^* = \eta/\eta_0$, and harmonic order l. The driving term for this system is the integral on the right in equation (18) in which the density contrasts are introduced by

$$\mathbf{b}(r) = \left[0 \ , \ 0 \ , \ rg(r)\delta\rho(r)/\eta_0 \ , \ 0 \ , \ 0 \ , \ 4\pi r^2 G \rho_0 \delta\rho(r)/\eta_0 \right]^T \tag{20}$$

where $g(r)$ is the unperturbed (hydrostatic) gravitational acceleration and $\delta\rho(r)$ is

the density contrast at radius r .

The problem is greatly simplified mathematically by casting the driving density structure not only as a sum over spherical harmonics but also as a sum over radial surface density contrasts; that is,

$$\delta\rho(r) = \sum_{b_i} \delta(r - b_i)\sigma_i \tag{21}$$

where $\delta(r)$ is the Dirac delta function and the σ_i are the surface density contrasts. Equation (18) becomes

$$\mathbf{u}(r) = \underline{\mathbf{P}}(r, r_0)\mathbf{u}(r_0) + \sum_{b_i} \underline{\mathbf{P}}(r, b_i)\mathbf{b}_i \tag{22}$$

where

$$\mathbf{b}_i = \left[0 , 0 , b_i g(b_i)\sigma_i / \eta_0 , 0 , 0 , 4\pi b_i^2 G \rho_0 \sigma_i / \eta_0 \right]^T \tag{23}$$

Now, as was indicated previously in expressions (14) through (17), we can characterize all solutions in terms of harmonic order l and radial level or depth of the driving density contrasts since, owing to the linearity of the field equations, these solutions or kernels can be superposed to represent any arbitrary density contrast in the mantle.

A familiar and useful property of the propagator matrix formulation is that solution vectors can be propagated through a series of different material layers by simply forming the product of the individual layer matrices:

$$\underline{\mathbf{P}}(r, r_0) = \underline{\mathbf{P}}(r, r_1)\underline{\mathbf{P}}(r_1, r_0) \tag{24}$$

Therefore, changes in viscosity (and density) with depth are easily incorporated into this formalism.

Boundary Conditions

We have discussed two types of boundary conditions: (1) A free-slip (denoted "F") boundary condition requires zero radial velocity (v_r) and zero shear stress ($\tau_{r\theta}$), a condition which applies at the core-mantle boundary. (2) A no-slip (denoted "N") boundary condition requires zero radial and tangential velocities (v_r and v_θ). Good arguments can be made for applying either of these boundary conditions at the surface. For completeness, and to gain insight into the physics of the problem we have modelled both combinations. For example, for no-slip at the deformed surface ($r = a + \delta r_a$) and free-slip at the core-mantle boundary ($r = c + \delta r_c$), we have, to first order,

$$\mathbf{u}^N(a+\delta r_a) = \left[0\ ,\ 0\ ,\ 0\ ,\ a\,\tau_{r\theta_a}/\eta_0\ ,\ \rho_0 a\,\delta V_a/\eta_0\ ,\ \frac{\rho_0 a^2}{\eta_0}\,\frac{\partial \delta V_a}{\partial r} \right]^T \qquad (25)$$

and

$$\mathbf{u}^F(c+\delta r_c) = \left[0,\ v_{\theta_c},\ c\,\tau_{rr_c}/\eta_0,\ 0,\ \rho_0 c\,\delta V_c/\eta_0,\ \frac{\rho_0 c^2}{\eta_0}\,\frac{\partial \delta V_c}{\partial r} \right]^T$$

where we have also set the normal stress to zero at the surface. These boundary conditions apply at the actual deformed boundaries (see Fig. 1), however equations (22) show only how to propagate from one spherical reference boundary to another. Therefore expressions (25) must be analytically continued to the reference boundaries via equations (5) through (8) cast in spherical coordinates. This is a tedious operation which involves finding expressions for $\tau_{rr_a}, \tau_{rr_c}, \delta V_a, \delta V_c$ in terms of the resulting harmonic surface deformations (δr_a, δr_c), and the details as well as the resulting system of equations are included in Appendix 1. This procedure involves two physical effects: (1) When solution vectors are referenced to the undeformed boundaries, there is an

apparent jump in normal stress at each boundary given by an expression similar to equation (8):

$$\delta\tau_{rr} = -\delta\rho g(r)\delta r \tag{26}$$

(2) There is a similar jump in gravity at each boundary (see Appendix 1). Accordingly, each boundary deformation makes a first-order contribution to the perturbed potential. This occurs because, as demonstrated above, the mass displaced is of the same order of magnitude as the driving density contrast. The important thing to note is that we can cast the problem in a form whose solution gives the deformation of boundaries as well as the gravitational potential at those boundaries as functions of the harmonic order and depth of loading. From these solutions we can generate the desired quantities (Love numbers and impedances) defined by expressions (14) through (17).

Equation (24) shows how to treat layering effects in material properties, but a layered flow system (Figure 1(b)) requires a separate boundary condition at the flow barrier. We model this boundary as a compositional change accompanied by a density jump which results in a simple flow barrier with shear coupling between the two layers. Mathematically, this can be expressed as

$$\mathbf{u}(r+\delta r) = \left[0,\ v_\theta,\ r\,\tau_{rr}/\eta_0,\ r\,\tau_{r\theta}/\eta_0,\ \rho_0 r\,\delta V/\eta_0,\ \frac{\rho_0 r^2}{\eta_0}\frac{\partial \delta V}{\partial r}\right]^T \tag{27}$$

in which the radial velocity is set to zero at the boundary. This also represents another boundary which will deform under loading and an additional apparent jump in normal stress and gravity will occur when (27) is analytically continued to its reference surface (e.g., 670km depth). For this two layer flow problem we have two systems of equations (22) that are coupled at an internal boundary whose field variables

are given by (27). We have not included the details here, but solution of these propagator equations proceeds straightforwardly as in Appendix 1, where details are given for the case of whole mantle flow.

RESPONSE FUNCTIONS

The mathematical formalism we have developed for solving the internal loading problem yields solutions in the form of boundary vectors that give the fluid velocities and stresses as well as the gravitational potential and its radial derivative at spherical reference boundaries corresponding to the unperturbed layer boundaries. These reference boundary vectors can be propagated (see equation 18) to any radial level in the Earth, so each solution implicitly contains the stress-flow field and gravitational field throughout the mantle. For any specific model, solutions vary with the depth of loading and harmonic degree so that, even for the limited variety of models we have considered here, a very large amount of information is generated. The spherical Earth results presented in this section are restricted to those involving either the geoid or boundary deformations. The results that follow involve only the approximations discussed above and are analytic, although the resulting algebraic expressions are evaluated on a computer.

Whole Mantle Flow

The simplest model is that for mantle-wide flow, and most of the physical ideas from spherical modelling can be demonstrated with this model. Figures 4(a)-(c) show for model A (see Table 1) the amount of mass per unit area, normalized by the amplitude of the load, that is displaced by deformation of the core-mantle boundary and

the upper surface as a function of the depth of loading for representative harmonic degrees 2, 7, and 20. The displaced mass is opposite in sign to that of the driving mass anomaly, so its negative is plotted for ease in comparison. Figures 4(a)-(c) are for free-slip at both the core-mantle interface and the upper surface ("FF" case) while (f)-(h) are for no-slip at the upper surface ("NF" case). The closer the load is to a boundary the larger are the resulting mass displacement and deformation at that boundary. Also plotted is the total amount of mass displaced at both boundaries. By analogy to the Airy or Pratt principles of isostatic compensation in the lithosphere, these curves represent *dynamic isostasy* for mantle loads in a spherical Earth. The total mass displaced is opposite in sign and comparable, but not identical, in magnitude to that of the load (dashed line) for long wavelengths. For the uniform viscosity model, $-\sigma_{disp}\,(total)/\sigma_b$ is of order unity for $l=2$ and $l=7$, but for higher values of l this ratio becomes much smaller if the load is not close to a boundary: this means that the load is almost entirely dynamically supported by flow in the interior. Figures 4(d) and (e) show the effects of one and two orders of magnitude viscosity contrast above 670 km depth (Model C) for $l=7$ for the "FF" case. The lower viscosity in the upper mantle lessens the coupling between the flow and the upper surface, thereby decreasing the deformation of the upper surface and increasing that of the core-mantle boundary. In Figure 4(e) the coupling is so weak that self-gravitation actually causes the deformation to reverse, resulting in the slightly negative excursion of its mass displacement curve. This effect will be addressed more fully below.

Comparison of Figures 4(a) and (f) shows that the main effect of the no-slip condition, as opposed to the free-slip condition, at the upper surface is to restrict the flow near that boundary, resulting in more deformation and mass displacement at the

upper boundary. This effect diminishes with increasing l as seen by comparison of Figures (b) and (g) as well as (c) and (h). Notice that for NF conditions the maximum mass displacement at the upper surface occurs with the load at depth rather than when it is nearest to the surface. A similar effect can be derived analytically for the two-dimensional case and is the result of flow restriction in a channel due to long-wavelength loading. In the three-dimensional (spherical) case this subsurface maximum in deformation is also enhanced considerably by the self-gravitation of the boundary. In addition to the stresses generated by the load "sinking" in the ambient (zeroth order) potential field, there is a first order perturbation in the ambient field due to both the load and the mass displacements at the boundaries. Although this idea is no more complicated than that of a self-consistent gravity field, the effect is physically subtle and warrants some discussion.

The basic propagator equations (18) are written for field variable six-vectors, the last two terms of which are the perturbed geopotential field and its radial derivative (gravitational acceleration). These two variables must satisfy Poisson's equation independently and it has recently been shown by O'Connell, Hager, and Richards (in preparation) that the 6x6 set of equations can be reduced to coupled 4x4 and 2x2 systems in which the 2x2 system involves only the potential variables and Poisson's equation. The 4x4 system is obtained by substitution of $u_3 + \rho^* u_5$ for u_3 in the six vector. This results in a decoupled four-vector system where

$$\mathbf{u}(6x\,6) \rightarrow \mathbf{u}'\ (4x\,4) = \left[v_r\ ,\ v_\theta\ ,\ r\,\tau_{rr}/\eta_0 + \rho r\,\delta V/\eta_0\ ,\ r\,\tau_{r\theta}/\eta_0 \right]^T$$

Physically, the normal stress term has been augmented by a "gravitational pressure" term, $\rho r\,\delta V/\eta_0$, to form a system of equations that is otherwise similar to the 4x4 propagator system used in two-dimensional problems (e.g., Cathles, 1975). This

formulation then shows explicitly how self-gravitation enters into the dynamics of the loading problem. Upon examination of the excitation vector (23) we notice that there are two driving terms: (1) The third term of the vector corresponds to the stress due to the density contrast being acted upon by the zeroth order field. (2) The sixth term represents the driving force due to the first-order field perturbation from the density contrast, that is, a gravitational pressure term. These extra pressure terms do not drive flow in steady-state, but they do affect boundary deformations.

In Appendix 2 we discuss the problem of viscous relaxation to steady-state in terms of the largest decay time associated with a given Earth model. However, this approach constitutes a worst case analysis since all of the relaxation modes are, in general, excited by loading. Although we were able to justify the steady-state assumption for our models even for these worst cases, it is possible with the analytical tools here to solve for mode excitation as a function of the depth of loading and harmonic degree. An eigenmode for the simple two-layer case can be represented by a unit normalized two-vector giving the relative amount of mass displaced at the upper surface and the core-mantle boundary. For models A and C there is a mantle mode (M0) and a core mode (C). For M0, both boundaries flex in the same sense; for the C mode their flexure is oppositely directed. The relative amounts of mode excitation are determined by finding the appropriate linear combination of M0 and C required to give the boundary mass displacements in Figure 4. Note that this matching also solves the unloading problem, that is, excitation of modes due to the sudden release of an internal load of long duration; the loading and unloading problems are equivalent in terms of relative mode excitation. Figures 5(a)-(c) show the results of the calculations for the FF models of Figure 4.

Figure 4 shows that, at least for long-wavelength loads, the amount of mass displaced at the boundaries is comparable to the mass of the load itself, so the total geoid anomaly at the surface involves significant contributions from these sources. Figure 6 shows the relative contribution from each of the three sources δV_a ,δV_c ,andδV_σ as functions of the depth of the load. The δV_σ ("σ") curve has a simple $(a/r)^{l+2}$ dependence derived solely from potential theory (see equation A7) and the δV_a ("a") and δV_c ("c") curves are proportional to the product of the mass displacement curves of Figure 4 and the $(a/r)^{l+2}$ factor. Potentials δV_a and δV_c are of opposite sign to δV_σ. Their absolute values are plotted normalized by the maximum value of δV_a, to facilitate direct comparison. Figures 6(a)-(c) are for FF conditions and (d)-(f) are for NF conditions. In most of the figures to follow we refer to potential anomalies since they are related to geoid anomalies simply through $\delta N = \delta V/g$, where δN is the geoid height due to δV and g is the gravitational acceleration at the surface. As was the case for the two-dimensional half space, the geoid contribution due to the deformation of the upper surface is generally larger than that due to the load. The contribution from the core-mantle boundary is generally small except for loads at great depth. Again, comparing Figures 6(a)-(c) with (d)-(f), the effect of stronger upper surface coupling due to the no-slip condition is evident. Notice that for $l=2$ and $l=7$ with NF conditions, the maximum δV_a contribution occurs at depth. In Figure 6(d) we have plotted (see curve "a' ") the result obtained ignoring self-gravitation in order to demonstrate its importance for lower degree harmonics. This was accomplished by ignoring the self-gravitation terms described above (at the expense of a self-consistent field). Since the difference between curve δV_σ and the sum of δV_a and δV_c determines the surface potential anomaly ,

this effect cannot be ignored for the lowest harmonic degrees.

The total surface potential, δV_{tot}, normalized by the load potential , δV_{σ}, results in the response function K, the modified Love number defined in equation (14). Figure 7 shows K as a function of loading depth and harmonic degree for the four possible combinations of boundary conditions. The differences among these results are not great, although the relative coupling effects due to N or F conditions can be seen, especially for low-order harmonics. The cases with no-slip at the core-mantle boundary are included because they simulate high viscosity in the lowermost mantle. In the more pertinent FF and NF cases, K is invariably negative for model A (no viscosity contrast). As predicted by equation 13, the magnitude of K can be much greater than unity; consequently, the geoid signature of a density contrast at depth is amplified. The straight light lines in Figures 7(a) and (b) show the two-dimensional half space values for K. Note that with the load at either boundary, compensation of the geoid is complete to first order since all the loading stress is absorbed by deflection of the boundary. The geoid is much more sensitive to density contrasts in the middle regions of the mantle than to comparable density contrasts near boundaries.

The dominating influence of the upper surface deformation is diminished by the effect of low viscosity in the upper mantle, resulting in less negative or even positive values for K. This is shown in Figure 8 for both FF and NF conditions. In this case the different boundary conditions result in more markedly different geoid signatures. The effect of the low viscosity channel in the upper mantle is strongest for shorter wavelengths (larger l), whereas the channel is almost transparent to $l=2$ loading. We have not presented many of the other models of viscosity stratification which are also

plausible, but their effect can be roughly extrapolated from these figures. For example, a thinner channel, say 200 km thick, remains transparent to much shorter wavelengths than for the 670 km case.

The ratio of geoid anomaly to surface deformation, the impedance function Z (equation 17), is shown in Figure 9 for models A and C for both FF and NF conditions. For uniform viscosity, Z is positive since the sign of the geoid is determined by the upper surface deformation. With a viscosity contrast, the functions can become positive since the geoid itself may be positive. Note that for large viscosity contrasts, say $\eta^* = 0.01$ (not shown), singularities in Z can occur since the surface deformation can change sign (go through a zero). In practical applications these singularities will be smoothed by integration over a depth distribution of density contrasts.

Layered Flow

The flow model representing a chemical discontinuity at 670 km depth is illustrated in Figure 1(b) corresponding to models D and E. Mass displacements at the boundaries are shown in Figure 10, comparable to Figure 4 for a uniform composition mantle. In these cases there is deformation and effective mass displacement at the layer boundary as shown by the "M" curves. For loads near the 670 km discontinuity the stress is taken up principally by the deformation of that boundary. The curves for total mass displacement in Figure 10, computed for NF boundary conditions, again represent dynamic isostatic compensation as discussed for the case of whole mantle flow. The sense of flow in both the upper and lower mantle is reversed for loading in the upper mantle from that resulting from loading in the lower mantle. Consequently, the sign of both the core-mantle boundary and upper surface

deformation depends upon whether the load is above or below the 670 km discontinuity; singularities occur in the corresponding impedance functions and the behavior of K becomes more complicated. Figure 11 shows the relative excitation of viscous relaxation normal modes for these layered models where we now have an additional mode, M1, associated with deformation of the 670 km discontinuity. The depth dependence for the M0 and C mode is strikingly similar to that for the whole mantle case. The M1 mode is, as expected, dominant near the 670 km discontinuity.

The chemical layer response functions K and Z for models D and E are shown in Figures 12 and 13. The potential function K exhibits a more complicated depth dependence than for the whole mantle case. In particular, for no viscosity contrast, the sign of the geoid anomaly reverses as we cross the 670 km discontinuity due to the dominance and reversal of the upper surface deformation; geoid anomalies due to correlated upper and lower mantle density contrasts are anticorrelated. Also, all functions K have an additional zero at 670 km depth. For a viscosity contrast at 670 km, the coupling at the upper surface is reduced sufficiently so that the deformation of the 670 km discontinuity dominates the surface potential resulting again in negative values for K. Therefore, a wide variety of behavior is possible for a relatively small range of viscosity contrasts (less than one order of magnitude). Upper surface impedance values, Z, are plotted in Figure 13, and these functions are also seen to be strongly model dependent.

Note that the maximum values of K for density contrasts in the upper mantle are small compared to those for the whole-mantle flow model (Figure 7) and those for density contrasts in the lower mantle for the stratified models. The physical interpretation of this behavior is useful in developing intuition about dynamic geoid

anomalies. As a first approximation, dynamic isostasy results in the conservation of mass in any column, at least at long wavelengths (see Figures 4 and 10). The total geoid anomaly results from a mass quadrupole consisting of a driving mass anomaly at depth and compensating mass anomalies at the deformed boundaries. The magnitude of the anomaly depends upon the separation of the boundaries--the "arm length" of the quadrupole. For a given mass anomaly, the deeper the convecting layer, the larger the arm length and the greater the geoid anomaly. In the limit of zero thickness, the geoid anomaly in a convecting layer goes to zero.

INTERPRETATION

The range of solutions for K obtained for the simple models we have described are illustrated in Figure 14. Instead of plotting K as a function of depth and harmonic degree, we have now plotted it as a function of harmonic degree and Earth model for representative depths of 300, 1400, and 2600 km in order to emphasize the most important conclusion resulting from this study: The relationship that exists among internal loading, surface deformation, and the geoid is a strong function not only of the depth and harmonic degree of loading but also of the mechanical structure of the mantle. The dashed reference lines in Figures 14(a)-(c) represent the value of K that would be observed for a rigid Earth, that is, if we ignore the dynamic response. Even the limited range of models we have explored exhibit a wide range of values for K that indicate the sensitivity of the observables to structure. Interpretation of the Earth's geoid in terms of internal processes demands careful consideration of a variety of physical effects, but much of the nonuniqueness inherent in surface gravity problems is removed because of the distinct signature of different models.

Figures 7-9 and 12-14 constitute "maps" that show how to relate geoid anomalies and surface deformations to the depth and harmonic degree of driving density contrasts. In most of the models there is roughly an order of magnitude amplification of the higher harmonic geoid anomalies for loads at great depth. For example, K attains its largest value of -12 in model A for $l=20$ with the load several hundred kilometers above the core-mantle boundary. This requires modification of simple state-of-stress type arguments concerning the maximum geoid anomalies which can be generated by loads supported at great depth (Kaula, 1963b). Required deviatoric stresses up to an order of magnitude smaller can support density contrasts generating a given geoid anomaly in dynamic Earth models as opposed to an elastic model. Of course, these modified Love numbers must still be multiplied by $(r/a)^{l+2}$ to give the total potential (see Figure 5 of Hager, 1984). Also from the figures showing K as a function of depth we see that, to first order, K is zero at the boundaries, which implies that compensation of loads near boundaries is essentially complete. This means that bumps due to a variable thermal boundary layer in a convecting mantle are essentially masked out of the geoid signature. Since these density contrasts are likely to be among the largest associated with convection, this becomes a serious constraint on the resolvability of these features in the geoid. A good example of this is the observation that mid-oceanic ridges have very little long-wavelength geoid signature. Also in reference to the upper boundary layer, crustal and lithospheric thickness and density are not in general very well known for the Earth. Application of the impedance response functions requires a more complete synthesis of information on lithospheric thickness and surface topography than is currently available and this problem is currently under study. In addition to these complications it should be

remembered that for a given density anomaly "map" for the mantle, say from seismic heterogeneity data or from a three-dimensional convection model, one must integrate $K(r,l)$ and $Z(r,l)$ over depth as in equation 16 (the numerator, δV, and the denominator, $g\ \delta r$, of Z must be integrated separately). This will tend to smooth the respective models summarized in Figure 14. Another important point illustrated by these figures is that long-wavelength geoid anomalies are influenced more by density contrasts in the middle mantle than in the uppermost or lowermost mantle. Also, for a given range of density anomalies, whole-mantle convection results in larger geoid anomalies than layered convection.

An example of the process of interpretation using dynamic response functions is found in Hager's (1984) analysis of the correlation between the geoid and subducted slabs as evidenced by deep focus earthquakes. Seismically active slabs represent known positive density contrasts that correlate spatially at better than the 99% confidence level in a positive sense with the degree 4-9 geoid. The positive correlation in this wavelength band requires an increase in viscosity with depth of two orders of magnitude between the upper and lower mantle in regions of active subduction. The amplitude of the observed geoid anomalies in the context of dynamic Earth models requires much more excess mass than can be provided by subducted slabs alone in the upper mantle. A straightforward explanation is that the positive density contrasts associated with subduction extend into the lower mantle.

Seismology is now reaching the point where it is possible to map lateral velocity variations in the mantle. Examples include the determination of degree 2 lateral heterogeneity in the upper mantle by Masters et al. (1982), more detailed surface wave studies including odd and higher order harmonics (Nakanishi and Anderson,

1982; Woodhouse and Dziewonski, 1984), and body wave studies of lateral velocity variations in the lower mantle (Dziewonski, Hager, and O'Connell, 1977; Dziewonski, 1984; Clayton and Comer, 1983). When the velocity anomalies determined by these studies are compared to the observed geoid by assigning reasonable density contrasts to the velocity anomalies (neglecting the dynamical effects we have discussed), the geoids predicted are several times larger than those observed and may be of opposite sign.

As we have shown in this chapter, the dynamics of flow in the mantle can reduce the long-wavelength geoid anomalies from those resulting from the driving density contrasts alone and can even lead to a reversal in sign. Thus, the seismological results are not qualitatively surprising. They are useful, when combined with the theory described here, in placing meaningful constraints on mantle dynamics. By combining observational seismology and the quantitative theory of dynamic geoid anomalies we can learn far more than we could by either technique alone. For example, Hager et al. (1985) have shown that 70% of the variance of the degree 2-3 geoid can be accounted for by seismically inferred density contrasts in the lower mantle, using the kernels of Figure 8(c), for a model with uniform composition and an increase in viscosity of a factor of 10 across the 670 km discontinuity.

The other geophysical observable we have discussed is surface deformation, which is expected to show a correlation with the long-wavelength geoid. Before this signature of mantle dynamics can be measured, however, the large effects of crustal thickness variations on topography must be removed. A simple, preliminary result is obtainable if we limit our comparison to old shield areas. For these areas, erosion can be assumed to have established a constant continental freeboard over geologic time.

Also limiting our comparison to regions removed from collision zones, we find that the African shield, in a major geoid high, is high standing, while the Siberian and the Canadian shields, in major geoid lows, are relatively low standing (NOAA, 1980). Similar conclusions can be reached from the hypsographic curves of Harrison et al. (1981). From these observations we estimate that the impedance, Z, at long wavelengths is of order +0.1. This is consistent with the results for the long-wavelength correlation between seismic velocity heterogeneity in the lower mantle and the geoid. More detailed analysis using crustal thickness and density data should yield more accurate quantitative results over a broader spectral range.

Within the framework of a spherically symmetric model, we are unable to reconcile the evidence from geoid anomalies over subduction zones that the effective viscosity increases by two orders of magnitude with the preliminary evidence from seismic studies and elevation of shield areas that the viscosity increases by only one order of magnitude. Perhaps not surprisingly, lateral variations in effective viscosity are suggested. Further theoretical improvements in our understanding of geoid anomalies in a dynamic Earth are clearly desirable. Modelling of the effects of lateral viscosity variations and nonlinear rheology would be particularly useful in understanding the geoid signature of subducted slabs, since they exist in zones characterized by large deviatoric stresses and temperature gradients. We would also like to model the effects of adiabatic compressibility and adiabatic phase changes in the mantle. These improvements will require numerical modelling and would therefore imply a major departure from the analytical methods we have described.

Summary

We have used spherical Newtonian Earth models to investigate the relationship between driving loads and their geoid and surface topographic signatures. Normalized surface potential, K, and deformation impedance, Z, have been calculated for representative cases of viscous and chemical stratification in the mantle. The following dynamical effects are found to be important for geoid interpretation:

(1) The response of the upper surface to loading has a large effect upon the behavior of the geoid signature, with negative geoid anomalies correlated with positive driving density contrasts for the simplest models without viscosity contrasts.

(2) Considerable amplification of deep, higher harmonic loads is reflected in the geoid due to the manner in which flow stresses drive boundary deformation.

(3) The choice of the upper surface boundary condition (free-slip vs. no-slip) does not strongly affect the basic behavior of the response functions.

(4) Lower viscosity in the upper mantle tends to drive K positive and Z toward larger values. For a very large viscosity contrast, the upper surface deformation may reverse sign due to gravitational pressure resulting in a singularity in Z.

(5) The introduction of a flow barrier corresponding to a chemical boundary has a pronounced effect on the magnitude of the response functions K and Z. In particular, density contrasts in the upper mantle have a much smaller geoid signature; this might help distinguish the two basic flow models when loads within the upper mantle can be estimated.

(6) Near-boundary density contrasts are masked by the deformation of the boundary.

(7) Self-gravitation is important for low harmonic degree loading.

(8) Viscous relaxation of boundaries occurs on a much shorter timescale than convective flow so that boundary deformation due to internal loading can be considered steady-state.

(9) Applications of this theory to global data from geodesy and seismology show that the dynamical effects we have predicted can be observed for the Earth. Improved analysis should yield a better understanding of mantle dynamics.

APPENDIX 1: Analytical Details for the Whole Mantle Problem

In order to solve equations (22) the boundary conditions (25) must be analytically continued to their respective spherical reference surfaces which are the mean Earth radius a and the mean core radius c. The field variables are continued within the medium through which they are propagated in equations (22), in this case the mantle. To first order, the only terms in vectors (25) affected are the radial normal stress and the gravitational acceleration. Since the stress above the Earth's surface is zero, the normal nonhydrostatic stress at the reference boundary is just the apparent jump described by equation (8), so

$$\mathbf{u}^N(a) = \left[0 \, , \, 0 \, , \, -\rho_m \, g(a) a \, \delta r / \eta_0 \, , \, a \, \tau_{r\theta_a} / \eta_0 \, , \, \rho_0 a \, \delta V_a / \eta_0 \, , \, \frac{\rho_0 a^2}{\eta_0} \, \frac{\partial \delta V}{\partial r} \right]^T \tag{A1(a)}$$

or

$$\mathbf{u}^F(a) = \left[0 \, , \, v_{\theta a} \, , \, -\rho_m \, g(a) a \, \delta r / \eta_0 \, , \, 0 \, , \, \rho_0 a \, \delta V_a / \eta_0 \, , \, \frac{\rho_0 a^2}{\eta_0} \, \frac{\partial \delta V_a}{\partial r} \right]^T \tag{A1(b)}$$

At the core, using equation (6) and the perturbed hydrostatic stress, $-\rho_c \, \delta V_c$, at the reference level as seen in the mantle we obtain

$$\mathbf{u}^F(c) = \left[0 \, , \, v_{\theta_c} \, , \, \delta\rho_{cm} \, g(c) c \, \delta r_c / \eta_0 - \rho_c \, \delta V_c \, c / \eta_0 \, , \, 0 \, , \, \rho_0 c \, \delta V_c / \eta_0 \, , \, \frac{\rho_0 c^2}{\eta_0} \, \frac{\partial \delta V_c}{\partial r} \right]^T \tag{A2}$$

Note that the normal stress term in this vector contains not only the effective stress discontinuity (proportional to δr_c) but also a gravitational pressure term (proportional to δV_c); this represents the pressure field within the inviscid core.

The deformations δr_a and δr_c cause first-order perturbations in the potential δV in addition to that due to the driving density contrast σ at depth b. These perturbations are appropriately treated as effective surface masses at the reference boundary levels as discussed above in our analytical treatment of boundary deformation. We now calculate the potential at $r = a$ (lithosphere) due to a surface mass distribution also at $r = a$. The perturbed potentials just above and below the surface are:

$$\delta V_a^+ = \sum_l A_l \frac{a^l}{r^{l+1}} Y_l \tag{A3}$$

$$\delta V_a^- = \sum_l A_l \frac{r^l}{a^{l+1}} Y_l$$

since $\nabla^2 \delta V = 0$ away from the surface density contrast.

At the surface $\nabla^2 \delta V = 4\pi G \rho$, so, integrating over a volume Ω enclosed by a surface S,

$$\int_\Omega (4\pi G \rho) d\Omega = \int_\Omega \nabla^2 (\delta V) d\Omega = \int_S \nabla(\delta V) \cdot \mathbf{n} da \tag{A4}$$

by Green's Theorem. Integrating over a "pill box" containing a piece of the surface density contrast and shrinking the radial thickness of the box to zero, $\rho \rightarrow \sigma dr$, $\mathbf{n} \rightarrow \hat{r}$, $\nabla(\delta V) \rightarrow \frac{\partial(\delta V)}{\partial r}$ and (A4) becomes

$$\int_S \frac{\partial(\delta V)}{\partial r} da = \left[\frac{\partial(\delta V)}{\partial r} \right]_{a^-}^{a^+} = 4\pi G \sigma \tag{A5}$$

For our perturbed boundary conditions we impose an effective surface mass σ_{eff} such that the apparent jump in normal stress at the reference boundary is given by $\delta \tau_{rr_a} = g(a) \sigma_{eff}$. Expanding $\delta \tau_{rr_a} = \sum_l \delta \tau_{rr_a}^l Y_l$, where we have made the l^{th}

harmonic dependence explicit, and using the above expansions for δV to calculate $\left[\frac{\partial(\delta V)}{\partial r}\right]_-^+$ we obtain the desired result:

$$\delta V_a^- = \frac{-4\pi G a}{g(a)} \sum_l \frac{\delta\tau_{rr_a}^l}{2l+1} (r/a)^l Y_l \tag{A6}$$

Similarly at $r = c$ (core-mantle boundary) we obtain:

$$\delta V_c^+ = \frac{4\pi G c}{g(c)} \sum_l \frac{\delta\tau_{rr_c}^l}{2l+1} (c/r)^{l+1} Y_l \tag{A7}$$

Again, for the density contrast at b:

$$\delta V_b^+ = 4\pi G b \sum_l \frac{\sigma_l}{2l+1} (b/r)^{l+1} Y_l \tag{A8}$$

$$\delta V_b^- = 4\pi G b \sum_l \frac{\sigma_l}{2l+1} (r/b)^l Y_l$$

The total potentials at a and at c are given by

$$\delta V_a^{tot} = (\delta V_a^- + \delta V_c^+ + \delta V_b^+)_{r=a} \tag{A9}$$

$$\delta V_c^{tot} = (\delta V_a^- + \delta V_c^+ + \delta V_b^-)_{r=c}$$

These expressions contain explicitly the perturbed potentials due to boundary deformation that are required for a self-gravitating model. Writing the $\delta\tau_{rr}^l$'s in terms of the δr's we obtain the following expressions for the potentials in terms of the boundary deformations and σ^l:

$$\delta V_a = \frac{4\pi G}{2l+1} \left[a\,\rho_m\,\delta r_a + c\,(c/a)^{l+1} \delta\rho_{cm}\,\delta r_c + b\,(b/a)^{l+1} \sigma^l \right] \tag{A10}$$

$$\frac{\partial \delta V_a}{\partial r} = \frac{4\pi G}{2l+1} \left[l\,\rho_m\,\delta r_a - (l+1)(c/a)^{l+2} \delta\rho_{cm}\,\delta r_c - (l+1)(b/a)^{l+2} \sigma^l \right]$$

$$\delta V_c = \frac{4\pi G}{2l+1}\left[a\,(c/a)^l \rho_m\,\delta r_a + c\,\delta\rho_{cm}\,\delta r_c + b\,(c/b)^l \sigma^l\right]$$

$$\frac{\partial \delta V_c}{\partial r} = \frac{4\pi G}{2l+1}\left[l(c/a)^{l-1}\rho_m\,\delta r_a - (l+1)\delta\rho_{cm}\,\delta r_c + l(c/b)^{l-1}\sigma^l\right]$$

Combining the first four of equations (22) with reference boundary expressions (A1(a)) and (A2) and potentials (A10), we obtain the following equations for δr_a and δr_c as well as for $v_{\theta c}$ and $\tau_{r\theta_a}$:

$$P_{ca}^{i2} v_{\theta c} + \left\{ P_{ca}^{i3}(1-\rho_c^* cC/\eta_0) + \left[P_{ca}^{i5} - (l+1)P_{ca}^{i6}\right] C \right\} \delta\rho_{cm}\, g\,(c)\delta r_c \qquad \text{(A11)}$$

$$+ \left[(P_{ca}^{i5} + lP_{ca}^{i6})A - \delta_{i3} - P_{ca}^{i3}\rho_c^* aA/\eta_0\right] \rho_m\, g\,(a)\delta r_a - \delta_{i4}\, a\,\tau_{r\theta_a}/\eta_0$$

$$= -P_{ca}^{i3}\rho_c^* B - P_{ba}^{i3} bg\,(b)/\eta_0 + P_{ba}^{i6} 4\pi b^2 G\,\rho_0/\eta_0 - [P_{ca}^{i5} + lP_{ca}^{i6}]B$$

and where the driving terms on the right are usually normalized by setting σ to unity. Exact values of the propagator elements $\underline{\mathbf{P}}_{ca}^{ij}$, $\underline{\mathbf{P}}_{ba}^{ij}$ can be calculated according to the procedures in Hager and O'Connell, 1981, and equations (A11) can be solved in a straightforward manner. With these solutions for the boundary deformations and the potentials via (A10) we can calculate the kernels defined by expressions (14) through (17).

APPENDIX 2: Viscous Relaxation Times for Spherical Earth Models

We need to demonstrate that the boundaries relax with time constants much smaller than the timescales for convective flow. These time constants can be obtained from consideration of the normal mode problem for relaxation in a radially stratified viscous Earth model. Viscoelastic solutions have been presented by Wu and Peltier (1982), but since convective timescales are far in excess of Maxwell times in the Earth the effect of elasticity can be ignored. The purely viscous normal mode problem is much less complicated and was first investigated by Parsons (1972). Using propagator matrix methods which are described in detail by O'Connell, Hager, and Richards (in preparation), we have solved for the relaxation spectra of the self-gravitating spherical models used in the geoid calculations that follow. By setting all the stress-flow variables and boundary deformations proportional to $exp\,(-t\,/\tau_i)$ and solving the resulting system of homogeneous equations (see Hager and O'Connell, 1979), the eigenvalues τ_i as well as the eigenmodes for flow, stress and deformation are obtained. Each *flow boundary* introduces an additional relaxation time constant and eigenmode. For example, for a simple model with an inviscid core overlain by a uniform mantle, we obtain a mantle and a core mode. These modes are, respectively, symmetric and antisymmetric with respect to the sense of boundary relaxation, and the time constant for the antisymmetric mode grows rapidly as the thickness of the flow layer decreases (Solomon, Comer, and Head, 1982).

In Table I we have listed the parameters used for the models presented in this chapter. Density values have been chosen to match the total mass of each layer (as well as the Earth) and the gravity at each boundary (Dziewonski, Hales, and Lapwood, 1975), although with such a layering scheme it is impossible to simultaneously

match other Earth parameters, such as moment of inertia, which are not important to this study. Also, for the viscous relaxation problem we use smaller, more realistic density contrasts across internal boundaries (adiabatic compression in the mantle being ignored), since these values strongly affect the time constants obtained.

The two basic models used are those of whole mantle and layered mantle flow, both with an inviscid core. Arbitrary viscosity and density layering can be treated, so the models presented here are chosen to be illustrative rather than exhaustive. In Figures A1 and A2 we plot the relaxation time constants (eigenvalues) and the associated boundary deformations associated with each eigenmode. An individual eigenmode consists of a flow field throughout the mantle and could be represented. However, for our purposes the boundary deformations serve to identify both the appropriate branch (mode) and the relative excitation of each mode as we demonstrate later. Figures A1(a) and (b) show the results which are obtained for the uniform mantle model (Model A). For each harmonic number l, following the nomenclature of Peltier (1976), there is a core mode (C) and a mantle mode (M0). For $l \leq 20$, the largest relaxation time obtained is less than 10^4 yrs. and is associated with the C mode. Note that for high harmonic order the relaxation time increases with increasing wavenumber as in equation (10). In Figure A1(b) we plot the core deformation amplitude normalized by the surface deformation amplitude for each mode. As we would expect, the modes are strongly coupled at low-harmonic order and relatively decoupled at higher values of l, thus distinguishing the C and M0 mode branches. Also shown in Figure A1(a) is the very slight change in relaxation times caused by modelling the upper 100 km of mantle ("lithosphere") with two orders of magnitude higher viscosity than the mantle ($\eta = 10^{23}$ Pa-sec, or $\eta^* = \eta/\eta_0 = 100$ with $\eta_0 = 10^{21}$

Pa-sec denoting the reference or lower mantle viscosity). For the wavelengths of interest here such a layer is essentially transparent. In Figures A1(c) and (d) and A1(e) and (f) we illustrate the effect of low viscosity ($\eta^* = .01$) in the upper mantle above 200 km and 670 km, respectively. There are three principal effects to be noted: (1) From the amplitude plots we see that the two modes tend to be decoupled by the low viscosity channel. (2) The C mode relaxation times are essentially unaffected while the mantle mode times are decreased by one to two orders of magnitude. (3) The strength of these effects increases with the thickness of the low viscosity channel. From these simple cases illustrating the effects of viscosity layering we conclude that, for a broad class of whole mantle flow models, no relaxation times greater than 10^4 yrs. are obtained for a lower mantle viscosity of 10^{21} Pa-sec.

We now consider models for two layer, shear coupled flow in the mantle (Models D and E) in which the depth of the top layer corresponds to the 670km discontinuity. Since the upper and lower mantle do not mix across the 670 km discontinuity in these models, we have introduced an internal boundary whose deformation contributes another mantle mode (M1). This boundary could be a chemical discontinuity or a phase boundary with sluggish kinetics. Figures A2(a) through (c) show, respectively, the relaxation times, the relative deformation of the core-mantle boundary, and the relative deformation of the 670 km discontinuity for each of the modes C, M0, and M1. The relaxation times for the C and M0 modes are essentially the same as those obtained for the whole mantle case. However, the M1 mode has a much longer relaxation time (about 10^5 yrs.). The boundary deformation amplitudes exhibit a much more complicated dependence upon l than for previous models, and the meaning of these eigenmodes will become more apparent when we address the problem of mode

excitation; for now we will concentrate on the relaxation times. In particular, when the density contrast across the 670 km discontinuity is decreased from 0.5 to 0.3 Mg/m^3, a significant increase in the M1 time occurs (Figure A2(a)). This can be easily understood physically since the buoyancy force that tends to restore a boundary to its reference configuration is proportional to the density jump, $\delta\rho$, at that boundary. Therefore, as $\delta\rho$ is made smaller the associated relaxation time increases accordingly. Since the actual density contrasts within the Earth are not exactly known, it is important to remember this effect when modelling relaxation times. In Figures A2(d) through (f) we illustrate the effects of low viscosity in the upper mantle for two-layer flow. Both the M0 and M1 modes accordingly exhibit smaller relaxation times, the effect on M1 being one-half to one order of magnitude. We conclude that for the two-layer flow model the longest relaxation time expected is about 10^5 yrs. An upper mantle flow layer involving chemical boundaries at say 400 km or 220 km (Anderson, 1979) would result in longer relaxation times, but we have not included these more complicated cases in our geoid models.

None of the relaxation times calculated so far have been in excess of 10^5 yrs., which for reasonable mantle flow velocities would allow for about 10 km transport in the mantle. This is indeed small compared to the flow dimensions, so, for lower mantle viscosities of 10^{21} Pa-sec, the assumption of steady-state flow is verified. Recent studies by Peltier (1981) and Yuen et al. (1982) indicate that the viscosity of the lower mantle is less than 10^{22} Pa-sec. Since the relaxation problem scales linearly with reference viscosity (which we always take to be that of the lower mantle), it is not likely that the steady-state hypothesis for boundary deformation is seriously violated for the overall convective circulation in the mantle. Alternatively, computing the

ratio of flow velocity to the velocity of relaxation of the boundary as in equation (12), the viscosity cancels, indicating that boundaries relax rapidly relative to changes in the flow regime whatever the mantle viscosity.

Acknowledgements

We thank Don L. Anderson for stimulating discussion and R. J. O'Connell, Roger Phillips, and an anonymous reviewer for very useful comments on the manuscript. This work was supported by NASA grants NSG-7610 and NAG-5315 and an Alfred P. Sloan Foundation Fellowship awarded to B. H. Hager. Contribution No. 3981, Division of Geological and Planetary Sciences, California Institute of Technology, Pasadena, CA 91125.

REFERENCES

Anderson, D. L., 1979, Chemical stratification of the mantle, *J. Geophys. Res., 84,* 6297-6298.

Ashby, M. F. and R. A. Verrall, 1977, Micromechanisms of flow and fracture, and their relevance to the rheology of the upper mantle, *Phil. Trans. R. Soc. Lond. A., 288,* 59-95.

Berckhemer, H., F. Auer, and J. Drisler, 1979, High temperature anelasticity and elasticity of mantle peridotites, *Phys. Earth Planet. Int., 20,* 48-59.

Cathles, L. M., III, 1975, *The Viscosity of the Earth's Mantle,* Princeton University Press, Princeton.

Chase, C. G., 1979, Subduction, the geoid, and lower mantle convection, *Nature, 282,* 464-468.

Chase, C. G. and M. K. McNutt, 1982, The geoid: effect of compensated topography and uncompensated oceanic trenches, *Geophys. Res. Lett., 9,* 29-32.

Clark, J. A., W. F. Farrell, and W. P. Peltier, 1978, Global changes in postglacial sea level: A numerical calculation, *Quaternary Research, 9,* 265-287.

Clayton, R. W. and R. P. Comer, 1983, A tomographic analysis of mantle

heterogeneities from body wave travel times, *EOS Trans. AGU, 62,* 776.

Crough, S. T. and D. M Jurdy, 1980, Subducted lithosphere, hotspots, and the geoid, *Earth. Planet. Sci. Lett., 48,* 15-22.

Dziewonski, A. M., 1984, Mapping the lower mantle: determination of lateral heterogeneity in P-velocity up to degree 6, *J. Geophys. Res., 89,* 5929-5952.

Dziewonski, A. M. and R. A. W. Haddon, 1974, The radius of the core-mantle boundary inferred from travel time and free oscillation data: A critical review, *Phys. Earth. Planet. Int., 9,* 28-35.

Dziewonski, A. M., B. H. Hager, and R. J. O'Connell, 1977, Large-scale heterogeneities in the lower mantle, *J. Geophys. Res., 82,* 239-255.

Dziewonski, A. M., A. L. Hales, and E. R. Lapwood, 1975, Parametrically simple earth models consistent with geophysical data, *Phys. Earth Plan. Int.,10,* 12.

Gantmacher, F. R., 1960, *The Theory of Matrices,* translated from Russian by K. A. Hirsch, *I, II,* Chelsea Publishing Co., New York.

Guier, W. H., 1963, Determination of the non-zonal harmonics of the geopotential from satellite Doppler data, *Nature, 200* , 124-125.

Hager, B. H., 1983, Global isostatic geoid anomalies for plate and boundary layer models of the lithosphere, *Earth Planet. Sci. Lett., 63,* 97-109.

Hager, B. H., 1984, Subducted slabs and the geoid; constraints on mantle rheology and flow, *J. Geophys. Res., 89,* 6003-6015.

Hager, B. H., R. W. Clayton, M. A. Richards, R. P. Comer, and A. M. Dziewonski, 1985, Lower mantle heterogeneity, dynamic topography, and the geoid, *Nature, 313,* 541-545.

Hager, B. H. and R. J. O'Connell, Subduction zone dip angles and flow driven by plate motion, 1978, *Tectonophysics, 50,* 111-133.

Hager, B. H. and R. J. O'Connell, 1979, Kinemetic models of large-scale mantle flow, *J. Geophys. Res., 84* , 1031-1048.

Hager, B. H., and R. J. O'Connell, 1981, A simple global model of plate dynamics and mantle convection, *J. Geophys. Res., 86* , 4843-4867.

Harrison, C. G. A., G. W. Brass, E. Saltzman, J. Sloan, II, J. Southam, and J. M. Whitman, 1981, Sea level variations, global sedimentation rates, and the hypsographic curve, *Earth Planet. Sci. Lett., 54,* 1-16.

Haskell, N. A., 1935, The motion of a viscous fluid under a surface load, *Physics,*

6 , 265-269.

Jacobsen, S. B. and G. J. Wasserburg, 1980, A two-reservoir recycling model for mantle-crust evolution, *Proc. Natl. Acad. Sci. USA, 77,* 6298-6302.

Jarvis, G. T. and D. P. McKenzie, Convection in a compressible fluid with infinite Prandtl number, 1980, *J. Fluid Mech., 96,* 515-583.

Kaula, W. M, 1963a, Tesseral harmonics of the gravitational field and geodetic datum shifts derived from camera observations of satellites, *J. Geophys. Res., 68,* 473-484..

Kaula, W. M., 1963b, Elastic models of the mantle corresponding to variations in the external gravity field, *J. Geophys. Res., 68,* 4967-4978.

Kaula, W. M., 1972, Global gravity and tectonics, in E. C. Robertson (ed.), *The Nature of the Solid Earth,* McGraw-Hill, New York, 386-405.

Love, A. E. H., 1911, *Some Problems of Geodynamics,* New York: Dover Publications.

Masters, G., T. H. Jordan, P. G. Silver, and F. Gilbert, 1982, Aspherical Earth structure from fundamental spheroidal-mode data, *Nature, 298,* 609-613.

McKenzie, D.P., 1977, Surface deformation, gravity anomalies and convection, *Geophys. J. Roy. Astron. Soc., 48,* 211-238.

McKenzie, D. P. and C. Bowin, 1976, The relationship between bathymetry and gravity in the Atlantic ocean, *J. Geophys. Res., 81,* 1903-1915.

Morgan, W. J., 1965, Gravity anomalies and convection currents 1. A sphere and cylinder sinking beneath the surface of a viscous fluid, *J. Geophys. Res., 70,* 6175-6185.

Munk, W. H. and G. J. F. MacDonald, 1960, *The Rotation of the Earth: A Geophysical Discussion,* Cambridge University Press, Cambridge.

Nakanishi, I. and D. L. Anderson, 1982, Worldwide distribution of group velocity of mantle Rayleigh waves as determined by spherical harmonic inversion, *Bull. Seismo. Soc. Am., 72,* 1183-1192.

National Oceanic and Atmospheric Administration, 1980, Environmental Data Service, NGS Data Center, Boulder, Colorado: Topographic data for one-degree size areas.

O'Connell, R. J., 1971, Pleistocene glaciation and the viscosity of the lower mantle, *Geophys. J. Roy. Astron. Soc., 23,* 299-327.

Parsons, B. E., 1972, Changes in the Earth's shape, *Ph.D Thesis,* Cambridge University.

Parsons, B., and S. Daly, 1983, The relationship between surface topography, gravity anomalies and the temperature structure of convection, *J. Geophys. Res., 88,* 1129-1144.

Passey, Q. R., 1981, Upper mantle viscosity derived from the difference in rebound of the Provo and Bonneville shorelines: Lake Bonneville Basin, Utah, *J. Geophys. Res., 86,* 11701-11708.

Pekeris, C. L., 1935, Thermal convection in the interior of the Earth, *Mon. Not. Roy. Astron. Soc., Geophys. Suppl., 3,* 343-367.

Peltier, W. R., 1976, Glacio-isostatic adjustment-II. The inverse problem, *Geophys. J. Roy. Astron. Soc., 46,* 669-705.

Peltier, W. R., 1981, Ice age geodynamics, *Ann. Rev. Earth Planet. Sci, 9,* 199-225.

Ricard, Y., L. Fleitout, and C. Froidevaux, 1984, Geoid heights and lithospheric stresses for a dynamical Earth, *Annales Geophysicae, 2,* 267-286.

Richards, M. A. and B. H. Hager, 1981, A dynamically consistent calculation of

geoid anomalies in a viscous planet with implications for geoid interpretation, *EOS Trans. AGU, 62,* 1077.

Richter, F. M. and D. P. McKenzie, 1981, On some consequences and possible causes of layered convection, *J. Geophys. Res., 86,* 6133-6142.

Runcorn, S. K., 1964, Satellite gravity measurements and a laminar viscous flow model of the Earth's mantle, *J. Geophys. Res., 69,* 4389-4394.

Runcorn, S. K., 1967, Flow in the mantle inferred from the low degree harmonics of the geopotential, *Geophys. J. Roy. Astron. Soc., 14,* 375-384.

Solomon, S. C., R. P. Comer, and J. W. Head, 1982, The evolution of impact basins: Viscous relaxation of topographic relief, *J. Geophys. Res., 87,* 3975-3992.

Twiss, R. J., 1976, Structural superplastic creep and linear viscosity in the Earth's mantle, *Earth Planet. Sci. Lett., 33,* 86-100.

Watts, A. B., 1978, An analysis of isostasy in the world's oceans 1. Hawaiian-Emperor seamount chain, *J. Geophys. Res., 83,* 5989-6004.

Weertman, J., 1968, Dislocation climb theory of steady-state creep, *Trans. Am. Soc. Met, 61,* 681-694.

Woodhouse, J. H. and A. M. Dziewonski, 1984, Mapping the upper mantle: three dimensional modelling of Earth structure by inversion of seismic waveforms, *J. Geophys. Res., 89,* 5953-5986.

Wu, P., and W. R. Peltier, 1982, Viscous gravitational relaxation, *Geophys. J. Roy. Astron. Soc., 70,* 435-486.

Yuen, D. R., Sabadini, and E. V. Boschi, 1982, Viscosity of the lower mantle as inferred from rotational data, *J. Geophys. Res., 87,* 10745-10762.

Table 1 - Basic models for spherical Earth calculations. Parameters include Earth and core radii, c and a, core, upper, and lower mantle densities, ρ_c, ρ_u, and ρ_l (in Mg/m^3), upper and lower mantle viscosities, η_u and η_l, effective density jumps at the core-mantle boundary and the 670 km discontinuity, $\delta\rho_{cm}$ and $\delta\rho_{lu}$, and the depth of the upper flow or viscosity layer, d.

TABLE 1: Model Parameters

All Models

c	a	ρ_c	$\delta\rho_{cm}$
3480km	6371km	11.0	4.5

Whole Mantle Flow

Model	ρ_l	$\delta\rho_{lu}$	ρ_u	η_l	η_u	d
A	4.43	0.0	4.43	10^{21}Pa s	10^{21}Pa s	---
B	4.43	0.0	4.43	10^{21}Pa s	10^{19} *or* 10^{20}Pa s	200km
C	4.43	0.0	4.43	10^{21}Pa s	10^{19} *or* 10^{20}Pa s	670km

Layered Flow

Model	ρ_l	$\delta\rho_{lu}$	ρ_u	η_l	η_u	d
D	4.92	0.5	3.50	10^{21}Pa s	10^{21}Pa s	670km
E	4.92	0.5	3.50	10^{21}Pa s	10^{19} *or* 10^{20}Pa s	670km

Figure 1 - Illustrations of flow models for spherical Earth calculations ($l=3$): (a) Whole mantle flow. (b) Flow with a chemical barrier at the 670 km discontinuity. The "+" and "-" signs indicate positive and negative density contrasts. The dashed lines are reference boundaries and the solid lines represent the displaced boundaries. Streamlines indicate the sense of flow.

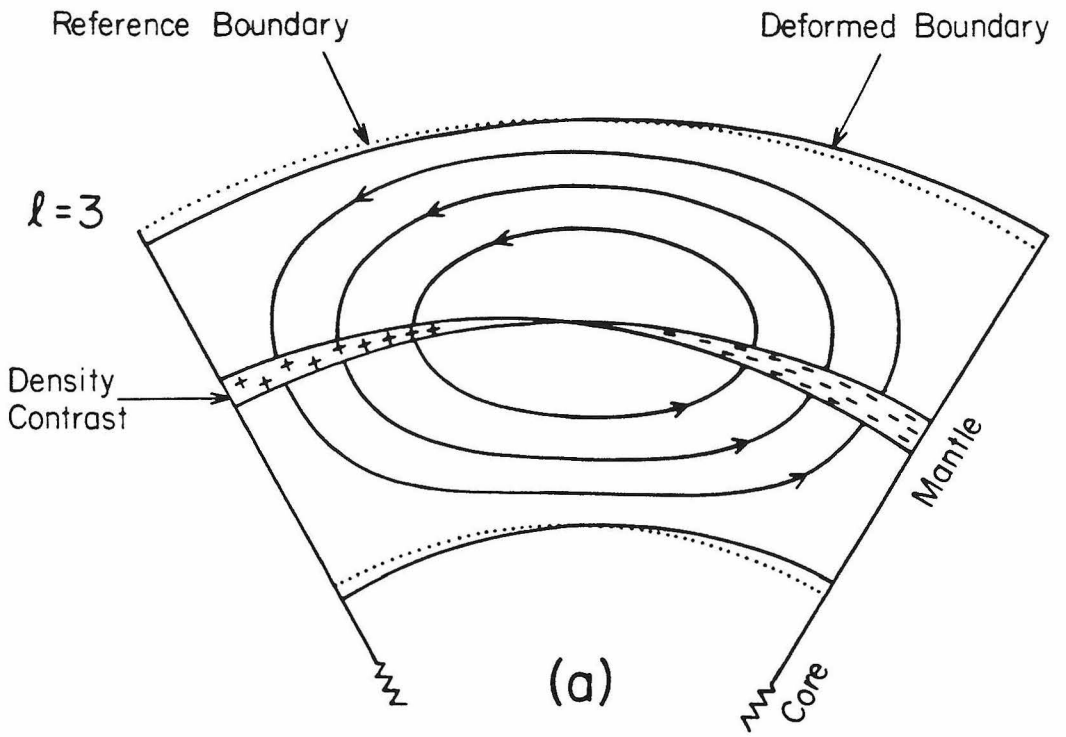
Reference Boundary
Deformed Boundary
ℓ=3
Density
Contrast
Mantle
(a)
Core

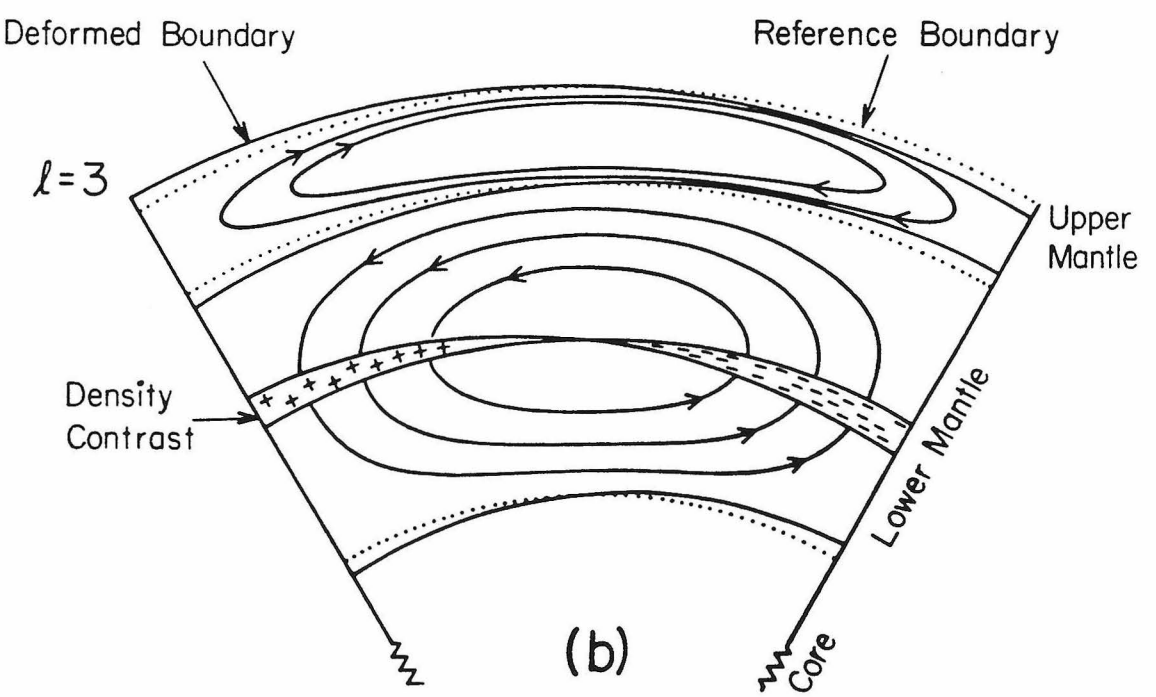
Deformed Boundary
Reference Boundary
ℓ=3
Upper
Mantle
Density
Contrast
Lower Mantle
(b)
Core

Figure 2 - Illustration of the geometry for the analytical treatment of deformation of the boundary between two fluid half spaces with densities ρ_1 and ρ_2. The actual boundary (solid line) is displaced an amount $\delta z(x)$ from the reference boundary (dashed line).

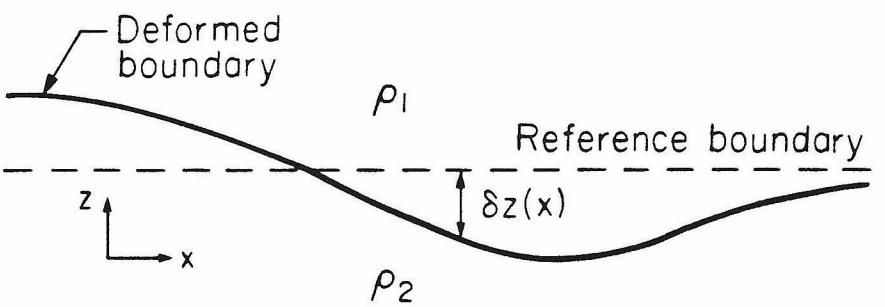
Deformed
boundary
ρ_1
Reference boundary
$\delta z(x)$
z
x
ρ_2

Figure 3 - Illustration of the Fourier flow analysis in a two-dimensional half space. The surface density contrast $\sigma_d(k)cos(kx)$ at depth d excites flow, resulting in deformation of the free surface. We assume here that the advection of the density contrast by the flow is negligible on the timescale for establishing the boundary deformation.

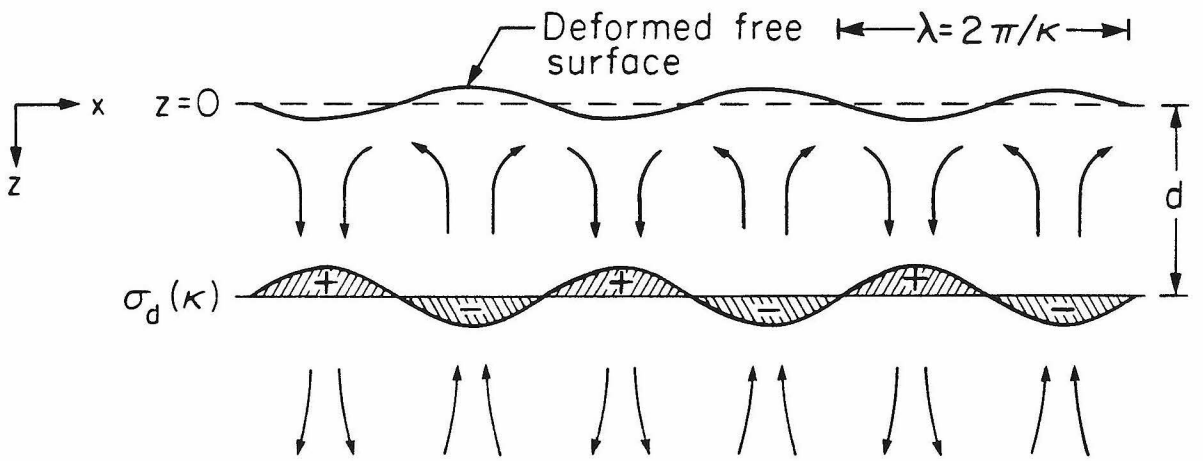
Deformed free surface
λ = 2π/κ
x
z
z = 0
d
σd (κ)
+
+
+
−
−
−

Figure 4 - Mass displacement at the boundaries as a function of loading depth for harmonic degrees 2, 7, and 20 (whole mantle flow). Plots are normalized to a unit density contrast load. The "S" curve is for the upper surface, "C" is for the core-mantle boundary, and "T" is the total mass displaced. Figures (d) and (e) show the effect of low viscosity in the upper mantle for harmonic degree 7. Figures (a) through (e) are for FF boundary conditions and (f) through (h) are for NF conditions.

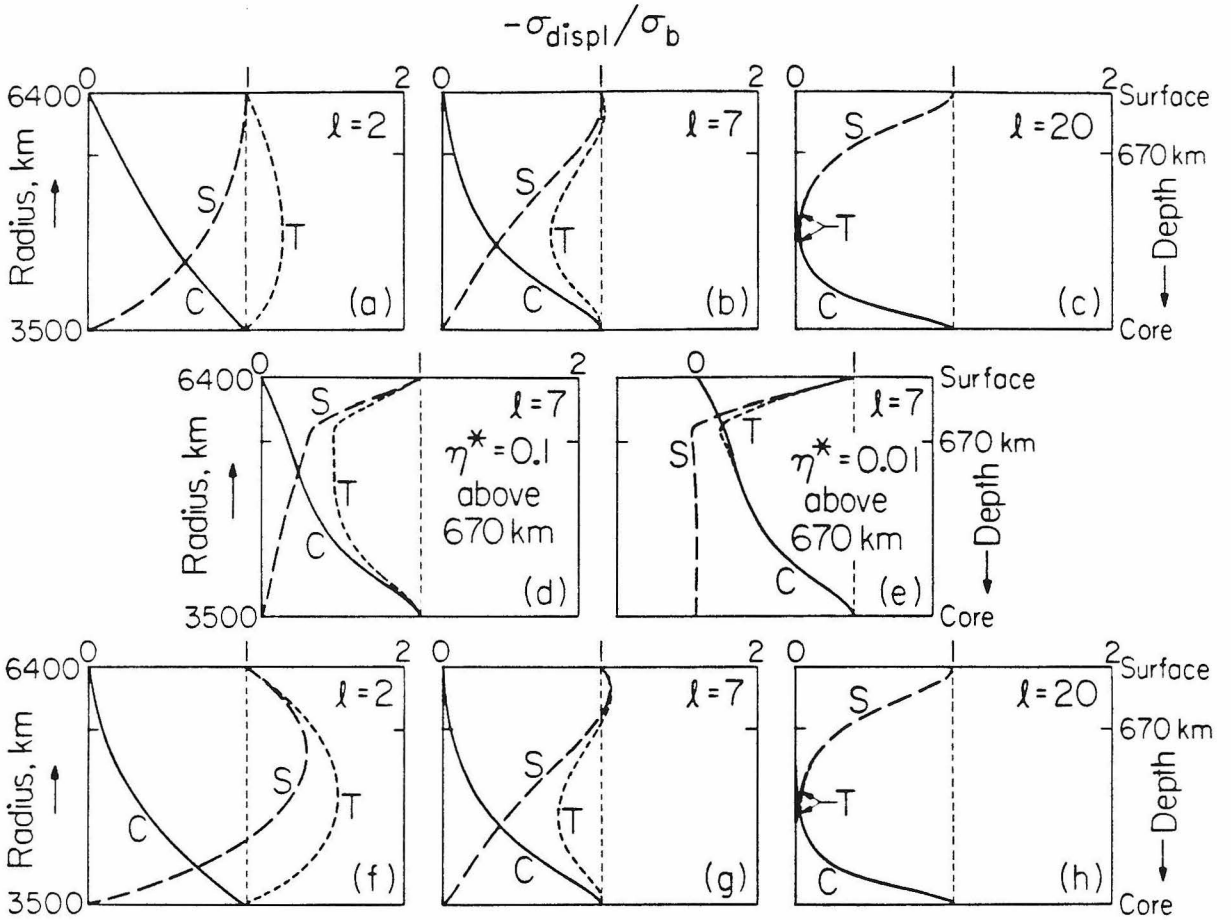
$-\sigma_{displ}/\sigma_b$
6400
3500
Radius, km
0
2
S
T
C
$\ell = 2$
(a)
$\ell = 7$
(b)
$\ell = 20$
(c)
Surface
670 km
Depth
Core
$\ell = 7$
$\eta^* = 0.1$
above
670 km
(d)
$\eta^* = 0.01$
above
670 km
(e)
(f)
(g)
(h)

Figure 5 - Viscous normal mode excitation as a function of loading depth for whole mantle models. The "C" (core) and "M0" (mantle) modes are unit normalized and their excitation amplitudes are plotted for harmonic degrees 2, 7, and 20. Figures (d) and (e) illustrate the effect of low viscosity in the upper mantle.

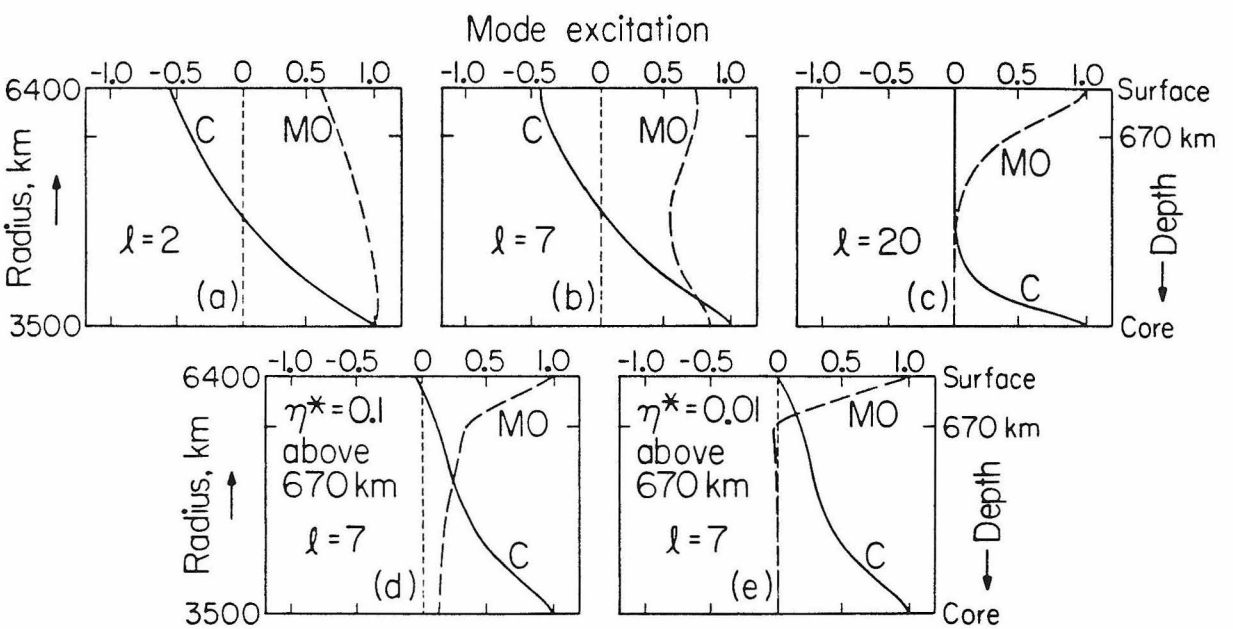
Mode excitation
-1.0 -0.5 0 0.5 1.0
6400
3500
Radius, km
C
MO
ℓ = 2
(a)
ℓ = 7
(b)
ℓ = 20
(c)
Surface
670 km
Depth
Core
η* = 0.1
above
670 km
(d)
η* = 0.01
above
670 km
(e)

Figure 6 - Absolute values of gravitational potential contributions from the density contrast at the indicated depth ("σ"), the deformation of the core-mantle boundary ("c"), and the upper surface deformation ("a") for harmonic degrees 2, 7, and 20. (The "a" and "c" curves actually have opposite sign from the "σ" curve). Values plotted are normalized by the maximum value of curve "a" for convenience in comparison. Figure (d) shows the upper surface deformation *not* corrected for self-gravitation (curve "a'"). Figures (a) through (c) are for FF boundary conditions and (d) through (f) are for NF conditions, all for uniform mantle viscosity.

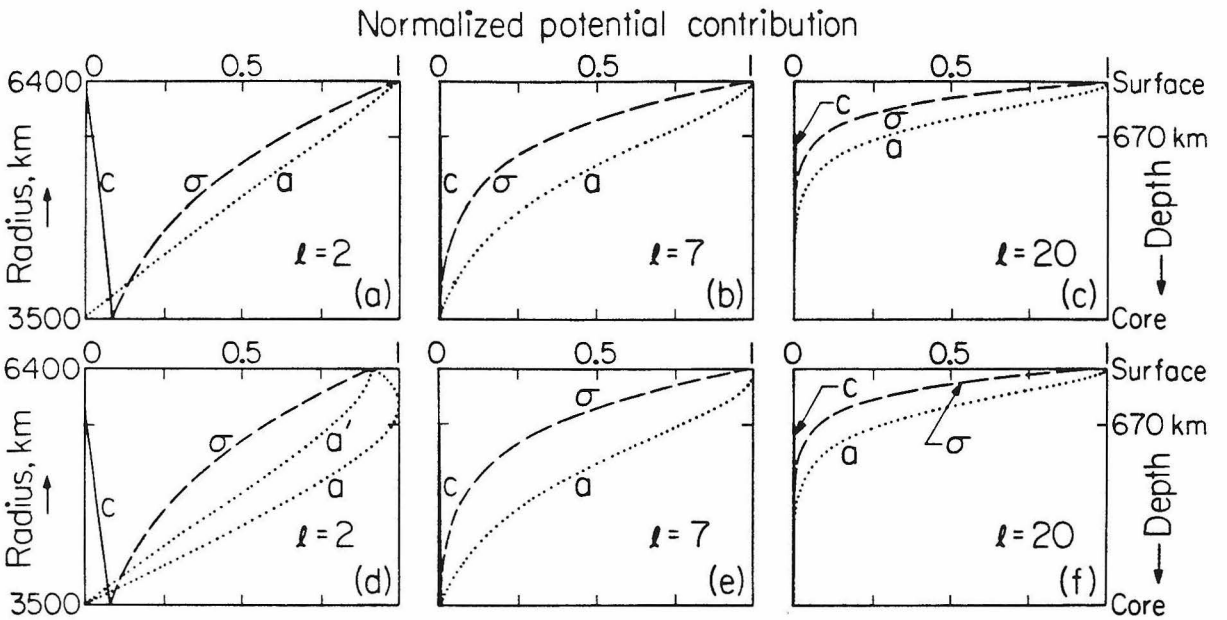
Normalized potential contribution
6400
3500
Radius, km
0
0.5
1
c
σ
a
ℓ = 2
(a)
ℓ = 7
(b)
ℓ = 20
(c)
(d)
(e)
(f)
Surface
670 km
Depth
Core

Figure 7 - Surface potential response, K, as a function of loading depth for harmonic degrees 2, 7, and 20. Illustrated are the four possible combinations of free-slip (F) and no-slip (N) boundary conditions, all calculated for a uniform viscosity mantle. The light, straight lines in (a) and (b) show the two-dimensional half space result, $K = -kd$. The dashed line at $K=1$ gives the rigid Earth result for comparison.

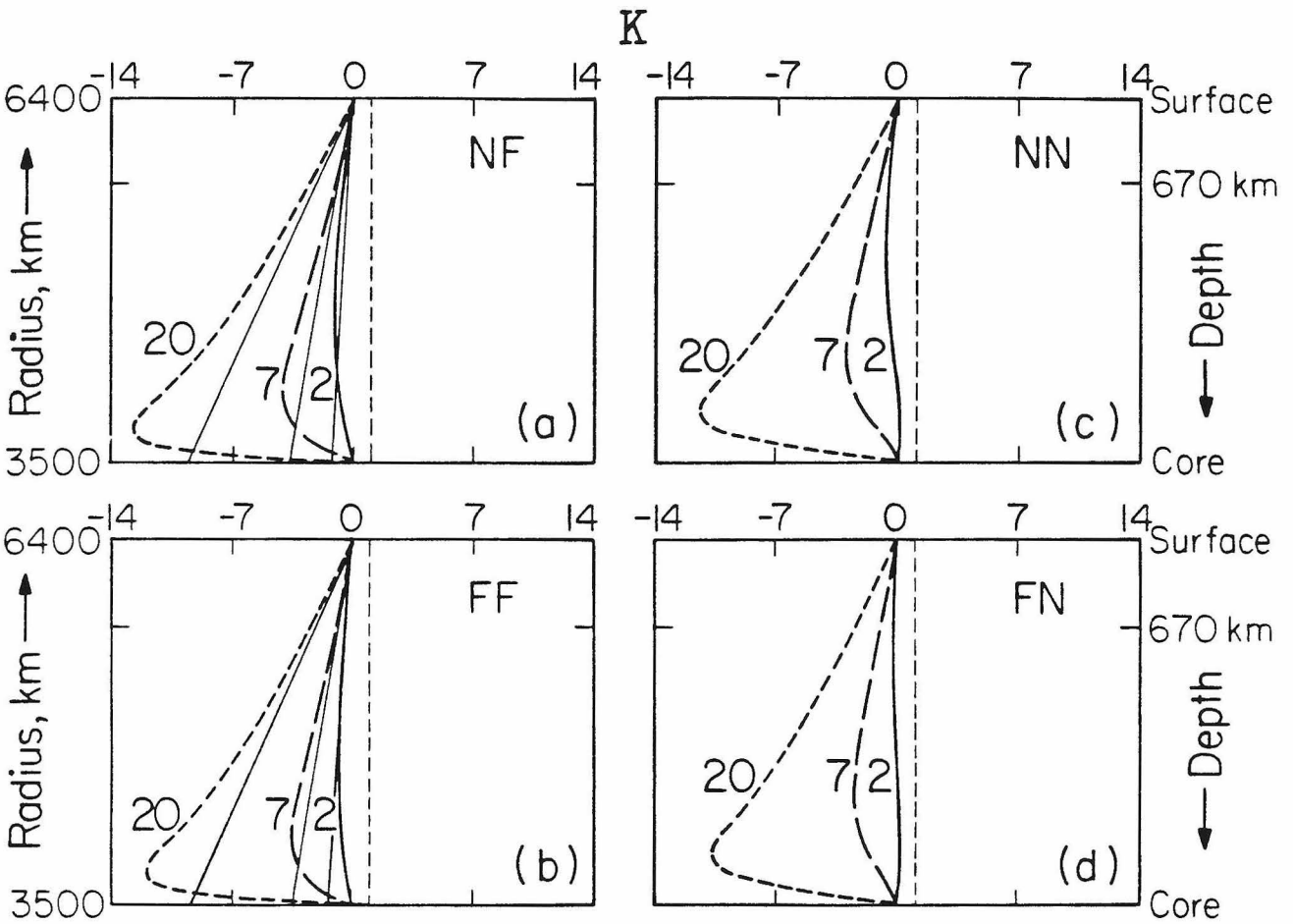
K
-14
-7
0
7
14
6400
3500
Radius, km
NF
NN
FF
FN
20
7
2
(a)
(b)
(c)
(d)
Surface
670 km
Depth
Core

Figure 8 - Surface potential response, K, as a function of loading depth for viscosity contrasts of 0.1 and 0.01 in the upper mantle. Figures (a) and (b) are for FF boundary conditions and (c) and (d) are for NF conditions.

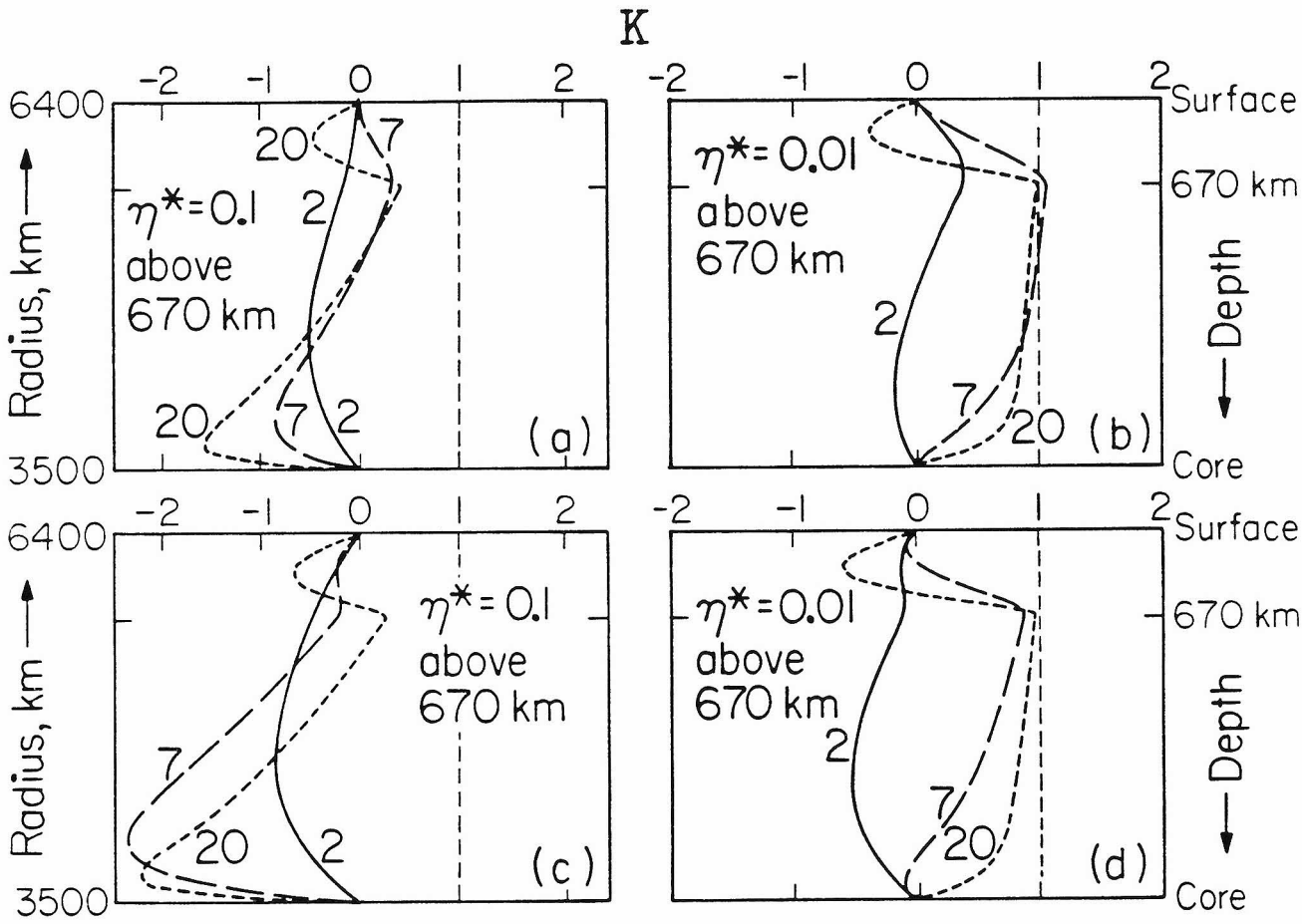
K
-2
-1
0
2
6400
3500
Radius, km
Surface
670 km
Depth
Core
η^*= 0.1
above
670 km
η^*= 0.01
20
7
2
(a)
(b)
(c)
(d)

Figure 9 - Surface deformation impedance, Z, as a function of loading depth illustrating the effect of low viscosity in the upper mantle for harmonic degrees 2, 7, and 20. Figures (a) and (b) are for FF boundary conditions and (c) and (d) are for NF conditions. The solid, long-dashed, and short-dashed lines are, respectively, for $l=2$, 7, and 20. The dashed line at $Z=0$ gives the "perfect" compensation result for comparison.

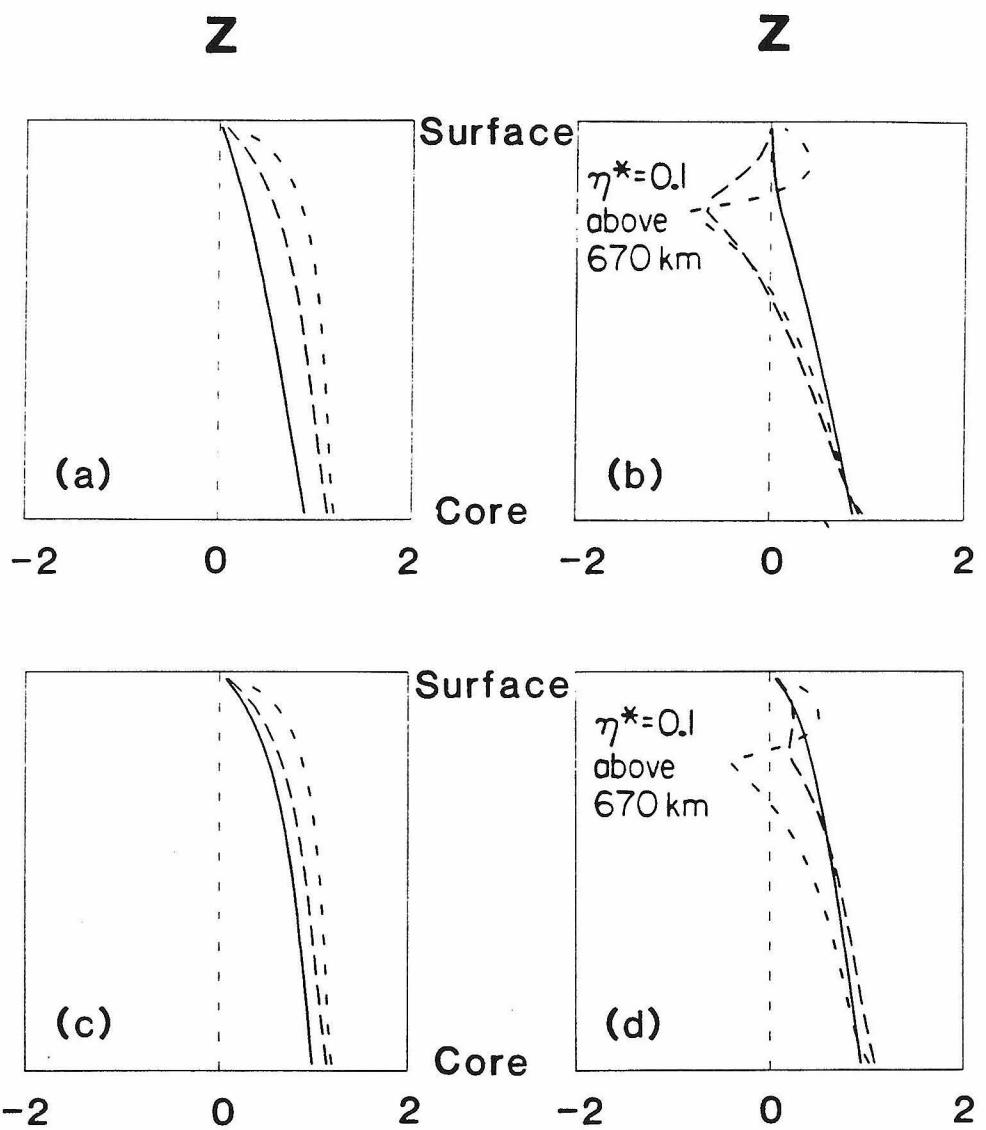
Z
Z
Surface
Core
(a)
(b)
(c)
(d)
η*=0.1
above
670 km
-2
0
2

Figure 10 - Mass displacement at the boundaries as a function of loading depth for two-layer flow models with uniform viscosity (same as Figure 4 with additional displacement curve "M" for the 670km discontinuity).

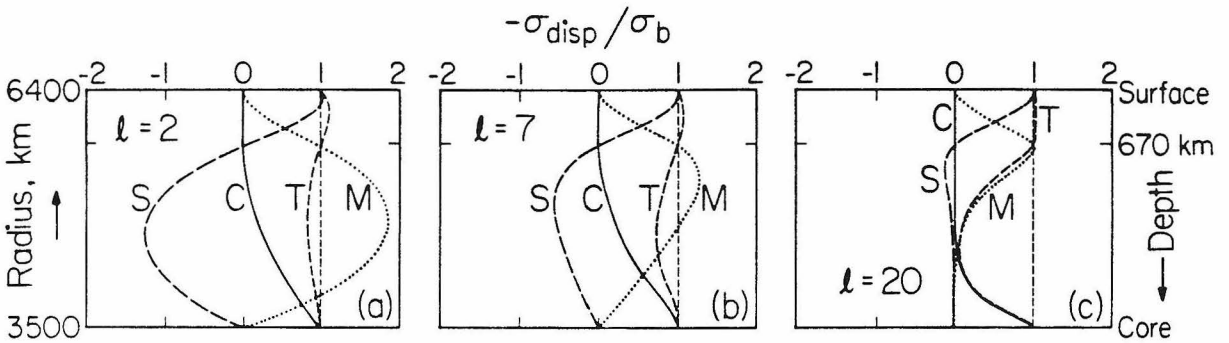
$-\sigma_{disp}/\sigma_b$
-2
-1
0
1
2
6400
3500
Radius, km
$\ell = 2$
S
C
T
M
(a)
$\ell = 7$
(b)
$\ell = 20$
(c)
Surface
670 km
Depth
Core

Figure 11 - Viscous normal mode excitation as a function of loading depth for two-layer flow models with uniform viscosity (same as Figure 5 with the additional M1 mode due to deformation of the 670km discontinuity).

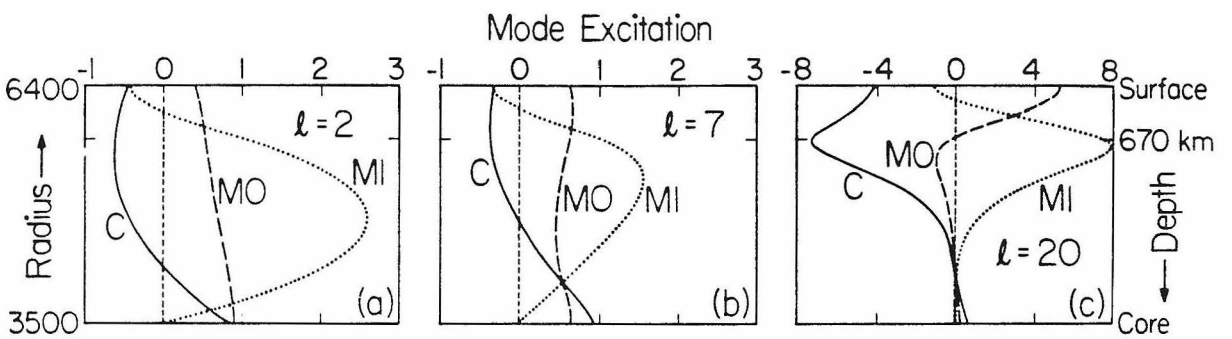
Mode Excitation
-1
0
1
2
3
6400
Radius
3500
ℓ = 2
C
MO
MI
(a)
-1
0
1
2
3
ℓ = 7
C
MO
MI
(b)
-8
-4
0
4
8
Surface
670 km
Depth
Core
MO
C
MI
ℓ = 20
(c)

Figure 12 - Surface potential response, K, as a function of loading depth for two-layer models, illustrating the effect of low viscosity in the upper mantle. Boundary conditions are no-slip (N) at the surface and free-slip (F) at the core-mantle boundary.

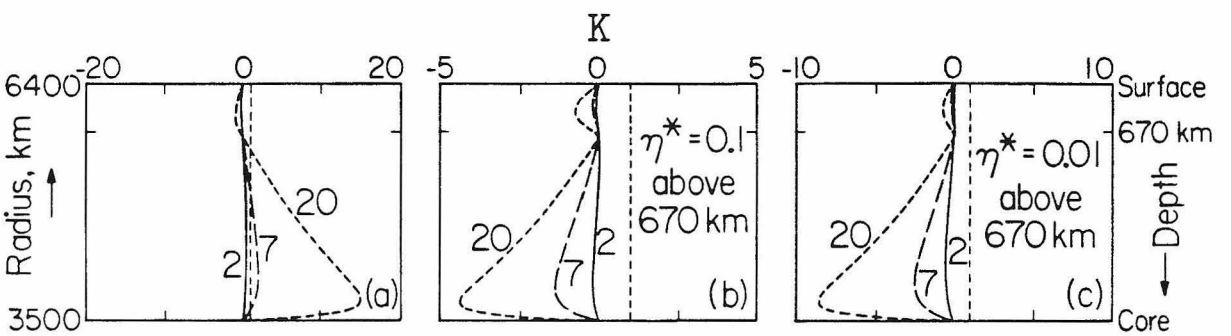
K
-20
0
20
-5
0
5
-10
0
10
6400
3500
Radius, km
Surface
670 km
Depth
Core
20
2
7
(a)
η^* = 0.1
above
670 km
(b)
η^* = 0.01
above
670 km
(c)

Figure 13 - Surface deformation impedance, Z, as a function of loading depth for two-layer models, illustrating the effect of low viscosity in the upper mantle. The solid, long-dashed, and short-dashed lines are, respectively, for $l=2$, 7, and 20.

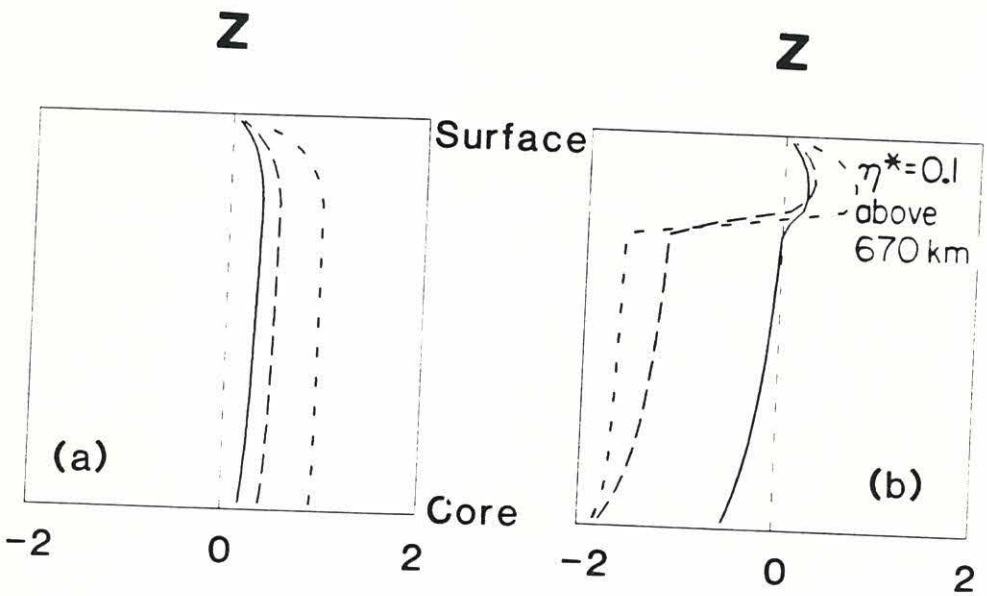
Z
Surface
(a)
Core
-2
0
2
Z
η*=0.1
above
670 km
(b)
-2
0
2

Figure 14 - Harmonic dependence of response functions, K, for representative loading depths of 300km, 1400km, and 2600km for a variety of models. Curves "a" and "c" are for whole mantle flow with FF boundary conditions and upper mantle viscosity contrasts of 1.0 and 0.01, respectively. Curves "d" and "f" are for two-layer flow with NF boundary conditions and upper mantle viscosity contrasts of 1.0 and 0.01.

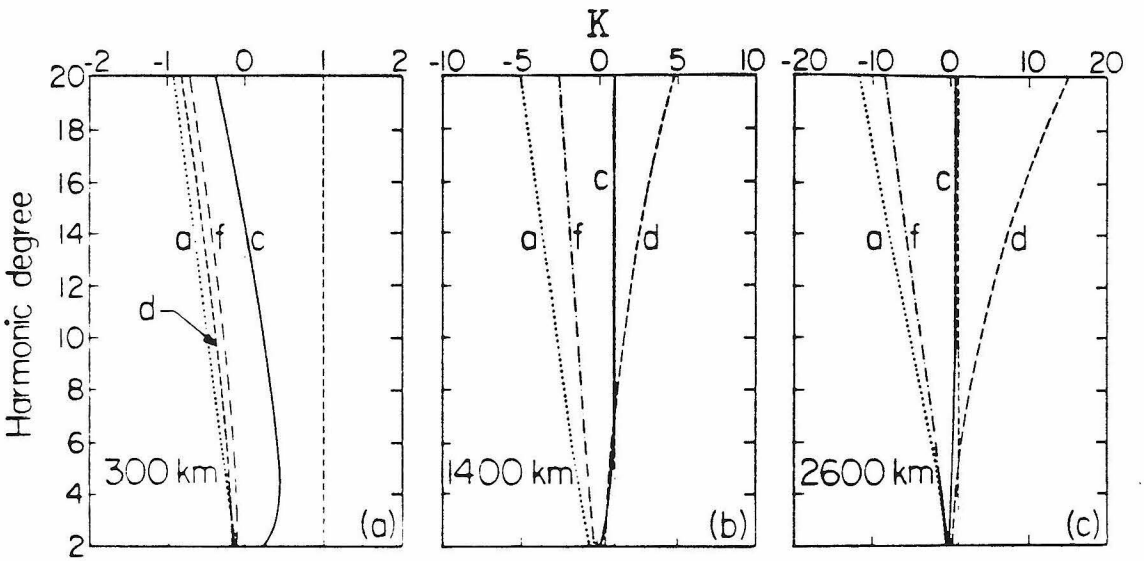
K
Harmonic degree
20
18
16
14
12
10
8
6
4
2
-2
-1
0
1
2
-10
-5
0
5
10
-20
-10
0
10
20
a
f
c
d
300 km
(a)
1400 km
(b)
2600 km
(c)

Figure A1 - Relaxation times and relative boundary displacement amplitudes for viscous normal modes as functions of harmonic degree for whole mantle flow. MO refers to the symmetric mantle mode and C refers to the asymmetric core mode. The notation "-C" in (b), (d), and (f) emphasizes that the boundary deformations are of opposite sign for the core mode. The models represented include uniform mantle viscosity and low viscosity channels above 200 km and 670 km depth. Figure (a) also shows the relatively minor effect of a high viscosity "lithosphere" layer.

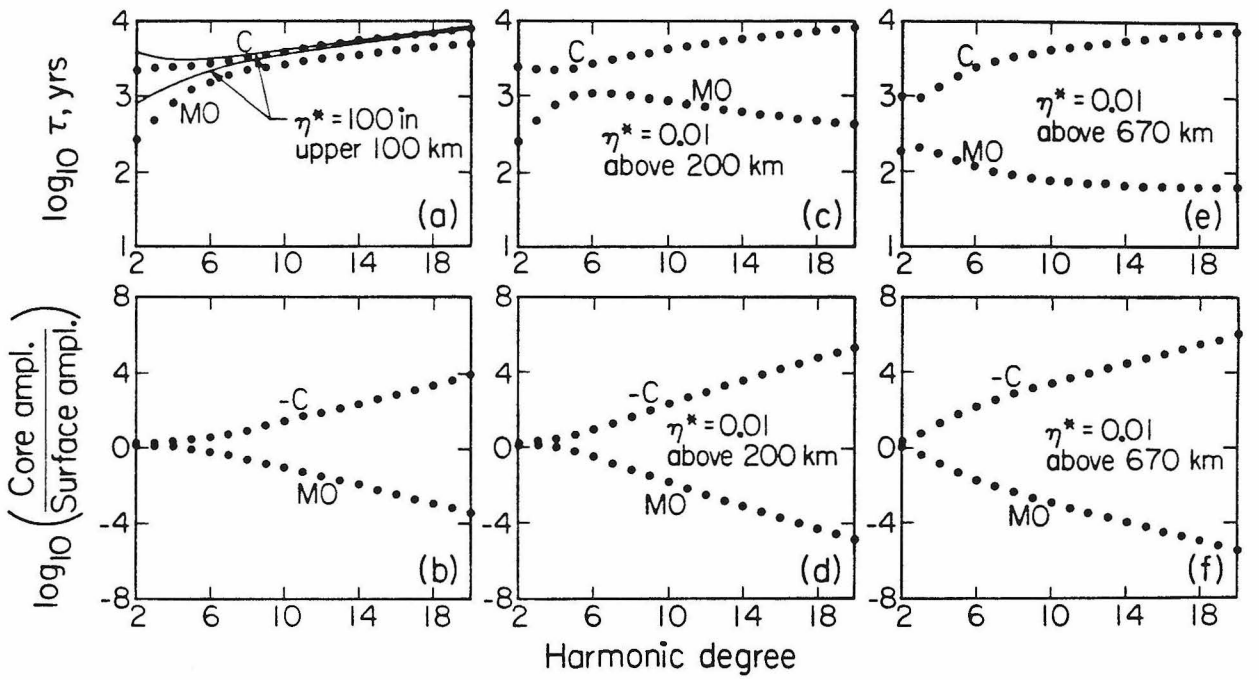
log10 τ, yrs
log10 (Core ampl. / Surface ampl.)
C
MO
-C
η* = 100 in upper 100 km
η* = 0.01 above 200 km
η* = 0.01 above 670 km
(a)
(b)
(c)
(d)
(e)
(f)
Harmonic degree

Figure A2 - Relaxation times and relative boundary amplitudes for viscous normal modes as functions of harmonic degree for two-layer flow. The M1 mode is generated by deformation of the flow barrier at 670 km depth, and the right-hand column of figures are for a low viscosity upper mantle. Plus and minus signs on the amplitude curves indicate sign reversals in the sense of deformation relative to that of the surface. Figure (a) also shows the effect of using a density jump of 0.3 instead of 0.5 Mg/m^3 at the 670 km discontinuity.

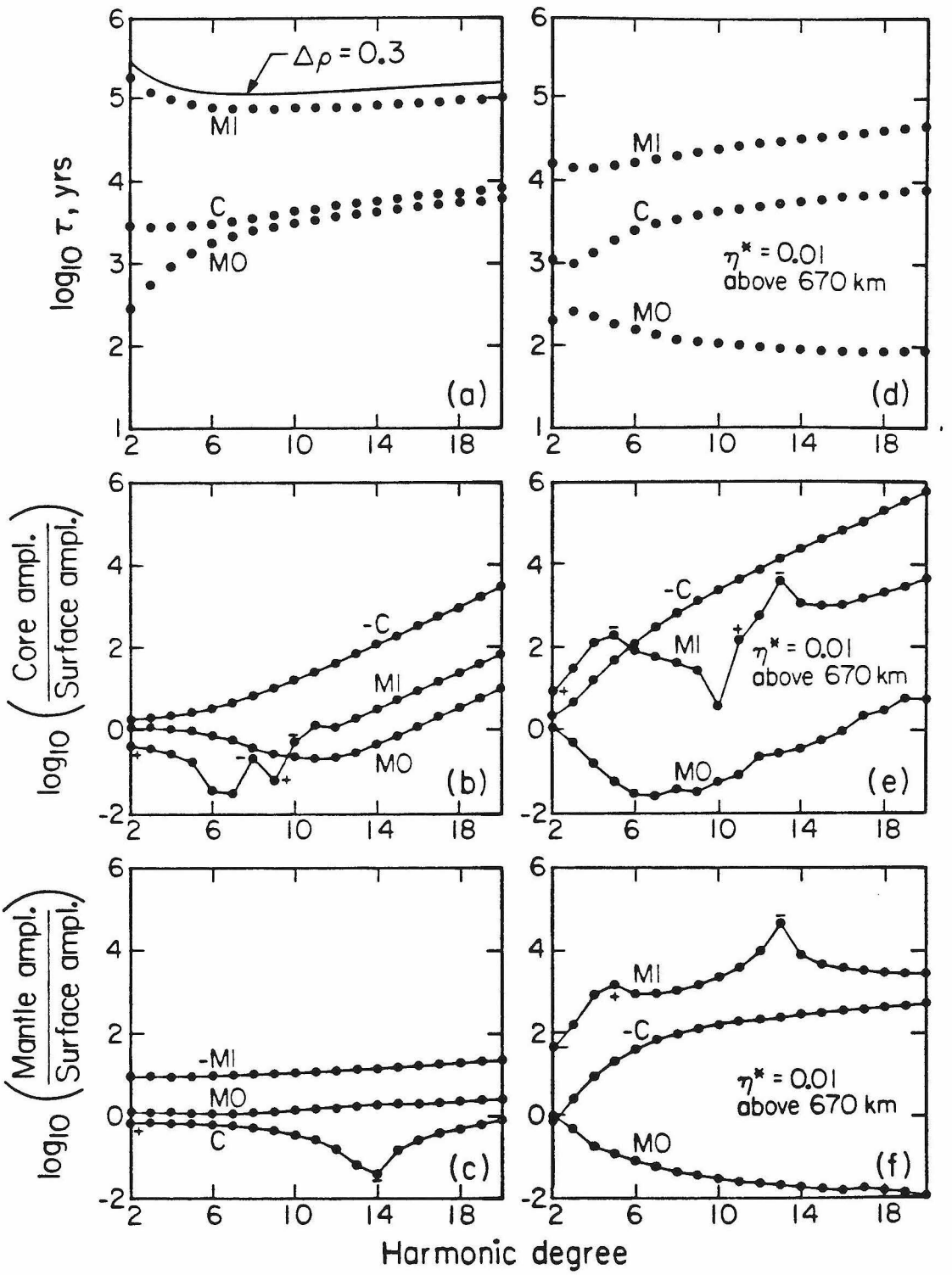
log10 τ, yrs
Δρ = 0.3
MI
C
MO
(a)
η* = 0.01
above 670 km
(d)
log10 (Core ampl. / Surface ampl.)
-C
(b)
(e)
log10 (Mantle ampl. / Surface ampl.)
-MI
(c)
(f)
Harmonic degree

Chapter 2

The Earth's Geoid and the Large-scale Structure of Mantle Convection

Introduction

Variations in the Earth's gravitational potential field, expressed as undulations of the geoid, are ultimately derived from density contrasts due to solid-state convection deep within the mantle. The observed long-wavelength geoid (Lerch et al., 1983), referenced to the equilibrium hydrostatic figure (Nakiboglu, 1982), is dominated by a very long wavelength pattern which shows little resemblance to the Earth's topography or to the present configuration of plate tectonics (Figure 1a). Less than 30 m of this signal of $\sim$200 m can be due to isostatically compensated variations in lithospheric thickness or density (Hager, 1983), so the remainder must be related to mantle convection. The question is then: if plate tectonics is the surface expression of mantle convection, and if convection causes variations in the geoid, why are the plates and the geoid not more obviously related?

By contrast, long-wavelength geoid highs on both Mars (Balmino et al., 1982) and Venus (Sjogren et al., 1980) are strongly correlated with topographic highs. The prominent Tharsis bulge on Mars, with its huge volcanic shields, is either an active or fossil expression of hot upwelling in the Martian mantle, and the Venusian highlands are straightforwardly explained as surface bulges due to mantle convection (Kiefer et

al., 1986). The apparent absence of plate tectonics on these terrestrial planets (Kaula and Phillips, 1981), as well as the presence of isostatically compensated, chemically buoyant continental masses on Earth, are probably the key differences. The Earth's lithospheric plates can move about on a timescale much shorter than that required for convective overturn of the lower mantle because of the decoupling effects of low viscosity in the asthenosphere. A likely cause for this decoupling zone is the approach of the geotherm to the wet peridotite solidus (Anderson and Sammis, 1970; Wyllie, 1971). This may result in a long ($\sim$100 Ma) time lag between the temperature contrasts due to the cooling of plates and their effect upon the large-scale temperature structure of the mantle.

Upon filtering out the longest wavelength components (harmonic degrees 2-3) of the geoid (Figure 1b) we find a remarkable correspondence between convergence or subduction zones and geoid highs, i.e., the circum-Pacific "ring of fire". These smaller, more "local" anomalies correspond to sinking lithosphere at least in the upper mantle, so the paradox discussed above is limited mainly to the dominant, lowest-degree pattern. In previous papers we have proposed that this very long wavelength pattern is derived mainly from lower mantle density contrasts (Hager et al., 1985), while much of the higher degree ($l \geq 4$) geoid is caused by slabs in the upper mantle (Hager, 1984).

In this paper we start with an empirical approach to understanding the Earth's geoid, the object being to contrast the global data that seem related to the geoid with global features that are apparently unrelated. We examine statistical correlations between the observed geoid and two types of data. The first type includes surface features (topography, plate velocities, subduction zones, hotspots) which are plausible

symptoms of mantle convection. The second data source is seismic tomography which has recently provided models of velocity heterogeneity in the mantle. The next step is to formulate geodynamic models that provide a physical connection between the geoid and the global data sets that correlate strongly with the geoid. The result is a model for the Earth's geoid, based mainly upon velocity heterogeneity in the lower mantle and upon the locations of subducting slabs, which explains most (>80%) of the observed geoid variance. This model presumably describes a similar proportion of the large-scale density and temperature contrasts that result from mantle convection.

Global Correlations with Surface Features

The Earth's topography is dominated by the distribution of continental and oceanic crust. For comparison with the long-wavelength geoid, we have used a harmonic expansion of $1^0 x\, 1^0$ averages of global topography (NOAA, 1980) corrected for oceanic and polar ice loads referred to a density of 2.7 g/cm ^{3}. The harmonic expansion of this equivalent rock topography, h, is

$$h(\theta,\phi) = \sum_{l=1}^{\infty} \sum_{m=-l}^{l} h_{lm}\, Y_{lm}(\theta,\phi) \tag{1}$$

where the Y_{lm}'s are surface spherical harmonics normalized so that their mean square value is unity (Kaula, 1967), i.e.,

$$\int_0^{2\pi} d\phi \int_0^{\pi} \sin\theta\, d\theta\; Y_{lm}(\theta,\phi) Y_{lm}^*(\theta,\phi) = 4\pi \tag{2}$$

where Y_{lm}^* denotes the complex conjugate of Y_{lm}. Similarly, the nonhydrostatic geopotential is represented by

$$g(\theta,\phi) = \sum_{l=2}^{\infty} \sum_{m=-l}^{l} g_{lm}\, Y_{lm}(\theta,\phi) \tag{3}$$

The geopotential coefficients may be converted to geoid elevation coefficients by simply dividing by the gravitational acceleration at the surface. Correlation coefficients, r_l, between topography and the geoid are given by the ratio of covariance to variance at each harmonic degree,

$$r_l(g,h) = \frac{\sum_m (g_{lm}\, h^*_{lm})}{\sqrt{\sum_m (g_{lm}\, g^*_{lm}) \sum_m (h_{lm}\, h^*_{lm})}} \tag{4}$$

Cumulative correlations for several or many harmonic degrees simultaneously can be misleading since spectral power is not uniform (Eckhardt, 1984), so we present raw degree correlations. The significance of a correlation is evaluated by a Student's t test for $2l$ degrees of freedom, and the computed correlations are shown in Figure 2a along with confidence limits. For example, a confidence level of 0.98 implies only a 2% chance that a correlation is random. Figure 2a verifies that there is no consistent correlation between topography and the low-degree geoid.

For higher degrees ($l \geq 6$) there is a consistent positive correlation between topography and the geoid which is due mainly to the ~5-10 m geoid elevations encountered in going from oceanic to continental crust (Haxby and Turcotte, 1978; Chase and McNutt, 1982). Hager (1983) has computed global isostatic geoid anomalies based upon a cooling plate model for oceanic lithosphere and isostatic compensation of 35 km thick continental crust. We have improved this global isostatic model by including geoid elevations calculated from Airy compensation of anomalously thick crust in continental convergence zones (Tibet, Andes, Iranian-

Caucasus highlands). These predicted anomalies also correlate well with the higher degree geoid (Figure 2a).

These isostatic anomalies actually contribute very little total power to the observed geoid as shown by the spectral amplitude comparison of Figure 2b. Here, the root mean square harmonic coefficient amplitude at each degree is given by

$$A_l(rms) = \sqrt{V_l^2(A)/(2l+1)} = \sqrt{\sum_m (A_{lm} A_{lm}^*)/(2l+1)} \qquad (5)$$

where $V_l^2(A)$ is the variance at each degree for a given set of expansion coefficients (A_{lm}). We have plotted $A_l(rms)$ as opposed to, e.g., variance, because the spectrum of random noise on a sphere is flat ("white") on such a plot. Therefore, any low-degree, or long-wavelength, bias ("reddening") will show up as a negative slope for $A_l(rms)$ vs. l. The observed geopotential shows a very strong long-wavelength bias.

The isostatic model predicts geoid anomalies of much lower amplitude than those observed (Figure 2b), especially at the lowest degrees (≤ 5) where the two data sets are uncorrelated. The relative lack of low-degree power in the isostatic model is to be expected for two reasons: (1) The topography spectrum is, itself, "whiter" than that of the geoid. (2) Compensation at relatively shallow lithospheric depths results in very little low-degree geoid signal.

In assessing the success of a model in explaining an observed surface field such as the geoid, we use the total variance, $\sum_l V_l^2$, because, unlike amplitude, this quantity is additive for uncorrelated signals and it is additive by degree. Subtracting our best estimate for isostatic anomalies from the observed geoid actually increases the total variance by 4.9% because of the poor fit at the low degrees. Even in the band l=6-20, where the correlation is good, we achieve only a 9.7% variance reduction.

For this reason, the isostatic correction has little effect upon the correlations that follow, and we have chosen to ignore it for the sake of simplicity.

We have also examined the relationship between the geoid and continental shield areas (Figure 2a) by using a harmonic expansion of areas classified as largely Archean, Proterozoic, or Precambrian undeformed terranes by Mauk (1977). For degrees 2-8, the correlation is consistently negative although not consistently significant. This implies a weak association of geoid lows with old shield areas. We note that Turcotte and McAdoo (1979) concluded that there was no systematic difference between continental and oceanic geoid elevations, but they used broad spatial averages over selected terranes rather than the global, wavelength dependent (harmonic) approach we have taken. Since shallowly compensated (crustal) topography results in a small but positive geoid anomaly, our observation suggests a deep, high density, continental root associated with the most stable terranes, perhaps of the order of several hundred kilometers in depth. Consistent with this speculation, Nakanishi and Anderson (1984) and Tanimoto and Anderson (1984) have noted a correspondence between high mantle Love wave velocities (periods $\leq$250 seconds) and both geoid lows and shields in the harmonic degree l=4-6 band. Although this is a topic of considerable interest (see Jordan, 1975; 1978), we shall not pursue it further here; the shield signal is weak, and, like the isostatic model, it explains little of the observed geoid variance. We conclude from our analysis of topographic and crustal/lithospheric effects that most of the Earth's geoid must be derived from density contrasts deep in the mantle due to convection.

A more direct connection between the convection derived geoid and surface features might be reflected in tectonic plate motions since they are coupled to flow in

the mantle. To investigate this possibility, we have obtained harmonic representations of both the poloidal and toroidal scalar fields that describe the plate velocity vector field (see Hager and O'Connell, 1978). The toroidal component, representing mainly transform motion between plates, is not significantly correlated with the geoid for any of degrees 2-20 (not shown). The poloidal component represents both the convergence (subduction) and divergence (sea-floor spreading) of plates. Since poloidal surface velocity fields imply vertical motions in the underlying mantle and can be driven by density contrasts (e.g., Hager and O'Connell, 1978), the poloidal velocity component might be expected to be directly related to the interior density contrasts that give rise to the observed geoid. However, there is only a weak correlation between the geoid and the poloidal plate velocity field for degrees 2-20 (Figure 2c). The single high correlation at degree 4 is about what is expected for a random sample of 20 degrees (Hager and O'Connell, 1978). Note from Figure 2d that the spectral power here, relative to the overall spectral trend, is not as large as degree 5 which does not correlate well. This correlation has, however, led some researchers to conclude that both ridges and trenches are strongly correlated with the geoid (Peltier and Forte, 1984).

Such a conclusion is misleading. Reference to Figure 1 shows that while convergence (subduction) zones correspond consistently with geoid highs, there is no consistent relationship between the geoid and spreading ridges. To investigate this quantitatively, we have correlated both divergence and convergence rates with the geoid (Figure 2c). Harmonic representations of convergence and divergence were obtained by expanding the product $v\,\delta l$ along all plate boundaries, where v is the convergence (positive) or divergence (negative) velocity (Minster and Jordan, 1978; Chase, 1978) of

each boundary segment length δl. For harmonic degrees 4-9 there is a very strong correlation between the geoid and convergence rate (Hager, 1982), but plate divergence is not correlated with the geoid for harmonic degrees <9. The isolated correlation at degree 3 corresponds to a relative low in the divergence spectrum (Figure 2d), and the sign of correlation is inconsistent for the low degrees. The weak correlation between the poloidal plate velocity field and the geoid is a result of the strong convergence zone correlation diluted by the uncorrelated divergence components. Specifically, there is no evidence in the geoid for deep thermal support or active mantle upwelling under ridges. The weak correlation between geoid highs and divergence rate for degrees ≥ 9 may be due to isostatically compensated lithospheric thickening away from ridges (Haxby and Turcotte, 1978). These observations are consistent with passive upwelling under mid-ocean ridges and the presence of cold, sinking slabs under subduction zones.

The geoid highs over subduction zones are evident in Figure 1b, and correlation coefficients between a predicted slab geopotential and the observed geoid (Figure 2c) are even stronger than those for convergence vs. the geoid; the total amount of subducted slab (proportional to the product of subduction rate and some characteristic time) is more physically related to the geoid than to the rate of subduction itself. The slab geoid signal was calculated by using deep seismicity to locate subducting lithosphere and by associating slabs with an average density contrast of 0.1 g/cm ^{3} (see Hager, 1984). This model predicts most of the geoid signal associated with subduction zones. An excellent fit is obtained without allowing for compensating downwarp of the lithosphere at subduction zones (i.e., trenches), and we further discuss this problem below.

By subtracting a model for the slab geoid from the observed geoid, we obtain a residual geoid which is even more dominated by harmonic degrees 2 and 3 (Figure 3c). Chase (1979) and Crough and Jurdy (1980) noticed that most of the Earth's hotspots (e.g., Hawaii and Iceland) occur in residual geoid highs. This is shown dramatically in Figure 4a, where the black dots correspond to 47 prominent hotspots. These volcanic centers are essentially fixed with respect to plate motions and are often attributed to the passage of the lithosphere over deep mantle plumes (Morgan, 1972). A spherical harmonic expansion of the global spatial density of hotspots is obtained by representing each hotspot as a point source of equal (unit) strength. Correlations with both the geoid and the residual geoid are shown in Figures 3a and 3b, respectively. For degrees 2-6 hotspots are strongly correlated with the residual geoid, as was obvious in Figure 4a, and the degree 2 and 6 correlations correspond to peaks in the hotspot distribution spectrum (Figure 3c). If the hotspots, or mantle plumes, are causing the residual geoid highs, these hot, low density upwellings must be well compensated by dynamic uplift of the lithosphere. This seems difficult to reconcile with the apparently weak compensation of slabs, but in following sections we will show how this paradox can be explained.

Seismic Heterogeneity in the Mantle

Analysis of seismic travel times and phase velocity delays are two methods available to estimate density contrasts at great depth in the mantle. Substantial velocity heterogeneity has been found both in the upper mantle (Masters et al., 1982; Woodhouse and Dziewonski, 1984; Nakanishi and Anderson, 1984; Nataf et al., 1984; Tanimoto, 1986) and in the lower mantle (Dziewonski et al., 1977; Clayton and Comer,

1983; Dziewonski, 1984). These velocity variations might be due to either thermal or compositional gradients in the mantle, and the associated density variations must contribute to the geoid.

Long period (>100 sec) surface waves are sensitive to shear velocity heterogeneity in the mid-upper mantle as well as to near surface effects. Here we examine two recent surface wave phase velocity inversions to see if upper mantle heterogeneity can explain the large geoid anomalies not associated with subduction zones. Woodhouse and Dziewonski ("WD") and Tanimoto ("Tan") found shear velocity variations as large as 3% at depths greater than 200 km. Correlations with both the observed geoid and the slab residual geoid are shown in Figure 3a,b for shear velocity averages over depth ranges of 200-500 km (WD) and 200-400 km (Tan). On the whole, these velocity anomalies are not well correlated with either the observed or the residual geoid. The Tanimoto model shows a strong correlation at degree 3, but the WD model does not. Degree 2 velocity anomalies in this depth range are not significantly correlated with the geoid, so little of the residual geoid can be accounted for by these models of mid-upper mantle heterogeneity. Curiously, at harmonic degree 6 the residual geoid is very significantly, and negatively, correlated with hotspots and with the surface wave models of WD and Tan as well as Nakanishi and Anderson (1984). This anomaly corresponds to the most prominent peak in the distribution spectrum of hotspots (Figure 3c) and to the degree 6 correlation failure for slabs (Figure 2b); we have proposed that all three correlated observations are related to upper mantle heating (Richards, Sleep, and Hager, to be submitted, 1986: Chapter 4). We also note that these surface wave models show no consistent correlation with subduction zones. This might seem surprising given the power in the long-wavelength geoid associated

with subducted slabs. Typical subduction zones are, however, characterized by (low velocity) arcs and back-arc basins overlying (high velocity) slabs (Nakanishi and Anderson, 1984). Surface waves integrate over depth (Tanimoto, 1986), and these effects apparently cancel in the seismic models leaving no strong subduction signal. This provides an interesting contrast to dynamic geoid kernels (see next section) which are insensitive to near-surface variations, such as back-arc spreading, but are sensitive to deeper variations such as subducted slabs.

By contrast, from analysis of longer period fundamental spheroidal modes, Masters et al. (1982) ("MJSG") inferred degree 2 velocity heterogeneity in the transition zone (400-670 km depth) that is strongly and positively correlated with the geoid (see Table). The WD model, in rough agreement with MJSG, is positively, although weakly, correlated with the geoid for degree 2 at depths of 550 and 650 km. (WD applied surface wave overtone data to help resolve these depths.) The Tanimoto model (450-650 km), which changes less rapidly with depth, shows a consistent, positive correlation with the degree 2 (as well as degree 3) geoid and with the MJSG transition zone model. Also shown in the Table are the more impressive correlations between these velocity models and the locations (from deep seismicity) of subducted slabs. Nataf et al. (1986) similarly find a high velocity signature at some depths below the oldest oceanic lithosphere and trenches. From these observations we infer that seismic heterogeneity as well as some of the degree 2 geoid are both due to slabs in the transition zone. However, the MJSG study was limited to harmonic degree 2, and the WD and Tanimoto models (450-650 km) are uncorrelated with both subducted slabs and the geoid at higher degrees. We cannot, therefore, place much confidence in higher-degree geoid models based upon these transition zone velocity

models.

A more likely source for the large degree 2-3 geoid anomalies is revealed by P-wave travel time residuals mapped by the least-squares inversion of Dziewonski (1984) and the tomographic inversion of Clayton and Comer (1983). Lower mantle compressional wave velocity anomalies from both studies are highly correlated with both the geoid and the slab residual geoid at harmonic degrees 2 and 3 (Figure 3). The velocity model of Clayton and Comer (1983) was integrated uniformly throughout the depth of the mantle in order to compute the correlations. This includes some poorly resolved regions near the core-mantle boundary and between 670 and 900 km depth which somewhat degrade these remarkable correlations. Otherwise, the low-degree velocity heterogeneities are largely coherent throughout the lower mantle; the degree 2 peak in the P-wave velocity spectrum (Figure 3c) is due to stronger depthwise coherence than at other degrees. We obtain similarly strong correlations between Dziewonski's (1984) degree 2-3 P-wave anomalies and the geoid (not shown) and between the two lower mantle P-wave models (Hager et al., 1985). For degrees ≥ 4 the geoid/tomography correlations fail for both of the lower mantle velocity models, and the seismic models no longer correlate with each other. Reasons to expect this are discussed in a forthcoming paper (Richards and Hager, manuscript in preparation: Chapter 3). The negative degree 2-3 correlation coefficients mean that slow velocity anomalies in the lower mantle underlie the low-degree geoid highs as shown in Figure 4. Slow velocity is also strongly correlated with the distribution of hotspots ($r = 0.85$) at degree 2, where both spectra are peaked.

The implied correspondence of hot, low velocity mantle to geoid highs may seem just as paradoxical as the lack of correspondence of the low-degree geoid to plate

tectonics. Even if we suppose that seismic velocity and density are inversely related, possibly due to chemical rather than thermal gradients, the implied velocity/density conversion factor, $\sim$ -12 km sec^{-1}/g cm^{-3}, is about a factor of 3 larger in magnitude than expected (Birch, 1961; Dziewonski et al., 1977).

Dynamic Geoid Models

These apparent contradictions are the result of the gravitational effects of large-scale, compensating deformations of the Earth's surface and the core mantle boundary in response to lower mantle density contrasts. Unfortunately, the Earth's dynamic surface deformations are obscured by the bimodal distribution of oceanic and continental lithosphere and by variations in crustal thickness (e.g., the Tibetan Plateau). We cannot at present distinguish the purely dynamic component of observed elevation differences (of the order of 1 km over distances greater than 10,000 km) from the large topographic signatures of isostatically compensated, near-surface features. However, it is possible to estimate these effects in the Earth based on our knowledge of mantle structure and viscosity.

In a convecting mantle, boundary surfaces are elevated by hot, upwelling material and depressed by cold downwellings (Figure 5). The contributions of these surface deformations to the geoid are of opposite sign and comparable magnitude to the contribution from the interior density contrasts that cause them (Pekeris, 1935; Runcorn, 1964; Morgan, 1965; McKenzie, 1977; Parsons and Daly, 1983; Ricard et al., 1984; Richards and Hager, 1984: Chapter 1). Therefore, geoid anomalies result from the balance of competing contributions, i.e., a relatively small difference of large numbers. The amplitude of boundary deformation depends strongly upon the

viscosity structure of the mantle, so the geoid is a sensitive indicator of mantle structure. We have calculated these effects for Newtonian viscous flow in spherically symmetric, incompressible, self-gravitating Earth models (Richards and Hager, 1984: Chapter 1).

If the viscosity structure varies only radially, then a given density contrast $\delta\rho_{lm}(r)$ at radius r excites only an lm^{th} harmonic boundary deformation. Since solutions for linear (Newtonian) rheology may be superposed, we can obtain the total harmonic geopotential coefficients from

$$g_{lm} = \frac{4\pi\gamma R}{2l+1} \int_c^R G_l(r)\delta\rho_{lm}(r)dr \qquad (6)$$

where γ is the gravitational constant, R the Earth's radius, c the core radius, and $G_l(r)$ is the dynamic response function or kernel. This kernel is independent of the azimuthal order m for the assumed spherically symmetric viscosity structure, and it contains contributions from both boundary deformations and the density contrast itself.

Response functions for both whole mantle flow and chemically layered flow are shown in Figure 6 with lower/upper mantle viscosity ratios of 1, 10, and 100. Although flow velocities depend upon the absolute value of viscosity, the stresses, boundary deformations, and geoid depend only upon the relative values. Free-slip boundary conditions are applied at the core-mantle boundary and at the surface. For uniform viscosity and whole mantle flow (model U1, Figure 6a) the geoid response is always negative because of the overwhelming gravitational effect of the deformed upper surface. The response functions, plotted as a function of depth, are normalized to the geoid that would be obtained if the uncompensated density contrast, $\delta\rho_{lm}(r)$,

were placed at the surface.

The U1 model could explain the negative correlation between lower mantle velocity anomalies and the geoid. The average degree 2-3 response in the lower mantle is about -0.2, so using equation (6) we can explain most of the low degree residual geoid with a velocity/density conversion factor of about +8 km sec $^{-1}$/g cm $^{-3}$. The positive sign of this factor is consistent with the effects of temperature upon velocity and density, although the magnitude is still about twice that expected from both low pressure laboratory measurements and the average adiabatic value for the lower mantle. Figure 6 shows that the low-degree geoid is most sensitive to density contrasts in the lower mantle, so such an explanation for the longest-wavelength geoid features is not surprising.

This simple model is consistent with the interpretation of post-glacial rebound data in terms of relatively uniform mantle viscosity (Cathles, 1975; Peltier, 1981). Low viscosity in the uppermost mantle or asthenosphere will not strongly affect the degree 2-3 response functions in the lower mantle. However, the U1 model is not compatible with the observed geoid highs caused by subducting slabs. In order to explain these geoid anomalies, the upper mantle response functions must be strongly positive for degrees 2-9 (i.e., little dynamic compensation). This requirement can be satisfied by a model with about a factor of 30-100 increase in viscosity through the upper mantle (Hager, 1984). Relatively low viscosity in the upper mantle reduces the negative geoid contribution from surface deformation and results in positive geoid response functions. An excellent fit to the slab/geoid data is obtained with model U100 (Figure 6c). However, this model cannot explain the lower mantle results, because the lower mantle response functions are also positive.

A chemical barrier model (Figure 6e,f) could solve this particular problem by giving opposite responses for the upper and lower mantle. However, we obtain response functions about a factor of 5 too small for slabs if compensation is allowed at the 670 km discontinuity for any models of viscosity layering in the upper mantle. For this reason we conclude that, even if the mantle is chemically stratified, at least the thermal structure of slabs must penetrate the 670 km seismic discontinuity. We find the alternative, that mass anomalies associated with slabs in the mid-upper mantle are a factor of five larger than our assumed value, implausible. Further evidence for mixing across this level is the correlation between the degree 2 distribution of hotspots and slow seismic velocity in the lower mantle.

A Refined Model for Whole Mantle Convection

Model U10, with a moderate (factor of 10) increase in viscosity with depth, shows that it is also possible to have both positive upper mantle and negative lower mantle responses for mantle-wide flow (Figure 6b). With two simple modifications to this model we can account for most of the subducted slab/lower mantle discrepancy. First, it is clear that we should include a high viscosity lithospheric layer. Second, the region above the transition zone (asthenosphere) should have low viscosity (Passey, 1981). These adjustments give upper mantle kernels like model U100 but tend to drive all the response functions more negative in the lower mantle. Response curves for such a 4-layer model are shown in Figure 7a. Here the lithosphere is assigned the same effective viscosity, η_0, as the lower mantle; the transition zone has viscosity $0.1\eta_0$, and the low viscosity channel in the upper mantle is assigned $0.3\eta_0$.

This model explains the lower mantle P-wave velocity/geoid correlations since the lower mantle degree 2-3 responses are negative. The relatively small responses for ($l \geq 4$) help explain why little of the higher-degree geoid correlates with the equally strong higher degree heterogeneity in the lower mantle. The upper mantle responses are still mostly positive, so this model remains compatible with the slab/geoid correlations. However, a much better fit to the slab data is obtained for a model such as U100, which has more strongly positive upper mantle response functions. Similar responses are obtained if the lithospheric viscosity is reduced by an order of magnitude in the 4-layer model (Figure 7b). Such a modification is physically reasonable since the effective viscosity of the lithosphere is probably weakened at subduction zones (Sleep, 1979). Also, the effect of high slab viscosity should transfer more stress toward the lower mantle and drive the responses more positive. Unfortunately, it is impossible to model these lateral variations in viscosity with our simple analytical models. We have addressed these problems in more detail using numerical methods, and the results verify the effects described above (Richards, Sleep, and Hager, to be submitted, 1986: Chapter 4).

The 4-layer model of Figure 7a, applied to the lower mantle P-wave heterogeneity and modified appropriately for slabs, allows us to successfully predict 82% of the observed geoid variance (Figure 7b,d). The best-fitting lower mantle P-velocity/density conversion factors are about 3 km sec $^{-1}$/g cm $^{-3}$ for both degrees 2 and 3, and the fact that they agree with each other indicates that we have used approximately the correct lower mantle response functions.

Thermal Properties of the Lower Mantle

Our estimate of the constant pressure derivative of compressional wave velocity with respect to density, $(\partial V_p / \partial \rho)_P \approx 3$ km sec $^{-1}$/g cm $^{-3}$, has relatively large uncertainty associated with it due to a variety of error sources in the data and modelling trade-offs (nonuniqueness). However, it is interesting to compare this result to laboratory data for candidate mantle minerals. If the lower mantle is well below the melting temperature (Anderson, 1981), it is likely that shear and compressional velocity behave similarly in response to temperature variations. If this condition holds, then a simple relation can be derived between the second isentropic Gruneisen parameter, δ_s, and the variation of P-wave velocity with density

$$\delta_s \equiv \left(\frac{\partial \log K_s}{\partial \log \rho} \right)_P \approx 1 + 2 \left(\frac{\partial \log V_p}{\partial \log \rho} \right)_P = 1 + 2 \frac{\rho}{v_p} \left(\frac{\partial V_p}{\partial \rho} \right)_P \qquad (7)$$

where K_s is the isentropic bulk modulus. Using the essentially constant ratio ρ / V_p =0.40 (Dziewonski and Anderson, 1981) for the lower mantle, we estimate an average lower mantle value of $\delta_s = 3.4$. This value, uncertain by a factor of at least 30%, falls in the middle to low range of values obtained from low pressure and temperature laboratory measurements (Anderson, 1968). The parameter δ_s, as well as $\left(\frac{\partial V_p}{\partial p} \right)_P$, is not expected to depend strongly upon temperature and pressure (Orson Anderson, personal communication) and should be essentially constant throughout the lower mantle barring a strong compositional gradient.

Implied lower mantle temperature variations corresponding to the broadscale (l = 2,3) lower mantle heterogeneity are only about ± 15 ^{0}C. By extrapolating the heterogeneity spectrum to higher degrees, O'Connell and Hager (1984) estimated a

minimum of about 10^{23} Poise for the lower mantle viscosity in the 4-layer model. This value is constrained by a maximum average global advected heat flux of about 80 mW/m ^{2}; hence, the lower bound.

Such small, broadscale temperature variations are likely to cause less than an order of magnitude lateral variation in viscosity. Although we have not included these variations in our geoid models, their dynamical effect is small for the lowest harmonic degrees (Richards and Hager, manuscript in preparation: Chapter 3). However, we expect that strong short-wavelength heterogeneities do exist in the lower mantle (e.g., mantle plumes), and large horizontal viscosity contrasts may complicate their geoid signatures. Also, we have not modelled the effects of stress dependent rheology which tend to homogenize the viscosity structure (Christensen, 1984). These problems can now be addressed via numerical modelling on a new generation of supercomputers, and it will soon be possible to derive better constraints on mantle rheology from our new knowledge of density contrasts in the mantle.

The Residual Geoid

Despite uncertainties in the seismic data and necessary oversimplifications in our dynamical models, comparison of Figure 7b,d with Figure 1a,b shows that we have accounted for most of the features in the Earth's long-wavelength geoid. The residual geoid obtained by subtracting that predicted in Figure 7 is shown in Figure 8a. Residual anomalies are reduced to about $\pm$40 m from the $\pm$100 m geoid anomalies observed. Low-degree ($\leq$5) correlations between the isostatic model and the residual geoid are not improved (Figure 8b) over those obtained previously (Figure 2a). However, we can tentatively recognize two other signals remaining in Figure 8a. First, the

upper mantle shear velocity model of Tanimoto (1986) is strongly correlated with the low-degree (2-5) residual geoid, so much of the residual geoid may be due to unmodelled density contrasts in the upper mantle. Secondly, we note that prominent geoid lows remain over Hudson Bay and Antarctica which suggest a signature of incomplete rebound from the last major Pleistocene deglaciation.

To test this latter possibility we have estimated the total unrebounded geoid signature due to the 18,000 B.P. deglaciation. The postulated ice sheets (Wu and Peltier, 1983) were "melted" and distributed over the oceans. An expansion of residual geoid lows was calculated from the estimated topographic depressions after deglaciation. Self-consistency was maintained by iterating upon the "new" geoid to properly redistribute the oceans. Correlations between this expansion and the residual geoid (Figure 8b) are consistently positive for degrees 2-11 and significant for degrees 2, 5, 9, 10, and 11. Of course, rebound has occurred to reduce these post-glacial geoid lows, but their shape and, hence, the correlations should be largely unaffected if viscous relaxation is linear. A more complete treatment of this problem using residual geoid anomalies may provide additional constraints on viscous relaxation models and mantle rheology.

Conclusions

On the basis of the global data we have examined we can draw a number of strong conclusions concerning the sources of long-wavelength geoid anomalies:

(1) Most of the Earth's low-degree geoid power is derived from density heterogeneity in the lower mantle. Compensating deformation of the upper surface and core-mantle boundary dominates this geoid signal and results in geoid highs over low

density, buoyant lower mantle.

(2) Much of the remaining geoid power is caused by high density slabs in active subduction zones. Compensation of these subducted slabs by deformation of the lithosphere is weakened by relatively low viscosity in the upper mantle, and geoid highs result over subduction zones.

(3) Compensated topography and lithospheric or crustal thickness variations contribute strongly to the observed geoid only for harmonic degrees ≥ 6.

(4) Spreading velocity is not strongly correlated with long-wavelength geoid anomalies ($l \leq 15$). This observation, along with the lack of seismic evidence for pronounced low velocity anomalies at great depth (>250 km) below ridges (Grand and Helmberger, 1984), leads to the conclusion that ridges, with the exception of hotspots, are mostly passive, tensional features and are not the direct result of thermally driven deep mantle upwelling.

(5) The spatial distribution of hotspots is significantly correlated with geoid highs for degrees ≤ 6 after the effect of subducted slabs is removed. Two prominent spectral peaks in the hotspot distribution also correspond to correlations of the geoid with low velocity in both the upper ($l = 6$) and lower ($l = 2$) mantle.

(6) There is considerable seismic heterogeneity in the mid-upper mantle (200-400 km), but relatively little geoid signal results at the longest wavelengths (degree 2-3). Heterogeneity in the transition zone is probably related to subduction and may contribute significant low-degree geoid power. If the upper mantle viscosity is much lower than that of the lower mantle, then we would expect less broadscale heterogeneity to be sustained below the lithosphere in the upper mantle (outside of subduction zones). The large upper mantle shear velocity variations observed may be

enhanced by the strong temperature dependence of the shear modulus above the solidus. Much of the unexplained 18% of the observed geoid variance, mainly at degrees $l \geq 4$, may result from upper mantle heterogeneity. Also, unmodelled lows over Hudson Bay and Antarctica (Figures 1b, 8a) may be due to incomplete rebound from Pleistocene deglaciation. These residual geoid lows may be largely responsible for the weak negative correlation between continental shields and the geoid.

The dynamical model we have used to explain these observations assumes whole mantle convection. Our evidence indicates that the upper and lower mantle are thermally continuous. We cannot, at present, determine whether or not mixing due to subducted slabs and, possibly, mantle plumes will destroy any tendency toward chemical stratification. Plate motions are driven largely by subducting slabs and lithospheric cooling, and spreading ridges do not represent return flow in closed cells either in the upper mantle or in the whole mantle (Hager and O'Connell, 1979). This view is consistent with convection driven largely by internal heating due to radioactive decay in the mantle.

The dominant degree 2-3 geoid lows (Figure 4a) correspond roughly to a ring of subduction around the Pangean continental assemblege which may have been stable for a very long time before its breakup $\sim$ 125 Ma ago (Anderson, 1982; Chase and Sprowl, 1983). We suspect that high velocity (density) anomalies in the lower mantle are due to dead slabs distributed through the lower mantle over the last $\sim$100-200 Ma. Along with a negative degree 2-3 lower mantle geoid response, these old slabs would cause the geoid lows which bound the large equatorial geoid highs over Africa (Pangea) and the central Pacific. Hotspots clustered in these geoid highs may be deep mantle plumes that have not been sheared or quenched by subducting slabs. If this

scenario is correct, very high Rayleigh number, presumably time-dependent convection in the mantle was, in the past, artifically stabilized at low degrees by the chemically buoyant continental assemblage.

Acknowledgments

We thank Bob Myers and Nancy Nichols for preparation of much of the data on topography, hotspots, glacial ice loading, and plate convergence/divergence rates. Rob Clayton and Toshiro Tanimoto kindly provided harmonic expansions of their seismic velocity models prior to publication. The estimate of the Gruneisen parameter resulted from discussions with Don Anderson, who also provided helpful comments on the manuscript. This work was supported by NASA grant NAG5-315 and by a Sloan Foundation Fellowship to BHH. Contribution 4304, Division of Geological and Planetary Sciences, California Institute of Technology, Pasadena, California.

References

Anderson, D. L., 1982, Hotspots, polar wander, Mesozoic convection, and the geoid, *Nature, 297,* 391-393.

Anderson, D. L. and C. Sammis, 1970, Partial melting in the upper mantle, *Phys. Earth Planet. Int., 3,* 41-50.

Anderson, O. L., 1981, Temperature profiles in the Earth, in *Evolution of the Earth,* R. J. O'Connell and W. S. Fyfe (eds.), Am. Geophys. Union, Washington, D.C., pp. 19-27.

Anderson, O. L., E. Schreiber, and R. C. Liebermann, 1968, Some elastic constant data on minerals relevant to geophysics, *Rev. of Geophys., 6,* 491-524.

Balmino, G., B. Maynot and N. Vales, 1982, Gravity field model of Mars in spherical harmonics up to degree and order eighteen, *J. Geophys. Res., 87,* 9735-9746.

Birch, F., 1961, Composition of the Earth's mantle, *Geophys. J. R. Astron. Soc., 4,* 295-311.

Cathles, L. M., III, 1975, *The Viscosity of the Earth's Mantle,* Princeton Univ. Press, Princeton, N.J.

Chase, C. G., 1978, Plate kinematics: the Americas, East Africa, and the rest of the world, *Earth Planet. Sci. Lett., 37,* 355-368.

Chase, C. G., 1979, Subduction, the geoid, and lower mantle convection, *Nature, 282,* 464-468.

Chase, C. G. and M. K. McNutt, 1982, The geoid: effect of compensated topography and uncompensated oceanic trenches, *Geophys. Res. Lett., 9,* 29-32.

Chase, C. G. and D. R. Sprowl, 1983, The modern geoid and ancient plate boundaries, *Earth Planet. Sci. Lett., 62,* 314-320.

Christensen, U., 1984, Convection with pressure and temperature dependent non-Newtonian rheology, *Geophys. J. R. Astr. Sco., 77,* 343-384.

Clayton, R. W. and R. P. Comer, 1983, A tomographic analysis of mantle heterogeneities from body wave travel times, *Eos, Trans. AGU, 62,* 776 (abstract).

Crough, S. T. and D. M. Jurdy, 1980, Subducted lithosphere, hotspots, and the geoid, *Earth Planet. Sci. Lett., 48,* 15-22.

Dziewonski, A. M., 1984, Mapping the lower mantle: Determination of lateral heterogeneity in P velocity up to degree and order 6, *J. Geophys. Res., 89,* 5929-5952.

Dziewonski, A. M. and D. L. Anderson, 1981, Preliminary reference Earth model, *Phys. Earth Planet. Int., 25,* 297-356.

Dziewonski, A. M., B. H. Hager, and R. J. O'Connell, 1977, Large-scale heterogeneities in the lower mantle, *J. Geophys. Res., 82,* 239-255.

Eckhardt, D. H., 1984, Correlations between global features of terrestrial fields, *Math. Geol., 16,* 155-171.

Grand, S. P. and D. V. Helmberger, 1984, Upper mantle shear structure beneath the northwest Atlantic ocean, *J. Geophys. Res., 89,* 11,465-11,475.

Hager, B. H., 1982, Subduction velocity and the geoid: an empirical relation, *Eos, Trans. AGU, 62,* 906 (abstract).

Hager, B. H., 1983, Global isostatic geoid anomalies for plate and boundary layer models of the lithosphere, *Earth Planet. Sci. Lett., 63,* 97-109.

Hager, B. H., 1984, Subducted slabs and the geoid: constraints on mantle rheology and flow, *J. Geophys. Res., 89,* 6003-6015.

Hager, B. H., R. W. Clayton, M. A. Richards, R. P. Comer, and A. M. Dziewonski, 1985, Lower mantle heterogeneity, dynamic topography, and the geoid, *Nature, 313,* 541-545.

Hager, B. H. and R. J. O'Connell, 1978, Subduction zone dip angles and flow driven by plate motion, *Tectonophysics, 50,* 111-133.

Hager, B. H. and R. J. O'Connell, 1979, Kinematic models of large-scale mantle flow, *J. Geophys. Res., 84,* 1031-1048.

Hager, B. H. and R. J. O'Connell, 1981, A simple global model of plate dynamics and mantle convection, *J. Geophys. Res., 86,* 4843-4867.

Haxby, W. F. and D. L. Turcotte, 1978, On isostatic geoid anomalies, *J. Geophys. Res., 83,* 5473-5478.

Jordan, T. H., 1975, The continental tectosphere, *Rev. Geophys. Space Phys., 13,* 1-12.

Jordan, T. H., 1978, Composition and development of the continental tectosphere, *Nature, 274,* 544-548.

Kaula, W. M., 1967, Theory of statistical analysis of data distributed over a sphere, *Rev. Geophys. Space Phys., 5,* 83-107.

Kaula, W. M. and R. J. Phillips, 1981, Quantitative tests for plate tectonics on Venus, *Geophys. Res. Lett., 8,* 1187-1190.

Kiefer, W. S., M. A. Richards, B. H. Hager and B. G. Bills, 1986, A dynamic model of Venus's gravity field, *Geophys. Res. Lett., 13,* 14-17.

Lerch, F. J., S. M. Klosko, and G. B. Patch, 1983, A refined gravity model from LAGEOS (GEM-L2), *NASA Tech. Memo., 84986.*

Masters, G., T. H. Jordan, P. G. Silver, and F. Gilbert, 1982, Aspherical Earth structure from fundamental spheroidal-mode data, *Nature, 298,* 609-613.

Mauk, F. J., 1977, A tectonically-based Rayleigh wave group velocity model for prediction of dispersion character through ocean basins, Ph.D. thesis, Univ. of Mich., Ann Arbor.

McKenzie, D., 1977, Surface deformation, gravity anomalies and convection, *Geophys. J. Roy. Astron. Soc., 48,* 211-238.

Minster, J. B. and T. H. Jordan, 1978, Present-day plate motions, *J. Geophys. Res., 83,* 5331-5354.

Morgan, W. J., 1965, Gravity anomalies and convection currents 1. A sphere and cylinder sinking beneath the surface of a viscous fluid, *J. Geophys. Res., 70,* 6175-6187.

Morgan, W. J., 1972, Plate motions and deep mantle convection, *Geol. Soc. Am.*

Mem., 132, 7-22.

Nakanishi, I., and D. L. Anderson, 1984, Measurements of mantle wave velocities and inversion for lateral heterogeneity and anisotropy - II. Analysis by the single-station method, *Geophys. J. R. Astron. Soc., 78,* 573-617.

Nakiboglu, S. M., 1982, Hydrostatic theory of the Earth and its mechanical implications, *Phys. Earth Planet. Inter., 28,* 302-311.

Nataf, H.-C., I. Nakanishi, and D. L. Anderson, 1984, Anisotropy and shear-velocity heterogeneities in the upper mantle, *Geophys. Res. Lett., 11,* 109-112.

Nataf, H.-C., I. Nakanishi, and D. L. Anderson, 1986, Measurements of mantle wave velocities and inversion for lateral heterogeneities and anisotropy part III: Inversion, *J. Geophys. Res.,* in press.

National Oceanic and Atmospheric Administration (NOAA), 1980, Topographic data for one-degree size areas, Environ. Data Service, NGS Data Center, Boulder, CO.

O'Connell, R. J. and B. H. Hager, 1984, Velocity anomalies, convection, heat transport, and viscosity of the lower mantle, *Eos, Trans. AGU, 65,* 1093 (abstract).

Parsons, B. and S. Daly, 1983, The relationship between surface topography, gravity anomalies, and the temperature structure of convection, *J. Geophys. Res., 88,* 1129-1144.

Passey, Q. R., 1981, Upper mantle viscosity derived from the difference in rebound of the Provo and Bonneville shorelines: Lake Bonneville Basin, Utah, *J. Geophys. Res., 86,* 11701-11708.

Pekeris, C. L., 1935, Thermal convection in the interior of the Earth, *Mon. Not. R. Astron. Soc., Geophys. Suppl., 3,* 343-367.

Peltier, W. R., 1981, Ice age geodynamics, *Ann. Rev. Earth Planet. Sci., 9,* 119-225.

Peltier, W. R. and A. Forte, 1984, The gravitational signature of plate tectonics, *Terra Cognita (EUG), 4,* 251.

Ricard, Y., L. Fleitout, and C. Froidevaux, 1984, Geoid heights and lithospheric stresses for a dynamical Earth, *Annales Geophysicae, 2,* 267-286.

Richards, M. A. and B. H. Hager, 1984, Geoid anomalies in a dynamic Earth, *J. Geophys. Res., 89,* 5987-6002.

Runcorn, S. K., 1964, Satellite gravity measurements and a laminar viscous flow

model of the Earth's mantle, *J. Geophys. Res., 69,* 4389-4394.

Sjogren, W. L., R. J. Phillips, P. W. Birkeland, and R. N. Wimberly, 1980, Gravity anomalies on Venus, *J. Geophys. Res., 85,* 8295-8302.

Sleep, N. H., 1979, The double seismic zone in downgoing slabs and the viscosity of the mesosphere, *J. Geophys. Res., 84,* 4565-4571.

Tanimoto, T. and D. L. Anderson, 1984, Mapping convection in the mantle, *Geophys. Res. Lett., 4,* 287-290.

Tanimoto, T., 1986, The Backus-Gilbert approach to the three-dimensional structure in the upper mantle - II. SH and SV velocity, in press, *Geophys. J. R. Astron. Soc.*

Turcotte, D. L. and D. C. McAdoo, 1979, Geoid anomalies and the thickness of the lithosphere, *J. Geophys. Res., 84,* 2381-2387.

Woodhouse, J. H. and A. M. Dziewonski, 1984, Mapping the upper mantle: Three dimensional modelling of Earth structure by inversion of seismic waveforms, *J. Geophys. Res., 89,* 5953-5986.

Wu, P. and W. R. Peltier, 1983, Glacial isostatic adjustment and the free air gravity anomaly as a constraint upon deep mantle viscosity, *Geophys. J., R.*

Astron. Soc., 74, 377-449.

Wyllie, P. J., 1971, The role of water in magma generation and initiation of diapiric uprise, *J. Geophys. Res., 76,* 1328-1338.

Table - Correlation coefficients at harmonic degree 2 between transition zone velocity models (Masters et al., 1982; Woodhouse and Dziewonski, 1984; Tanimoto, 1986) and both the observed geoid and subducted slabs (Hager, 1984). Positive correlations indicate the correspondence of geoid highs and subducted slabs to high seismic velocity. Confidence levels for these correlations may be read from, e.g., Figure 3a,b. Note: a correlation with the geoid of +0.79 was found by Masters et al. using an earlier geoid model and a slightly different hydrostatic correction.

TABLE: Upper Mantle Degree 2 Correlations

Model	vs. Geoid	vs. Slabs	vs. MJSG(400-670km)
MJSG(400-670km)	+.71	+.87	----
WD(450km)	+.05	+.77	+.59
WD(550km)	+.49	+.93	+.79
WD(650km)	+.61	+.90	+.78
Tan(450km)	+.58	+.73	+.62
Tan(550km)	+.63	+.77	+.65
Tan(650km)	+.67	+.78	+.66

Figure 1 - Observed long-wavelength geoid (Lerch et al., 1983) referred to the hydrostatic figure of the Earth (Nakiboglu, 1982). (a) Spherical harmonic degree and order 2-20 representation. (b) Degrees 4-20 only. Continents are outlined for reference, and plate boundaries are also shown in (a). Geoid lows are shaded; cylindrical equidistant projection.

Observed Geoid: degree 2-20

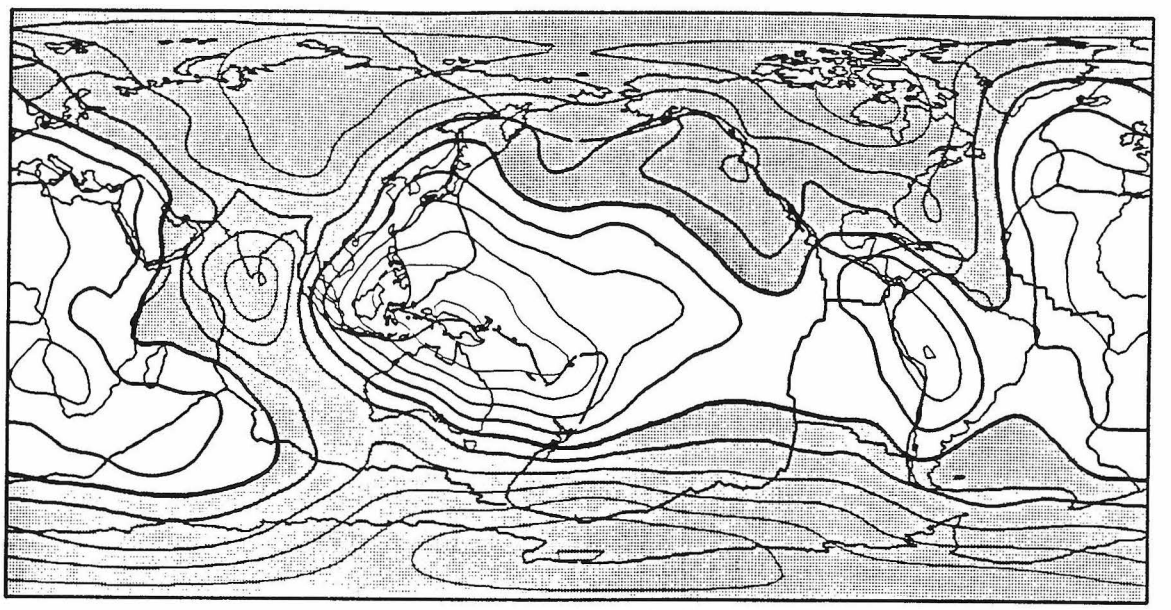

contour interval: 20 m

(a)

Observed Geoid: degree 4-20

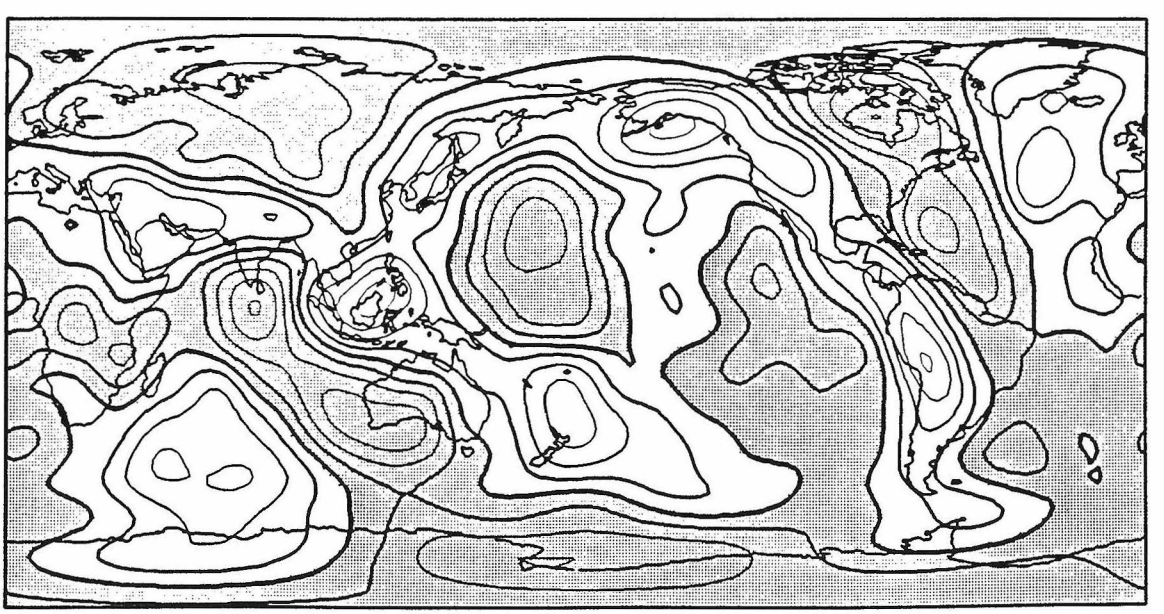

contour interval: 10 m

(b)

Figure 2 - (a),(c) Degree-by-degree correlations, r_l, between the observed, nonhydrostatic geoid and surface features. Contours give the confidence of correlation, with a confidence level of 0.98 indicating a 2% chance that the correlation is random.

(b),(d) Log-log comparison of root mean square harmonic coefficient amplitudes, $\sqrt{V_l{}^2/(2l+1)}$. Units are as follows: Observed geopotential, $\gamma M/R$ (fraction of average geopotential at surface); Topography, 10^5 km (equivalent rock topography referred to density 2.7 g/cm ^{3}); Isostatic model, $\gamma M/R$; Shields, $4.0x\,10^3$ fraction of shield terrane per unit surface area; Convergence and Divergence, 100 km ^{2}/yr; Plate velocity (poloidal component), $1.2x\,10^5$ cm/yr; Slab potential, $\gamma M/R$. Geopotentials, in units $\gamma M/R$, may be converted to geoid elevations by dividing by the gravitational acceleration at the surface or by multiplying by R . (γ is the gravitational constant, M the mass of the Earth, and R the Earth's radius.)

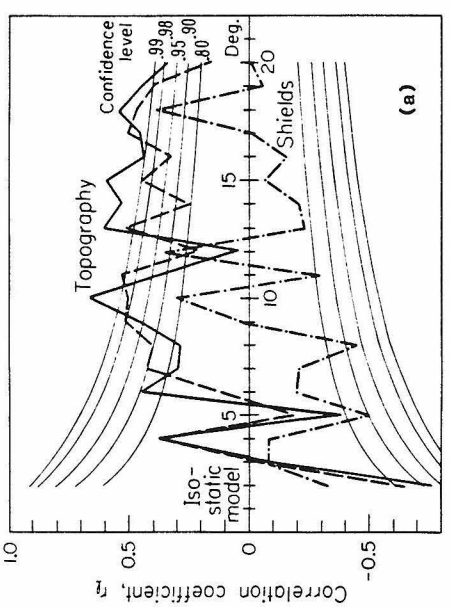
Correlation coefficient, r
1.0
0.5
0
-0.5
Topography
Shields
Iso-
static
model
Confidence
level
.99
.98
.95
.90
.80
Deg.
5
10
15
20
(a)

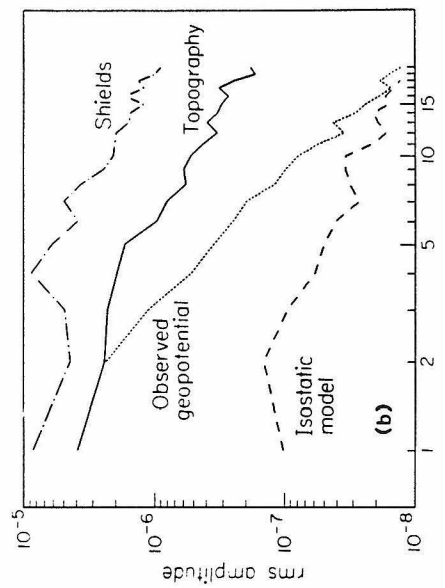
rms amplitude
10^{-5}
10^{-6}
10^{-7}
10^{-8}
Shields
Topography
Observed
geopotential
Isostatic
model
(b)
1
2
5
10
15

Correlation coefficient, r
1.0
0.5
0
-0.5
Convergence
Slab potential
Plate
vel.
Divergence
Confidence
level
.99
.98
.95
.90
.80
Deg.
5
10
15
20
(c)

rms amplitude
10^{-5}
10^{-6}
10^{-7}
10^{-8}
Plate velocity
Convergence
Divergence
Slab
potential
(d)
1
2
5
10
15
Degree

Figure 3 - (a) Correlations, r_l, between the observed geoid and both hotspots and seismic velocity heterogeneity. (b) Correlations between the slab residual geoid (subducted slab signal removed) and both hotspots and seismic velocity. The WD velocity model extends only to degree 8.

(c) Log-log comparison of root mean square harmonic coefficient amplitude. Units are: Residual geopotential, $\gamma M/R$ (fraction of average geopotential at surface); Upper mantle S-velocity (Woodhouse and Dziewonski, 1984; Tanimoto, 1986), 10^4 km/sec; Lower mantle P-velocity (Clayton and Comer, 1983), 10^4 km/sec; Hotspot distribution, $4.1x\,10^6$ hotspots per Earth area.

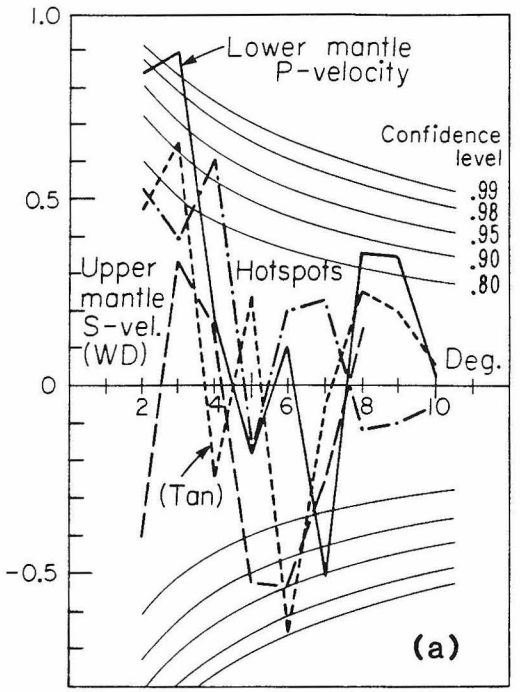
1.0
0.5
0
-0.5
Lower mantle
P-velocity
Confidence
level
.99
.98
.95
.90
.80
Upper
mantle
S-vel.
(WD)
Hotspots
Deg.
2
4
6
8
10
(Tan)
(a)

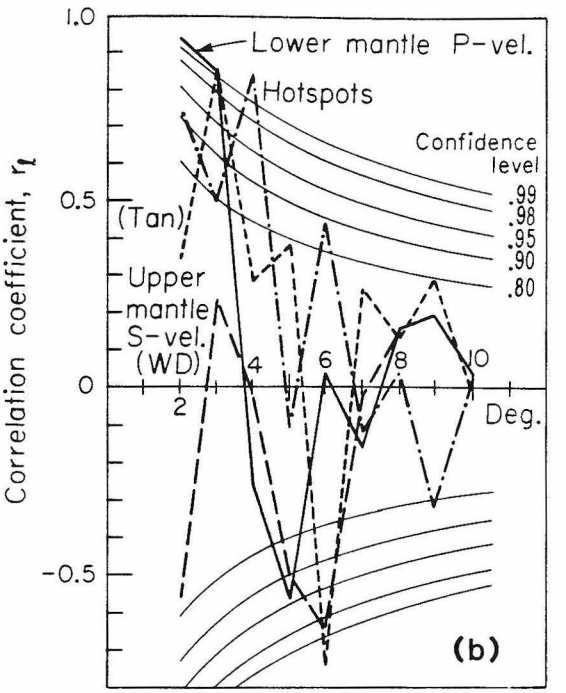
1.0
0.5
0
-0.5
Correlation coefficient, r_l
Lower mantle P-vel.
Hotspots
Confidence
level
.99
.98
.95
.90
.80
(Tan)
Upper
mantle
S-vel.
(WD)
2
4
6
8
10
Deg.
(b)

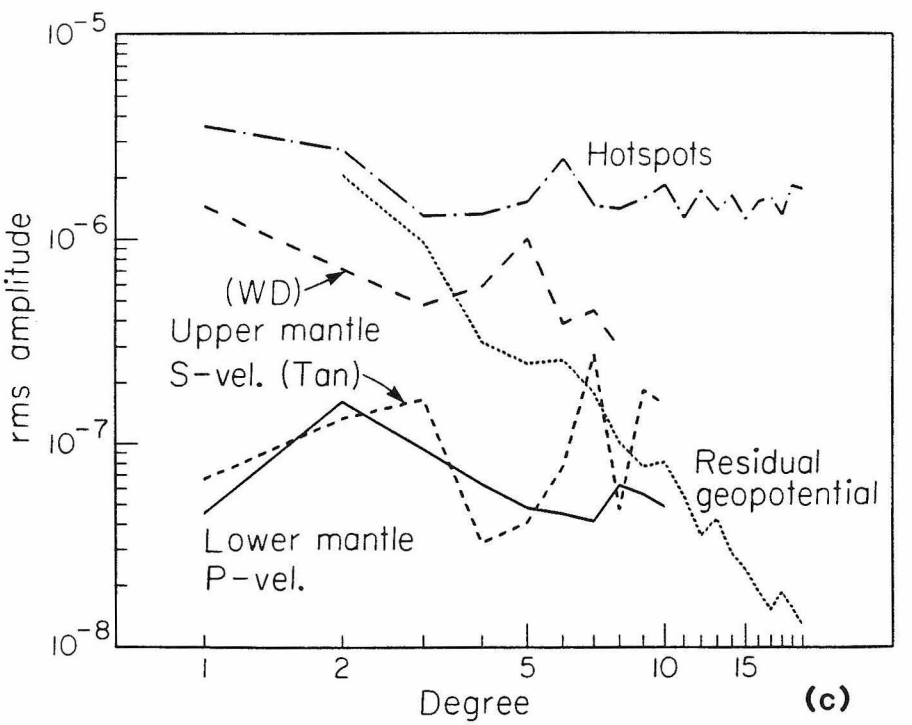
10^{-5}
10^{-6}
10^{-7}
10^{-8}
rms amplitude
Hotspots
(WD)
Upper mantle
S-vel. (Tan)
Residual
geopotential
Lower mantle
P-vel.
1
2
5
10
15
Degree
(c)

Figure 4 - (a) Observed, nonhydrostatic geoid (degrees 2-10) after the subducted slab geoid signal (Hager, 1984) is removed. Black dots represent hotspot locations used to obtain the harmonic expansion of the hotspot distribution; geoid lows are shaded. (b) Average degree 2-3 seismic compressional wave velocity anomalies in the lower mantle; low velocity is shaded.

Slab Residual Geoid: degree 2-10

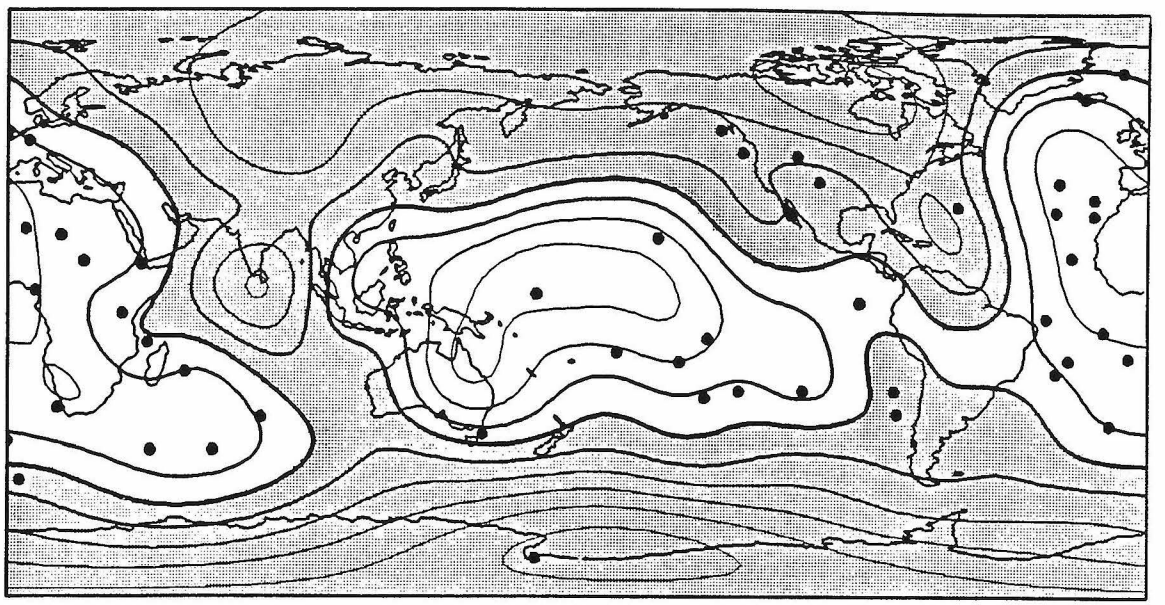

(a) contour interval: 20 m

Lower Mantle P-Wave Velocity: degree 2-3

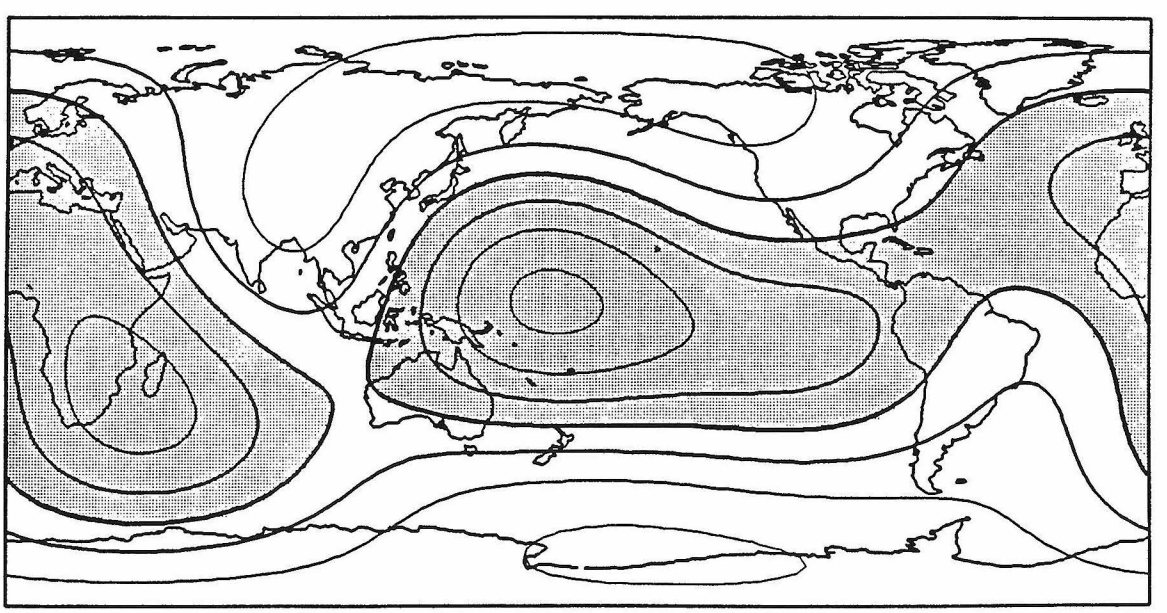

(b) contour interval: 3 m/sec

Figure 5 - Illustrations of flow models for spherical Earth calculations (l =3). (a) Whole mantle flow. (b) Flow with a chemical barrier at the 670 km discontinuity. Plus and minus signs indicate positive and negative density contrasts. The dashed lines are reference boundaries, and the solid lines represent the displaced boundaries. Streamlines indicate the sense of flow.

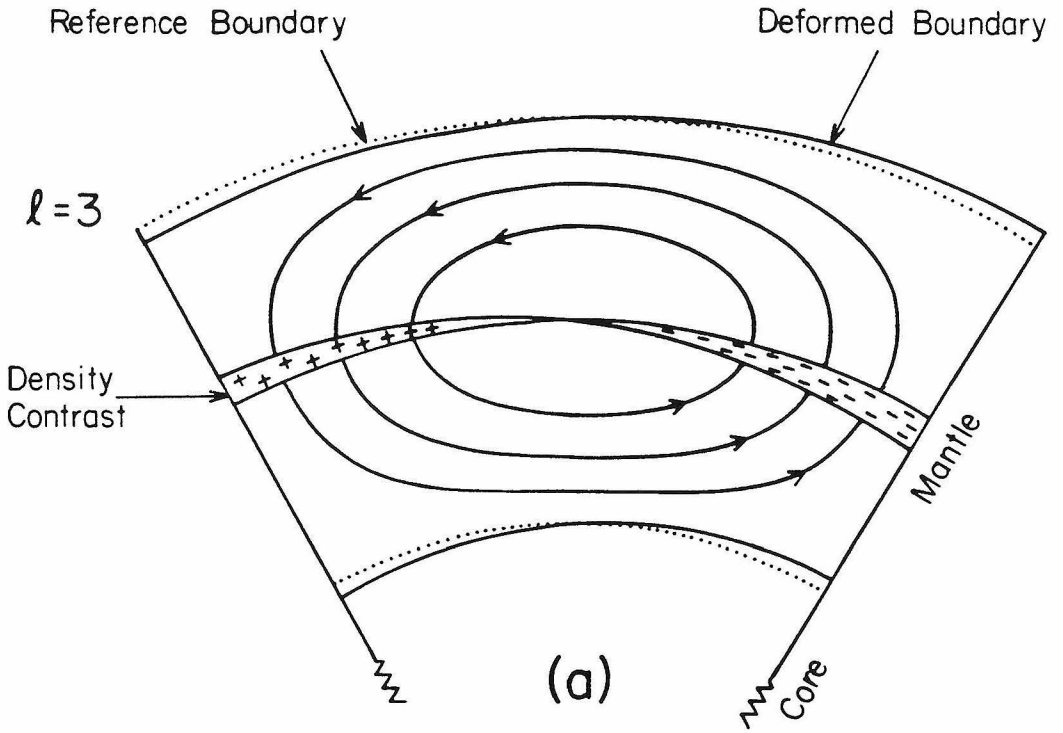
Reference Boundary
Deformed Boundary
ℓ=3
Density
Contrast
Mantle
Core
(a)

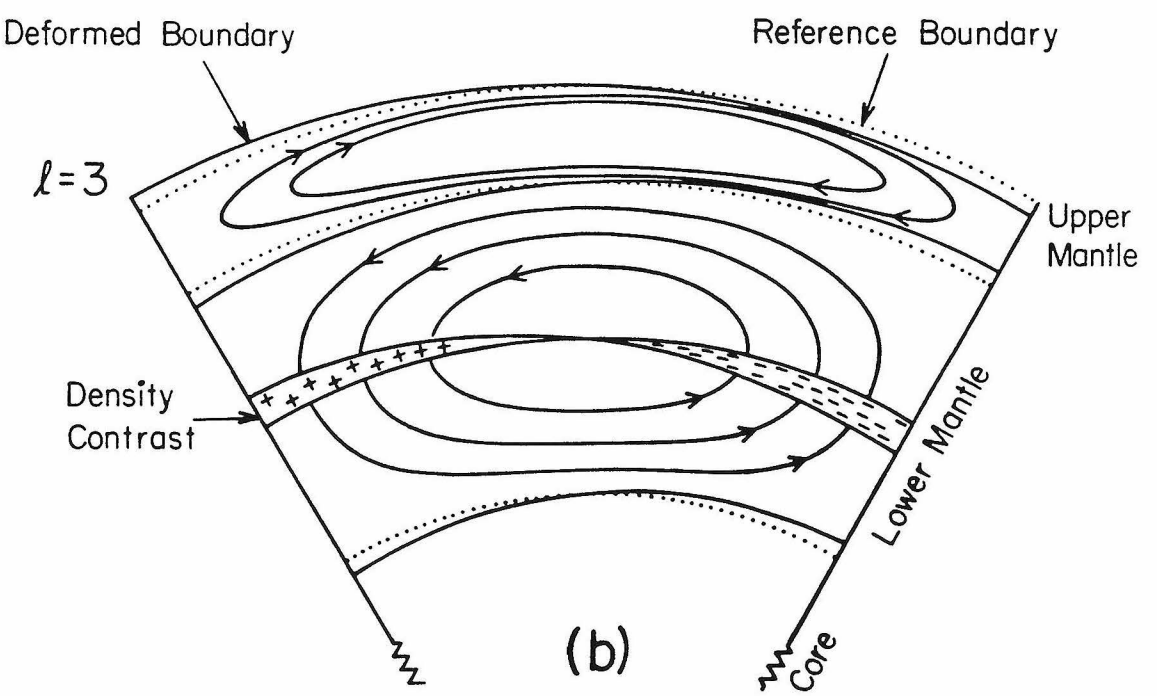
Deformed Boundary
Reference Boundary
ℓ=3
Upper
Mantle
Density
Contrast
Lower Mantle
Core
(b)

Figure 6 - Dynamic response function, $G_l(r)$, for surface density contrasts of spherical harmonic degrees 2, 4, 6, and 8 plotted against radius, r, for six Earth models. Models U, left, permit mantle-wide flow; models C, right, have a (chemical) barrier at 670 km depth, causing stratification into separate upper and lower mantle flow systems. Models U1 and C1 have uniform viscosity; models U10 and C10 have a factor of 10 viscosity increase below 670 km; models U100 and C100 have a factor of 100 increase. The geoid responses are normalized to the geoid which would be obtained if the harmonic density contrasts were placed at the top surface with no dynamic compensation allowed.

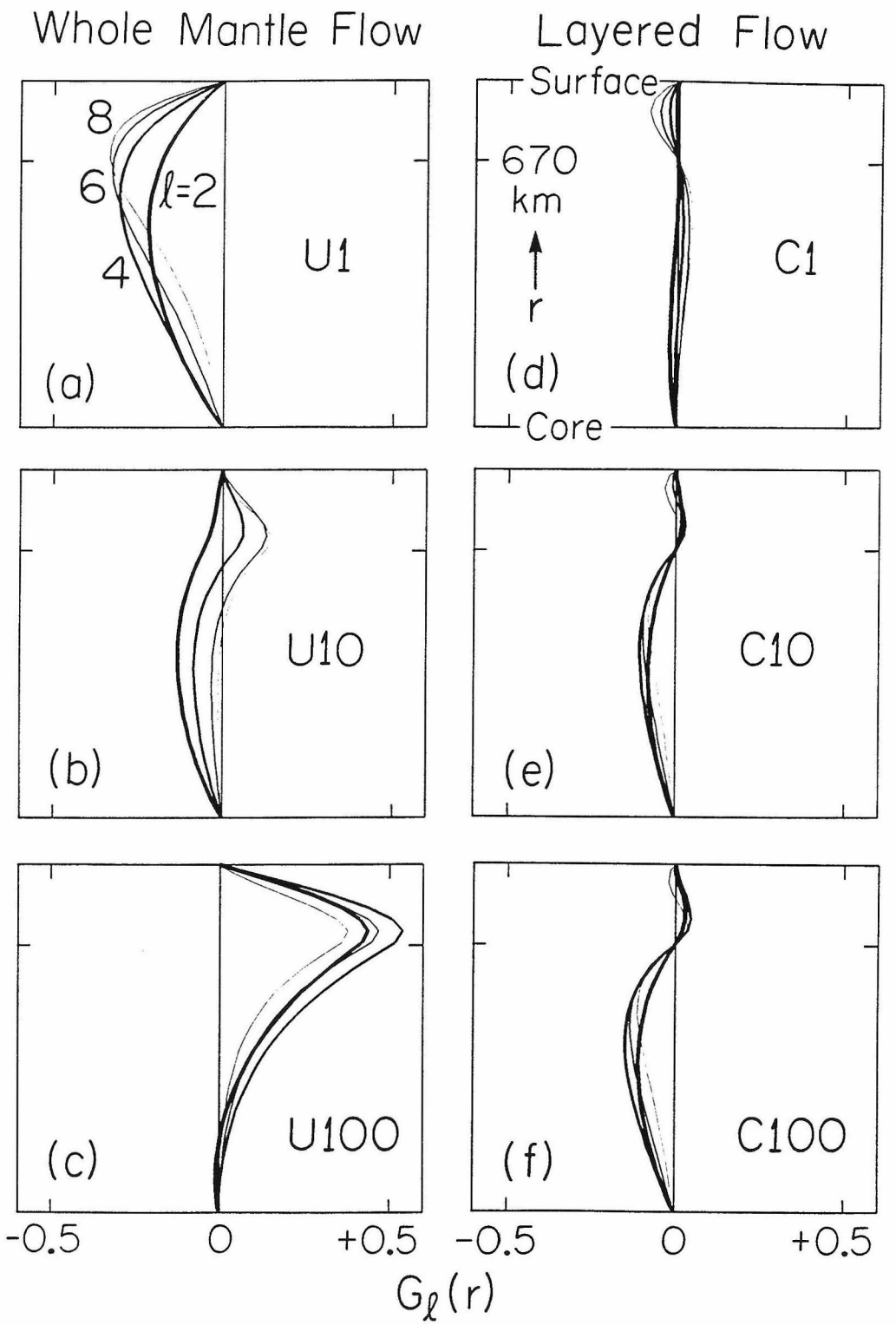
Whole Mantle Flow
Layered Flow
Surface
670
km
r
Core
8
6
4
ℓ=2
U1
C1
(a)
(d)
U10
C10
(b)
(e)
U100
C100
(c)
(f)
-0.5
0
+0.5
-0.5
0
+0.5
$G_\ell(r)$

Figure 7 - (a),(c) Dynamic response functions for two slightly differing 4-layer viscosity models with mantle-wide flow. The viscosity of the transition zone (400-670 km depth) is a factor of 10 smaller than that of the lower mantle, η_0, and the viscosity between 200 and 400 km depth is a factor of 300 lower than η_0. In (a) the lithospheric viscosity is η_0 while in (b) the lithospheric viscosity is lowered to $0.1\eta_0$. Response functions are plotted for harmonic degrees 2, 4, and 8.

(b),(d) Predicted long-wavelength geoid anomalies for harmonic degrees 2-9 and 4-9, respectively; geoid lows are shaded. Predicted anomalies are computed by convolving the 4-layer dynamic model responses of (a) and (c), respectively, with lateral density variations inferred from lower mantle P-wave tomography and the locations of subducted slabs.

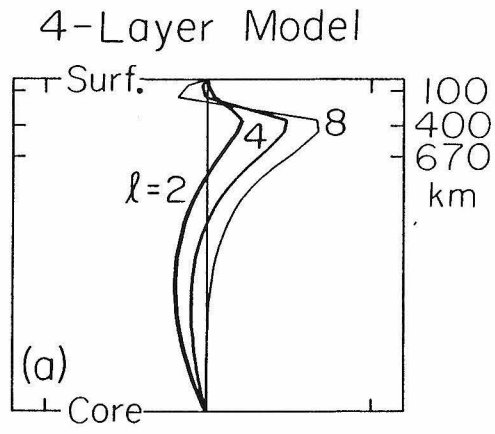
4-Layer Model
Surf.
100
400
670
km
8
4
ℓ=2
(a)
Core

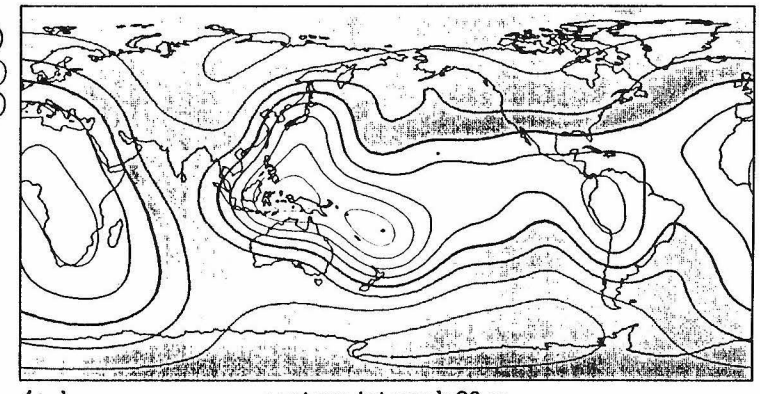
Predicted Geoid: degree 2-9
(b)
contour interval: 20 m

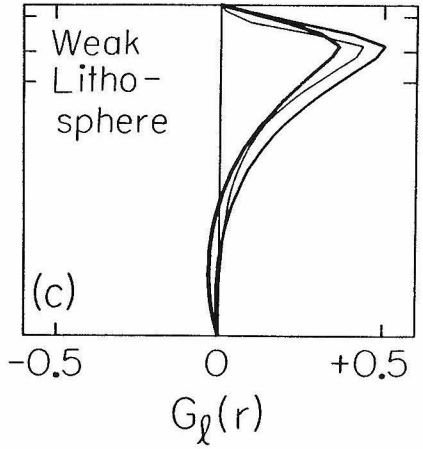
Weak
Litho-
sphere
(c)
-0.5
0
+0.5
$G_\ell(r)$

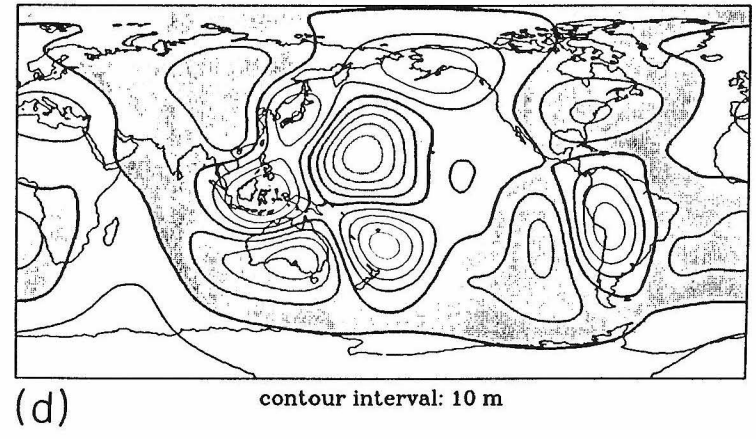
Predicted Geoid: degree 4-9
(d)
contour interval: 10 m

Figure 8 - (a) Residual geoid after the predicted slab-lower mantle geoid model (previous figure) is subtracted from the observed geoid (Figure 1). In (b) we show correlation coefficients, r_l, between this residual geoid and upper mantle shear velocity (Tanimoto, 1986), the isostatic model (see Figure 2), and the geoid predicted from Pleistocene (18,000 B.P.) deglaciation (Wu and Peltier, 1983) without viscous readjustment.

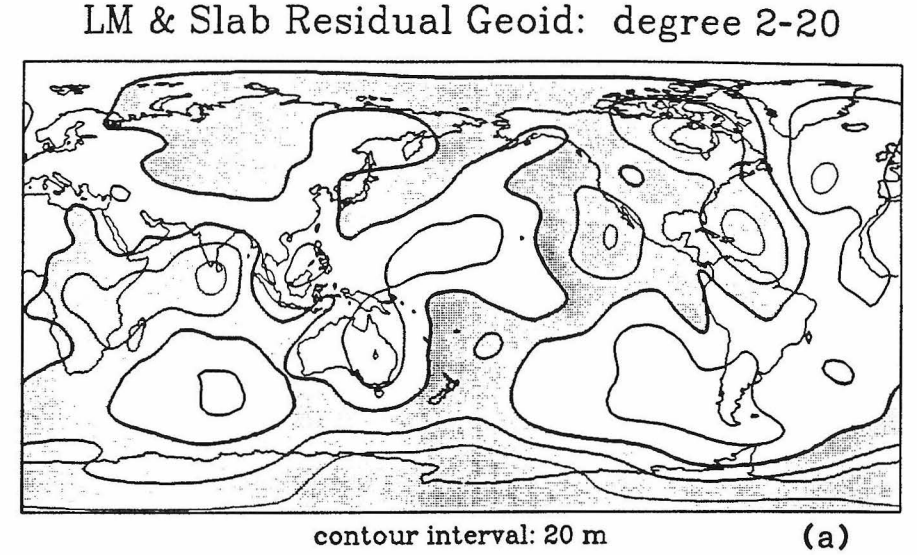
LM & Slab Residual Geoid: degree 2-20
contour interval: 20 m
(a)

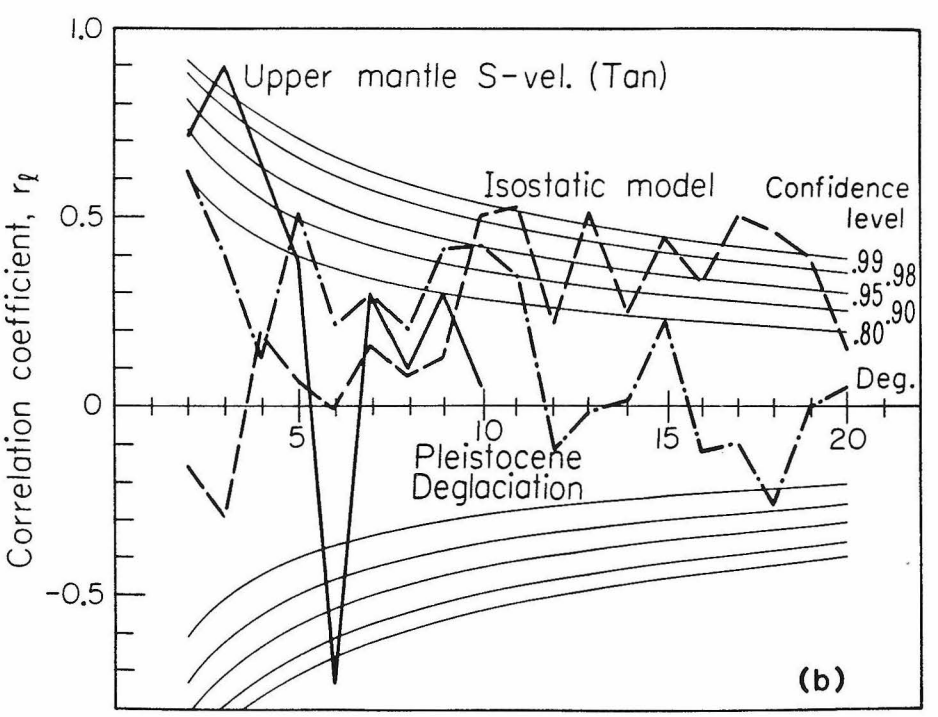
1.0
0.5
0
-0.5
Correlation coefficient, r_ℓ
Upper mantle S-vel. (Tan)
Isostatic model
Confidence level
.99
.98
.95
.90
.80
Deg.
5
10
15
20
Pleistocene Deglaciation
(b)

Chapter 3

Modelling Effects of Long-wavelength Lateral Viscosity Variations on the Geoid

Introduction

The Earth's long-wavelength, nonhydrostatic geoid is primarily the result of density contrasts associated with mantle convection. Although the geoid alone cannot be inverted uniquely to determine these density contrasts, it does provide a well-measured constraint with which any complete theory of convection must be consistent. However, the deformations of the surface, the core-mantle boundary, and, possibly, internal chemical boundaries due to convective stresses complicate the interpretation of geoid anomalies. It has been shown by many authors (Pekeris, 1935; Runcorn, 1964; Morgan, 1965; McKenzie, 1977; Parsons and Daly, 1983; Ricard et al., 1984; Richards and Hager, 1984: Chapter 1) that dynamic compensation due to boundary deformation is of dominant importance in determining the nonhydrostatic geoid of a convecting planet. Induced boundary deformations cause geoid anomalies that are of opposite sign and comparable magnitude to the geoid due to interior density contrasts. Long-wavelength geoid anomalies are therefore the relatively small difference of large numbers. Because the details of boundary deformation depend strongly on the viscosity structure and presence or absence of chemical layering in the mantle (Richards and Hager, 1984: Chapter 1; henceforth referred to as "RH"),

knowledge of both the geoid and the thermal density structure of the mantle can provide powerful constraints on mantle dynamics.

In the previous chapter we have presented results that explain more than 80% of the Earth's geoid variance on the basis of seismically determined lateral density contrasts. The principal sources of the geoid appear to be subducted slabs (Hager, 1984) and a large-scale pattern of density heterogeneity inferred from recent studies of seismic velocity heterogeneity in the lower mantle (Dziewonski, 1984; Clayton and Comer, 1983; Hager et al., 1985). Subducting slabs represent convective downwelling, and the lower mantle seismic tomography reveals low velocity and, presumably, hot buoyant material under the large, low-degree geoid highs centered on Africa and the central Pacific (see Figure 1, Chapter 2). Our models include the geoid contributions due to boundary deformation and include the effects of radial variations (due to composition or pressure) in effective viscosity. However, we have ignored the effects of viscosity variations due to stress-dependence and lateral variations in the mantle temperature field associated with convection.

The effects of temperature on viscosity and flow could be quite large (Torrance and Turcotte, 1971; Christensen, 1984). The strong temperature- and pressure-dependence of viscosity is a key element in the self-regulation of solid state convection in the terrestrial planets (Tozer, 1967; 1972) and must be responsible in large part for the very existence of plate tectonics. The density heterogeneities we believe to be responsible for the geoid necessarily imply temperature variations and, therefore, viscosity variations whose effects on dynamic compensation of the geoid must be considered. We find it somewhat surprising that our simple geoid models, which assume spherically symmetric viscosity structure, have worked so well, but there are some

discrepancies in our results: (1) We cannot explain very much of the geoid for harmonic degrees ≥ 6; our success in describing most of the variance applies mainly to the lowest degrees which dominate the geoid (see Table). (2) Subducted slabs appear to sense more viscosity increase with depth or, alternatively, a weaker lithosphere, than the density anomalies inferred from lower mantle tomography. (3) Both subducted slabs and presumed low density material (hotspots) in the upper mantle are associated with geoid highs. Although other sources of error are present, these observational problems may be explained as effects due to expected lateral variations in effective viscosity.

In order to model the geoid more accurately we need to understand how horizontal viscosity contrasts affect the dynamic response functions used in the previous chapter. Radial viscosity stratification and/or layered convection have a large effect upon these kernels (Figure 6, Chapter 2), and this strong sensitivity to radial structure serves as a standard for evaluating the importance of lateral viscosity variations. Such comparisons will be the principal focus of this chapter.

The effects of lateral viscosity variations are quite complicated, largely because all wavelengths become coupled and the harmonic degree independence of the response kernels (equation 6, Chapter 2) no longer applies. It is, therefore, difficult to address the problem in any general way. As a matter of experience we have found a logical separation between the lateral viscosity effects of very short wavelength thermal density contrast sources, such as subducting slabs and mantle plumes, and much more broadscale density and temperature fluctuations. Plumes and slabs are treated in detail in Chapter 4, and in this chapter we concentrate on the effects of truly long-wavelength variations in viscosity. The principal application of this approach is

to modelling of the low-egree geoid components from lower mantle heterogeneity. However, the calculations we present are applicable to the general case in which most of the horizontal density contrasts occur at wavelengths comparable to or larger than the depth of convection.

Large-scale Mantle Heterogeneity

The observed geoid spectrum is very strongly biased toward the long wavelengths or low harmonic degrees and is peaked at degree 2 as shown in Figure 1. (For a comparison with other terrestrial planets see Mottinger et al., 1985.) Upon removal of the modelled slab signal (Hager, 1984), which represents a short wavelength source, an even stronger low degree spectral bias is obtained. This slab residual geoid is dominated by a harmonic degree 2-3 pattern with two large, antipodal equatorial highs (Figure 4, Chapter 2). This does not necessarily mean that the lateral density structure of the mantle is also spectrally "red", because, for some dynamic models, short wavelength geoid anomalies from deep sources are more attenuated than those of longer wavelengths (Figure 6, Chapter 2).

Seismic models of lower mantle P-wave velocity heterogeneity are, in general, spectrally "white" by comparison with the geoid, but at the present time we have no satisfactory check on their resolution beyond harmonic degree 4. Also, although a degree 1 geoid term is absent by definition, there is degree 1 heterogeneity in the Earth as evidenced by the 1.1 km center of figure/center of mass offset (Balmino et al., 1973). The peak at degree 2 in the geoid might, therefore, be misleading if equally strong heterogeneity exists at degree 1. However, much of the degree 1 offset could be due to variations in crustal or lithospheric thickness which contribute very

little geoid signal (~2-4 m) (Hager, 1983).

When averaged vertically (from the core-mantle boundary to 670 km depth) the lower mantle P-wave velocity heterogeneity model of Clayton and Comer (1983) is highly correlated with the geoid for degrees 2 and 3 (Chapter 2), and the spectrum is peaked at degree 2 (Figure 1). The 22 depth layers (100 km thick) are themselves spectrally white; the longest wavelengths are, not surprisingly, more coherent depth-wise. In addition, the peak at degree 2 is preserved by the fact that the lower-most and uppermost degree 1 heterogeneities in the lower mantle velocity model are anticorrelated and cancel to a large extent. The evidence for a dominant degree 2 convection pattern must, therefore, be considered somewhat ambiguous, especially since the current lower mantle P-wave models neither agree with each other nor correlate with the geoid for degrees $l \geq 4$.

The degree 2-3 lower mantle seismic velocity variations, of the order of 0.1%, are consistent with at most $\sim 50^0$ K horizontal temperature differences at these very long wavelengths. This suggests that relatively modest thermal viscosity variations may suffice in modelling the large-scale flow pattern and geoid. If the spectral characteristics of seismic velocity variations in Figure 1 are assumed valid, a rough constraint on the average lower mantle viscosity can also be obtained. By extrapolating the spectrum to higher degrees and by simultaneously matching the Earth's advective heat flux (~80 mW/m ^{2}) and the geoid, O'Connell and Hager (1984) determined that the large-scale convection associated with the dominant, low-degree geoid anomalies requires a minimum lower mantle viscosity of 10^{22} Pa-sec. Lower viscosities give larger flow velocities and require even smaller lateral temperature contrasts.

Whether or not a dominant, large-scale pattern should exist on Earth is questionable on theoretical grounds. Marginal stability theory (e.g., Chandrasekhar, 1961) suggests that an Earth-like planet should stabilize its convective pattern at degree 3 or higher, although such criteria ignore the stabilizing effects of temperature-dependent viscosity on the upper boundary layer. More importantly, it is possible that the low-degree heterogeneity (and geoid) results mainly from very strong, small-scale temperature contrasts. Very high Rayleigh number convection should result in heterogeneity and temperature contrasts of dimensions comparable to a relatively small boundary layer (lithospheric) thickness. Subducted slabs and possibly mantle plumes, manifested as hotspots, suggest a small horizontal length scale for very large density contrasts. Hotspots are strongly correlated with the degree 2-6 slab residual geoid highs (Chapter 2) as well as with slow velocity in the lower mantle at degree 2 (also a relative spectral peak for hotspots). However, the low-degree geoid may be a memory of the insulating effects of the stable Pangean continental assemblage as suggested by Anderson (1982), and hotspots could be a symptom of hotter than average mantle on a very broad scale. Unfortunately, we cannot at present resolve this issue with the information available. It is, however, difficult to explain the long-wavelength geoid in terms of mantle plumes because of the required spectral characteristics (Richards, Sleep, and Hager, to be submitted, 1986; Chapter 4). The main certainty is that high temperature and low viscosity should be associated with upwelling material (and *vice versa* for cold downwellings), and our emphasis here is on broad-scale convection.

Temperature- and Stress-Dependent Viscosity

Experimental studies of mantle constituents such as olivine show that the viscosity of the mantle is be strongly temperature, pressure, and probably stress-dependent (Kohlstedt and Goetze, 1974; Berckhemer, Auer, and Drisler, 1979; Twiss, 1976). Mechanisms of dislocation climb or glide (Weertman, 1968) may be responsible for power-law type flow in which the effective viscosity decreases approximately as the square of the shear stress. Diffusion rates which govern creep generally increase exponentially with temperature, T, and a theoretical law is often used to describe the relationship between shear stress, σ, and strain rate, $\dot{\epsilon}$

$$\dot{\epsilon} = A\,\sigma^q \exp\left[(E^* + pV^*)/RT\right] \tag{1}$$

where E^* and V^* are activation energy and volume, R is the gas constant, p is the pressure, q is the power-law exponent, and A is a constant.

The pressure-dependence is almost purely a function of depth in the mantle due to the lithostatic load (lateral pressure gradients are small by comparison) and may well be dominated by phase changes, either abrupt or gradual, in the upper mantle. For uniform composition, pressure alone might conceivably increase the viscosity of the mantle by as much as 6 orders of magnitude from top to bottom (Sammis et al, 1977). In principle, pressure-dependent viscosity can be modelled by a sufficiently fine spacing of radial layers; these are the viscosity contrasts we have modelled in a rough form in Chapter 2.

Temperature increases with depth tend to counteract the influence of increasing pressure, and again, the effect on viscosity may be many orders of magnitude for the possible $\sim 1000^0$K non-adiabatic temperature difference between the core-mantle

boundary and the lithosphere. Rising and falling plumes of hot and cold material derived from the boundary layers will give rise to lateral changes in temperature and therefore viscosity. The most conspicuous example of this in the Earth is that of subducting slabs remaining cold enough to cause earthquakes as deep as 700 km, the slabs being perhaps as much as 1000^0K colder than the surrounding upper mantle. If hotspots are derived from the core-mantle boundary they may cause excess temperatures of $>700^0$K in plumes as narrow as 20 km (Verhoogen, 1973; Stacey and Loper, 1983). The accompanying viscosity changes raise doubts about the applicability of the layered models. However, as discussed above, horizontal temperature contrasts in excess of $\sim 100^0$K are unlikely on a global scale, and the resulting thermal viscosity contrasts may be only about an order of magnitude.

Stress dependent rheology reduces the effective viscosity in zones of high stress and diminishes the effects of temperature in a convecting system (Christensen, 1984) by driving it back toward an isoviscous state. This is a possible regulating mechanism which may help explain the interpretation of post-glacial rebound data in terms of a relatively isoviscous mantle (Peltier, 1981). However, studies of post-glacial rebound do not provide unique constraints on stress-dependent rheology, because the deviatoric stress field due to ice loading is contaminated by the *in situ* stresses due to convection. For the same reason, stress-dependence destroys the linear superposition principle assumed in equation (6) of Chapter 2 and can be addressed only for specific cases in which all loading stresses can be treated simultaneously. We have included several examples of stress-dependence in the numerical experiments that follow.

Perturbation Theory

Steady-state loading problems for which viscosity is a function only of depth can be solved by analytical methods in which the flow and stress variables are Fourier analyzed in the transverse coordinates. The resulting equations governing flow are linear in the transformed variables within each layer and the whole solution is formed by analytically "propagating" solutions from one viscosity layer to the next. The spherical Earth response functions (shown in Figure 6 of the previous chapter) which include the effects of radial viscosity variations were calculated using such a technique (RH). However, if viscosity varies transversely the Fourier components (or spherical harmonics) are no longer decoupled and the analysis becomes difficult. The reason for this can be seen immediately upon examination of the Newtonian constitutive law

$$\underline{\tau} = -p\,\underline{\mathbf{I}} + 2\eta\underline{\epsilon} \tag{2}$$

where $\underline{\tau}$ is the stress tensor, p the pressure, $\underline{\mathbf{I}}$ the identity matrix, η the effective viscosity, and $\underline{\epsilon}$ the strain-rate tensor. Since both η and $\underline{\epsilon}$ are functions of the transverse coordinates, the resulting transformed equations are no longer linear and other solution methods are required.

Before resorting to numerical methods, such as the finite element calculations that follow, it is instructive to extend the analytical formulation to include small lateral perturbations in viscosity. Many of the important effects upon the long-wavelength loading problem can be derived in this way. Consider a two-dimensional fluid layer in which the viscosity is given by a background value, η_0, plus a perturbation term $\delta\eta$

$$\eta = \eta_0 + \delta\eta(x) \tag{3}$$

We assume the flow to be periodic in L in the x (horizontal) direction and express all velocity and stress variables in Fourier series

$$v_z(x,z) = \sum_{m=1}^{\infty} \left[v_{z_c}^m(z) cos(k_m x) + v_{z_s}^m(z) sin(k_m x) \right] \tag{4}$$

$$\tau_{zz}(x,z) = \sum_{m=1}^{\infty} \left[\tau_{zz_c}^m(z) cos(k_m x) + \tau_{zz_s}^m(z) sin(k_m x) \right]$$

$$etc.$$

as well as the viscosity

$$\eta = \eta_0 + \sum_{m=1}^{\infty} \left[\delta\eta_c^m(z) cos(k_m x) + \delta\eta_s^m(z) sin(k_m x) \right] \tag{5}$$

where $k_m = 2\pi m/L$. The density contrasts which drive flow are arbitrary and are represented by

$$\delta\rho = \sum_{m=1}^{\infty} \delta\rho^m(z) cos(k_m x)$$

If we substitute these expressions into the constitutive equations (2) and exploit their orthogonal properties we obtain, for example

$$\tau_{zz_c}^m = -p_c^m + 2\eta_0 Dv_{z_c}^m + \sum_{q=1}^{\infty} \left[\left(\delta\eta_c^{m+q} + \delta\eta_c^{|m-q|} \right) Dv_{z_c}^q + \left(\delta\eta_s^{m+q} - \delta\eta_s^{|m-q|} \right) Dv_{z_s}^q \right] \tag{6}$$

$$\tau_{zz_s}^m = -p_s^m + 2\eta_0 Dv_{z_s}^m + \sum_{q=1}^{\infty} \left[\left(-\delta\eta_c^{m+q} + \delta\eta_c^{|m-q|} \right) Dv_{z_s}^q + \left(\delta\eta_s^{m+q} + \delta\eta_s^{|m-q|} \right) Dv_{z_c}^q \right]$$

where $D = \frac{d}{dz}$. Similar expressions result for τ_{xz} and τ_{xz}. The terms within the summations show that each spatial wavenumber $k_m = 2\pi m/L$ is coupled to spatial wavenumber k_q via the Fourier viscosity components at sum and difference wavenumbers. This means that for arbitrary viscosity variations one can no longer

associate a given m^{th} component of density contrast only with an m^{th} component flow field, surface deformation, or geoid response. Therefore, the harmonic geoid response functions are contaminated by this coupling.

In applying this theory to mantle convection we can introduce three conditions which greatly simplify the analysis: (1) Viscosity contrasts occur spatially in phase with density contrasts. (2) There are dominant spatial wavelengths associated with a given convective style. (3) The viscosity contrasts corresponding to each spatial wavenumber are small. We will examine just what is meant by "small" at a later point. The first assumption is obviously reasonable for temperature-dependent viscosity since the buoyancy forces are also thermal in origin. Furthermore, even though viscosity is probably exponentially dependent upon temperature, the spectra of density and viscosity fluctuations are similar as long as the temperature contrasts are small compared to the background mantle temperature (e.g., $\leq 100^0\ K$). In the case of stress-dependent rheology with power law $q=3$, the effective viscosity, η_{eff}, depends on the second stress invariant, τ, such that

$$\eta_{\text{eff}} \approx \tau^2 \tag{7}$$

so effective viscosity will vary roughly in phase with the load but at the doubled (squared) harmonic.

We implement the "in phase" condition by eliminating the sinusoidal viscosity variation components, $\delta\eta_s^m$. If we now substitute our Fourier expansions into the consitutive equations as well as the incompressible continuity equation,

$$\nabla \cdot \mathbf{v} = 0 \tag{8}$$

and the equations of motion

$$\nabla \cdot \mathbf{T} + \rho \mathbf{g} = 0 \tag{9}$$

where $\rho \mathbf{g}$ is the gravitational body force, we obtain the following set of first order differential equations

$$D v_{z_c}^m + k v_{x_s}^m = 0 \tag{10}$$

$$-k \tau_{xx_c}^m + D \tau_{xz_s}^m = 0 \tag{11}$$

$$k \tau_{xz_s}^m + D \tau_{zz_c}^m - \delta \rho_c^m g = 0$$

$$\tau_{zz_c}^m = -p_c^m + 2\eta_0 D v_{z_c}^m + \sum_{q=1}^{\infty} \left(\delta\eta_c^{m+q} + \delta\eta_c^{|m-q|} \right) D v_{z_c}^q \tag{12}$$

$$\tau_{xx_c}^m = -p_c^m + 2\eta_0 k_m v_{x_s}^m + \sum_{q=1}^{\infty} \left(\delta\eta_c^{m+q} + \delta\eta_c^{|m-q|} \right) k_q v_{x_s}^q$$

$$\tau_{xz_s}^m = \eta_0 \left(D v_{x_s}^m - k_m v_{z_c}^m \right) + \frac{1}{2} \sum_{q=1}^{\infty} \left(\delta\eta_c^{m+q} - \delta\eta_c^{|m-q|} \right) \left(k_q v_{z_c}^q - D v_{x_s}^q \right)$$

Note that these equations contain only the in phase field components (v_{z_c}, v_{x_s}, τ_{zz_c}, τ_{xx_c}, τ_{xz_s}, p_c) and, except for the coupling terms containing the $\delta\eta$'s, are identical to the uniform layer equations for which we have analytical solutions.

The appropriateness of the second simplifying assumption, that of a dominant (degree 2) wavelength, was discussed earlier in reference to observations of mantle convection. Let us suppose for now that we have a harmonic temperature field, wavenumber k_n, that causes a corresponding harmonic density fluctuation, $\delta\rho^n \cos(k_n x)$, in a medium with mildly temperature-dependent viscosity which is approximately $\delta\eta^n \cos(k_n x)$. We shall refer to this special case as the "self-coupled" problem. The consitutive equations for the k_n stress field become

$$\tau_{zz_c}^n = -p_c^n + 2\eta_0 D v_{z_c}^n + \delta\eta D v_{z_c}^{2n} \tag{13}$$

$$\tau^n_{xz_c} = -p_c{}^n + 2\eta_0 k_n\, v^n_{x_s} + \delta\eta^n\, k_{2n}\, v^{2n}_{x_s}$$

$$\tau^n_{zz_s} = \eta_0 \left(Dv^n_{x_s} - k_n\, v^n_{z_c} \right) + \frac{1}{2}\delta\eta^n \left(k_{2n}\, v^n_{z_c} - Dv^n_{x_s} \right)$$

For the $2k_n$ stress field we have

$$\tau^{2n}_{zz_c} = -p_c{}^{2n} + 2\eta_0 Dv^{2n}_{z_c} + \delta\eta^n\, Dv^n_{z_c} \tag{14}$$

$$\tau^{2n}_{xz_c} = -p_c{}^{2n} + 2\eta_0 k_{2n}\, v^{2n}_{x_s} + \delta\eta^n\, k_n\, v^n_{x_s}$$

$$\tau^{2n}_{zz_s} = \eta_0 \left(Dv^{2n}_{x_s} - k_{2n}\, v^{2n}_{z_c} \right) - \frac{1}{2}\delta\eta^n \left(k_n\, v^n_{z_c} - Dv^n_{x_s} \right)$$

and for the $3k_n$ field,

$$\tau^{3n}_{zz_c} = -p_c{}^{3n} + 2\eta_0 Dv^{3n}_{z_c} + \delta\eta^n\, Dv^{2n}_{z_c} \tag{15}$$

etc.

If we now require that $\delta\eta$ be "small" we can at least formally solve each set of field equations. The zeroth order field is that driven by $\delta\rho^n$, namely, the n^{th} harmonic field. Equations (14) show that a $2n^{th}$ harmonic field is generated in proportion to $\delta\eta$, which makes it a first-order field in $\delta\eta$. Via equations (13) there then arises an additional n^{th} harmonic field component to second order in $\delta\eta$ as well as a second-order $3n^{th}$ harmonic field via equations (15), a third-order $4n^{th}$ field, etc. The main point is that the strongest effect is the generation of flow (and hence surface deformation) at the doubled harmonic and that self-coupling and higher order coupling are at most second-order in the viscosity perturbation.

In a similar development for an idealized stress-dependent, self-coupled case in which η_{eff} behaves like the doubled harmonic, we can now see upon inspection of equation (6) that first-order perturbations are expected in the n^{th} and $3n^{th}$ fields,

second-order perturbations in the $2n^{th}$, etc. These conclusions might have been guessed from the presence of the $\eta\underline{\epsilon}$ product terms in (2), but this formal framework will be useful later in understanding the numerical solutions.

We can use equations (14) with (10) and (11) to calculate the first-order $2n^{th}$ field for the self-coupled case. These equations can be rearranged to yield

$$D\,\mathbf{u} = \underline{\mathbf{A}}\mathbf{u}^{2n} + \mathbf{b} \tag{16}$$

where

$$\mathbf{u}^{2n} = \begin{bmatrix} v_z^{2n} \\ v_x^{2n} \\ \tau_{zz}^{2n}/2\eta_0 k \\ \tau_{zz}^{2n}/2\eta_0 k \end{bmatrix}$$

$$\underline{\mathbf{A}} = \begin{bmatrix} 0 & k_{2n} & 0 & 0 \\ -k_{2n} & 0 & 0 & 2k_{2n} \\ 0 & 0 & 0 & k_{2n} \\ 0 & 2k_{2n} & -k_{2n} & 0 \end{bmatrix}$$

and

$$\mathbf{b} = \frac{\delta\eta k_{2l}}{\eta_0} \begin{bmatrix} 0 \\ -u_4^n \\ 0 \\ u_2^n/2 \end{bmatrix}$$

Since $\mathbf{u}^n$ can be determined to first order by analytical methods, equations (16) may, with the appropriate boundary conditions, be integrated through a given series of depth layers. In practice this turns out to be tedious even for a single layer problem. However, we can get two very useful results by simple inspection of Eqns. (16). Upon

integration these equations would be expected to yield

$$\mathbf{u}^{2n} \sim \mathbf{u}_0^n + \delta\eta k_n \, \delta z \, \mathbf{u}^n \tag{17}$$

where δz is the layer depth and similarly

$$\mathbf{u}^n \sim \mathbf{u}_0^n + (\delta\eta k_n \, \delta z)^2 \mathbf{u}^n \tag{18}$$

This means that the self-coupled anomalous surface deformation and, consequently, anomalous geoid will behave as $(k_n \, \delta z)^2$. On the other hand, the geoid due to loading in a viscous layer behaves as $k_n \, \delta z$ (RH) so that the percent geoid error due to self-coupling will be proprotional to $k_n \, \delta z$. This result, which is born out by the numerical calculations, shows that long-wavelength (small k) loading is much less susceptible than shorter wavelengths to the effects of lateral viscosity variations. This result was not obvious at the start because, even though the anomalous surface deformation must vanish for the limit of very thin layers, so also must the geoid.

The other point to note from equations (16) is that the zeroth order shear stress, u_4^n, drives the $2n^{th}$ stress field (τ_{xz}^{2n}), via the vector $\mathbf{b}$, in phase with positive buoyancy and therefore high viscosity. At the same time it drives the $2n^{th}$ velocity field ($v_x{}^{2n}$) in phase with negative buoyancy and low viscosity. This can be stated more clearly without reference to this highly idealized case of self-coupling: flow is enhanced and stress and surface deformation are diminished over hot, buoyant, low viscosity material. The opposite effect occurs for cold, high viscosity material, and this could be important with respect to mantle viscosity structure inferred from the subducted slab geoid signal (e.g., Hager, 1984).

Numerical Tests

The theory developed above describes qualitatively the major effects on surface deformation and the geoid due to long-wavelength lateral variations in viscosity. In order to evaluate these effects quantitatively and also in order to address the non-linear problem of stress-dependent rheology, it is necessary to resort to numerical methods. We have used the finite element method in the two-dimensional calculations that follow for both Stokes flow and thermal convection. Our computer codes use a penalty function formulation (Hughes et al, 1979) for viscous, incompressible flow. Stress-dependent rheology is handled by damped iteration on the effective viscosity field until suitable convergence is achieved. We use grids of rectangular elements which typically range in number from 24 to 48 depthwise and 40 to 120 in the horizontal direction. The finite element code was tested for accuracy by comparing numerical solutions for plane-layered viscosity with exact analytical results obtained from a 2-D propagator matrix method (e.g., Cathles, 1975; Hager and O'Connell, 1981). Sufficient resolution was obtained by using successively refined grids until calculated surface deformations were accurate to 1% or better for all wavelengths of interest.

We begin by testing the predictions of perturbation theory for the self-coupled case. These results must hold for very small lateral viscosity variations, so we need to determine how well they hold for larger, more realistic variations. At the top of Figure 2 we illustrate a cosinusoidal load located at half the depth (z=0.5) of a 2-D, Cartesian, Newtonian fluid box of unit depth. We have also imposed a cosinusoidal viscosity variation in phase with the load throughout the depth of the box

$$\eta = \eta_0 + \delta cos\,(2\pi n x\,/L\,) = \eta_0 + \delta cos\,(k_n\,x\,) \qquad (19)$$

where L is the width of the box. The ratio of wavelength to box depth, which we shall refer to as the aspect ratio, is L/n, where n is called the mode number. We have set L=11.0 in the following examples so that mode 2 has approximately the same aspect ratio as spherical harmonic degree 2 for the Earth's mantle, mode 4 similarly corresponds to degree 4, etc. (The appropriate aspect ratios are computed roughly by dividing the average mantle radius by the product of mantle depth and harmonic degree.)

Figure 2 shows the anomalous upper surface deformation in terms of displaced mass as a percentage of the driving load (mode 2) for modes 2-10. The odd modes are absent by symmetry. By "anomalous" we mean surface deformation that would not be present in the isoviscous case. The different curves represent viscosity perturbations ranging from 0.1 to 0.9 times the background viscosity. The amount of surface distortion due to the viscosity perturbation is quite small ($< 5\%$) in all cases and the curves are strongly peaked at the doubled mode number n=4, as expected. We have also plotted the theoretically predicted anomalous deformations as dashed lines. These were calculated by scaling the small δ=$0.1\eta_0$ values by δ for mode 4, δ^2 for modes 2 and 6, δ^3 for mode 8, etc., as prescribed by perturbation theory. For δ=0.1, 0.25, and $0.5\eta_0$ the dashed lines overlay the solid lines from the numerical calculations. Only for the case $\delta = 0.9\eta_0$, corresponding to a factor of 19 lateral viscosity variation, does the perturbation theory depart significantly from the numerically determined values. Figure 3 shows how the percent anomalous geoid in the fundamental mode varies with the aspect ratio, or self-coupling mode number. As predicted in equation (18), the size of the effect increases linearly with the fundamental mode number, n, or wavenumber, k_n. In other words, shorter wavelengths are more

strongly contaminated than larger wavelengths.

Our calculations show that the analytical theory developed above is accurate for $\delta \leq 0.75\eta_0$ (see Figure 2) and that very little anomalous surface deformation is introduced for large aspect ratios. By varying the depth of loading it is possible to constuct apparent geoid response curves at the loading wavelength, i.e., the ratio of the total geoid, including deformation of the top and bottom boundaries, to the geoid obtained if the load is placed at the top surface with no compensation allowed. In analogy to the U1 model of Figure 6, Chapter 2, Figure 4a shows the two-dimensional uniform viscosity response (solid line) compared to that obtained for $\delta = 0.75\eta_0$ (dashed line), which gives a factor of 7 lateral viscosity variation. Similar curves are shown for a low viscosity "upper mantle" in Figures 4b,c; in these cases the upper one-quarter of the box was assigned factors of 10 and 100 lower viscosity than the lower three-quarters to simulate, respectively, models U10 and U100. All three cases show that the self-coupling effect is small and certainly not comparable to the effects of depthwise viscosity variation or layered convection. However, these curves represent only the second-order, self-coupling component of contamination and not the cross-coupling terms, some of which are first-order, which occur in a real convecting system.

The case of simple cross-coupling, in which the load mode (at depth 0.5) is again 2 but the viscosity variation mode is allowed to vary, is shown in Figure 5a. The anomalous geoid is strongly peaked ($\sim$9% at $\delta = 0.5\eta_0$) for viscosity mode 4. This occurs because modes 2 and 4 give rise to a difference mode 2 first-order perturbation as shown by equations (12). This case is similar to what we would expect for simple loading of a fluid with stress-dependent rheology, and we see that the effect is

somewhat stronger than the self-coupled case. In Figure 5b we show anomalous first-order cross-coupling into mode 2 surface deformation due to other difference modes, which is seen again to be small. However, for a more "white" spectrum of viscosity and density perturbations the integrated effect may be more important. For these relatively mild viscosity variations, modes greater than about 9-11 do not contribute strongly to contamination of mode 2. A similar curve results when viscosity and load modes are interchanged. The peak at about 6-4 is result of the chosen aspect ratio.

As a bridge between the highly idealized calculations above and the more elaborate convection calculations that follow, we consider another intermediate example. We now let the viscosity depend exponentially upon density contrast (i.e., temperature)

$$\eta/\eta_0 = e^{C\cos(2\pi n x/L)} \tag{20}$$

where C is chosen to model the desired viscosity contrast. The cosinusoidal load (n =2) is now distributed throughout the box as is the viscosity function, and we calculate the total surface deformation and geoid. Figure 6a compares deformation profiles for uniform viscosity (C=0) and for two orders of magnitude viscosity variation (C=-4.6), and the two profiles differ only slightly. Figures 6b,c show the deformation and geoid spectra, both normalized to the mode 2 load. The effect upon the mode 2 ("fundamental") geoid is negligible, but the upward coupled higher harmonic ("overtone") contamination is considerable. This upward coupling is enhanced by the strong exponential temperature-dependence of viscosity. The lack of downward coupling is due to the lack of shorter wavelength load in this example, and in spectrally whiter convection cells there will be some downward coupling. Also plotted in Figure 6c are the results for one order of magnitude viscosity contrast with and without

stress-dependent (power-law exponent $q=3$) flow. (We can solve for stress-dependence now that the entire box is loaded.) Stress dependent flow, as predicted above, couples more strongly into degree 6 and less so into degree 4, and increases the upward coupling to some extent. In Figure 6c,d,e we show the same results for a fundamental aspect ratio that corresponds to harmonic degree 6 instead of 2 (aspect ratio=11.0/6). In this case, only one order of magnitude viscosity contrast causes almost a 100% change in maximum surface deformation and $\sim$50% change in the fundamental (mode 6) geoid. Only a factor of 3 difference in the wavelength to mantle depth aspect ratio strongly degrades the geoid results for these simple cells.

The surface deformation and geoid are determined by the pressure induced at the boundaries due to flow. The flow velocities themselves are much more strongly affected by viscosity variations than the stress field for prescribed loads. Fortunately for geoid modelers, seismic heterogeneity is much more directly related to density and velocity fluctuations than to viscosity variations. Figure 7a compares horizontal profiles of vertical velocity at mid-depth and very near the top of the box for only one order of magnitude viscosity contrast. These curves are very different in shape and higher harmonic content from their isoviscous (cosinusoidal) counterpart. This means that, at least at long wavelength, variable viscosity is much more important in modelling transport properties than in modelling the geoid. Transient deformations (e.g., post-glacial rebound) might also be strongly affected by lateral viscosity variations due either to temperature or stress-dependent effects (Crough, 1977).

To emphasize this last point, we have made the following example calculation. A viscous box whose width is 5.5 times its depth (aspect ratio=5.5) is loaded at the upper free surface by a cosinusoidal load (the lower boundary is a free-slip boundary),

thus mimicking a degree 2 type glacial loading/unloading problem. If the box is of uniform viscosity, the vertical velocity at the surface is also cosinusoidal and the effective load is reduced by relaxation of the boundary. If we allow one order of magnitude viscosity contrast, which we have placed in phase with the load only for convenience, the instantaneous vertical velocity profile at the surface is strongly altered (Figure 7b). Consequently, the simple exponential relaxation and harmonic mode independence assumed in most studies of post-glacial rebound (Wu and Peltier, 1982) is not strictly applicable. In the spectral domain, the time evolution of the effective load will suffer strong cross-contamination, although this problem will be self-correcting to some extent. To state things more simply, low viscosity areas rebound faster than areas of high viscosity, and transient responses may be as sensitive to lateral viscosity variations as to radial variations. This example calculation is presented by way of comparison to the resolving power of geoid modelling with respect to radial viscosity contrasts, which we believe to be robust at long wavelengths. In this context we note that Laurentide, Hudson Bay, and Antarctic rebound are all occurring over areas of the mantle that may be anomalously cold and, presumably, of relatively high viscosity (Chapter 2). More complete numerical experiments with transient responses are needed to properly compare our geoid/internal loading work with results for post-glacial rebound, but this is a major undertaking beyond the scope of this paper.

Convection Solutions

The examples above apply to very gentle, broadscale temperature variations which may or may not be applicable to mantle convection. For systems with high Rayleigh number, the rising and falling convection currents are sharper (spectrally whiter) than these examples. Even at modest Rayleigh numbers, e.g., $Ra < 10^6$, there is a great deal of loading at wavelengths shorter than the fundamental cell width. Such intermediate wavelength cases cannot be idealized as above, and it is more satisfying at this point to use load/viscosity fields from self-consistent calculations of convection with fully temperature and/or stress-dependent viscosity. Geoid anomalies and surface deformation for temperature-dependent convection in unit aspect ratio cells have been treated by McKenzie (1977) and have recently been reexamined by Jian and Parmentier (1985) for a range of Rayleigh numbers, $Ra_{critical} < Ra < 10^6$. Here we examine three example solutions for large aspect ratio cells with both bottom heating and internal heating which probe the effects of lateral viscosity variations on the lowest-order harmonics of the geopotential.

We begin by considering a form of the rheological law in equation (1) introduced by Torrance and Turcotte (1971) and subsequently applied by Christensen (1984),

$$\eta = \frac{1}{\sigma^{q-1}} \exp\left[\frac{76.912 + 36.912(1-z)}{2.088+\delta T}\right] \qquad (21)$$

$$0 \leq z \leq 1 \quad , \quad 0 \leq \delta T \leq 1$$

to simulate strongly temperature-, stress-, and pressure-dependent convection in numerical experiments. Here η is the effective viscosity, σ the second stress invariant, q the stress-dependence exponent (e.g., $q = 1$ for Newtonian rheology), z the dimensionless depth, and δT the dimensionless nonadiabatic temperature drop. The

depth-dependent term gives the viscosity variations with lithostatic pressure and does not result in lateral viscosity variations. The simpler, layered viscosity geoid models can in principle account for these changes and we will ignore this term in order to more directly address the effects of temperature. Expression (21) (for z=1) gives 5 1/2 orders of magnitude decrease in viscosity as δT goes from 0 to 1; this will give an almost equally large viscosity variation between the rising and falling limbs of convection cells.

In comparing uniform, temperature-dependent, and stress-dependent viscosity convection an immediate problem arises as to what parameters are to be held constant. Christensen (1984) has shown that the flow pattern, isotherms, and Nusselt number (net heat transport) for strictly temperature-dependent ($q=1$) viscosity are almost identical to those for stress- ($q=3$) and temperature- dependent viscosity if the activation enthalpy, $H^*=E^*+pV^*$, is reduced by a factor of about β=0.3–0.5 in the former case. The viscosity fields are, of course, quite different (see Figure 13 of Christensen, 1984). If we use equation (21) for the power-law case (with z=1), then we should get similar isotherms (i.e., density contrasts) for the two rheological laws

$$\eta = \exp\left[\frac{76.912\beta}{2.088+\delta T}\right] \quad \text{and} \quad \eta = \frac{1}{\sigma^2}\exp\left[\frac{76.912}{2.088+\delta T}\right] \tag{22}$$

Qualitatively, this can be understood by noting that temperature dependent viscosity drives narrower upwellings and broader downwellings, whereas purely stress-dependent rheology has the opposite effect. Adding stress-dependence to temperature-dependence reduces effective viscosity contrasts in high stress areas (cold downwellings) and generally reduces the dynamical effects of temperature-dependence by mobilizing otherwise "frozen" regions of convection cells.

In Figure 8a we show the isotherms for a bottom heated convection cell with insulated sidewalls. The Rayleigh number, through which the buoyancy forces are introduced, is set to 10^5 ($\sim$100 times critical) for the viscosity corresponding to δT=0.7. This is the average temperature of the "core" of the convection cell so that the overall Rayleigh number is also roughly 10^5 (Nataf and Richter, 1983). By setting β=0.3 in (22) we introduce about 1 1/2 orders of magnitude lateral viscosity variation. This temperature-dependence stabilizes larger aspect ratio cells than are normally obtained for uniform viscosity because of the stability of the upper boundary layer. We were able to get steady-state solutions for a half-cell aspect ratio of 2.5:1. Since reflection symmetry is imposed at the vertical boundaries, this yields a 5:1 dominant horizontal scalelength to depth ratio which is appropriate for degree 2-3 convection in the whole mantle. The grid contains 48 elements vertically and 100 elements horizontally, and convergence was demonstrated by obtaining the same solution with a 24 x 50 grid. Our finite element method uses a penalty function formulation to solve the flow equations (same as in previous section), while the energy equation is solved by a streamline upwind Petrov-Galerkin method. Results using this code have been presented by Daly et al. (1982), Hager and Mori (1984), and Ho-Liu, Hager, and Raefsky (manuscript in preparation).

Let us for the moment assume that we are provided by seismic tomographers with a mantle density field which can be assumed, without much loss in accuracy, to be linearly related to the convective temperature field, e.g., Figure 8a. The question for the geoid modeller then becomes that of how much our lack of knowledge about mantle rheological laws degrades our ability to infer mantle structure and dynamics from geoid modelling. We can use the thermal field in Figure 8a (β=0.3;Ra =10^5) to

test model resolution, only in this case we have the benefit of knowing the formal calculation parameters. These isotherms could be roughly consistent, according to Christensen (1984), with either power-law (q =3) flow, with over 5 orders of magnitude temperature-dependence in viscosity (β=1.0), as well as with 1 1/2 orders of magnitude of simple temperature-dependence as was actually calculated. Using thermal buoyancy forces proportional to temperature we can compare geoids for these two cases with the isoviscous geoid response. The surface deformations that control the geoid can be found by feeding a Stokes flow finite element calculation these buoyancy forces and modifying the flow law for each case to be tested.

The results of such an experiment are shown in Figure 9a, which gives the total geoid as a function of mode number for the differing assumptions of uniform, temperature-dependent, and temperature-stress dependent viscosity. The completely self-consistent calculation is the one labeled $\eta(T)$, but as explained above, the $\eta(T,\sigma)$ calculation might also be a good approximation. (Only the even harmonics appear due to the symmetry of the temperature field.) Also shown is the geoid obtained using the horizontally averaged viscosity due to temperature alone, $\eta(T)_{av}$. This accounts for the strictly vertical viscosity variations that occur mainly in the boundary layers (e.g., lithosphere) which we can account for with simple layered models. As in Figure 6, both the surface deformation and the geoid are normalized to the total mode 2 load since we are interested in comparing these quantities for various models, not in calculating the Earth's geoid from first principles. (The geoid scaling is non-unique, because the temperature differences which cause the buoyancy forces enter only through the Rayleigh number, which involves other physical parameters.)

The upper portion of Figure 9a shows the surface deformation profile across the convecting half-cell. The gentle deformation on the left side is due mainly to thickening of the cold upper boundary layer toward the right side of the cell which contributes little to the geoid due to near surface compensation. The narrow, low viscosity upwelling does not cause much deformation. The broad, largely "frozen" downwelling on the right causes a sharper deformation profile, and it is mainly this feature that is affected by thermal viscosity variations and which, in turn, has the most effect upon the geoid. In the spatial wavenumber domain the error introduced by ignoring viscosity variations ranges from about 20% at mode 2 to over 100% at mode 8, and much of the discrepancy at mode 2 is removed by the average model, $\eta(T)_{av}$. (In this convection calculation, we have for simplicity taken the origin, $x=0$, to be the right-hand side boundary. Reflection symmetry is imposed at $x=0$ and all the geoid components are negative; this convention is also maintained in the remaining examples.) Stress dependence, $\eta(T,\sigma)$, changes the geoid very little from the purely temperature-dependent case, both of which have the principal effect of increasing the higher mode spectral components. The broad, cold, high viscosity downwelling is strongly coupled to the upper surface, which results in enhanced short-wavelength downwarping of the boundary.

For $\beta=0.5$ (Figure 8b) the total lateral viscosity contrast is increased to about 2 1/2 orders of magnitude, with consequent broadening of the cold downwelling and narrowing of the hot upwelling compared with $\beta=0.3$. For this case ($\beta=0.5$) the upward coupling into higher mode deformation is stronger. This gives almost 15% error in the mode 2 (fundamental) geoid due to lateral variations in viscosity only and, again, introduces a strong negative geoid response at the higher modes. The

stress-dependent calculation ($q=3;\beta=1.0$) somewhat underestimates the total geoid. As a slight variant on this kind of experiment we have compared the surface deformation and geoid (Figure 9c) that would result from purely stress- dependent rheology, $\eta(\sigma)$, and the Newtonian, isoviscous assumption, $\eta=\eta_0$. (Here the isotherms of Figure 8b are used simply as an arbitrarily prescribed buoyancy field, not as a self-consistent convection calculation.) These two calculations differ very little, and we conclude that, for this scale of convection, it is much more important in geoid modelling to include temperature-dependent effects than those due to power-law creep.

Although we can measure only the total geoid at the surface, the depth resolution of lateral variations in seismic velocity from tomography allows us to model the geoid by integrating through the depth of the mantle along dynamic response curves. Perhaps a better way to evaluate the effects of viscosity variations is to examine the harmonic geoid components as a function of depth for the temperature-dependent convection cells. This is accomplished by evaluating the geoid due to a single depth layer of the convecting fluid at a time in a box with the viscosity distribution of the fully temperature dependent convection. This simulates, for example, the procedure we use in modelling the seismic tomography data -- the seismically inferred density contrasts at each harmonic degree, or wavelength, are multiplied by a model response at each depth to produce a harmonic geoid contribution from each depth level.

The results of this forward modelling simulation are shown in Figure 10a,b where we compare the depthwise geoid contributions for horizontally averaged viscosity with those obtained with the full 2 1/2 orders of magnitude lateral viscosity variation ($\beta=0.5;Ra=10^5$). We see that the mode 2 (labelled "$l=2$") curves in Figures 10a and 10b are almost indistinguishable and that only small changes occur for modes

4 and 6. By comparison with changes due to viscosity and flow layering (Figure 6, Chapter 2) these differences are inconsequential; i.e., they would have virtually no effect upon models of the low-degree geoid contribution from the lower mantle.

The relative loading for each mode is shown in Figure 10c which emphasizes the large boundary layer density contrast at the fundamental wavelength, mode 2. Apparent response functions, like those of Figure 4, are obtained by dividing the curves of Figure 10b by those of Figure 10c. These functions (Figure 11b) are also similar to those obtained for laterally averaged viscosity (Figure 11a). The mode 4 and 6 responses are increased somewhat in magnitude due to the increase in short-wavelength depression above the high viscosity downwelling. The largest differences occur where the loading is nearly zero (Figure 11c) and cross-contamination from other modes causes near singularities in the apparent response at some particular depth. For this reason the curves of Figure 10a,b, which give the product of response function and load, provide a more meaningful comparison.

In these first examples, the steady-state solutions were artifically dominated by mode 2 wavelengths, and the odd modes were absent by symmetry. As a final test we have used a convection model (half-cell aspect ratio 5:1) that contains mode 1 temperature contrasts so that first-order upward contamination of mode 2 is present. The numerical grid here is 24 x 120 elements. We have also switched to internally heated convection (see Daly, 1980) with an insulated bottom boundary. We have kept the pure temperature-dependence of equation (21) (stress exponent $q=1; z=0$) which results in a factor of 25 total lateral viscosity variation across the box. For an effective Rayleigh number $Ra=10^5$ (computed at the dimensionless core temperature $\delta T \approx 0.2$; the maximum temperature in the cell is $\delta T_{max} \approx 0.28$) the convection in this

long box is time dependent. At the top of Figure 12 we show the temperature field for a particular instant in time (chosen at random) long after the heat flow and kinetic energy have reached a steady level of fluctuation.

Convection is unsteady (chaotic), and there is no dominant wavelength of temperature (density) contrast as shown in Figure 12c. Figures 12a,b give the harmonic geoid contributions (as in Figure 10) for laterally averaged and fully temperature dependent viscosity. The response curves are largely unaffected by the lateral viscosity variations despite contamination by strong higher mode (q =3-4) heterogeneity. This result is even more encouraging than the previous examples, because it allows us to relax the hypothetical condition that there is a dominant, low-degree pattern of heterogeneity in the mantle. Less well-organized systems will, evidently, not result in much long-wavelength geoid contamination due to lateral viscosity variations, which means that the low-degree (2-3) geoid components may be fairly accurately modelled by simple layered-earth models.

The results of these numerical convection experiments are not qualitatively different from the simple cases of the previous section, even though we have modelled very large viscosity variations and more realistic thermal fields: cold downwellings give enhanced long-wavelength deformation while the opposite (milder) effect is observed for hot upwellings, the longest-wavelengths (large compared to box depth) are less strongly affected, etc. These results can be expected to apply for the Earth if there indeed is a relatively gentle, large-scale mantle temperature field. It is not our purpose to exhaust the parameter space for convection models, but any long-wavelength, low Rayleigh number calculations will give essentially the same results we have shown. As the Rayleigh number is increased we can expect the resulting lateral

heterogeneity and geoid spectra to become whiter (see Jarvis and Peltier, 1986, for unit aspect ratio, constant viscosity examples at high Rayleigh number) and more contaminated due to temperature-dependent viscosity effects. However, it is not clear that a catalogue of progressively higher Rayleigh number calculations would be worth the computational requirements involved. For example, one might say that subduction is an example of very vigorous convection, but that this process is probably controlled by lithospheric and/or asthenospheric rheological variations that are too complicated for the present models based on simple boundary layer convection theory to simulate accurately. Even though the effective Rayleigh number for the Earth may exceed 10^7, we cannot confidently model convection for $Ra > 10^6$ in large aspect ratio systems with our present computational facilities. Instead, we have taken a different approach to calculations involving plumes and slabs, and those results are contained in Chapter 4.

Conclusions

The theoretical examples we have considered have been necessarily two-dimensional due to computational constraints. For broad-scale flow three-dimensional and spherical effects will come into play, but the spatial wavelength scaling of the effects due to rheological variations, both vertically and horizontally, should not be seriously altered. For example, the results of the 2-D perturbation theory involving sum and difference spatial wavenumbers have obvious analogues in product-sum formulas for spherical harmonics (Kaula, 1975). We are currently developing 3-D spherical finite element codes for use on a new generation of computers that will allow us to directly model the global geoid/heterogeneity data with complicated rheologies, and

the conclusions of the present work will serve as a guide in evaluating the relative importance of lateral viscosity variations.

Considering the complicated mathematical and physical nature of the problem, we find the following conclusions remarkably straightforward insofar as technical points for the geoid modeller are concerned:

(1) The geoid due to the very longest wavelength convective patterns ($l \leq 4$) on Earth is probably not seriously contaminated by lateral variations in effective viscosity due either to temperature- or stress-dependence. This statement is qualified by the assumption that the low-degree components of density heterogeneity inferred from seismology are not just the low-degree signature of spectrally white upwellings and downwellings (e.g., plumes). This is a possibility that is now being tested more rigorously in the resolution of seismic tomography, but which seems on the whole unlikely given the bimodal pattern of hotspots and their association with the Pangean continental assemblage (Anderson, 1982) as well as the overwhelming spectral peak in the geoid at degree 2. In general, geoid wavelengths much greater than the depth of a convecting system, either whole mantle (degrees $\leq$ 6) or the upper mantle (degrees $\leq$ 20) should be affected much more strongly by radial stratification in viscosity due to lithostatic pressure, phase changes, or partial melting than by expected lateral viscosity variations.

(2) Considerable contamination of the higher degree geoid ($l \geq 4$) is to be expected due to lateral viscosity variations in phase with the fundamental convection scalelength. Given the strength of the degree 2 geoid and density heterogeneity in the mantle, we can expect great difficulty in modelling the degree ≥ 4 geoid (this does not necessarily apply to subducted slabs). For the Earth we would expect strong

contamination of the degree 4 geoid due to degree 2 heterogeneity in both density and viscosity. A comparison of the degree 2 lower mantle tomography geoid and the residual (unmodelled) degree 4 geoid after the lower mantle and slab signal are removed (Figure 13a,b) suggests that this contamination may be observable. The theory we have developed predicts that degree 4 should be contaminated by additional (doubled harmonic) lows over both upwelling and downwelling degree 2 zones. The equatorial residual degree 4 low pattern corresponds roughly with both the large antipodal lower mantle upwellings (Figure 13a) and major equatorial subduction zones (Figure 13c), and the strong degree 4 zonal pattern is of the correct sign to similarly correspond to the zonal degree 2 pattern. This suggests that much of the unexplained degree 4 geoid could be due to lateral viscosity coupling for degree 2 as well as mismodelling of the subduction geoid. By comparing the amplitude of the residual degree 4 geoid ($\sim$15 meters) and the observed degree 2 geoid ($\sim$70 meters) we can constrain the low-degree variation in effective viscosity to less than an order of magnitude (see Figures 2 and 6), consistent with the inferred large-scale temperature contrasts of $\leq 50^0$K. In order to address this problem properly it is necessary to model the entire mantle flow system driven by subduction, lower mantle heterogeneity, etc., with temperature-dependent rheology. Three-dimensional, spherical numerical models will eventually allow us to deal more quantitatively with these observations, but this emphasizes that we are already reaching a stage in our understanding of the geoid at which these considerations are important.

(3) Broad-scale, gentle, relatively low Rayleigh number convection will produce mild lateral variations in viscosity, and these effects can be qualitatively understood by a simple perturbation theory approach. This procedure could be applied in 3-D as

well as 2-D and remains remarkably accurate for viscosity variations of less than an order of magnitude at long wavelength.

(4) While the internal loading geoid problem is relatively insensitive to long-wavelength lateral viscosity contrasts, transient problems such as glacial unloading and transport phenomena such as heat advection appear to be more sensitive. For these problems involving mantle flow velocities, the mode decoupling or harmonic independence and superposition principle may break down for viscosity variations greater than half an order of magnitude. Geoid modelling might, therefore, be a better method for determining the radial stratification of mantle viscosity as well as the possible presence of chemical layering.

(5) Stress dependent rheology reduces the effects of temperature-dependent convection, but the difference between boundary deformations for power-law (q =3) flow and Newtonian flow are in general small compared to substantial temperature variations. The induced lateral viscosity variations due to stress-dependence alone are not nearly as important as vertical viscosity stratification in determining the geoid.

Our results are in qualitative agreement with the unit aspect ratio calculations of Jian and Parmentier (1985). Under no conditions do we obtain upper surface depressions over convective upwelling, so we conclude, as they did, that contrary findings by McKenzie (1977) are due to numerical problems. Additional comparisons to other previous work are difficult because most surface deformation and geoid results are not presented in the spectral domain.

The effects of broadscale lateral viscosity variations in the mantle are expected to be second-order in comparison with those due to radial stratification. However, having formulated a model for 82% of the observed geoid variance (Chapter 2), these

effects may give rise to unmodelled geoid signals comparable to the remaining unexplained geoid anomalies. More powerful, fully three-dimensional numerical modelling of the global seismic and geodetic data should not only help us to better understand the geoid and seismic data, but will also enable us to formulate a much more realistic picture of heat and mass transport in the mantle which will bear on many aspects of global geodynamics. Modelling of temperature and stress-dependent rheology will be an important consideration in this effort, but other effects may also require some modification of the simple layered geoid models. For example, mantle compressibility may affect the longest-wavelength surface deformations (Ricard et al., 1984; Hong and Yuen, 1985), and the dynamical effects of phase transitions may be more complicated than the simple radial viscosity changes we have modelled. These are areas for future theoretical development which can, perhaps, be constrained by modelling of the geoid and the new observations of deep mantle structure.

References

Anderson, D. L., 1982, Hotspots, polar wander, Mesozoic convection, and the geoid, *Nature, 297,* 391-393.

Balmino, G., K. Lambeck, and W. M. Kaula, 1973, A spherical harmonic analysis of the Earth's topography, *J. Geophys. Res., 78,* 478-481.

Balmino, G., B. Maynot and N. Vales, 1982, Gravity field model of Mars in spherical harmonics up to degree and order eighteen, *J. Geophys. Res., 87,* 9735-9746.

Berckhemer, H., F. Auer, and J. Drisler, 1979, High temperature anelasticity and elasticity of mantle peridotites, *Phys. Earth Planet. Int., 20,* 48-59.

Cathles, L. M., III, 1975, *The Viscosity of the Earth's Mantle,* Princeton Univ. Press, Princeton, N. J.

Chandrasekhar, S., 1961, *Hydrodynamic and Hydromagnetic Stability,* 652 pp., Oxford Univ. Press, Oxford.

Christensen, U., 1984, Convection with pressure- and temperature-dependent non-Newtonian rheology, *Geophys. J. R. Astr. Soc., 77,* 343-384.

Clayton, R. W. and R. P. Comer, 1983, A tomographic analysis of mantle

heterogeneities from body wave travel times, *Eos, Trans. AGU, 62,* 776 (abstract).

Crough, S. T., 1977, Isostatic rebound and power-law flow in the asthenosphere, *Geophys. J. R. Astron. Soc., 50,* 723-738.

Daly, S. F., 1980, Convection with decaying heat sources: constant viscosity, *Geophys. J. R. Astron. Soc., 61,* 519-547.

Daly, S. F., B. H. Hager, and A. Raefsky, 1982, Convection in a long box with heterogeneous velocity boundary conditions: Implications for mantle convection, *Eos, Trans. AGU, 63,* 1104 (abstract).

Dziewonski, A. M., 1984, Mapping the lower mantle: Determination of lateral heterogeneity in P velocity up to degree and order 6, *J. Geophys. Res., 89,* 5929-5952.

Hager, B. H., 1983, Global isostatic geoid anomalies for plate and boundary layer models of the lithosphere, *Earth Planet. Sci. Lett., 63,* 97-109.

Hager, B. H. and A. Mori, 1984, Color movies of two-dimensional transient convection, *Eos Trans. AGU, 65,* 272 (abstract).

Hager, B. H. and R. J. O'Connell, 1981, A simple global model of plate dynamics

and mantle convection, *J. Geophys. Res., 86,* 4843-4867.

Hager, B. H., R. W. Clayton, M. A. Richards, R. P. Comer, and A. M. Dziewonski, 1985, Lower mantle heterogeneity, dynamic topography, and the geoid, *Nature, 313,* 541-545.

Hong, H. J. and D. A. Yuen, 1985, Dynamical consequences on surface deformations and geoids from equation of state, *Eos, Trans. AGU, 66,* 1075 (abstract).

Hughes, T. J. R., W. K. Liu, and A. Brooks, 1979, Finite element analysis of incompressible viscous flows by the penalty function formulation, *J. Comp. Phys., 30,* 1-60.

Jarvis, G. T. and W. R. Peltier, 1986, Lateral heterogeneity in the convecting mantle, *J. Geophys. Res., 91,* 435-451.

Jian, Lin and E. M. Parmentier, 1985, Surface topography due to convection in a variable viscosity fluid: application to short wavelength gravity anomalies in the central Pacific ocean, *Geophys. Res. Lett., 12,* 357-360.

Kaula, W. M., 1975, Product-sum conversion of spherical harmonics with application to thermal convection, *J. Geophys. Res., 85,* 7031-7044.

Kohlstedt, D. L. and C. Goetze, 1974, Low-stress high-temperature creep in

olivine single crystals, *J. Geophys. Res., 79,* 2045-2051.

McKenzie, D., 1977, Surface deformation, gravity anomalies and convection, *Geophys. J. Roy. Astron. Soc., 48,* 211-238.

Morgan, W. J., 1965, Gravity anomalies and convection currents 1. A sphere and cylinder sinking beneath the surface of a viscous fluid, *J. Geophys. Res., 70,* 6175-6187.

Mottinger, N. A., W. L. Sjogren, and B. G. Bills, 1985, Venus gravity: a harmonic analysis and geophysical implications, *J. Geophys. Res., 90,* C737-C756.

Nataf, H. C. and F. M. Richter, 1983, Convection experiments in fluids with highly temperature-dependent viscosity and the thermal evolution of the planets, *Phys. Earth Planet. Int., 29,* 320-329.

O'Connell, R. J. and B. H. Hager, 1984, Velocity anomalies, convection, heat transport, and viscosity of the lower mantle, *Eos, Trans. AGU, 65,* 1093 (abstract).

Parsons, B. and S. Daly, 1983, The relationship between surface topography, gravity anomalies, and the temperature structure of convection, *J. Geophys. Res., 88,* 1129-1144.

Pekeris, C. L., 1935, Thermal convection in the interior of the Earth, *Mon. Not. R. Astron. Soc., Geophys. Suppl., 3,* 343-367.

Peltier, W. R., 1981, Ice age geodynamics, *Ann. Rev. Earth Planet. Sci., 9,* 119-225.

Ricard, Y., L. Fleitout, and C. Froidevaux, 1984, Geoid heights and lithospheric stresses for a dynamical Earth, *Annales Geophysicae, 2,* 267-286.

Richards, M. A. and B. H. Hager, 1984, Geoid anomalies in a dynamic Earth, *J. Geophys. Res., 89,* 5987-6002.

Runcorn, S. K., 1964, Satellite gravity measurements and a laminar viscous flow model of the Earth's mantle, *J. Geophys. Res., 69,* 4389-4394.

Sammis, C. G., J. C. Smith, G. Schubert, and D. A. Yuen, 1977, Viscosity-depth profile in the Earth's mantle: effects of polymorphic phase transitions, *J. Geophys. Res., 85,* 3747-3761.

Stacey, F. D. and D. E. Loper, 1983, The thermal boundary-layer interpretation of D'' and its role as a plume source, *Phys. Earth Planet. Int., 33,* 45-55.

Torrance, K. E. and D. L. Turcotte, 1971, Thermal convection with large viscosity variations, *J. Fluid Mech., 47,* 113-125.

Tozer, D. C., 1967, Towards a theory of thermal convection in the mantle, in *The Earth's Mantle,* T. F. Gaskell (ed.), Academic Press, London, pp. 325-353.

Tozer, D. C., 1972, The present thermal state of the terrestrial planets, *Phys. Earth Planet. Int., 6,* 182-197.

Twiss, R. J., 1976, Structural superplastic creep and linear viscosity in the Earth's mantle, *Earth Planet. Sci. Lett., 33,* 86-100.

Verhoogen, J., 1973, Thermal regime of the Earth's core, *Phys. Earth Planet. Int., 7,* 47-58.

Weertman, J., 1968, Dislocation climb theory of steady-state creep, *Trans. Am. Soc. Met., 61,* 681-694.

Wu, P. and W. R. Peltier, 1982, Viscous gravitational relaxation, *Geophys. J., R. Astron. Soc., 70,* 435-486.

Table - Residual variance after the subducted slab/lower mantle geoid model is subtracted from the observed geoid. The middle column gives the residual variance at each spherical harmonic degree, while the right-hand column gives the cumulative residual variance from degree 2 through the degree indicated in the left-hand column.

TABLE

DEGREE	RESIDUAL VARIANCE	
	by degree	cumulative
2	6%	6%
3	33%	11%
4	44%	14%
5	49%	15%
6	107%	17%
7	86%	17%
8	74%	18%
9	63%	18%

Figure 1 - Log-log comparison of root mean square harmonic coefficient amplitudes (see Chapter 2 for definition). Units are as follows: Observed geopotential (also slab residual and lower mantle/ slab residual), $\gamma M/R$ (fraction of geopotential at surface); Lower mantle P-velocity (Clayton and Comer, 1983), 10^4 km/sec; Hotspot distribution, $4.1x\,10^6$ hotspots per Earth area. Geopotentials, in units $\gamma M/R$, may be converted to geoid elevations by dividing by the gravitational acceleration at the surface or by multiplying by R. (γ is the gravitational constant, M the mass of the Earth, and R the Earth's radius.)

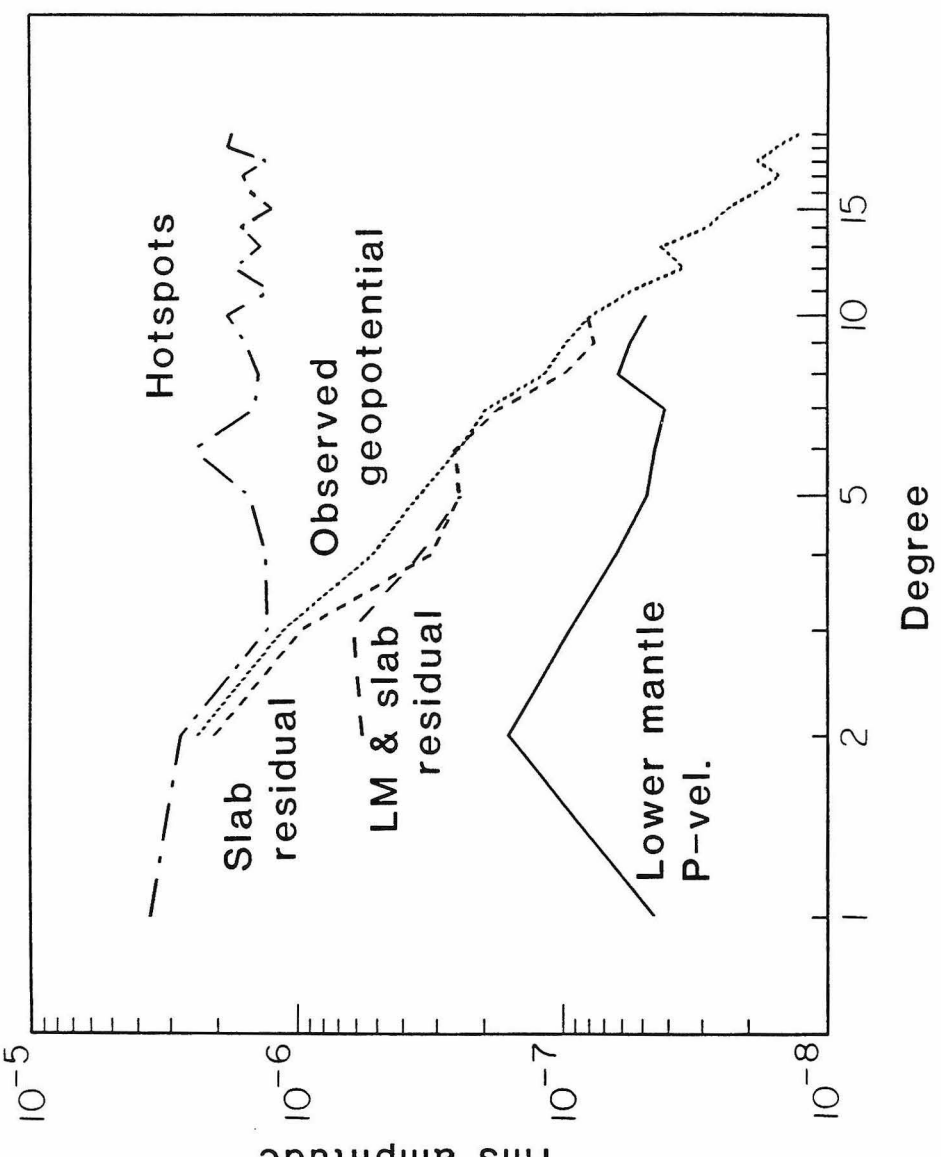
Hotspots
Observed geopotential
Slab residual
LM & slab residual
Lower mantle P-vel.
rms amplitude
10^{-5}
10^{-6}
10^{-7}
10^{-8}
1
2
5
10
15
Degree

Figure 2 - Spectrum of anomalous upper surface deformation produced by a mode 2 load at mid-depth in a box with mode 2 viscosity variation given by δ. The dashed line for δ=$0.9\eta_0$ is computed by scaling the deformation from the finite element calculation for a small perturbation (δ=$0.1\eta_0$) to δ=$0.9\eta_0$ according to the perturbation theory. Similar scaling leads to dashed lines for $\delta \leq 0.5\eta_0$ that are indistinguishable from the solid lines from numerical experiments.

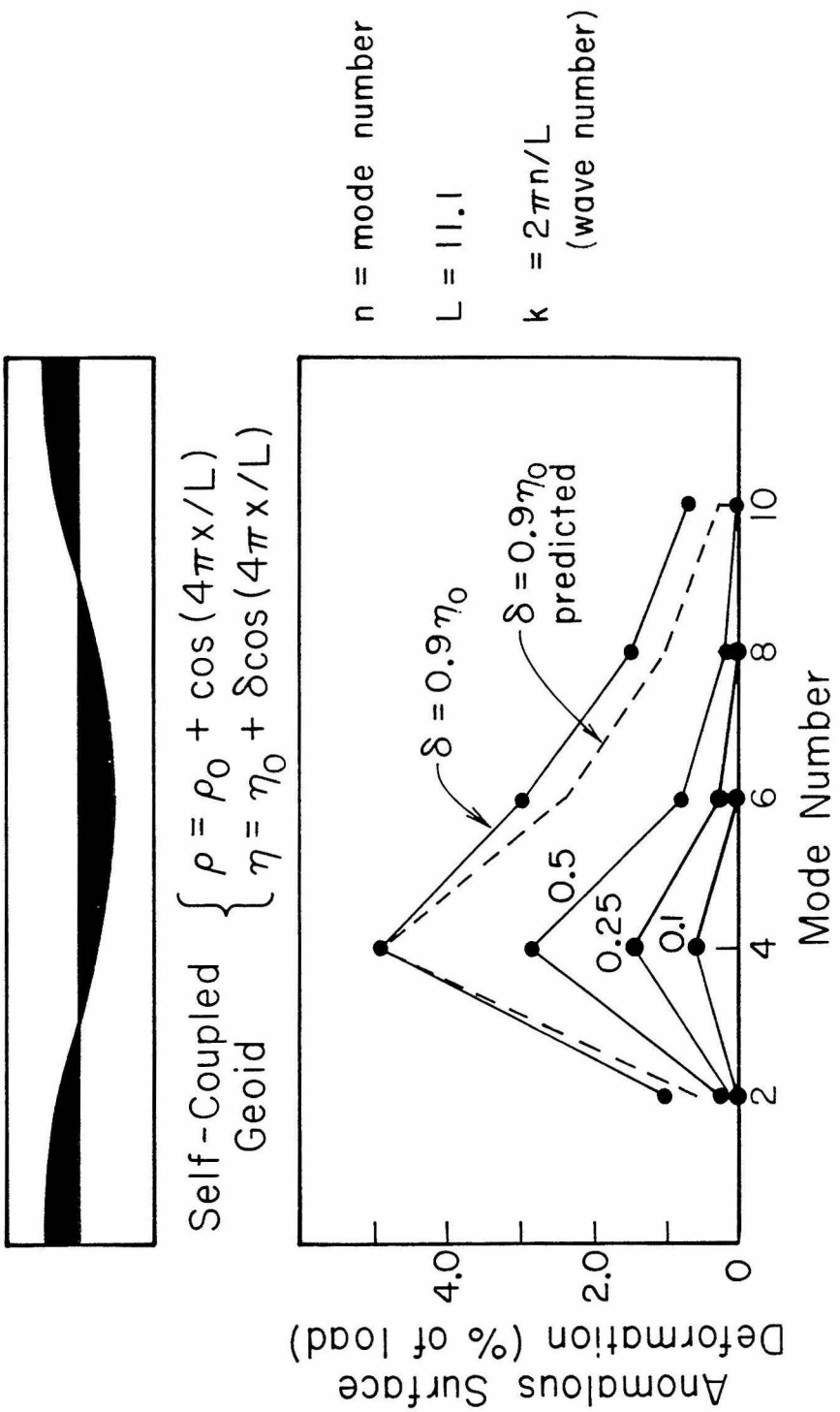
Self-Coupled Geoid
$\rho = \rho_0 + \cos(4\pi x/L)$
$\eta = \eta_0 + \delta\cos(4\pi x/L)$
n = mode number
L = 11.1
k = 2πn/L (wave number)
Anomalous Surface Deformation (% of load)
4.0
2.0
0
2
4
6
8
10
Mode Number
δ = 0.9η0
δ = 0.9η0 predicted
0.5
0.25
0.1

Figure 3 - Anomalous geoid (% of load) at the load/viscosity mode number from a finite element calculation for viscosity variation δ=$0.75\eta_0$. The vertical axis gives the self-coupled load/viscosity mode number. The dashed line gives the scaling, according to perturbation theory, based on the numerically determined value at mode 2.

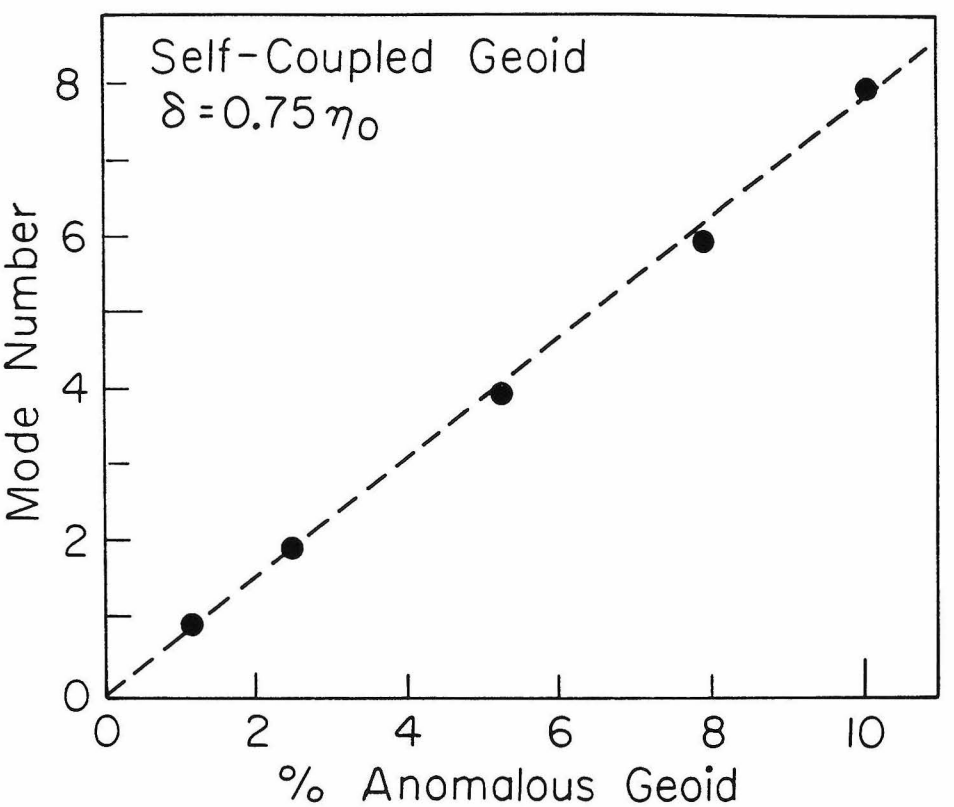
Self-Coupled Geoid
$\delta = 0.75\,\eta_0$
Mode Number
% Anomalous Geoid
0
2
4
6
8
10

Figure 4 - Apparent dimensionless dynamic geoid response as a function of depth for mode 2 loading and viscosity variation. Model "U1" has uniform background (unperturbed) viscosity, while "U10" and "U100" have factors of 10 and 100, respectively, lower background viscosity in the upper one-quarter of the box. The geoid responses are normalized to the geoid which would be obtained if the mode 2 loads from each depth level were placed at the top surface with no dynamic compensation allowed.

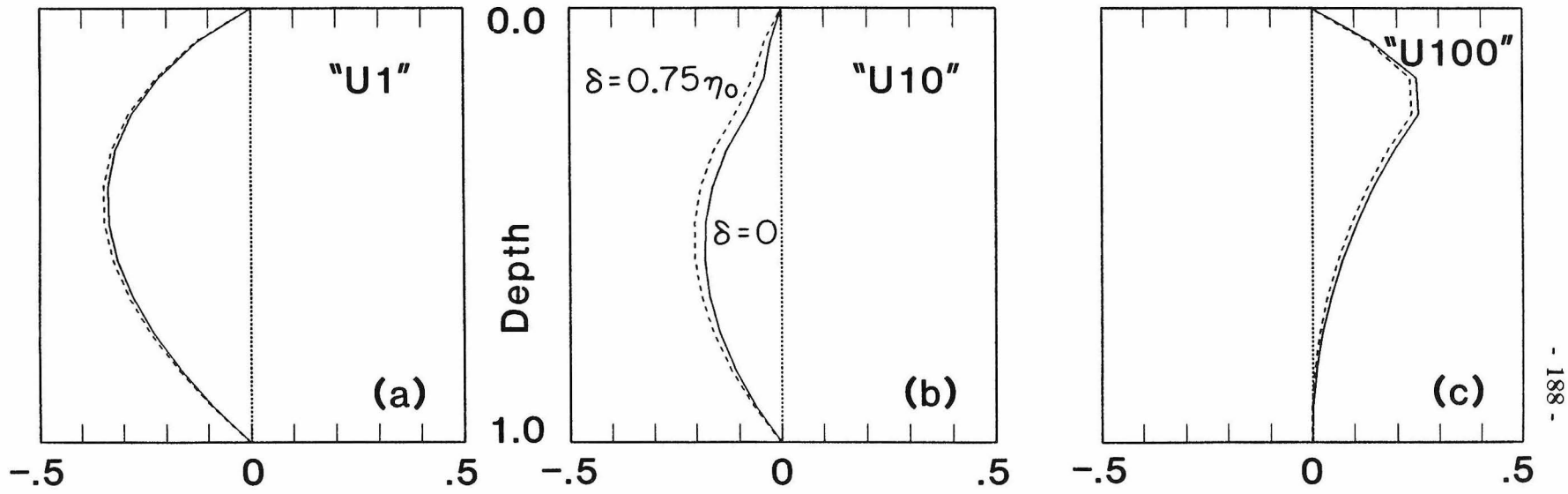
"U1"
(a)
0.0
Depth
1.0
δ=0.75η₀
δ=0
"U10"
(b)
"U100"
(c)
-.5
0
.5
Dynamic Geoid Response
(self-coupled mode 2)

Figure 5 - (a) Error in geoid caused by ignoring anomalous surface deformation due to cross-coupling from viscosity variations at modes different from the load mode.

(b) First-order surface deformation coupling into mode 2 (load and viscosity modes differ by 2).

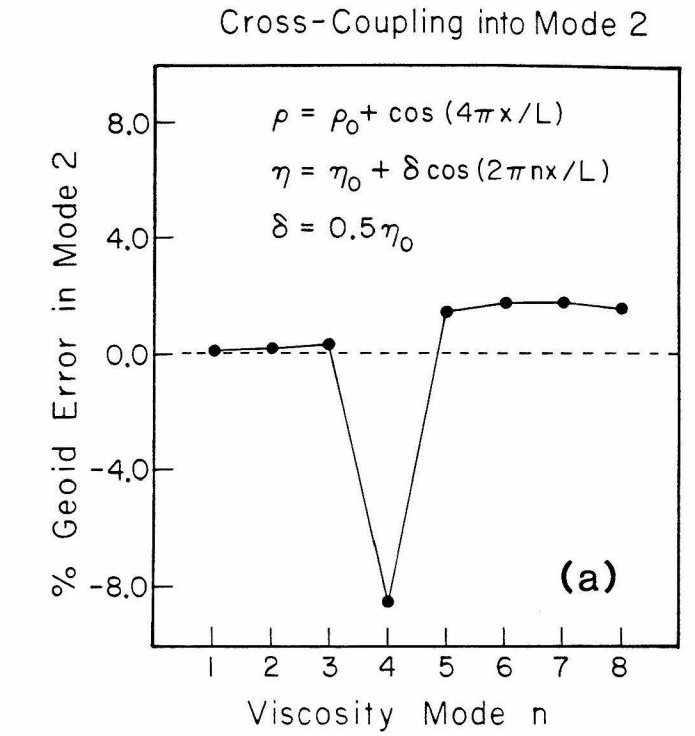
Cross-Coupling into Mode 2
$\rho = \rho_0 + \cos(4\pi x/L)$
$\eta = \eta_0 + \delta\cos(2\pi nx/L)$
$\delta = 0.5\eta_0$
% Geoid Error in Mode 2
8.0
4.0
0.0
-4.0
-8.0
(a)
1 2 3 4 5 6 7 8
Viscosity Mode n

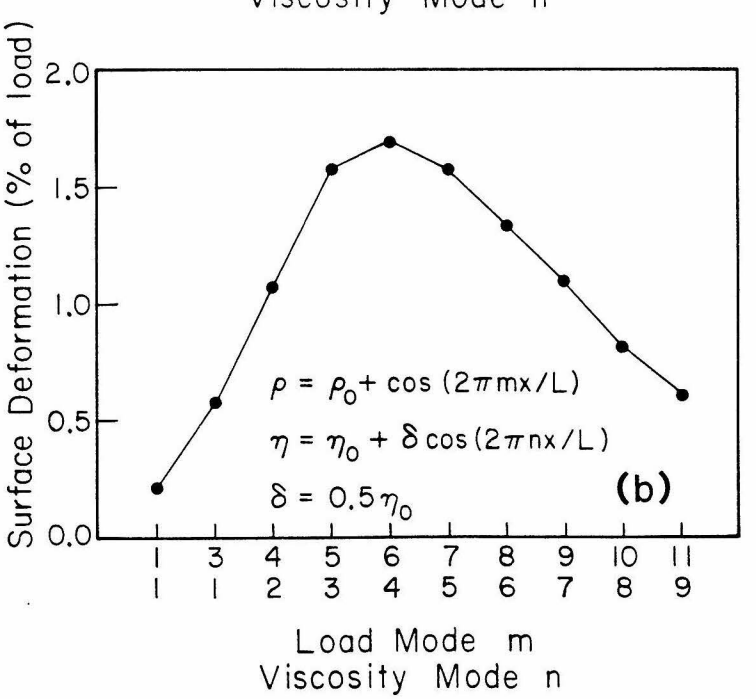
Surface Deformation (% of load)
2.0
1.5
1.0
0.5
0.0
$\rho = \rho_0 + \cos(2\pi mx/L)$
$\eta = \eta_0 + \delta\cos(2\pi nx/L)$
$\delta = 0.5\eta_0$
(b)
1 3 4 5 6 7 8 9 10 11
1 1 2 3 4 5 6 7 8 9
Load Mode m
Viscosity Mode n

Figure 6 - (a),(b),(c) Mode 2 loading with a factor of 100 exponential temperature-dependence of viscosity (solid lines). Dotted lines indicate uniform viscosity calculations with the same loading. In (c) the long-dashed line gives the geoid spectrum for only a factor of 10 lateral viscosity variation, and the short dashed line is for a factor of 10 variation with stress-dependent ($q = 3$) rheology. Surface deformations and geoid are normalized to the total mode 2 load which is distributed uniformly throughout the box.

(d),(e),(f) Same as (a),(b),(c) except that loading and visocity have one-third the wavelength/depth ratio (mode 6) and the lateral (exponential) viscosity variation is only a factor of 10.

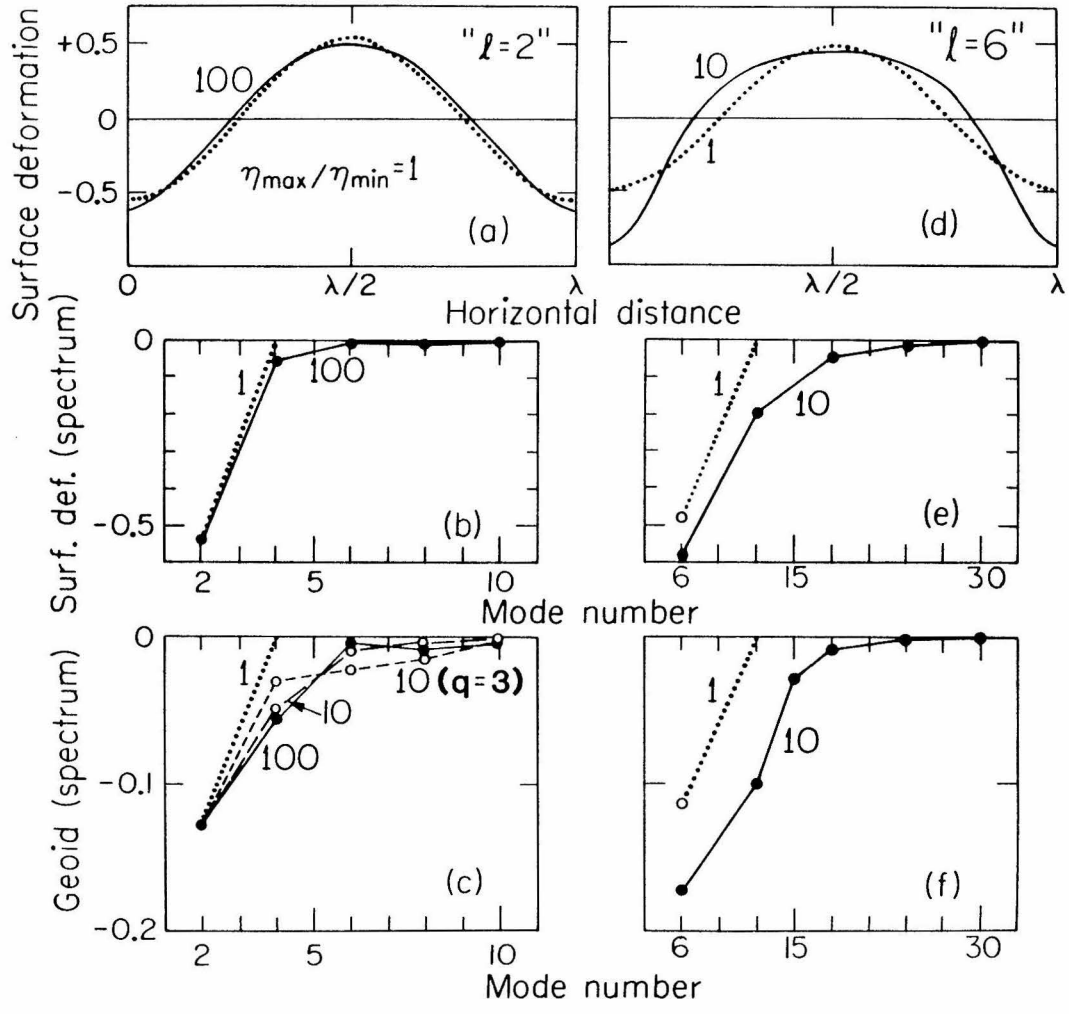
Surface deformation
+0.5
0
-0.5
"ℓ=2"
100
$\eta_{max}/\eta_{min}=1$
(a)
0
λ/2
λ
"ℓ=6"
10
1
(d)
λ/2
λ
Horizontal distance
Surf. def. (spectrum)
0
-0.5
1
100
(b)
2
5
10
1
10
(e)
6
15
30
Mode number
Geoid (spectrum)
0
-0.1
-0.2
1
10 (q=3)
10
100
(c)
2
5
10
1
10
(f)
6
15
30
Mode number

Figure 7 - (a) Relative vertical fluid velocities for the mode 2 ("l=2") experiment of Figure 6 with a factor of 10 viscosity variation. The dotted line gives the velocity profile at mid-depth for uniform viscosity. The solid and dashed lines give the profiles for variable viscosity at mid-depth and at one-tenth of the box depth, respectively.

(b) Vertical upper surface velocity profiles for a mode 2 load at the upper free surface. Dotted line is for uniform viscosity. The solid line is for a factor of 10 viscosity variation arbitrarily chosen to be in phase with the "glacial" load.

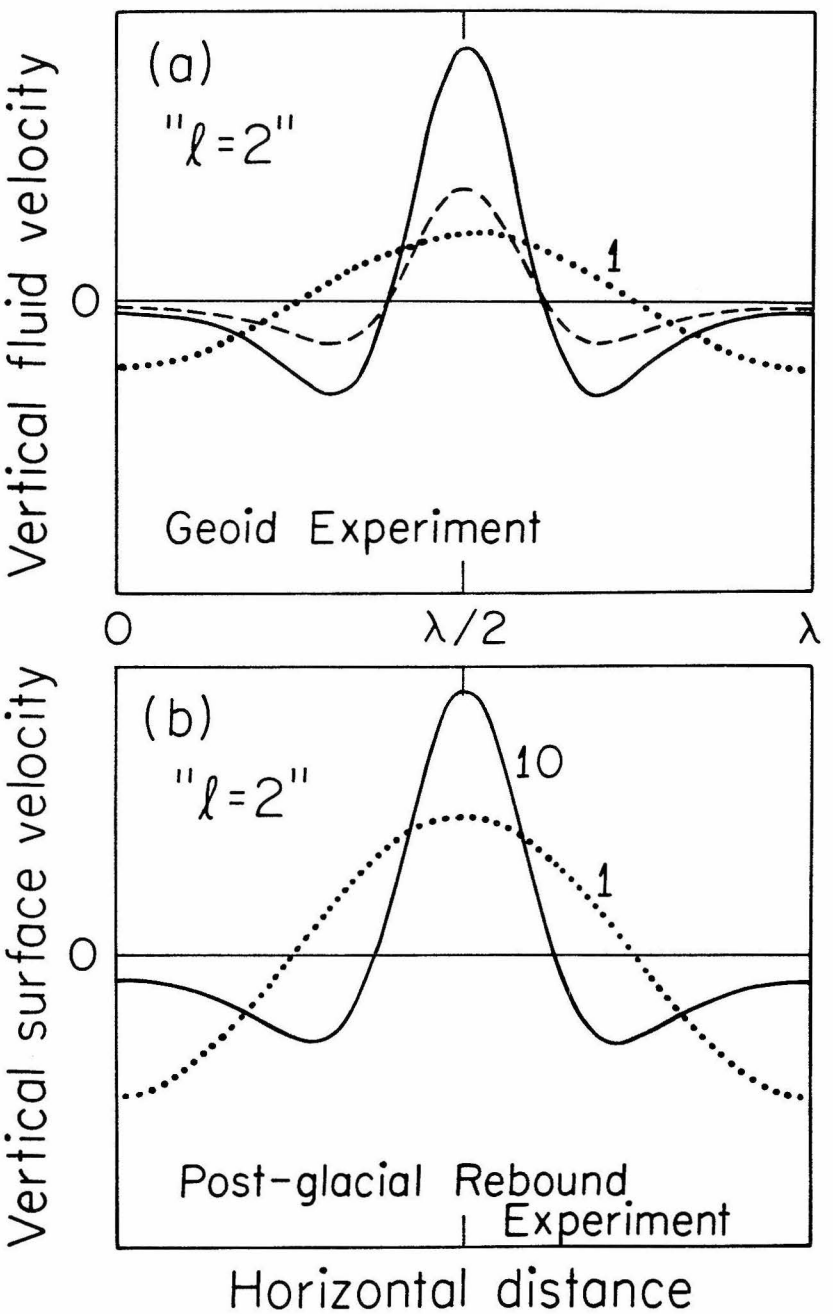
(a)
"ℓ=2"
1
Vertical fluid velocity
0
Geoid Experiment
0
λ/2
λ
(b)
"ℓ=2"
10
1
Vertical surface velocity
0
Post-glacial Rebound
Experiment
Horizontal distance

Figure 8 - Upper panels: temperature contours for bottom heated temperature dependent convection ($Ra = 10^5$) with β=0.3 (a) and β=0.5 (b). Contour interval is 0.1 of dimensionless temperature. True relative vertical and horizontal dimensions are shown.

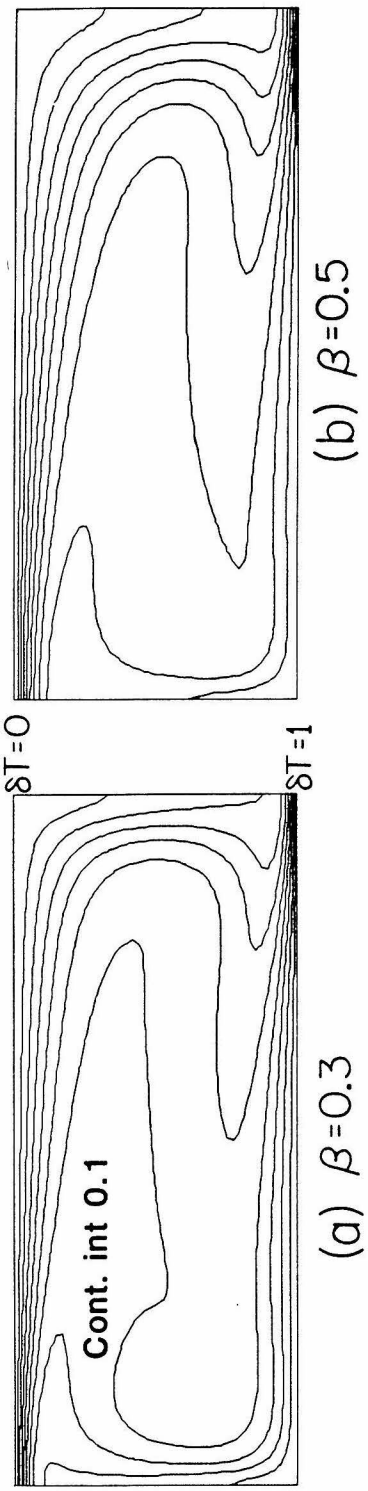
δT=0
δT=1
Cont. int 0.1
(a) β=0.3
(b) β=0.5

Figure 9 - Upper panels show relative surface deformation across the top of the mode 2 convection half-cells of Figure 8. Lower panels give the geoid spectra, normalized to the total mode 2 load, for various rheological experiments. Reflection symmetry is applied about the vertical coordinate axis ($x=0$) which is chosen to be at the right-hand side of the half-cell in order to make all the spectral geoid components negative. The various labels for line types, given in (b) are explained in the text and apply in both the upper and lower panels of (a) and (b). The lines in the upper and lower panels in (c) correspond similarly.

Surface Deformations

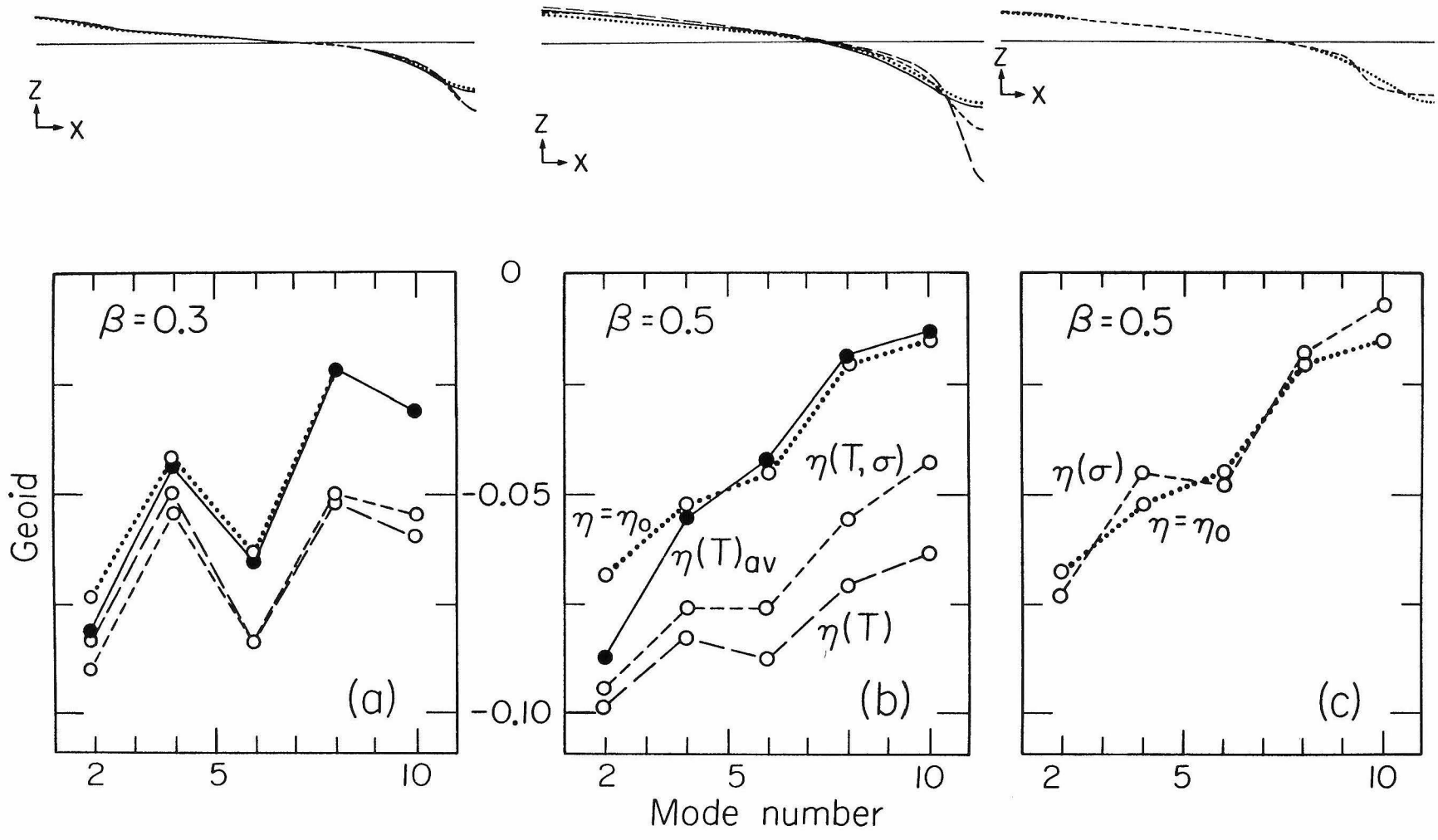

Figure 10 - Geoid signal for modes 2,4,6 (corresponding in aspect ratio to harmonic degrees l=2,4,6) as a function of depth (mode 2 convection; β=0.5; Ra=10^5). Curves in (a) are for horizontally averaged viscosity, and curves in (b) are for fully temperature-dependent viscosity. The mode 2,4,6 loads at each depth level are shown in (c) in units of dimensionless temperature contrast. Units for (a) and (b) are the same since the geoid is proportional to the product of the thermal load and a dimensionless geoid response (see Figure 11).

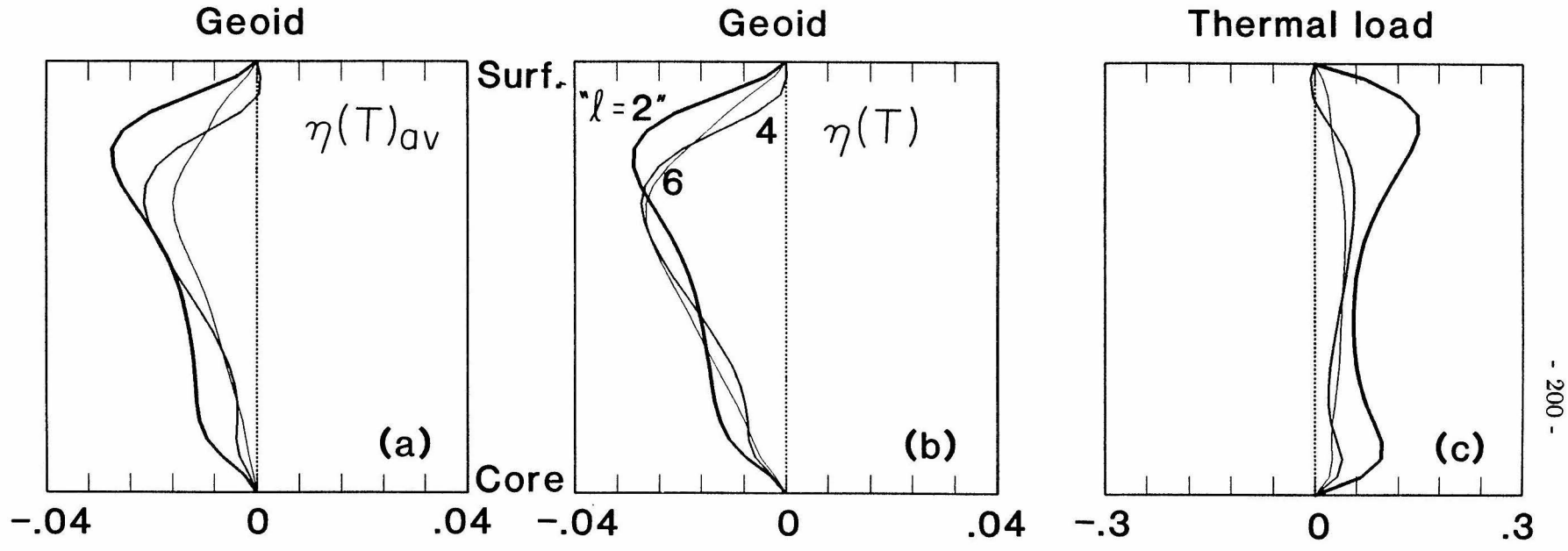
Geoid
Geoid
Thermal load
Surf.
Core
$\eta(T)_{av}$
$\eta(T)$
"$\ell = 2$"
4
6
(a)
(b)
(c)
−.04
0
.04
−.04
0
.04
−.3
0
.3

Figure 11 - (a),(b) Apparent dimensionless dynamic geoid response functions (mode 2 convection; β=0.5; $Ra = 10^5$) computed by dividing curves (a) and (b) of Figure 10 by (c) at each depth level.

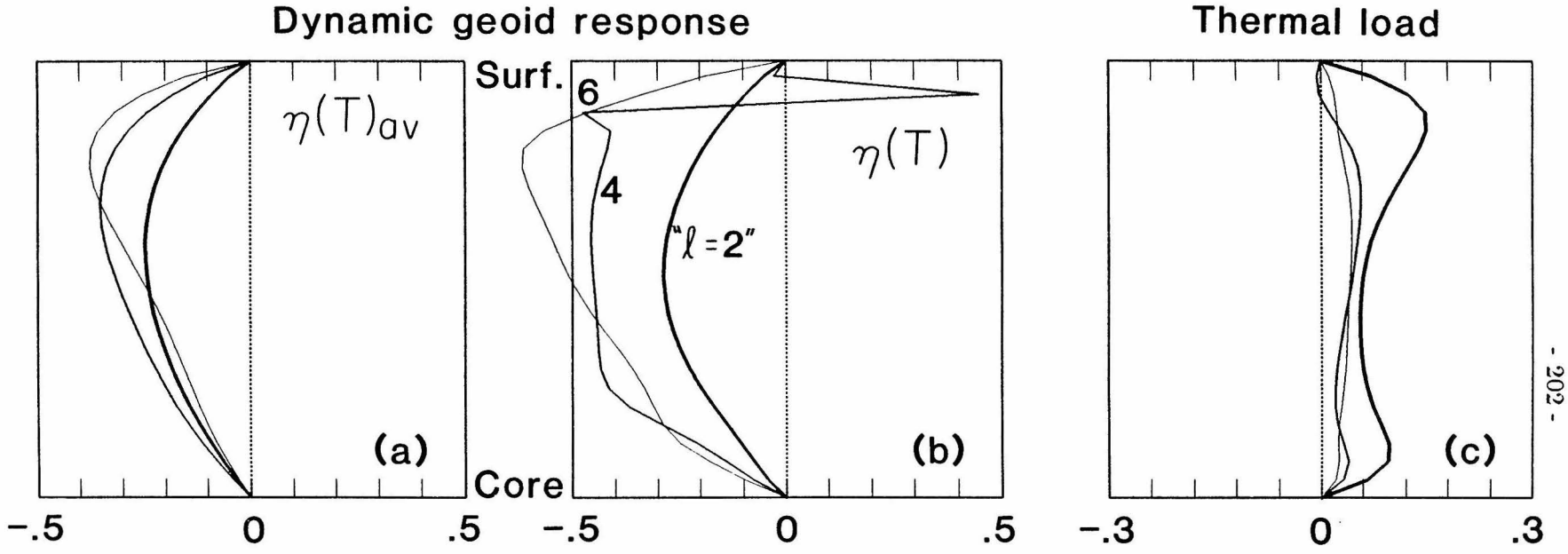
Dynamic geoid response
Thermal load
Surf.
Core
6
4
$\eta(T)_{av}$
$\eta(T)$
"$\ell=2$"
(a)
(b)
(c)
−.5
0
.5
−.5
0
.5
−.3
0
.3

Figure 12 - Upper panel: temperature contours for internally heated, temperature dependent convection ($Ra = 10^5$; $\beta = 1.0$). Contour interval is 0.033 of dimensionless temperature. True relative vertical and horizontal dimensions are shown. Lower panels: geoid signal for modes 1,2,3,4 (corresponding in aspect ratio to spherical harmonic degree 1,2,3,4) and thermal loads as functions of depth. Curves in (a) are for horizontally averaged viscosity, and curves in (b) are for fully temperature-dependent viscosity. Units are as in Figure 10.

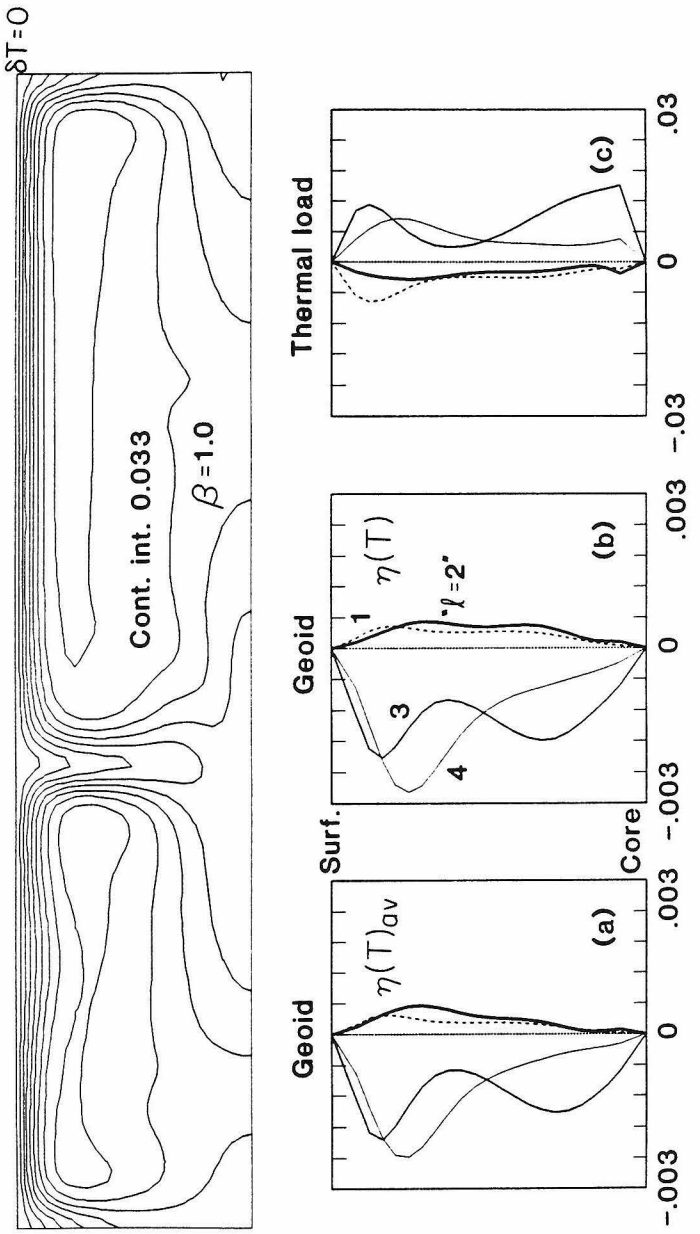
δT=0
Cont. int. 0.033
β=1.0
Geoid
η(T)av
(a)
Surf.
Core
Geoid
η(T)
1
3
4
l=2
(b)
Thermal load
(c)
-.003
0
.003
-.003
0
.003
-.03
0
.03

Figure 13 - Global maps, in cylindrical equidistant projection, with outlines of continents. (a) The harmonic degree 2 component of the geoid signal modelled from lower mantle seismic P-wave tomography (Chapter 2). (b) The residual degree 4 geoid after the modelled geoid signals of subducted slabs and the lower mantle are removed. (c) The degree 2 component of the subducted slab geoid signal. Lows are shaded; geoid signals are in meters.

LM Predicted Geoid: degree 2

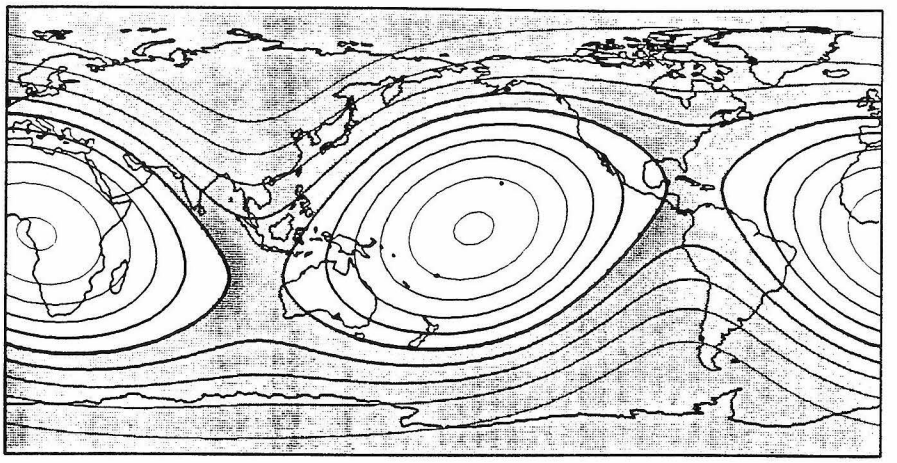

contour interval: 10 m

(a)

LM & Slab Residual Geoid: degree 4

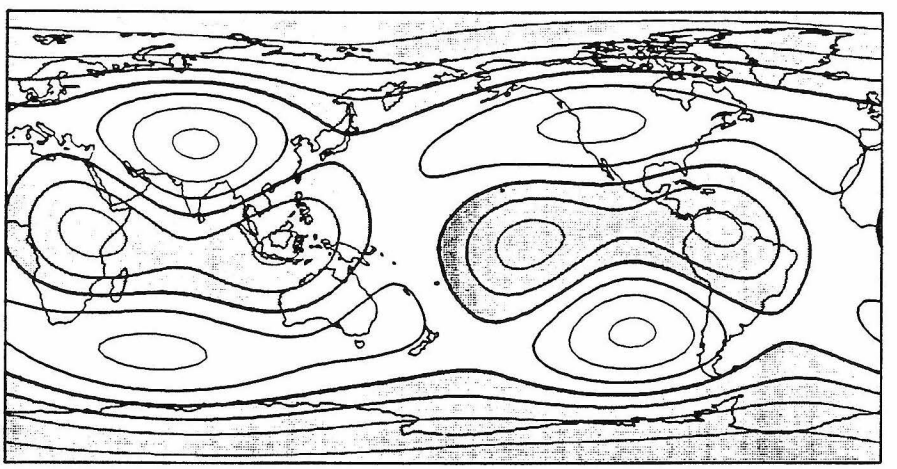

contour interval: 5 m

(b)

Slab Predicted Geoid: degree 2

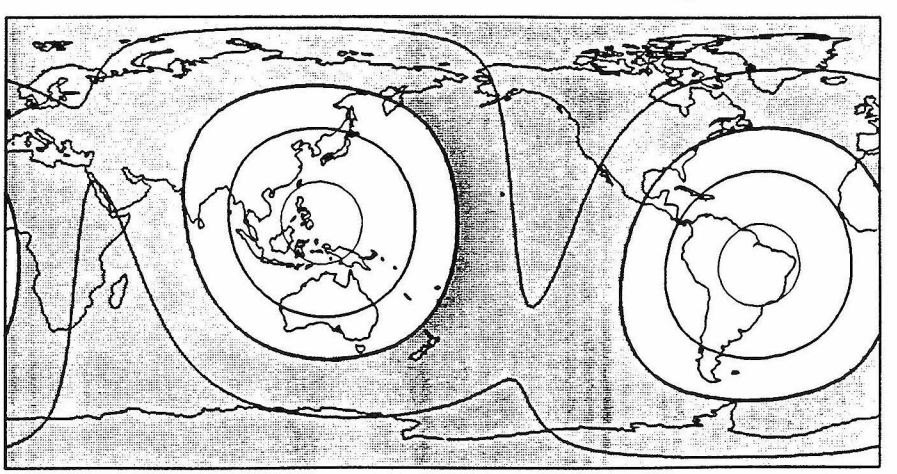

contour interval: 10 m

(c)

Chapter 4

Dynamically Supported Geoid Highs Over Hotspots: Observation and Theory

Introduction:

Linear seamount and island chains, such as the Hawaiian islands, have frequently been attributed to the passage of the lithosphere over deep convective upwellings (Wilson, 1963; Morgan, 1972; 1981). The age progression from the active "hotspot" to the guyots on the inactive end of the chain is particularly well established for Hawaii (Jarrard and Clague, 1977; Dalrymple and Clague, 1976), and relative motion among the more prominent of these "hotspots" is constrained to be about an order of magnitude less than typical plate rates (Morgan, 1972; 1981; Engebretson et al., 1984; Chase, 1984). Therefore, the thermal plumes, or whatever process is responsible for hotspots, must be essentially stationary with respect to tectonic plate motions.

The theory of mantle plumes has not received universal acceptance, because much mid-plate volcanic activity is not easily associated with hotspot traces. For example, the Tertiary volcanic activity in eastern Australia (Pilger, 1982) and the recent volcanism near Easter Island (Bonatti et al., 1977) are actually "hot lines" rather than hot spot tracks. The Line Islands require either widespread contemporaneous volcanism or several hot spot tracks (Schlanger et al., 1984; Epp, 1984b).

Alternative explanations for mid-plate volcanism have usually involved propagating cracks or faults in the lithosphere (Betz and Hess, 1942; Turcotte and Oxburgh, 1973; 1976; Sleep, 1974; 1984a; Solomon and Sleep, 1974), even though there is no resemblance between the surface morphologies of mid-oceanic swells and other tensional features in the lithosphere such as mid-ocean ridges and continental rifts.

The crack theory and the plume theory predict very different sub-lithospheric structures beneath a hot spot. These differences can be inferred by considering mid-plate swells such as the one associated with the Hawaiian Islands. These $\sim$1000 km wide features are attributed to heating of the lower lithosphere as it passes over the hotspot (Detrick and Crough, 1978; Crough, 1978; Von Herzen et al., 1982; Epp, 1984a). The topographic uplift appears to form within a few million years at the hotspot and then subside similarly to young seafloor. The thermal origin (within the lithosphere) of the swells is further indicated by their elevated heat flow (Von Herzen et al., 1982) and the systematics of volcano heights (Epp, 1984a). The formation of the hotspot swells is sufficiently rapid that bulk replacement of the lower lithosphere, as opposed to thermal conduction, is required (Detrick and Crough, 1978). The replacement process could be intrusion of hot plume material into the lower lithosphere or, in the crack theory, bulk stoping or delamination of the lower lithosphere which then sinks as dense blobs into the underlying mantle. The two hypotheses therefore predict opposite types of structures underlying hotspots: a hot, low density plume or cold, sinking lithospheric material.

Since cases intermediate between these end members are conceivable, it is necessary to clarify our terminology. By "plumes" we mean more or less cylindrical zones of upwelling with radii of the order of 10-100 km. Plumes might either be strong and

supply the bulk of the heat needed to thin the lithosphere, or they may be weaker and act mainly as a trigger for delamination. Broad zones of mantle upwelling are distinguished from narrow plumes. Mostly passive "blobs" in the upper mantle (Allegre et al., 1984; Batiza et al., 1984) which may cause chemical and isotopic anomalies in off-axis volcanism are also distinct from active plumes. We use the term "delamination" to describe either thermally or mechanically triggered sinking of blobs of high viscosity material at the base of the lithosphere, i.e., convective instability. We distinguish this process from lithospheric thinning due only to thermal erosion of the lithosphere by a plume.

Geophysical methods that might discriminate among these alternatives include modelling the gravity signatures of hotspot traces and studies of the deep seismic velocity structure beneath active hotspots. Seismic evidence would seem to favor the plume hypothesis since certain hotspots such as Yellowstone are underlain by slow velocity material to a considerable depth below the lithosphere (Iyer, 1975; Hadley et al., 1976). Short-wavelength ($<$1000 km) gravity anomalies, although conspicuous, are largely the result of lithospheric thinning and compensated swell topography (Detrick and Crough, 1978; McNutt, 1984) and do not offer much direct information concerning dynamic processes deep in the mantle. However, very long-wavelength geoid anomalies (harmonic degrees $<$10) are relatively insensitive to contamination from lithospheric heterogeneity (Hager, 1983) and are most sensitive to the deep-seated density contrasts in the mantle (Richards and Hager, 1984: Chapter 1, henceforth referred to as "RH") that are presumably the result of convection.

The general association of hotspots with long-wavelength geoid highs both globally (Crough and Jurdy, 1980; Chase, 1979) and more locally (Kaula, 1970; Morgan,

1972) suggests that, if hot plumes cause hotspots, topographic compensation dominates their geoid signature; otherwise, low density material would result in geoid lows. Paradoxically, subducted slabs representing cold, sinking material in the upper mantle are associated with geoid highs (Kaula, 1970; Chase, 1979; Crough and Jurdy, 1980; Hager, 1984), indicating that dynamic surface topography is not the overwhelming effect there. Kaula explained this apparent contradiction as the result of differing rheology under hotspots and subduction zones. The effect of subducting slabs encountering a relatively high viscosity lower mantle may be to reduce the resulting surface topography ("trench") at long-wavelengths so that the positive geoid anomaly due to the dense slab dominates the geoid signature. An alternative explanation for the geoid highs over hotspots is that cold, dense lithospheric blobs are delaminated at hotspots and result in geoid highs just as do subducting slabs.

The purpose of this study is to provide a test of the various hotspot theories by modelling the long-wavelength geoid anomalies with which they are associated. We use models of hot plumes and cold downwellings (slabs), which include temperature dependent rheology, to predict long-wavelength geoid anomalies which can then be compared with observations. We also consider other quantities of interest such as heat flow and long-wavelength dynamic topography, but they are more difficult to constrain via observation. A key question which we state now and expand upon later is: Could narrow mantle plumes be directly responsible for the geoid highs over hotspots, or are hotspots and, perhaps, plumes associated with more broad-scale convection patterns in the mantle which cause geoid highs? Emphasis in modelling will be placed on the conspicuous geoid high over Hawaii since it is the classic hotspot. However, in order to provide a more general observational base, we begin by

analyzing quantitatively the relationship between hotspots and the geoid in a global sense, including information from recent seismic studies of mantle heterogeneity.

Global Observations and Hotspots

The Earth's long-wavelength geoid (shown in Figure 1a referred to the hydrostatic figure) has been well determined from observations of satellite orbits (Kaula, 1963; Lerch et al., 1983), but its interpretation has remained somewhat enigmatic because of its lack of resemblance to surface features such as continents and mid-ocean ridges. However, by filtering out the lowest harmonics (degrees 2-3) which dominate the geoid spectrum (see Figure 2), it is obvious that many of the "intermediate" wavelength geoid highs are located over active subduction zones (Figure 1b). This subduction signal can be removed from the geoid with moderate confidence because of the high degree of formal correlation between slabs and the geoid at harmonic degrees 4-9 (see Figure 3). Hager (1984) has presented a model, which we review in more detail below, that allows us to subtract a subduction geoid signal, calculated using a fluid dynamical model, from the observed geoid to obtain the residual geoid shown in Figure 1c.

The residual geoid is dominated by two large highs centered over Africa - north Atlantic and over the west-central Pacific. Crough and Jurdy (1980) and Chase(1979) recognized that residual geoid highs (left after subtracting slab effects) cover areas that include most of the world's hotspots (marked with dots in Figure 1). Although not as striking as with all degrees included, upon filtering the lowest degree (2-3) components (Figure 1d) we still find more "local" residual geoid highs over many of the hotspot provinces including Hawaii, Tasmania, Raton - Yellowstone - Bowie - Juan de

Fuca, Christmas Island - Kerguelen - Crozet - Vema, Afar, Easter - Juan Fernandez, and Iceland - Madeira - Canary - Azores - Cape Verde - Rio Grande - Fernando. The Hawaiian anomaly is very striking and less likely than, e.g., Iceland to be contaminated by plate boundary effects. There are conspicuous exceptions including Mt. Erebus, Samoa, and Bermuda which occur in pronounced residual geoid lows. Also, geoid highs remain over the Iranian-Caucasus-Tibetan highlands, which are related to convergence and thickening of the continental crust (Hager, 1983).

We have selected our list of 47 hotspots (Table I) based on the compilations of Morgan (1981) and Crough and Jurdy (1980). Although exception may be taken with any of several inclusions or deletions (conceivably, only some hotspots are associated with plumes), this list probably represents the distribution fairly well. The compilation by Burke and Wilson (1976) of 115 possible hotspots also exhibits a strong association with the low-degree geoid as shown by Crough and Jurdy (1980). The dynamic geoid response of the Earth to internal density contrasts depends quite strongly on the wavelength considered (RH). It is convenient, as well as instructive, to calculate models for comparison to observations in the spectral domain using spherical harmonics. The spherical harmonic representation of hotspots which we use for statistical correlations is obtained by mathematically representing hotspots as point sources of equal (and arbitrary) strength on the surface of the Earth. We have made no attempt to selectively weight certain hotspots such as Hawaii, Iceland, and Kerguelen, which are surely more important than others, such as Raton, whose legitimacy as hotspots may be questioned.

The hotspot distribution spectrum is shown in Figure 2 along with the geoid and residual geoid spectra. These spectral amplitude plots are obtained from the square

root of the sum of squares of harmonic coefficients at each harmonic degree:

$$A(l) = \sqrt{\sum_{m=0}^{l} (c_{lm}^2 + s_{lm}^2)/(2l+1)} \tag{1}$$

The c_{lm} and s_{lm} are the cosine and sine coefficients for a fully normalized spherical harmonic expansion. The factor $1/(2l+1)$ is included because a random distribution of delta functions (hotspots) on a sphere will have a flat ("white") spectrum with this normalization. The hotspot spectrum (Figure 2) is much whiter than either of the geoid spectra; it is mildly peaked at degrees 1-2 with a striking peak also at degree 6. (Because the geoid is referred to the center of mass coordinate system, it has no degree 1 component.)

The correlation coefficient, r_l, between the geoid and hotspots may be obtained from

$$r_l = \frac{\sum_{m} (c_{lm}\, g_{lm} + s_{lm}\, h_{lm})}{\sqrt{\sum_{m=0}^{l} (c_{lm}^2 + s_{lm}^{2})} \sqrt{\sum_{m=0}^{l} (g_{lm}^2 + h_{lm}^{2})}} \tag{2}$$

where (c_{lm}, s_{lm}) are the geoid coefficients and (g_{lm}, h_{lm}) are the hotspot coefficients. Cummulative correlations with several or many harmonic degrees simultaneously can be misleading since spectral power is not uniform (Eckhardt, 1984), so we examine only degree-by-degree correlations. Hotspots are significantly correlated with the observed geoid only at degree 2, but the low-degree correlations for hotspots vs. the slab residual geoid are higher as shown in Figure 3. Confidence limit contours determined by a Student's t test with $2l$ degrees of freedom are also shown in Figure 3. A confidence level of 0.95 implies that there is a 5% probability that the two sets of functions are random.

The residual geoid is significantly correlated with hotspots at degrees 2, 4, and 6 with some correlation at degree 3. Higher harmonics are essentially uncorrelated (no correlations are significant with $>90\%$ confidence for $l=7$–20). The correlations at degrees 2 and 6 are particularly noteworthy because they correspond to peaks in the hotspot spectrum. Crough and Jurdy (1980) found a correlation coefficient of 0.85 at degree 2, significant with $>95\%$ confidence, that is even higher than our value of 0.75; the difference arises from different methods of calculating the slab signal.

The degree 2 correlation is made even more compelling by recent observations of seismic velocity heterogeneity in the lower mantle. Both the tomographic inversions of Clayton and Comer (1983) and the least-squares inversion of Dziewonski (1984) of P-wave travel times show that low velocity in the lower mantle is very strongly correlated with low-degree (2-3) geoid highs (Hager et al, 1985). We also find that slow velocity and presumably hot, low density anomalies are well correlated with the hotspot distribution at degree 2 ($r_2=0.85$). Figure 4 emphasizes this point by comparing harmonic degree 2 maps of the slab residual geoid, a depth average of seismic heterogeneity from Clayton and Comer (1983), and the hotspot distribution. All of these fields closely resemble the entire low-degree residual geoid (Figure 1c) because the geoid spectrum is so strongly peaked at degree 2. (The vertically averaged lower mantle P-wave velocity model is also peaked at degree 2 as shown in Figure 2.) These three phenomena are apparently related, and even though statistical correlations contain no information concerning cause-and-effect relationships, we form the following hypotheses: Occurrences of hotspots (mantle plumes) are directly related to the broad-scale temperature structure of the lower mantle, and the largest residual geoid highs are the result of long-wavelength topographic highs that are dynamically

supported by either broad scale or plumelike (hotspot) thermal anomalies.

Additional evidence of this kind comes from studies of upper mantle heterogeneity from surface wave studies (Masters et al, 1982; Woodhouse and Dziewonski, 1984; Nataf, Nakanishi, and Anderson, 1984; Tanimoto, 1986). At degree 2, there is a high velocity feature in some models of the transition zone that correlates well with the geoid (e.g., Masters et al., 1982; Woodhouse and Dziewonski, 1984; Nataf et al., 1986). This feature is even better correlated with subducted slabs than with the observed geoid (Hager, 1984; Richards and Hager, 1986: Chapter 2) and appears to be associated with cold downwellings rather than hot plumes. Both the Woodhouse and Dziewonski and the Tanimoto studies show a remarkable correlation with both the residual geoid and hotspots at degree 6. Table II gives the degree 6 correlation coefficients, and the negative signs indicate that slow shear velocity is correlated with both geoid highs and hotspots. Since there is a spectral peak in the hotspot distribution at degree 6, the correlation at degree 6 is expected if hotspots are to show a strong relationship to either the geoid or shear velocity anomalies. If the upper mantle is near the solidus, then shear waves should be very sensitive to elevated temperature. In Figure 5 we compare the degree 6 surface wave velocity heterogeneity, residual geoid, and hotspot distributions to illustrate the strength of an $\sim$0.7 correlation coefficient at degree 6. (We should note that the lower mantle heterogeneity models do not correlate with hotspots or the geoid at harmonic degrees $>$4. Lack of resolution may be at fault, and other possible reasons for this are addressed in Richards and Hager, manuscript in preparation: Chapter 3.) Also note that degree 6 is the one harmonic degree for which slabs do not correlate well with the observed geoid. However, it is only when the dynamically modelled degree 6 slab geoid is removed that

the hotspot distribution shows good correlation with the geoid. Figure 5 shows that the degree 6 hotspot peak represents the large groupings of hotspots (e.g., Christmas Island - Kerguelen - Crozet - Vema) rather than individual spacings which appear to be random. (The hotspot spectrum beyond degree 10 is essentially white.) Again, we can formulate a testable hypothesis concerning hotspots: Plumes are directly related to either heating or chemical heterogeneity in the upper mantle at degree 6, which may be a dominant wavelength for their formation.

These observations suggest that we formulate a quantitative global test to determine whether mantle plumes might be directly responsible for the density contrasts that cause the large-scale residual geoid features as well as the seismic velocity anomalies. The question then becomes that of whether reasonable models of hotspots, either mantle plumes or delaminating lithosphere, can explain the slab residual geoid. The alternative, of course, is that hotspots are only symptoms of a broad-scale thermal field or, perhaps, compositional heterogeneity in the mantle.

The correlations of Figure 3 suggest to us that much of the long-wavelength slab residual geoid is causally related to hotspots. We assume that for each harmonic degree this relationship can be written in the linear form

$$residual\ \ geoid\ = (dynamic\ \ response) * (hotspot\ \ distribution) + (noise)$$

or, for example,

$$(c_{lm}, s_{lm}) = b_l (g_{lm}, h_{lm}) + (noise) \tag{3}$$

From our analysis we obtain the least-squares estimates for the dynamic response functions, b_l, shown in Figure 6. The coefficients (g_{lm}, h_{lm}) are in units of hotspots, and the spectral "response" curve is in the rather peculiar units of geoid/hotspot.

Although we cannot reliably determine the response at degree 5, where the correlation is poor, it appears that the response is a relatively smooth, monotonic function of harmonic degree, suggestive of a dynamical filtering process as discussed below. Also shown are the values of b_l obtained if, instead of assuming that all the error in estimation is the result of other density heterogeneity signals in the geoid, we perform the mutual correlation of residual geoid and hotspots under the pessimistic assumption of equal noise in each signal. The extra noise on the geoid (left) side of equation 3 may be due primarily to mismodelling of the subduction signal; at these wavelengths the geoid can otherwise be considered to be perfectly measured. The "equal noise" response is not substantially different than the initial model (equation 3), so our response curve is robust at least in this respect. Unfortunately, the least-squares fits for the coupling coefficients, b_l, are less well constrained as shown by the 2σ error bars at each harmonic degree. The best fitting response amplitudes give about a factor of 8 decrease from harmonic degree 2 to degree 6. This spectral shape is largely that of the residual geoid, since the hotspot spectrum does not show the same long-wavelength bias.

In addition to the global association of hotspots with geoid highs, we can also use the local $\sim$13 m geoid high (degrees 4-10) centered on Hawaii to constrain our models (see Figures 1b,c). The contours are not elongated in the direction of the older islands and seamounts in the chain (toward the northwest), so it is difficult to explain this long-wavelength signal as an effect of the lithospheric swell itself. The anomaly actually appears to be elongated toward the upstream direction (southeast), suggesting, perhaps, that the active Hawaiian shield is lagging slightly behind a deep thermal source.

The spectral content of the Hawaiian geoid anomaly is difficult to assess quantitatively because it is necessary to arbitrarily select some spatial subdomain within which to perform spectral analysis. However, Figures 7a,b show that about 10 m of the 13 m signal occur in the harmonic degree 4-6 band, while less than ~3 m occur in the degree 7-12 band. Figure 7c shows that the degree 10-20 geoid signal over Hawaii is almost zero, and also verifies the lack of any consistent correspondence between geoid highs and hotspots (noted above) in this wavelength band. (Note, however, that there is a strong shorter-wavelength signal over Yellowstone.) Since the Hawaiian swell is of relatively small width (~1000 km), the lack of degree 7-20 signal makes it an implausible source for the longer-wavelength positive geoid anomaly. These observations for the isolated case of Hawaii are consistent with the pronounced long-wavelength bias of the inferred global hotspot geoid response curve of Figure 6. We use both the local and global observations to discriminate among long-wavelength geoid responses for the competing hotspot models discussed below.

Dynamic Response Functions

It is necessary at this point to review some basic ideas about how long-wavelength geoid anomalies are generated in a viscous, convecting planet like the Earth. Chase and McNutt (1982) and Hager (1983) have shown that only about 20 meters out of a total long-wavelength geoid signal of about 200 meters can be generated by uncompensated topography and lithospheric or crustal thickness variations, e.g., the geoid high over the Tibetan Plateau. Therefore, most of the geoid must result from the internal density contrasts that drive convective flow: subducted slabs, mantle plumes, or broader scalelength variations.

Interior density contrasts drive flow that causes deformations of the surface, the core-mantle boundary, and possibly, internal chemical boundaries. At very long wavelengths ($l \leq 10$) the lithosphere has effectively no long-term flexural strength (McKenzie and Bowin, 1976), and deformation will occur rapidly compared to the timescale for convection (RH). These deformed surfaces have an important effect on geoid anomalies. In order to correctly model the long-wavelength geoid, a fluid dynamic Earth model must be used to calculate the geoid contributions due to these boundary deformations. It has been shown by many authors (e.g., Pekeris, 1935; Runcorn, 1964; Morgan, 1965; McKenzie, 1977; Parsons and Daly, 1983; Ricard et al, 1984; RH) that dynamic compensation due to boundary deformation is of dominant importance in determining the geoid. Since induced boundary deformations cause geoid anomalies that are of opposite sign and comparable magnitude to the geoid due to interior density contrasts, long-wavelength geoid anomalies are the difference of large numbers. The details of boundary deformation depend strongly on the viscosity structure of the mantle, so the geoid is a sensitive indicator of mantle structure (RH).

If the viscosity structure varies only radially (i.e., is spherically symmetric), then a given density contrast $\delta\rho_{lm}(r)$ at radius r excites only an lm^{th} harmonic flow field and causes only lm^{th} harmonic boundary deformation. Since solutions for linear (Newtonian), spherically symmetric viscosity may be superposed, we can obtain the total harmonic geopotential coefficients from

$$U_{lm} = \frac{4\pi\gamma R}{2l+1}\int_{c}^{R} G_l(r)\delta\rho_{lm}(r)dr \qquad (4)$$

where γ is the gravitational constant, R the Earth's radius, c the core radius, and $G_l(r)$ is the dynamic response function or kernel. This kernel is independent of the

azimuthal order m and contains contributions from both boundary deformations and the density contrast itself. In RH we showed how to analytically calculate $G_l(r)$ for spherically symmetric, incompressible, self-gravitating Earth models.

Response functions for both whole mantle flow and chemically layered flow are shown in Figure 8 with lower/upper mantle viscosity ratios of 1, 10, and 100. Note that although flow velocities depend on the absolute value of viscosity, the stresses, boundary deformations, and geoid depend only on the relative values. Free-slip boundary conditions are imposed at the core and at the surface; the difference between no-slip and free-slip is discussed in RH. For uniform viscosity and whole mantle flow (Figure 8a) the geoid response is always negative because of the overwhelming gravitational effect of the deformed upper boundary. Decreasing the viscosity of the upper mantle causes less deformation of the upper boundary (Figure 8b,c) and tends to drive the geoid response toward more positive values. Therefore, both the size and magnitude of the geoid response are strongly affected by relatively mild changes in viscosity with depth. These pressure induced changes can occur either gradually due to compaction or abruptly due to phase changes; phase changes probably do not otherwise strongly affect the flow field (Richter and McKenzie, 1981). However, a chemical discontinuity acting as a barrier to radial flow will deform and also affect the geoid. This forces the geoid response to zero at the boundary (in the same way that we get perfect compensation at the surface and core) and generally reduces the magnitude of the response functions (Figure 8d,e,f).

In addition to the response function $G_l(r)$ we have also calculated dynamic impedance functions, $z_l(r)$ which give the ratio of induced topography to observed geoid (RH). Unfortunately, the Earth's dynamically supported topography is obscured

at long-wavelength due to gravitationally compensated continental masses and thermal plate thicknesses, and there is no consistent correlation between topography and gravity. At the present time we cannot reliably estimate the global long-wavelength (degrees$<$10) dynamic topography associated with mid-oceanic swells or hotspots.

An obvious application of the response functions of Figure 8 is in modelling the subducted slab geoid signal (see Figure 1b). A dynamical model using deep seismicity to locate subducted slabs was developed by Hager (1984). By associating slabs with approximately 0.1 gm/cm ^{3} density contrast and convolving these mass anomalies with various response functions, the following conclusions were reached based on comparison of the observed and predicted geoids: (1) The magnitude of the observed geoid response is consistent with only a small degree of dynamic compensation. (2) The sign of the response function is positive for harmonic degrees 2-9 in the upper mantle, requiring a viscosity increase with depth. (3) Chemically layered models require about a factor of 5 more density contrast associated with subducting slabs than expected. (4) The best-fitting two-layer viscosity model is that of whole mantle flow with a factor of about 30-100 increase in viscosity between the upper and lower mantle (see Figure 8c).

Figures 8b,e,f show that it is possible to have positive responses in the upper mantle and negative ones in the lower mantle for a variety of models. This at first suggests one easy solution to the problem of geoid highs over both slabs and plumes, namely, that plumes are primarily lower mantle features. (More realistic models that include a low viscosity asthenosphere and high viscosity lithosphere added to model U10 give more positive upper mantle kernels but maintain negative kernels in the lower mantle.) This idea turns out to be basically correct in the numerical plume

models which are discussed below. However, we feel that it is important to assess the impact on our response kernels caused by neglecting the large viscosity variations expected to be associated with slabs and plumes. One motivation for numerical modelling is the hypothesis that these viscosity variations might be responsible for the paradox of having geoid highs over both slabs and plumes. An alternative explanation is that the geoid highs over hotspots are due to delamination of cold lithosphere, consistent with the slab results. With the upper mantle "calibrated" by the geoid response of cold, subducting slabs, it is straightforward to estimate the geoid signature of unstable lithosphere sinking below a hotspot if we can estimate the amount of high density material present. We present both types of models in the following sections.

Delaminated Blobs

Although the uppermost 30 km of the lithosphere under Hawaii behaves elastically (e.g., Watts, 1978), the portion of the thermal lithosphere below the elastic layer should behave as a cold, dense, high viscosity boundary layer. It is convectively unstable and might sink into the mantle, or "delaminate." For Hawaii, if all of the swell topography is attributed to delamination, the flux of delaminated blobs is comparable to that of slabs at subduction zones. The age of the crust around Hawaii is about 90 Myr and the apparent thermal age after the $\sim$ 1 km uplift of the swell is around 25 Myr (Epp, 1984a). The elevation and hence the average mass anomaly in the lithosphere is proportional to the square root of age, so the delamination is equivalent to subduction of a 20 Myr plate at the rate of hot spot migration (100 mm/yr) across the $\sim$1000 km width of the swell. We assume that large-scale

horizontal motions in the mantle are much less than plate velocities (e.g., Hager and O'Connell, 1979), so that the locus of delamination is roughly fixed with respect to the mantle, not the plates. If we assume 10 Myr as a characteristic time of transit through the upper mantle, then, for a slab of material 1000 km long (along swell) by 1000 km wide with an excess mass per unit area of $3.3x\,10^6$ kg/m ^{2} (associated with the uplift of the swell), the excess mass of lithospheric material in the mantle beneath Hawaii is $\sim 3x\,10^{18}$ kg.

This load can be convolved with the preferred geoid response curves ("U100") for subducted slabs (Figure 8c) to estimate the long-wavelength geoid. If the excess mass is roughly distributed in a cylinder $<$1000 km in radius and 1000 km deep beneath Hawaii, we predict about an 6.3 m geoid high over Hawaii for harmonic degrees 4-9, which is about half the observed signal. However, the spectral response for this model is not nearly as strongly peaked at the lowest degrees as the global response curve (see Figure 18 for a comparison) owing to the small horizontal scale of the load. The degree 2-10 topographic downwarp is about 85 m, a value not likely to be resolved by analysis of bathymetric data given other perturbing influences. The lithospheric swell itself will generate relatively little geoid signal since it is isostatically compensated at shallow depth; whatever signal is generated will also be essentially "white" at low harmonic degrees since the swell is only $\sim$1000 km wide.

The shorter wavelength ($l>10$) geoid contribution could be as much as 10 m if there is little compensation, but this value depends strongly on the detailed viscosity structure of the upper mantle (RH). It is evident that the short-wavelength geoid is not elevated 10 m near the hotspot, and about 300-400 m of downwarp is required to keep the $l \geq 10$ geoid anomaly small. If this downwarp occurs, a place on the seafloor

would be expected to experience subsidence (superimposed on the lithospheric swell due to delamination) as it approached the hotspot, and then uplift as it drifted further west. Since we cannot predict the detailed timing of the delamination it is difficult to model the upstream (east) side of the hotspot. On the west side of Hawaii, simple thermal contraction should produce about 350 m of downwarp in the first 11 Myr if the lithosphere is reset to a thermal age of 25 Myr. If this downwarp is superimposed on an uplift of $\sim$300-400 m due to rebound as the lithosphere moves away from the sinking, delaminated blobs, we obtain approximately a neutral net uplift/subsidence on the downstream side of the hotspot. Although this computation is crude, this might explain the fact that the Hawaiian swell has not substantially subsided as far as 10^0 West of the hotspot as shown in Figure 9. (This topographic variation could conceivably be attributed to greater activity of the hotspot 11 Myr ago.) This description of swell topography due to delamination can be contrasted with the following model based on heat flux from a mantle plume.

Plume Kinematics

Before describing our numerical plume models, we consider a simplified kinematic description of a plume for Hawaii that relates the heat flow, mass flux, temperature excess, and swell topography. Assuming for now that there is no triggered lithospheric delamination, the plume must diverge widely enough beneath the lithosphere to account for the swell width and must also supply enough heat to thin the lithosphere. That is, the flux of positive buoyancy from the plume should equal the rate of production of positive buoyancy in the swell. Using, as before, a migration rate of 100 mm/yr, a width of 1000 km, an elevation of 1 km and a density of 3300

kg/m ^{3} for the swell, the net flux $\dot{m}$ of negative buoyancy is 10 Mg/sec. The actual mass flux in the plume is the buoyancy flux divided by the fractional density contrast in the plume, $\dot{m}\,\rho/\delta\rho$. For thermal expansion the density contrast is $\delta\rho=\rho\alpha\Delta T$, where ΔT is the excess plume temperature and α is the volume thermal expansion coefficient, $3x\,10^{-5}/^0$K. The resulting heat flux from the Hawaii hotspot, $C\dot{m}\,/\alpha$, ($C=1.2x\,10^3$ J/kg ^{0}K is the specific heat) is $4.2x\,10^{11}$ W or about 1% of the global mantle heat flux. The volume of flow, Q, through the plume necessary to make the swell is inversely proportional to the temperature contrast

$$Q = \dot{m}\,/\alpha\rho\Delta T \tag{5}$$

(For reference, a plume with $\Delta T=100^0$K, 100 km diameter, and $\dot{m}=10$ Mg/sec ascending as a cylindrical plug will have an ascent velocity of 4 m/yr.)

Next, the flow from the plume must diverge widely enough to produce the observed swell. To a first approximation this flow can be considered to be the interaction of radial flow from the plume through an asthenospheric channel and the horizontal drag produced by the motion of the plate over the hot spot. The average velocity in the asthenosphere far away from the center of the plume is

$$\mathbf{v}_{plume} = (Q\,/2\pi rA\,)\hat{\mathbf{a}}_r \tag{6}$$

where r is the horizontal distance from the plume, A is the thickness of the asthenosphere, and $\hat{\mathbf{a}}_r$ is a unit radial vector from the hotspot. The average velocity in the asthenosphere from drag at the base of the plate is about half the plate velocity if the base of the asthenosphere is moving much more slowly than the overlying plate:

$$\mathbf{v}_a = (Q\,/2\pi rA\,)\hat{\mathbf{a}}_r - v_L\,/2\hat{\mathbf{a}}_x \tag{7}$$

where the x direction is positive upstream from the plume and v_L is the plate

velocity. The upstream stagnation point occurs at $r_s = Q/\pi A v_L$. The stagnation streamline assuming 100 km asthenosphere thickness is shown for temperature contrasts of 300^0K and 1000^0K (Figure 9) and the flux computed above. The 1000^0K curve is narrower than the swell, but the 300^0K curve is a fairly good fit to the edge of the swell, which extends about 500 km ahead of the hotspot. (The topographic contours for the Hawaiian swell in Figure 9 have been adapted from Schroeder, 1984, who computed the anomalous seafloor topography in the Pacific ocean after corrections were made for isostatic loading, sediment thickness, seafloor age, etc. Note that the islands and seamounts themselves involve many kilometers of topography, but these loads occur at short wavelength and are partially supported by lithospheric flexure, e. g., Watts, 1978.)

The preceeding calculation is crude, but it shows that the swell shape and buoyancy flux are kinematically consistent with a plume delivering several or many hundreds of degrees excess temperature and also with a reasonable limit for the heat flux due to the Hawaii hotspot. (This heat flux is probably at least a factor of 2 or 3 too high for an average hotspot, since 47 hotspots would otherwise account for half of the Earth's entire heat budget.) It remains to be seen whether a mantle plume fitting this surface kinematic model can also satisfy the geoid observations and constraints from convection theory on the thermal structure of plumes. We consider more refined models in the next section.

Fluid Dynamical Models of Plumes

Our basic idea of a plume is that of a narrowly confined, stable, hot upwelling from a deep boundary layer due to bottom heating. The seismic D'' layer at the bottom of the Earth's mantle may be in part the result of heating of the base of the mantle by radioactive or latent heat within the core. Most estimates for the amount of core heat flux are somewhat less than 10% of the total geothermal flux (Gubbins et al, 1979). If there is a plume under Hawaii it is probably less than $\sim$200 km in radius as evidenced by the width of the volcanic trace (Morgan, 1972b). This small dimension is consistent with a very high effective Rayleigh number and the strong temperature dependence of viscosity, as shown by the stability analysis of Yuen and Peltier (1980).

The thermal structure of a plume is dependent upon such unknowns as the rheological laws of the mantle and plume material, the amount of heat being vented, the superadiabatic temperature drop, whether the plume is chemically distinct from the upper mantle, and the possible influence of partial melting. Thus, we do not know the plume structure very well. By contrast, we can make an educated guess as to the thermal structure of a subducted slab or even a delaminated lithospheric blob. Our approach is to address some general questions about plume dynamics and compare the results to the observations discussed above. In particular, we ask: (1) How does the low viscosity of the plume alter the geoid responses derived for purely layered viscosity? (2) Is the thermal buoyancy of a narrow plume consistent with both the observed amplitude of hotspot geoid anomalies and reasonable limits on the amount of heat flow due to a hotspot?

The main difficulty in modelling is the result of the extreme horizontal variations in viscosity expected for a thermal plume. No analytical methods exist to treat this problem in detail, so a numerical solution is required. We need to calculate very long-wavelength (~10,000 km) stress fields to obtain long-wavelength surface deformation and geoid estimates, but we must also resolve the strong short-wavelength (~10-100 km) plume structures which drive the flow. The finite element method is well suited to this problem because of the advantage of variable grid size, and a typical grid for our plume models is shown in Figure 10. In all of the calculations that follow we have used 10 km horizontal grid spacing for treating the prescribed buoyancy forces and viscosity variations for both plumes and slabs, thus allowing good resolution of thermal structures as thin as 50 km or less. Much smaller spacings are possible by further packing the nodal lattice at the origin, but this was not necessary except as a check on solution accuracy. We have also used 20 km vertical spacing in the top 200 km and bottom 100 km of the mantle to properly resolve viscosity changes in the lithosphere/asthenosphere and core-mantle boundary (D'') region. Rotational or reflection symmetry imposed about $r=0$ (r is the radial distance from the plume center) or $x=0$ gives a total effective width of 10,000 km in both cylindrical and Cartesian geometry. (In the cylindrical calculations we assume a free-slip boundary at the outer boundary of the cylinder, $r=d$.) The numerical code is based on a penalty method formulation (Hughes et al., 1979) of the Stokes flow problem (steady, incompressible, very low Reynold's number flow with spatially variable Newtonian rheology). The code handles nonlinear rheology by damped iteration upon the viscosity field.

We are currently limited to numerical solutions in two dimensions (2-D Cartesian or cylindrical geometry with axial symmetry) rather than the spherical geometry for which we earlier showed analytical solutions. The two-dimensional results that follow are represented in the horizontal spatial wavelength domain, just as we represented our spherical, analytical models (Figure 7) in spherical harmonics. In Cartesian coordinates (appropriate for subducted slabs) we have the approximate spatial wavelength equivalence,

$$\lambda_F \approx 2\pi R / \sqrt{l(l+1)}$$

where λ_F is the Fourier transformed spatial wavelength, l is the corresponding spherical harmonic degree and R is the Earth's radius. In cylindrical coordinates (r, z) with no θ dependence, we use the Fourier-Bessel transform of the spatial coordinate r (see Appendix A). Therefore, for axial symmetry (appropriate for plumes) we have the approximate wavelength equivalence,

$$2\pi d / p_n' \approx 2\pi R / \sqrt{l(l+1)}$$

where p_n' is the n^{th} zero of the derivative of the zeroth order Bessel function, $J_0(r)$, and d is the radius of the cylindrical domain. For our numerical grid, d =5000 km and λ_F =10,000 km for Cartesian geometry, so the maximum allowable wavelengths in both cases correspond approximately to spherical harmonic degree 4. (This was the maximum horizontal dimension our computer model could handle with accuracy and still provide high resolution at the center of symmetry.) The first and second "overtones" in both coordinate systems correspond to harmonic degrees 8 and 12, respectively.

In the absence of lateral viscosity variations, the flow and stress fields due to a density contrast of a given spatial wavelength are independent of disturbances at other wavelengths. Two-dimensional geoid response functions similar to G_l in equation 4 can be calculated analytically as a function of spatial wavelength, and the dotted lines in Figure 11 show responses for a uniform mantle (model A, Figure 12) at spatial wavelengths corresponding to harmonic degrees 4, 8, and 12. These functions are exactly the same in Cartesian and cylindrical geometry for a given wavelength (see Appendix A). The response is uniformly negative due to the dominance of boundary deformation, and the curves are similar to those for the U1 model of Figure 8.

We now consider three different cases in which the low viscosity of a plume may affect the geoid signal. The first case is that of hot blobs (such as those investigated experimentally by Olson and Singer, 1985) guided in their ascent by a narrow, preestablished pathway. The upper surface deformation and geoid due to these solitary blobs can be adequately modelled by the analytical theory (RH). Unless the blobs are very closely spaced, i.e., connected, there will not be an effective low viscosity *stress* pathway to the upper surface (or the core-mantle boundary), so induced surface deformations will not be very different from those calculated using the ambient mantle viscosity structure. Their buoyancy will act approximately as point sources, with respect to the long-wavelength flow-stress field, embedded in a high viscosity background (mantle). The particular case of a hot blob impinging on the lithosphere is a special case which we will discuss later. A more closely spaced string of low viscosity hot blobs might behave more like the plume models described next.

The other two plume types with which we are concerned are like the more classical, steady-state structures in which vertical flow is very rapid with respect to mantle

flow as a whole and is nearly uniform, with convergence at the bottom toward the plume and divergence at the top. The probable narrowness (<200 km) of mantle plumes implies that the zones of flow convergence/divergence will be of equally small dimension (perhaps that of the D'' layer and the asthenosphere); we temporarily ignore these complications. We can envision two end-member classes of these steady-state plumes for which the low plume viscosity may affect the geoid signature. Mantle plumes may be essentially low viscosity "pipes" in which low viscosity rising fluid is contained by the relatively rigid walls (mantle). The other type is more typical of mantle convection models in which the radial excess temperature profile decays smoothly away from the axis of the plume (e.g., Parmentier et al., 1975; Yuen and Schubert, 1976; Boss and Sacks, 1985). If the plume is not distinct chemically from the surrounding mantle, a long-lived plume should evolve to this latter state as the surrounding mantle is heated conductively and, possibly, by viscous dissipation. We concentrate on this "thermal halo" case in the models that follow, returning to the "pipe" case when a comparison is needed.

The thermal profile for the halo model can be parameterized by a characteristic width, r_0, and by a peak (axial) excess temperature, ΔT_0, which should be essentially independent of depth if the plume rises nearly adiabatically. The temperature profile near the plume axis must satisfy the condition

$$\frac{\partial T}{\partial r} = 0 \quad at \ r = 0 \tag{8}$$

Since most of the flow and transport will occur very near the axis due to temperature softening of the mantle material, the dynamics of the plume is sensitive to the excess temperature profile. In accord with equation 8, we have adopted the form used by

Loper and Stacey (1983)

$$\Delta T = \Delta T_0[1-(r/r_0)^2] \tag{9}$$

where ΔT_0 is the peak excess temperature in the plume and r_0 is a characteristic plume radius. Expression (9) can be modified to include a thermal "halo" surrounding the mobile near axis region by a temperature profile of the form

$$\Delta T = \Delta T_0 \exp[-(r/r_0)^2] \tag{10}$$

where r_0 gives the characteristic thermal width of the plume. Estimated values for ΔT_0 associated with the superadiabatic increase across D'' vary widely up to a maximum of about 1000^0K (Verhoogen, 1973). This parameter is not well constrained by observation, and we consider a wide range of values in our models.

The density contrast in the plume is given by

$$\delta\rho = -\rho_0 \alpha \Delta T \tag{11}$$

where ρ_0 is the density at the background mantle temperature and α is the volume coefficient of thermal expansion. We have taken ρ_0=5.14 g/cm ^{3} and $\alpha = 3x\,10^{-5}/^0$K. The uplift above an inviscid plume is given by $\frac{1}{2}(D\,\delta\rho/\rho_0)$, where D is the mantle depth, so a temperature contrast of only 100^0K results in an excessive uplift of 4.3 km. Therefore, viscous drag must limit flow in the plume.

The viscosity of mantle minerals is a strongly decreasing function of temperature, and we have used the exponential form

$$\eta = \eta_0 \exp(-\beta \Delta T / T') \tag{12}$$

which also closely mimics the form used by Loper and Stacey (1983) for a characteristic temperature T' =2300^0K and $\beta \leq 35$. For example, with ΔT =800^0K and β=35,

we obtain more than five orders of magnitude viscosity decrease from the colder surrounding mantle to the hot plume axis. Stress-dependent rheology, by diffusing viscous stresses away from the plume, lowers the effective value of β (Christensen, 1984).

Note that for large values of β or ΔT_0 the combination of exponential dependences in expressions 10 and 12 will restrict most of the flow to a very narrow region near the axis, even though most of the thermal buoyancy, or "halo," may lie outside of this region. Expressions 10 and 12 allow us to characterize a wide variety of dynamical behavior by using β, ΔT_0, and r_0 to specify, independently, the maximum viscosity contrast, the thermal buoyancy, and the characteristic width of the plume. This parameterization could closely match most published temperature and viscosity profiles for plume models, e.g., Yuen and Schubert (1976).

In our first model (A) (see Figure 12) we consider a plume of characteristic width r_0=70 km and peak excess temperature 700^{0}K through the entire depth of the mantle. Using expressions 10-12 to specify the load and laterally varying plume viscosity structure, we have calculated the total geoid response by obtaining the induced boundary deformation from a finite element solution. Strictly speaking, the depthwise, wavelength dependent response functions of equation 4 do not exist for laterally varying viscosity; the different spatial wavelengths are mutually coupled. However, we can construct "pseudo response functions" for comparison with analytic kernels by considering all of the geoid at a particular wavelength to be due only to the load component at that wavelength. The depthwise pseudo response functions for a plume with about 4 1/2 orders of magnitude viscosity contrast (β=35) are shown in Figure 11. These curves are more negative in the upper mantle than for the uniform viscosity

case in the upper mantle, but the effect is rather small in comparison to that of depthwise viscosity variation or chemical stratification (Figure 8). One reason for this is that much of the plume buoyancy, or thermal halo, lies outside of the very low viscosity plume core and the resulting change in surface deformation is relatively small. The change that does occur causes the geoid response to become more negative due to enhanced long-wavelength boundary deformation. We note here that changes in the outer radius boundary condition (at $r=d$) from free-slip to rigid have less than a 5% effect upon the geoid calculations. Therefore, the finite cylinder radius probably has less effect than other neglected effects such as the dynamical interaction of plumes. The long-wavelength deformation field is even less sensitive, so it is safe to conclude that the 5000 km maximum radius for the finite element grid is not a severe limitation in these calculations. Extrapolation to a degree 2 wavelength may be more questionable, but in that case the effects of self-gravitation (RH), sphericity, and self-compression (Ricard et al, 1984; Hong and Yuen, 1985) are even more important. The response curves in Figure 11 are truncated at 200 km depth, because the solution accuracy degrades ($>1\%$ error in the $l=4$ surface deformation compared to analytical solutions) for loads above this level.

The narrowness of a single plume gives essentially equal loading at all wavelengths of interest (a spectrally "white" load) so that the relative geoid response at each wavelength can be obtained by integrating along the response curves. From Figure 11 we see that the low plume viscosity causes enhancement of the shorter wavelength ($l=8,12$) geoid and surface deformation compared to the longer wavelengths ($l=4$). The low plume viscosity allows more efficient transfer of the buoyancy forces ("head") in the plume to the upper and lower surfaces, so that the

load is effectively closer to these boundaries. The magnitude of the effect upon the total geoid signature is shown in Figure 13 for a wide range of the parameters β and ΔT_0. (The relative size of this effect also increases with the plume radius as demonstrated for the pipe models in Figure 16.) Our numerical experiments show that for $(\beta \Delta T_0 / T') < 6$ (less that 2 1/2 orders of magnitude viscosity contrast) the geoid signal is enhanced by a relatively modest factor of 20% or less. Unless the temperature dependence of viscosity is much stronger than given by the rather high value of $\beta = 35$, a plume temperature excess of at least 600–800^{0}K will be required to substantially affect the geoid signature of this type of mantle plume.

The plume radius, $r_0 = 70$ km, in the example of model A was chosen so that the amplitude of the long-wavelength geoid signal ($l = 4,8$) would be comparable to that observed over Hawaii ($\sim$13 m) for $\Delta T_0 = 700^0$K. The geoid elevation (per ^{0}K temperature contrast) from this halo model with *no* viscosity perturbation ($\beta = 0$) is (0.72, 0.72, 0.55) cm/ ^{0}K for $l = (4, 8, 12)$ scale lengths. These values can be scaled by the cross-sectional area of the plume ($\sim r_0^2$) within a few percent accuracy over the range 30 km $< r_0 <$ 100 km. The Δgeoid curves of Figure 13 give the geoid signal ($\beta > 0$) in excess of the unperturbed signal ($\beta = 0$). The size of the geoid anomaly will scale roughly as $\Delta T_0 \, r_0^2$ unless the effects of low viscosity are large.

In matching the observed geoid signal, we must not greatly exceed the approximate upper limit of $\sim$10 Mg/sec buoyancy flux (see previous section). Figure 14 shows the buoyancy flux, normalized to a background mantle viscosity $\eta_0 = 10^{21}$Pa-sec, for $r_0 = 70$ km plumes with varying ΔT_0 and β. For $\beta = 35$, $\Delta T_0 = 700^0$K, we obtain $\sim$200 Mg/sec buoyancy flux, so the mantle viscosity must be raised by a factor of 20 to $2x\,10^{22}$Pa-sec to lower the flux to 10 Mg/sec. (Flow velocities in all of our

examples scale inversely as η_0.) Flow in these plume models is limited by viscous drag in the surrounding mantle; the buoyancy flux varies little with depth except very near the top and bottom of the mantle, and the values in Figure 14 are calculated at mid-depth. Figure 15 shows that the buoyancy flux scales linearly with the 4^{th} power of the radius, r_0^4, as expected for flow in a long, narrow conduit.

We now consider a "pipe" model in which the temperature profile is steplike, i.e.,

$$\Delta T = constant\,,\ r < r_0 \tag{13}$$

$$\Delta T = 0,\ r > r_0$$

Both temperature and viscosity are uniform within the pipe. Figure 16 shows the geoid effect of low viscosity for a suite of pipe models parameterized by the radius, r_0, and by the viscosity contrast relative to the background mantle viscosity. The unperturbed geoid signal (pipe viscosity = 1.0) is (0.63, 0.63, 0.48) cm/ ^{0}K for r_0=70 km (almost the same as for the halo model) and scales as $\Delta T\ r_0^2$ as for the halo model. We get about 10 m of geoid signal for 800^{0}K excess temperature in the pipe.

Now we ask: How does the pipe model compare to the halo model in perturbing the geoid signal? We begin by locating a pipe model, r_0=70 km, in Figure 16 that gives about the same perturbation (~30%) to the l=4 geoid signal (see Figure 13) as did halo model A. This requires a viscosity contrast of about a factor of 0.006 within the pipe. The buoyancy flux for the pipe models is mapped in Figure 17 and scales as the square of the excess temperature (buoyancy x force). For a temperature contrast of 800^{0}K, radius r_0=70 km, and a pipe viscosity contrast of 0.006, we obtain a buoyancy flux of 36 Mg/sec, or about a factor of 3 1/2 more than for the comparable halo

model. Therefore, given the restriction on the maximum allowable buoyancy flux and given the requirement for the amplitude of the geoid signal, the pipe model is not as efficient as the halo model in perturbing (increasing) the size of the geoid signal from the uniform viscosity value. Similar comparisons show that this difference between the pipe and halo models persists, to a varying degree, for other plume radii. Also shown for comparison in Figure 17 (dashed lines) are the fluxes calculated analytically for an infinitely long pipe in a rigid mantle, but with the same pipe viscosity and buoyancy forces; i. e., classical Poiselle flow (proportional to the fourth power of the pipe radius). For very low pipe viscosities (.001-.0001 mantle background), the flow in numerical experiments is limited by the finite pipe length. For high pipe viscosity (.1-1.0 mantle background), induced flow in the mantle becomes significant and the flux in numerical experiments is higher than the analytical result.

In the models that follow we find that large perturbations in the geoid signal (e.g., sufficient alone to account for geoid highs over both subducted slabs and hotspots) often require unacceptably large buoyancy fluxes. Therefore, in seeking to understand the largest effects on the geoid of low plume viscosity, we concentrate on the halo model. Before presenting more sophisticated models for hot plumes, we investigate the geoid signature for a very simple model of a cold subducting slab.

We model a high viscosity slab by considering (in Cartesian geometry) a 100 km wide slab, density contrast 0.1 g/cm ^{3}, and having two orders of magnitude higher viscosity than the surrounding mantle. The "slab" for this first example extends throughout the depth of the mantle, so this case and the previous plume models might be taken to simulate the rising and falling hot and cold columns in a very high Rayleigh number, bottom heated, whole mantle convection system. The pseudo

response curves for the slab model in Figure 11 show that for $l=4$ and 8 as well as for $l=12$ in the upper mantle, the high slab viscosity causes the response to be much less negative (more positive) than for a uniform mantle viscosity. If the background viscosity layering in the mantle gives a "marginal" upper mantle response, perhaps with a zero crossing such as for model U10 (Figure 8b), both slabs and plumes residing entirely in the upper mantle are qualitatively consistent with positive geoid anomalies. A more quantitative test is thus suggested.

We start by repairing some of the obvious inadequacies in plume model A. In model B we have added a high viscosity lithosphere, a low viscosity asthenosphere or outlet channel, and a low viscosity D'' layer which simulates the lower boundary layer feeding the plume (see Figure 12b). The plume parameters are similar to those of model A with $\Delta T_0=700^0$K, $\beta=35$, and a slightly diminished radius, $r_0=60$ km. The total resulting buoyancy flux, 11.0 Mg/sec, accounts for the maximum heat flux for Hawaii if the mantle reference viscosity, η_0, is 10^{22} Pa-sec. The peak velocity in the plume is then 2.3 m/yr.

The long-wavelength dynamic topography ($l=4,8$) for plume model B is about 165 m. The total long-wavelength geoid signature ($l=4,8$) is 10.9 m, and the degree 4 and 8 responses are plotted along with the estimated global response curve in Figure 18. (The $l=4$ and $l=8$ geoid anomalies from the plume calculation are divided by 4 as plotted in Figure 18; in a real Earth the power concentrated at these wavelengths due to the limited radius of the finite element geometry will actually be smeared over an interval of approximately 4 harmonic degrees.) Although we have obtained a geoid amplitude and buoyancy flux compatible with observation, there are three serious problems with this plume model which are very instructive:

(1) The background mantle viscosity of 10^{22} Pa-sec required to keep the buoyancy flux down to a reasonable value is probably too high a viscosity to assign to the *entire* mantle based on post-glacial rebound and rotational data (Peltier, 1981; Yuen et al., 1982). (This viscosity is probably not too high for the lower mantle, and we shall explore this point further in model C.)

(2) The geoid spectrum from model B is much too white (Figure 8). If we sum up contributions for all wavelengths less than 500 km, we get a total geoid signature of 40 m and 2.6 km of dynamic uplift (in addition to the uplift due to lithospheric thinning). Such a model is clearly not acceptable for any hotspot, including Hawaii. Increasing or decreasing the viscosity of the lithosphere in the model does not substantially alter the large dynamic uplift; it is mainly the result of allowing the outlet of a strong narrow plume to be within 200 km of the surface.

(3) Subducted slabs in the upper mantle part of model B will not give a positive geoid signal, even if we assign the same viscosity to a downgoing slab as to the lithosphere (see Appendix B). In order to get positive upper mantle geoid response curves similar to those in model U100 of Figure 8 (required in order to fit the observed geoid anomalies over subduction zones), the viscosity of the asthenospheric channel must be at least a factor of 10,000 smaller than the underlying mantle, which we find implausible.

Problem (1) in model B can be eliminated by decreasing the average viscosity contrast in the plume by simply lowering β or by simultaneously lowering ΔT_0 while increasing r_0 (in order to conserve the total geoid signal). Problems (2) and (3) are more difficult and are addressed in model C.

We have yet to find a model that can explain the apparent geoid signatures of both slabs and plumes. An obvious way to approach this problem is to start with a reference model whose upper mantle responses are neither strongly negative nor positive. Model C (Figure 11) satisfies this criterion by including a high viscosity lithosphere, a low viscosity zone extending to 400 km depth, a moderate viscosity increase through the transition zone, and a higher viscosity lower mantle. We have also included a low viscosity D'' layer in which the viscosity profile is determined by a temperature gradient of 7^0K/km (β=35) in accord with the boundary layer model of Stacey and Loper (1983). This layer does not significantly affect the lower geoid harmonics or mid-mantle buoyancy flux, but it is included for consistency with the idea of plumes originating at the core-mantle boundary. If there are no lateral viscosity variations, the response functions for this model (Figure 19, dotted lines) are small and negative in the lower mantle and are small and positive in the upper mantle.

To obtain the geoid response for model C we have used the same plume parameters as in models A and B for the lower mantle except for the plume radius, r_0, which we have increased to 100 km to compensate for the generally smaller low-degree response functions. In the two low viscosity upper mantle layers the plume must diminish in radius if the plume buoyancy flux is approximately constant throughout the entire mantle (i.e., steady-state). If we assume that the temperature excess at the plume's center is also constant (both the plume and mantle are adiabatic) and that β does not vary with depth, then the plume radius, r_0, must decrease as the fourth root of the layer viscosity as demonstrated above. Therefore, a constant flux plume of 100 km radius in the lower mantle should neck down to $\sim$32 km radius in the upper mantle since $\eta \rightarrow \eta_0/100$. Since the plume buoyancy and geoid signature are

proportional to r_0^2, the upper mantle plume will contribute relatively little to the total long-wavelength geoid signature. Most of the geoid signal will result from the lower mantle plume. The reduction of width as the plume rises will also be enhanced if a large fraction of the plume partially melts and causes a large decrease in the plume viscosity. For a temperature excess of 300–700^{0}K the plume might encounter the solidus as little as $\sim$1000 km above the core-mantle boundary (Anderson, 1981). Plumes in the upper mantle may only be streamers of melt from more substantial solid state plumes in the lower mantle.

The depthwise pseudo response functions for this plume model are shown in Figure 19. The lighter line in the upper mantle emphasizes that even though the normalized response is of the same order for the upper and lower mantle, the upper mantle buoyancy multiplying this response (equation 4) is very small by comparison. Again, the response curves are more negative than for the purely layered case, but when integrated through the lower mantle the resulting geoid spectrum is much stronger at the longer wavelengths (l=4) than at shorter wavelengths (l=12). Note that this would be the case *regardless* of whether or not the low viscosity in the plume affects the response (compare the solid and dotted curves of Figure 19). The plume radius of 100 km for this model results in a geoid signature of similar amplitude to the global response curve as shown in Figure 18. The geoid spectrum is now much more "red" (biased toward long-wavelengths) and is a more satisfactory approximation to the global response spectral shape than any of our previous models. (The total signature for l=4,8 is less than 5 m, so scaling the plume radius up to about r_0=140 km will account for the Hawaiian anomaly.) The short wavelength geoid signature (l >12) is only a few meters, so model C does not suffer the problems of very large geoid

anomalies at shorter wavelengths that we found for model B. The shear stress, τ_{rz}, at the base of the lithosphere drops from about 10 bars at a distance of 200 km from the plume center to only about 1 bar at a distance of 1200 km, so the plume will not drive much plate motion. The shear stress at plume center is over 200 bars and could result in erosion of the lithosphere.

The buoyancy flux for model C (r_0=100 km) is 85 Mg/sec for a lower mantle reference viscosity $\eta_0=10^{22}$Pa-sec, so, unless the average viscosity of the lower mantle is as high as 10^{23} Pa-sec, this model must be considered unacceptable. However, if we use a weaker temperature dependence for effective viscosity (likely due to stress-dependent effects) or a lower excess plume temperature, we can greatly reduce the flow while preserving the geoid signature. For example, a reduced value of β=22 produces essentially the same geoid signature as for β=35 with a buoyancy flux of only 10.5 Mg/sec for $\eta_0=10^{22}$ Pa-sec. Alternatively, for $\Delta T_0=300^0K$ and β=35, essentially the same geoid response may be produced by a plume of radius 200 km in the lower mantle and with a buoyancy flux of only 0.52 Mg/sec. A wide range of plume parameters can, therefore, match the geoid and flux constraints either globally or for the particular case of Hawaii.

Both the low viscosity plume geoid response curves and the purely layered viscosity curves (dotted) in Figure 19 will give the correct long-wavelength spectral characteristics for hotspots. The overall negative response functions (resulting in geoid highs for low density plumes) in the lower mantle overwhelm the upper mantle plume signal because the plume's radius is smaller in the low viscosity upper mantle. This necking down effect may be very important to the dynamics of mantle plumes, especially plumes of lower mantle origin, and appears to be a neglected phenomenon in

both numerical and experimental modelling.

To emphasize the relative importance of vertical stratification of mantle viscosity, we have included two additional models in the spectral response plot of Figure 18. First, model C′ (β=0) is the same as model C, except that there is no viscosity contrast between the plume and surrounding mantle. Its spectrum is somewhat more "red" than for β=35, and, according to the numerical experiments (model A type) discussed above, this purely layered model is probably sufficiently accurate for up to two orders of magnitude viscosity contrast within the plume. However, we can perform this type of calculation (β=0) analytically for *spherical* Earth models including all harmonic degrees. For a 300^{0}K plume of 200 km radius (no viscosity contrast) in the model C type layered mantle, we obtain the response given by dashed lines in Figure 18. This response curve gives a reasonable fit, at least for $l \leq 8$, to the observed global response curve. Clearly, increasing mantle viscosity with depth can result in a strong low-degree bias in the geoid signature of a plume (or any convective upwelling or downwelling), regardless of the viscosity of the plume itself. This is the main point to be gained from our numerical models.

Our geoid models involve the balance between dynamic surface deformation and the (plume) load. Figure 20 shows the actual radial profiles of surface deformation from models B and C. Shown for comparison are Hawaiian swell profiles A-A′ and B-B′ from Figure 9, which cross the island of Hawaii and a point 500 km "downstream," respectively. Figure 20 shows the relative richness in long-wavelength surface deformation in model C compared to model B. Dashed lines also give the deformation with no viscosity contrast in the plumes (β=0). For our "preferred" model C, the predicted long-wavelength deformation outside of the swell is several hundred

meters, which is probably not resolvable from bathymetric anomalies. However, the swell topography itself is not explained by this model. Furthermore, since the ridge-like swell topography extends far toward the WNW from the active hotspot, lithospheric thinning (effectively resetting the thermal age of the lithosphere) is obviously a more satisfactory explanation (Detrick and Crough, 1978). The predicted short-wavelength ($<$500 km wide) deformation from model C of more than 1 km will be reduced by lithospheric flexure and masked to a great extent by the $\sim$8 km seamount topography (volcanic edifice) itself, which does not appear in Figure 20.

We now have an acceptable working model for a plume derived long-wavelength geoid, but the main virtues of model C are that it has a generally negative lower mantle geoid response for $l \leq 8$ and that it involves a substantially reduced upper mantle contribution. We must now determine if this model is compatible with the observed subducted slab geoid response. For a 100 km wide slab with the same viscosity as the lithosphere and extending to 1100 km depth, we get an effect opposite to that found in model A. The response (Figure 19, heavy-dashed line) is now more negative than the purely layered response and produces almost a null geoid signature for slabs at degrees 4 and 8. The slab load is coupled more efficiently to the lithosphere, which results in more surface deformation. This coupling may not occur in the real Earth since the lithosphere at subduction zones is probably weaker than normal (e.g., Sleep, 1979; Hager and O'Connell, 1981). If we simulate the weak plate boundary by reducing the effective viscosity of the lithosphere by two orders of magnitude within 100 km of the subducting slab, the slab is supported more by the high viscosity of the lower mantle. This results in less long-wavelength surface deformation and a much more positive response (Figure 19, heavy, dash-dot line).

Comparing the slab-with-weakened-lithosphere response with either the plume response or the purely layered response, we see that it is possible to have geoid highs over both plumes and slabs. This in itself is not too surprising considering the results of model A. However, the detailed rheology and dynamics of subduction are of even more importance than the influence of low plume viscosity. The "calibration" of the upper mantle geoid response using subducted slabs depends strongly on the parameterization of the lithosphere. Hager's (1984) conclusions that the slab-geoid observations require penetration of the 670 km discontinuity by slabs and require a one to two order of magnitude increase in mantle viscosity through the upper mantle are still valid, but the details of the upper mantle structure are not resolved. In Appendix B we have included a more systematic analysis of models for rheological variations associated with subducting slabs. On the basis of these models we conclude that the lithospheric weakening effect is the most efficient way to make the slab geoid response more positive than for purely layered viscosity. Slab models including nonlinear rheology (not presented here) tend, in general, to drive the slab geoid response more negative due to the homogenizing effect of power law flow on effective mantle viscosities. A more extensive treatment of the large-scale dynamic support of subducting slabs, including such effects as dip angle and non-linear rheology, might yield important new insights, but such a study is beyond the scope of this paper.

In order to obtain average subducted slab velocities of about 100 mm/yr in model C, it is necessary to set the lower mantle reference viscosity η_0 to 10^{22} Pa-sec. This value, which is substantially higher than recent estimates from post-glacial rebound (Peltier, 1981) and rotational data (Yuen and Sabadini, 1982), served as the reference viscosity in our model C plumes. We can think of two resolutions of this

apparent paradox. One is that the rotational response is actually on the high viscosity branch (O'Connell, 1971). The other is that postglacial rebound samples transient rheology while convection responds to steady-state rheology.

Finally, we consider an upper mantle plume for model C, i.e., one that originates above 670 km depth. In order to get the l=4,8 purely layered responses to become negative in the upper mantle, it is necessary to have more than 3 orders of magnitude viscosity contrast in the plume. As before, a plume radius $\geq$70 km is required to produce the observed geoid anomaly over Hawaii. However, we again obtain too much heat flow (even for an *upper* mantle viscosity as high as 10^{21} Pa-sec) just as we did for plume model B. This problem results from the low viscosity of the plume, and this is the main difference between our calculation and Morgan's (1972) estimate of a 75 km radius upper mantle plume. The plume can only overcome the effects of viscosity stratification (required by slabs) by stronger coupling of buoyancy from the lower parts of the plume to the surface through the low viscosity channel. It is very difficult then to produce large positive geoid anomalies over primarily upper mantle plumes without violating reasonable limits on plume heat flow. Since the conditions under which model C can satisfy the slab observations are somewhat extreme (high viscosity slab and very weak lithosphere), this conclusion is difficult to avoid by contrivances in the upper mantle viscosity structure. This is not to say that strictly upper mantle plumes do not exist, but only to imply that they are an unlikely source of long-wavelength geoid highs.

Larger-scale Plumes in the Upper Mantle?

The final issue we address is that of more broad-scale heating associated with hotspots in the upper mantle, or, perhaps, a solitary blob of hot material impinging on the base of the lithosphere. (The correlation of surface wave velocities with the degree 6 geoid and hotspot expansion may be symptomatic of a hotter than average asthenosphere.) In order to fit the observed long-wavelength bias described above, the basic horizontal scalelength of heating surrounding a hotspot must be $>$5000 km. This will lower the average viscosity of the upper mantle on a scale much larger than the depth of the upper mantle, resulting in geoid response curves that are more *positive* , not more negative (see Chapter 3). In other words, coupling of the buoyancy forces to the lithosphere will be weakened by higher temperature and lower than average viscosity, resulting in less surface deformation. Therefore, given the requirement of increasing upper mantle viscosity with depth (based on slab modelling), we cannot explain geoid highs over such broadscale hot blobs in the uppermost mantle. Again, this does not exclude the existence of hotter than average asthenosphere associated with hotspots (which we would expect at the head of any thermal plume), but our models imply a deeper source for the associated geoid anomalies.

In this same vein, it is curious that the strong correlations of the residual geoid with hotspots at degrees 2 and 4 are not accompanied by significant correlations between hotspots and upper mantle seismic velocity variations (Richards and Hager, 1986: Chapter 2). This also suggests a deep source associated with, if not caused by, plumes, and is consistent with the greater sensitivity of the lower geoid harmonics to density heterogeneities at great depth in the mantle. Lastly, we note that the surficial evidence for mantle plumes indicates that they are very narrow, at least in the upper

mantle. The Hawaiian swell is only of order 1000 km in width, and the volcanic shields (islands) form a much narrower track within the swell. An active thermal source at the base of the lithosphere an order of magnitude wider seems unlikely.

Discussion

The geoid models we have presented show that there is no inherent contradiction in having geoid highs produced by both subducted slabs in the upper mantle and mantle-wide plumes. If the thermal buoyancy of the plume directly generates the observed geoid highs, we can offer some restrictions on their characteristics:

(1) Plumes that are of uniform strength in terms of thermal buoyancy (approximately constant in radius), or that are primarily upper mantle phenomena, cannot produce the very long-wavelength bias (degrees 2-6) of the observed geoid. They are also unlikely candidates to produce the more local ($l \geq 4$) geoid highs over hotspots.

(2) Plumes that are of radius ~100-200 km ($\Delta T_0 \approx 200$–700^0K) in the lower mantle, but that become much more confined as they rise due to decreasing mantle viscosity, can produce the low-order geoid (degrees 2-6). However, such plumes must be restricted to about 3 orders of magnitude or less viscosity contrast in order not to exceed maximum estimates for heat flux from the core. Much narrower, low viscosity plumes (e.g., Loper and Stacey, 1983) can also account for the heat flux, but they cannot cause the long-wavelength geoid anomalies.

(3) More local, intermediate wavelength ($l \geq 4$) geoid anomalies associated with hotspots may be caused by either the plume itself or triggered lithospheric delamination due to the plume. Unfortunately, this study has not revealed a method based on geoid models to discriminate between these alternatives. It is remarkable that the

delamination could indeed cause large (>5 m) geoid anomalies, but this process is not able to produce the low-order (l =2–6) observed geoid without producing much more pronounced and consistent local (l >6) anomalies over hotspots. Of particular importance is the temperature of the sublithospheric upper mantle, which would be heated by plumes but cooled by delaminated blobs. (The mantle at lithospheric depths is heated by both processes.) The strong association of hotspots with both low velocity upper mantle (degree 6) and lower mantle (degree 2) as revealed by seismic studies, along with the relatively stationary nature of hotspots with respect to plate motions, implies that they are at least symptomatic of deep thermal processes. None of these observations supports passive lithospheric delamination (e.g., due to cracks) as the primary source of either hotspots or the observed geoid.

The correlation of hotspots with low-order residual geoid highs (Figure 1c) and with seismic velocity anomalies (Figure 4) does not necessarily imply that the thermal anomalies within the plumes associated with hotspots are the primary cause of these phenomena. The considerable effort we have made to explore the conditions for which this is possible should not be taken to imply that we necessarily believe in such a strong role for hotspots. Even our "preferred" model C appears unsatisfactory in some respects. In order to explain the low-degree (2-3) geoid, nearly all 47 of our selected hotspots would have to be associated with very large plumes (e. g., radius=200 km and average temperature contrast 300^0K), and with conspicous "local" ($l \geq 4$) geoid anomalies. Hawaii and a few other major hotspots might fullfill this prescription, but many others would seem unlikely candidates.

Further insight into this question may be gained from consideration of the global hotspot distribution. Hotspots are distributed almost randomly over about half the

Earth's surface (contained by the large residual geoid highs), but are almost absent in the other half of the globe. Stefanic and Jurdy (1984) have claimed less than 1% likelihood that such a broad-scale bimodal pattern is random, and we suspect that the location of hotspots is controlled by some other global thermal pattern in the mantle that limits their surface access to the areas of the large-scale geoid highs. An alternative explanation related to a process of delamination is not evident.

A candidate control mechanism is found by considering the reconstruction of paleo-subduction zones proposed by Chase and Sprowl (1983). If, as they claim, the Pangean supercontinental assemblage was surrounded by subduction zones at ~125 Myr B.P., then the major residual geoid lows (Figure 1c) correspond to areas which have experienced subduction as the American continents have swept westward during the last ~100 Myr. These are also areas largely devoid of hotspots, with some exceptions such as Yellowstone. Intense shearing in the mantle and/or thermal quenching due to deeply subducted material may block or completely shut off mantle plumes. Strong plumes such as Hawaii, Iceland, and Kerguelen have probably been shielded from subduction for 100 Myr or more. Chase and Sprowl also point out that other hotspots such as Mt. Erebus, having only recently escaped a subducting slab, are relatively weak newcomers.

This conceptual model provides an alternative explanation for the correlation of low seismic velocity in the lower mantle with both the largest geoid highs and hotspots. High seismic velocity in the lower mantle may be giving us a broad-scale map of dead slabs that have been deposited in the lower mantle during the last 100-200 Myr, and these positive mass anomalies, combined with negative lower mantle response kernels, would generate geoid lows. Both Figures 8 and 19 show that this

would not be a contradiction of the fact that currently subducting slabs in the upper mantle cause geoid highs. Lower mantle response functions are probably negative even with a low viscosity upper mantle. We can roughly estimate the degree 2 geoid from ancient subducted slabs in the lower mantle as follows:

Subducted slabs currently residing in the upper mantle cause about +20 m of degree 2 geoid for an average upper mantle response of +0.3 (see Figure 8c). For a purely layered C type model we calculate an average lower mantle degree 2 response (using the spherical, analytic model of RH) of about -0.1. If we assume that the ancient subduction zones have put 10 times as much lithosphere into the lower mantle over the past 100 Myr as currently resides in the upper mantle due to recent subduction, then we estimate $\sim$70 m amplitude degree 2 geoid lows associated with these old subduction zones. This is about the right size to explain the current low-degree geoid. Also, dead slabs in the lower mantle will produce a very attenuated signal at higher harmonic degrees, resulting in a geoid spectrum strongly peaked at degree 2. Further reddening of the geoid would result from shearing and diffusing away of short wavelength slab heterogeneities. Since at least 70% of the Earth's heat flow is involved in the cooling of lithospheric plates (O'Connell and Hager, 1980), this explanation is satisfactory in that the largest geoid features are related to the dominant mode of convection. This scenario, with a relatively passive lower mantle, is similar to the recently proposed whole mantle convection model of Loper (1985), although we have been motivated by different observations. The mantle convecting system, dominated by internal heating and driven by subduction of the upper boundary layer (plates), would be semi-transparent to mantle plumes resulting from a relatively small heat flux from the core. Such plumes could, of course, be much smaller in radius

than those required to directly cause the long-wavelength slab residual geoid.

If the Pangean supercontinent was stable for a long period of time, the geoid may have a long-term memory of that episode as proposed by Anderson (1982). A ring of subduction around this supercontinent may also have resulted in antipodal rifting and broad-scale upwelling in the central Pacific which is also "remembered" by a large residual geoid high. Hotspots shielded from subduction beneath the supercontinent would have caused long-term heating beneath the continental lithosphere. This may have eventually led to the breakup of the stable configuration as evidenced by the many hotspots along the mid-Atlantic ridge and the rapidly disintegrating African continent. Thus, the two convecting systems interacted strongly at this point. The chemically buoyant supercontinent may have stabilized a degree 2 convection mode on Earth of which the present geoid is a fossil, and the correlation of hotspots with the low-degree geoid is symptomatic rather than causal.

This hypothesis stands in contrast to the possible dominant role of hotspots on Mars and Venus. The largest gravity and topography anomalies on Mars are due to the Tharsis bulge (Sleep and Phillips, 1985) which contains huge shield volcanoes. On Venus, the large gravity highs over the highland areas are most easily attributed to large mantle plumes in a relatively isoviscous mantle (Kiefer et al., 1986). A central question that remains, in our view, is that of just which density contrasts in the Earth's mantle cause the large-scale shape of both the geoid and the lower mantle velocity variations. We cannot completely resolve this issue on the basis of our study, even though only a restricted class of hotspot models can account for the geoid. However, because not all hotspots are associated with local geoid highs, even our "preferred" plume model is not a very satisfactory explanation for low-degree (2-3)

geoid highs. More broad-scale sources appear to offer a less problematic explanation (Hager et al., 1985). This work might be improved by substituting a variety of convective plume solutions for our generalized plume models. We hope that some of our obvious oversimplifications may spur other workers to predict long-wavelength geoid anomalies from their plume models. Improvement in the resolution of seismic velocity anomalies in the deep mantle can be expected, since this is a relatively recent area of research. A rigorous test of resolving power with respect to thermal plumes might be of great value in understanding the correlations we have noted.

Appendix A: Flow in Cylindrical Geometry

The governing first-order differential equations for incompressible flow at very low Reynold's number include the continuity condition

$$\nabla.\mathbf{v} = 0$$

the equations of motion

$$\nabla.\underline{\tau} + \delta\rho\mathbf{g} = 0$$

and the Newtonian constitutive law

$$\underline{\tau} = -p\,\underline{\mathbf{I}} + 2\eta\underline{\epsilon}$$

where $\mathbf{v}$ is the velocity vector, $\mathbf{g}$ the gravitational acceleration, $\delta\rho$ the density contrast, $\underline{\tau}$ the stress tensor, $\underline{\epsilon}$ the strain rate tensor, η the viscosity, p the pressure, and $\underline{\mathbf{I}}$ the identity matrix. In cylindrical coordinates (r, z) we have

$$\frac{\partial v_z}{\partial z} + \frac{1}{r}\frac{\partial}{\partial r}(r v_r) = 0 \qquad \text{(A1)}$$

$$\frac{\partial \tau_{rr}}{\partial r} + \frac{\partial \tau_{zr}}{\partial z} + \frac{1}{r}(\tau_{rr} - \tau_{\theta\theta}) = 0 \qquad \text{(A2)}$$

$$\frac{\partial \tau_{zr}}{\partial r}+\frac{1}{r}\tau_{zr}+\frac{\partial \tau_{zz}}{\partial z} = -\delta\rho g \tag{A3}$$

$$\tau_{zz} = -p+2\eta\frac{\partial v_z}{\partial z} \tag{A4}$$

$$\tau_{rr} = -p+2\eta\frac{\partial v_r}{\partial r} \tag{A5}$$

$$\tau_{zr} = \eta\left(\frac{\partial v_r}{\partial z}+\frac{\partial v_z}{\partial r}\right) \tag{A6}$$

$$\tau_{\theta\theta} = -p+2\eta\frac{v_r}{r} \tag{A7}$$

We can eliminate the r dependence by an appropriate Fourier-Bessel respresentation. For example, for a finite cylinder of radius a the radial velocity must vanish at a, so we can write the inverse discrete transform

$$v_r(r,z) = \sum_{n=1}^{\infty} v_r^n(z) J_1\left(\frac{p_n' r}{a}\right) = F_1^{-1}[v_r^n]$$

where $[v_r^n]$ is the discrete Fourier-Bessel transform of $v_r(r,z)$ and p_n' is the n^{th} zero of the first-order Bessel function J_1. With some foresight concerning the use of orthonormal expansions, and with F_0 respresenting the zeroth order transform, we also write:

$$v_z = F_0^{-1}[v_z^n]$$

$$\tau_{zz} = F_0^{-1}[\tau_{zz}^n]$$

$$\tau_{rz} = F_1^{-1}[\tau_{rz}^n]$$

$$p = F_0^{-1}[p^n]$$

$$\delta\rho = F_0^{-1}[\delta\rho^n]$$

The stresses $\tau_{\theta\theta}$ and τ_{rr} will turn out to be mixtures of J_0 and J_1, but will be formally eliminated from the equations in a later step.

Some useful orthogonality and completeness properties of Fourier-Bessel transforms are summarized below (see Sneddon, 1951).

Orthogonality:

$$\int_0^a r J_l\left(\frac{p_m r}{a}\right) J_l\left(\frac{p_q r}{a}\right) dr = \begin{bmatrix} \frac{a^2}{a} J_{l+1}^2(p_m),\ m = q \\ 0,\ m \neq q \end{bmatrix}$$

where p_m and p_q can be either the zeros or the zeros of the first derivative of J_l.

Representation (completeness):

$$f(r) = \sum_{m=1}^{\infty} J_l\left(\frac{p_m r}{a}\right) \left[\frac{2}{a^2 J_{l+1}^2(p_m)} \int_0^a f(r) J_l\left(\frac{p_m r}{a}\right) r dr\right.$$

Useful derivatives:

$$\frac{\partial}{\partial r} J_0(kr) = -kJ_1(kr)$$

$$\frac{1}{r}\frac{\partial}{\partial r}\left[rJ_1(kr)\right] = kJ_0(kr)$$

for any real k.

By taking $\int_0^{\infty} rJ_0(kr)$ [eq. (1)] dr and using the expansions for v_z and v_r, we obtain a transformed equation:

$$Dv_z^n + kv_r^n = 0 \qquad \text{(A1')}$$

where $D \equiv \frac{d}{dz}$ and the wavenumber is $k = \frac{p_n'}{a}$. Similarly we obtain for Equations 6

and 3

$$\tau_{zr}^{n} = \eta(Dv_r^{n} - kv_z^{n}) \tag{A6'}$$

$$0 = D\,\tau_{zz}^{n} + k\,\tau_{rz}^{n} - \delta\rho^{n}\,g \tag{A3'}$$

If we use equations 1, 5, 6, and 8 to eliminate $\tau_{rr} - \tau_{\theta\theta}$, $\frac{\partial \tau_{rr}}{\partial r}$, and $\frac{\partial v_z}{\partial z}$ from equation 2, we obtain

$$D\,\tau_{rz}^{n} = k\,\tau_{zz}^{n} + 4\eta k^2 v_r^{n} \tag{A2'}$$

Equations $1'$, $6'$, $3'$, and $2'$ are identical in form to the two-dimensional Cartesian formulation of Cathles (1975) and Hager and O'Connell (1981)

$$D\begin{bmatrix} v_z \\ v_r \\ \tau_{zz} \\ \tau_{zr} \end{bmatrix} = \begin{bmatrix} 0 & -k & 0 & 0 \\ k & 0 & 0 & \frac{1}{\eta} \\ 0 & 0 & 0 & -k \\ 0 & 4\eta k^2 & k & 0 \end{bmatrix} \begin{bmatrix} v_z \\ v_r \\ \tau_{zz} \\ \tau_{zr} \end{bmatrix} + \begin{bmatrix} 0 \\ 0 \\ \delta\rho g \\ 0 \end{bmatrix} \tag{A8}$$

where we have dropped the wavenumber superscript n . This system of equations can be solved analytically for $\mathbf{v}$ and $\underline{\tau}$ via a propagator matrix technique for arbitrary layering of viscosity with depth (z) (see Hager and O'Connell, 1981, for examples).

Thus the depth dependence for cylindrically symmetric flow in layered media can be solved in exactly the same way as for 2-D Cartesian coordinates. For a prescribed cylindrically symmetric loading problem driven by $\delta\rho\left(\frac{p_n'}{a}\right)$ we can write

$$\begin{bmatrix} v_z \\ v_r \\ \tau_{zz} \\ \tau_{zr} \end{bmatrix}_{cylindrical} = \begin{bmatrix} v_z \\ v_x \\ \tau_{zz} \\ \tau_{zx} \end{bmatrix}_{Cartesian}$$

with the Cartesian solution driven by $\delta\rho(k)$, where $k=2\pi/\lambda$ and λ is the spatial wavelength, if

$$k = \frac{p_n{}'}{a}$$

In other words, cylindrical and Cartesian flow are "wavenumber equivalent". Note also that in an effectively infinite domain ($a \rightarrow \infty$) we can use the integral transform

$$v_r(r,z) = \int_0^\infty v_r(z,\alpha) J_1(\alpha r)\alpha d\alpha$$

to again obtain equations 8. In practice, we have used the discrete transform to represent our finite element results in the wavenumber domain.

Appendix B: Slab Geoid Models with Variable Viscosity

We have tested two series of models. The first ("L100") has a 100 km thick high viscosity ($100\eta_0$) lithosphere with a uniform background mantle viscosity (η_0). Geoid anomalies are calculated in a box of width 4000 km (corresponding to $l=5$ with reflection symmetry imposed at the left side boundary). The finite element grid is the same one shown in Figure 10. The 100 km thick slab extends to 1100 km depth (Figure B1) and is assigned a density contrast of 0.1 g/cm ^{3}. (The density contrast actually normalizes out of the response curves.) Pseudo response functions are calculated at four depth intervals ranging from 200 to 1100 km depth (accuracy is not sufficient for loads above 200 km) and are plotted in Figure B2 for the first and second harmonics ($l=5,10$) of the box.

Model L100.u (Figure B2, dotted lines) gives the purely layered response. In model L100.slab (solid lines) the slab is assigned viscosity $100\eta_0$. In models

L100.slab200 and L100.slab400 (long and short dashes) the lithospheric viscosity is lowered to η_0 within 200 km and 400 km, respectively, of the center of the downgoing slab. As shown in Figure B2, the effects of these rheological variations are relatively mild. Stronger coupling of the slab load to the lithosphere through the high viscosity slab causes the responses to become more negative in the deeper part of the slab.

The second series of models ("LU100") is the same as the L100 series except that the background viscosity of the lower mantle (below 670 km) is increased to $100\eta_0$. Figure B3 gives the pseudo response curves for models LU100.u, LU100.slab, LU100.slab200, and LU100.slab400 (dotted, solid, long-dashed, and short dashed lines, respectively). Here the effect of decreased lithospheric strength near the slab is more pronounced. The slab is less strongly coupled to the lithosphere and more strongly coupled to the high viscosity lower mantle. This results in less upper surface deformation and gives a much more positive geoid signature for models LU100.slab200 and LU100.slab400. Again, we cannot resolve the geoid anomalies accurately for loads above 200 km depth. However, our parameterization is probably too coarse to represent the subduction process in this complicated zone even if a finer grid spacing was possible.

References

Allegre, C. J., B. Hamelin, and B. Dupre, 1984, Statistical analysis of isotopic ratios in MORB: the mantle blob cluster model and the convective regime of the mantle, *Earth Planet. Sci. Lett., 71,* 71-84.

Anderson, D. L., 1975, Chemical plumes in the mantle, *Geol. Soc. Am. Bull., 86,* 1592-1600.

Anderson, D. L., 1982, Hotspots, polar wander, Mesozoic convection, and the geoid, *Nature, 297,* 391-393.

Anderson, O. L., 1981, Temperature profiles in the Earth, in R. J. O'Connell and W. S. Fyfe (eds.), *Evolution of the Earth,* Am. Geophys. Union, Washington, D. C., pp. 19-27.

Batiza, R. and D. Vanko, 1984, Petrology of young Pacific seamounts, *J. Geophys. Res., 89,* 11235-11260.

Betz, F. and H. H. Hess, 1942, The floor of the north Pacific ocean, *Geograph. Rev., 32,* 99-116.

Bonatti, E., C. G. A. Harrison, D. E. Fischer, J. Honnorez, J. G. Schilling, J. J. Stipp, and M. Zentelli, 1977, Easter volcanic chain (southeast Pacific): A mantle hot line, *J. Geophys. Res, 82,* 2457-2478.

Boss, A. B. and I. S. Sacks, 1985, Formation and growth of deep mantle plumes, *Geophys. J. Roy. Astron. Soc., 80,* 241-255.

Burke, K. and J. T. Wilson, 1976, Hot spots on the Earth's surface, *Sci. Am., 235,* 46-57.

Cathles, L. M., III, 1975, *The Viscosity of the Earth's Mantle,* Princeton Univ. Press, Princeton, N. J.

Chase, C. G., 1979, Subduction, the geoid, and lower mantle convection, *Nature, 282,* 464-468.

Chase, C. G. and M. K. McNutt, 1982, The geoid: effect of compensated topography and uncompensated oceanic trenches, *Geophys. Res. Lett., 9,* 29-32.

Chase, C. G. and D. R. Sprowl, 1983, The modern geoid and ancient plate boundaries, *Earth Planet. Sci. Lett., 62,* 314-320.

Chase, C. G. and D. R. Sprowl, 1984, Proper motion of hotspots: Pacific plate, *EOS, Trans. AGU, 65,* 1099 (abstract).

Christenson, U., 1984, Convection with pressure and temperature dependent non-Newtonian rheology, *Geophys. J. Roy. Astron. Soc., 77,* 343-384.

Clayton, R. W. and R. P. Comer, 1983, A tomographic analysis of mantle heterogeneities from body wave travel times, *EOS Trans. AGU, 62,* 776 (abstract).

Crough, S. T., 1978, Thermal origin of mid-plate hot-spot swells, *Geophys. J. Roy. Astron. Soc., 55,* 451-469.

Crough, S. T. and D. M Jurdy, 1980, Subducted lithosphere, hotspots, and the geoid, *Earth Planet. Sci. Lett., 48,* 15-22.

Dalrymple, G. B. and D. A. Clague, 1976, Age of the Hawaiian-Emperor bend, *Earth Planet. Sci. Lett., 31,* 313-329.

Detrick, R. S. and S. T. Crough, 1978, Island subsidence, hot spots, and lithospheric thinning, *J. Geophys. Res., 83,* 1236-1244.

Dziewonski, A. M., 1984, Mapping the lower mantle: Determination of lateral heterogeneity in P velocity up to degree and order 6, *J. Geophys. Res., 89,* 5929-5952.

Eckhardt, D. H., 1984, Correlations between global features of terrestrial fields, *Math. Geol., 16,* 155-171.

Engebretson, D. C., A. Cox, and R. G. Gordon, 1984, Relative motions between oceanic plates of the Pacific basin, *J. Geophys. Res., 89,* 10291-10310.

Epp, D., 1984a, Implications of volcano and swell heights for thinning of the lithosphere by hotspots, *J. Geophys. Res., 89,* 9991-9996.

Epp, D., 1984b, Possible perturbations to hotspot traces and implications for the origin and structure of the Line islands, *J. Geophys. Res., 89,* 11273-11286.

Gubbins, D., T. G. Masters, and J. A. Jacobs, 1979, Thermal evolution of the Earth's core, *Geophys. J. Roy. Astron. Soc., 59,* 57-99.

Hadley, D. M., G. S. Stewart, and J. E. Ebel, 1976, Yellowstone: Seismic evidence for a chemical plume, *Science, 193,* 1237-1239.

Hager, B. H., 1983, Global isostatic geoid anomalies for plate and boundary layer models of the lithosphere, *Earth Planet. Sci. Lett., 63,* 97-109.

Hager, B. H., 1984, Subducted slabs and the geoid: Constraints on mantle rheology and flow, *J. Geophys. Res., 89,* 6003-6015.

Hager, B. H., R. W. Clayton, M. A. Richards, R. P. Comer, and A. M. Dziewonski, 1985, Lower mantle heterogeneity, dynamic topography, and the geoid, *Nature, 313,* 541-545.

Hager, B. H. and R. J. O'Connell, 1979, Kinemetic models of large-scale mantle flow, *J. Geophys. Res., 84* , 1031-1048.

Hager, B. H. and R. J. O'Connell, 1981, A simple global model of plate dynamics and mantle convection, *J. Geophys. Res., 86* , 4843-4867.

Hong, H. J. and D. A. Yuen, 1985, Dynamical consequences on surface deformations and geoids from equation of state, *EOS, Trans. AGU, 66,* 1075 (abstract).

Iyer, H. M., 1975, Anomalous delays of teleseismic P waves in Yellowstone National Park, *Nature, 253,* 425-428.

Jarrard, R. D. and D. A. Clague, 1977, Implications of Pacific island and seamount ages for the origin of volcanic chains, *Rev. Geophys. Space Phys., 15,* 57-76.

Kaula, W. M., 1963, Tesseral harmonics of the gravitational field and geodetic datum shifts derived from camera observations of satellites, *J. Geophys. Res., 68,* 473-484..

Kaula, W. M., 1970, Earth's gravity field: Relation to global tectonics, *Science, 167,* 977-985.

Kiefer, W. S., M. A. Richards, B. H. Hager, and B. G. Bills, 1986, A dynamic model of Venus' gravity field, *Geophys. Res. Lett.,* in press.

Lerch, F. J., S. M. Klosko, and G. B. Patch, 1983, A refined gravity model from LAGEOS (GEM-L2), *NASA Tech. Memo. 84986.*

Loper, D. E., 1985, A simple model of whole-mantle convection, *J. Geophys. Res., 90,* 1809-1836.

Loper, D. E. and F. D. Stacey, 1983, The dynamical and thermal structure of deep mantle plumes, *Phys. Earth Planet. Int., 33,* 304-317.

Masters, G. T. H. Jordan, P. G. Silver, and F. Gilbert, 1982, Aspherical Earth structure from fundamental spheroidal-mode data, *Nature, 298,* 609-613.

McKenzie, D. P., 1977, Surface deformation, gravity anomalies and convection, *Geophys. J. Roy. Astron. Soc., 48,* 211-238.

McKenzie, D. P. and C. Bowin, 1976, The relationship between bathymetry and gravity in the Atlantic ocean, *J. Geophys. Res., 81,* 1903-1915.

McNutt, M. K., 1984, Lithospheric flexure and thermal anomalies, *J. Geophys. Res., 89,* 11180-11194.

Morgan, W. J., 1965, Gravity anomalies and convection currents. I. A sphere and cylinder sinking beneath the surface of a viscous fluid, *J. Geophys. Res., 70,* 6175-6187.

Morgan, W. J., 1972, Plate motions and deep mantle convection, *Geol. Soc. Am. Mem., 132,* 7-22.

Morgan, W. J., 1981, Hot spot tracks and the opening of the Atlantic and Indian oceans, in *The Sea, 7,* C. Emiliani (ed.), Wiley Interscience, NY, pp. 443-487.

Nakiboglu, S. M., 1982, Hydrostatic theory of the Earth and its mechanical implications, *Phys. Earth Planet. Int., 28,* 302-311.

Nataf, H.-C., I. Nakanishi, and D. L. Anderson, 1984, Anisotropy and shear-velocity heterogeneities in the upper mantle, *Geophys. Res. Lett., 11,* 1109-1112.

Nataf, H.-C., I. Nakanishi, and D. L. Anderson, 1986, Measurements of mantle wave velocities and inversion for lateral heterogeneities and anisotropy. Part III: Inversion, *J. Geophys. Res.,* in press.

O'Connell, R. J., 1971, Pleistocene glaciation and the viscosity of the lower mantle, *Geophys. J. Roy. Astron. Soc., 23,* 299-327.

O'Connell, R. J. and B. H. Hager, 1980, On the thermal state of the Earth, in *Physics of the Earth's Interior,* A. Dziewonski and E. Boschi (eds.), North-Holland, Amsterdam, pp. 270-317.

Olson, P. and H. Singer, 1985, Creeping plumes, *J. Fluid Mech., 158,* 511-531.

Parmentier, E. M., D. L. Turcotte, and K. E. Torrance, 1975, Numerical experiments on the structure of mantle plumes, *J. Geophys. Res., 80,* 4417-4424.

Parsons, B. and S. Daly, 1983, The relationship between surface topography, gravity anomalies and the temperature structure of convection, *J. Geophys. Res., 88,* 1129-1144.

Pekeris, C. L., 1935, Thermal convection in the interior of the Earth, *Mon. Not. Roy. Astron. Soc., Geophys. Suppl., 3,* 343-367.

Peltier, W. R., 1981, Ice age geodynamics, *Ann. Rev. Earth Planet. Sci., 9,* 199-225.

Pilger, R. H., 1982, The origin of hotspot traces: Evidence from eastern Australia, *J. Geophys. Res., 87,* 1825-1834.

Ricard, Y., L. Fleitout, and C. Froidevaux, 1984, Geoid heights and lithospheric stresses for a dynamical Earth, *Annales Geophysicae, 2,* 267-286.

Richards, M. A. and B. H. Hager, 1984, Geoid anomalies in a dynamic Earth, *J. Geophys. Res., 89,* 5487-6002.

Richards, M. A. and B. H. Hager, 1986, The Earth's geoid and the large-scale structure of mantle convection, *Proc. NATO Adv. Study Inst.,* S. K. Runcorn (editor), in press.

Richter, F. M. and D. P. McKenzie, 1981, On some consequences and possible causes of layered convection, *J. Geophys. Res., 86,* 6133-6142.

Runcorn, S. K., 1964, Satellite gravity measurements and a laminar viscous flow model of the Earth's mantle, *J. Geophys. Res., 69,* 4389-4394.

Schlanger, S. O., M. O. Garcia, B. H. Keating, J. J. Naughton, W. W. Sager, J. A. Haggerty, J. A. Philpotts, and R. A. Duncan, 1984, Geology and geochronology of the Line islands, *J. Geophys. Res., 89,* 11261-11272.

Schroeder, W., 1984, The empirical age-depth relation and depth anomalies in the Pacific ocean basin, *J. Geophys. Res., 89,* 9873-9883.

Sleep, N. H., 1974, Segregation of magma from a mostly crystalline mush, *Geol. Soc. Am. Bull., 85,* 1225-1232.

Sleep, N. H., 1979, The double seismic zone in downgoing slabs and the viscosity of the mesosphere, *J. Geophys. Res., 84,* 4565-4571.

Sleep, N. H., 1984a, Tapping of magmas from ubiquitous mantle heterogeneities:

An alternative to mantle plumes? *J. Geophys. Res., 89,* 10029-10041.

Sleep, N. H., 1984b, Lithospheric delamination beneath Hawaii: No plume, *EOS, Trans. AGU, 65,* 1087 (abstract).

Sleep, N. H. and R. J. Phillips, 1985, Gravity and lithospheric stress on the terrestrial planets with reference to the Tharsis region of Mars, *J. Geophys. Res., 90,* 4469-4489.

Solomon, S. C. and N. H. Sleep, 1974, Some models for absolute plate motions, *J. Geophys. Res., 79,* 2537-2567.

Sneddon, I. N., 1951, *Fourier Transforms,* McGraw-Hill, New York.

Stacey, F. D. and D. E. Loper, 1983, The thermal boundary-layer interpretation of D′′ and its role as a plume source, *Phys. Earth Planet. Int., 33,* 45-55.

Stefanic, M. and D. M. Jurdy, 1984, The distribution of hot spots, *J. Geophys. Res., 89,* 9919-9925.

Tanimoto, T., 1986, The Gilbert-Backus approach to the three-dimensional structure in the upper mantle. II. SH and SV velocity, *Geophys. J. Roy. Astron. Soc.,* in press.

Turcotte, D. L. and E. R. Oxburgh, 1973, Mid-plate tectonics, *Nature, 244,* 337-339.

Turcotte, D. L. and E. R. Oxburgh, 1976, Stress accumulation in the lithosphere, *Tectonophysics, 35,* 183-199.

Verhoogen, J. 1973, Thermal regime of the Earth's core, *Phys. Earth Planet. Int., 7,* 47-58.

Von Herzen, R. P., R. S. Detrick, S. T. Crough, D. Epp, and V. Fehn, 1982, Thermal origin of the Hawaiian swell: Heat flow evidence and thermal models, *J. Geophys. Res., 87,* 6711-6723.

Watts, A. B., 1978, An analysis of isostasy in the world's oceans. I. Hawaiian-Emperor seamount chain, *J. Geophys. Res., 83,* 5989-6004.

Wilson, J. T., 1963, A possible origin of the Hawaiian Islands, *Can. J. Phys., 41,* 863-870.

Woodhouse, J. H. and A. M. Dziewonski, 1984, Mapping the upper mantle: three dimensional modelling of Earth structure by inversion of seismic waveforms, *J. Geophys. Res., 89,* 5953-5986.

Yuen, D. A. and W. R. Peltier, 1980, Mantle plumes and the thermal stability of

the D′′ layer, *Geophys. Res. Lett., 9,* 625-628.

Yuen, D. R., Sabadini, R., and E. V. Boschi, 1982, Viscosity of the lower mantle as inferred from rotational data, *J. Geophys. Res., 87,* 10745-10762.

Yuen, D. A. and G. Schubert, 1976, Mantle plumes: A boundary layer approach for Newtonian and non-Newtonian temperature-dependent rheologies, *J. Geophys. Res., 81,* 2499-2510.

Table 1 - Hotspot locations used to obtain the spherical harmonic expansion of the hotspot distribution.

TABLE I: Hotspot Locations

Lat.	Long.	Name
50	7	Eifel, Belgium
23	6	Hoggar Mountains, Algeria
21	17	Tibesti, Chad
13	24	Jebel Marra, Sudan / Darfur
4	9	Mt. Cameroon
-3	36	Lake Victoria / East Africa
12	42	Afar / Ethiopia
-12	44	Comores Islands
-21	56	Reunion
-45	45	Crozet
-45	65	Kerguelen
-35	80	Christmas Island, Indian Ocean / Amsterdam
-40	150	Tasmania
45	-111	Yellowstone
37	-104	Raton, New Mexico
27	-113	Baja California / Guadalupe Seamount
53	-135	Bowie Seamount / Kodiak Seamounts
46	-128	Juan de Fuca / Cobb Seamount
20	-155	Hawaii
-29	-140	MacDonald Seamount / Cook--Austral Islands
-18	-148	Mehetia / Society Islands / Tahiti
-27	-129	Pitcairn Island / Gambier Islands
3	167	Caroline Islands
-11	-139	Marquesas Islands
-27	-109	Easter Island
0	-91	Galapagos Islands
-27	-80	San Felix, Nazca Plate
-34	-79	Juan Fernandez, Nazca Plate
72	-8	Jan Mayen
64	-20	Iceland
30	-60	Bermuda
38	-28	Azores
33	-17	Madeira
28	-17	Canary Islands
29	-29	New England Seamounts / Great Meteor Seamount
15	-24	Cape Verde
-4	-32	Fernando
-17	-25	Arnold Seamount
-21	-29	Trindade
-8	-14	Ascension
-16	-6	St. Helena
-37	-12	Tristan de Cunha
-42	0	Discovery Seamount
-54	4	Bouvet
-32	16	Vema Seamount
-78	167	Mt. Erebus
-15	-168	Samoa

Table 2 - Correlation coefficients at harmonic degree 6 between upper mantle shear velocity models (Tanimoto, 1986; Woodhouse and Dziewonski, 1984) and the observed geoid, the slab residual geoid, and the hotspot distribution.

TABLE II: Degree 6 Correlations (confidence)

	Upper Mantle Velocity Model		
	Tan(350km)	Tan(250km)	W&D(200-500km)
Geoid	-.63 (98%)	-.67 (99%)	-.58 (95%)
Residual Geoid	-.72 (99%)	-.74 (99%)	-.65 (99%)
Hotspots	-.54 (95%)	-.49 (90%)	-.70 (99%)

Figure 1 - (a),(b) Observed long-wavelength geoid (Lerch et al., 1983) referred to the hydrostatic figure of the Earth (Nakiboglu, 1982). In (b) the degree 2-3 components have been removed. Hotspot locations are indicated by black dots. Continents are outlined and plate boundaries are also shown. Geoid lows are shaded; cylindrical equidistant projection.

(c),(d) Residual geoid after the subducted slab geoid model of Hager (1984) is removed.

Observed Geoid: degree 2-10

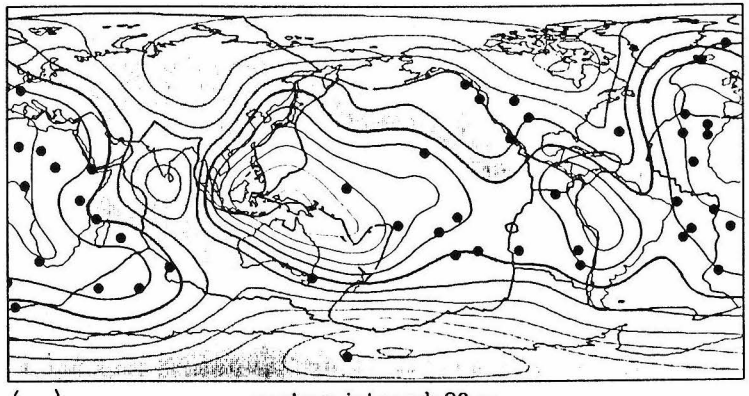

(a) contour interval: 20 m

Residual Geoid: degree 2-10

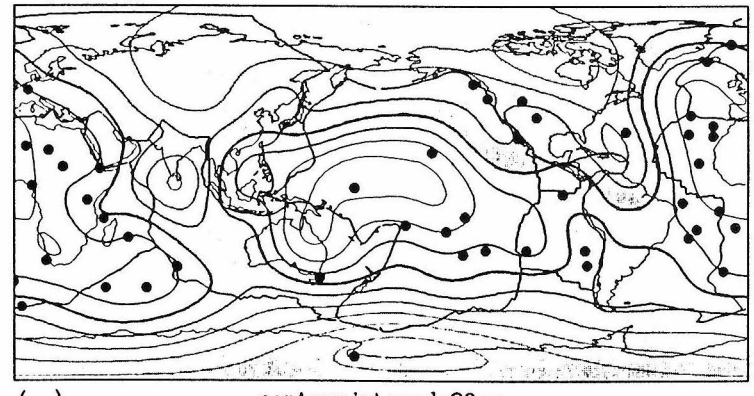

(c) contour interval: 20 m

Observed Geoid: degree 4-10

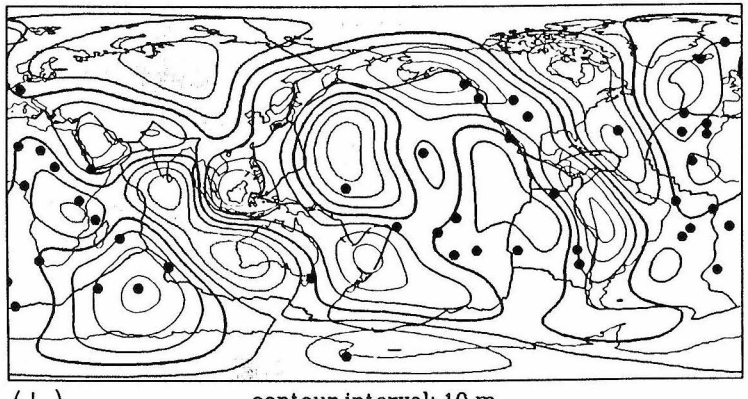

(b) contour interval: 10 m

Residual Geoid: degree 4-10

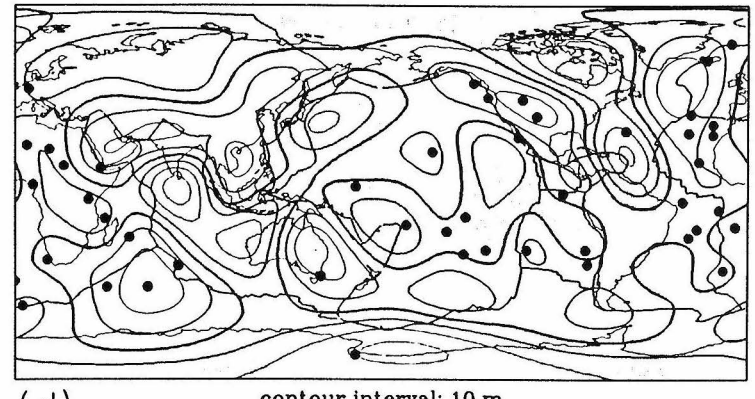

(d) contour interval: 10 m

Figure 2 - Log-log comparison of root mean square harmonic coefficient amplitudes. Units are as follows: Observed and residual geopotentials, $\gamma M/R$ (fraction of geopotential at surface); Hotspot distribution, $4.1x\,10^6$ hotspots per Earth area; Lower mantle P-velocity (Clayton and Comer, 1983), 10^4 km/sec; Geopotentials, in units $\gamma M/R$, may be converted to geoid elevations by dividing by the gravitational acceleration at the surface or by multiplying by R. (γ is the gravitational constant, M the mass of the Earth, and R the Earth's radius.)

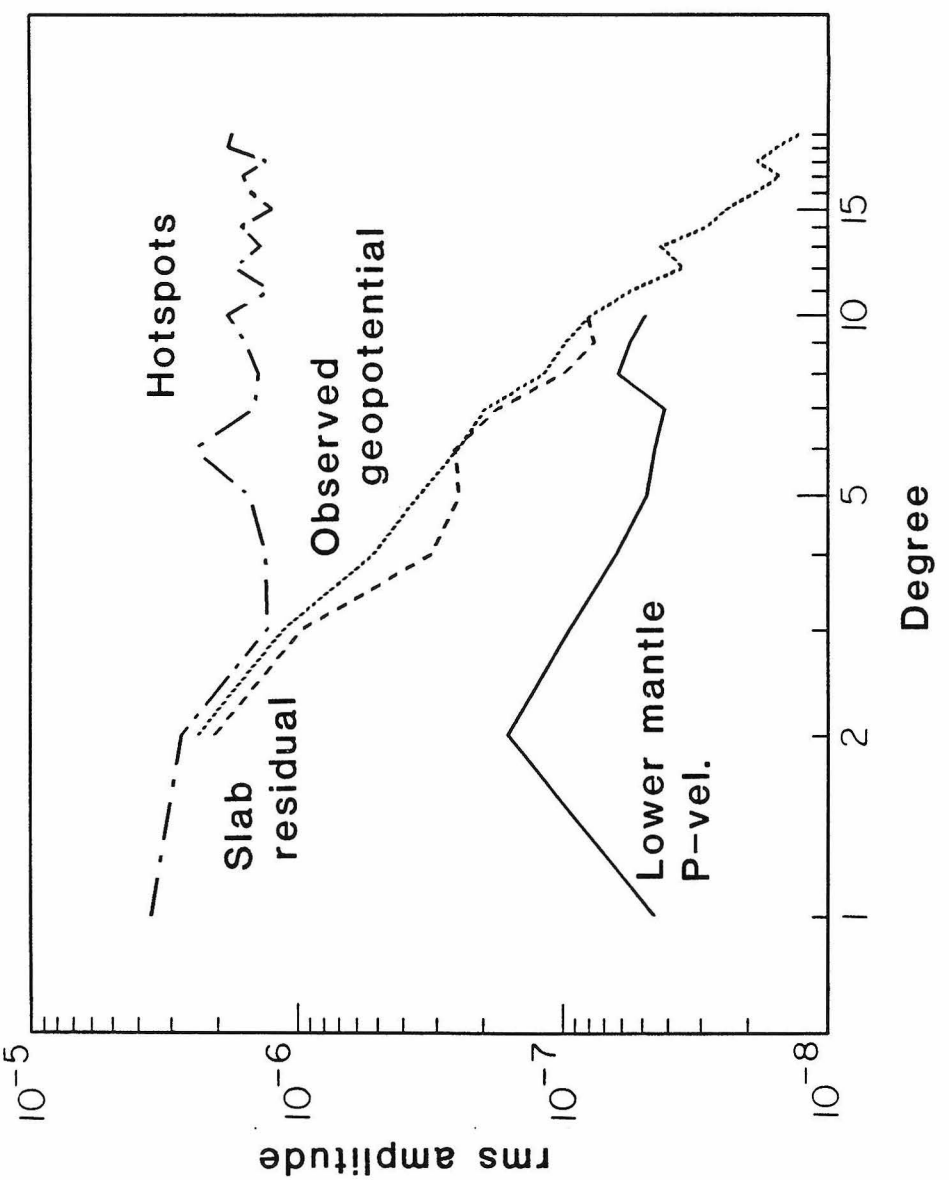
Hotspots
Observed geopotential
Slab residual
Lower mantle P-vel.
rms amplitude
10^{-5}
10^{-6}
10^{-7}
10^{-8}
1
2
5
10
15
Degree

Figure 3 - Degree-by-degree correlations, r_l, between the hotspot distribution and the slab residual geoid (solid line). Correlations between the slab geoid model (Hager, 1984) and the observed geoid are shown for comparison (dashed line). Contours give the confidence of correlation, with a confidence level of 0.98 indicating only a 2% chance that the correlation is random.

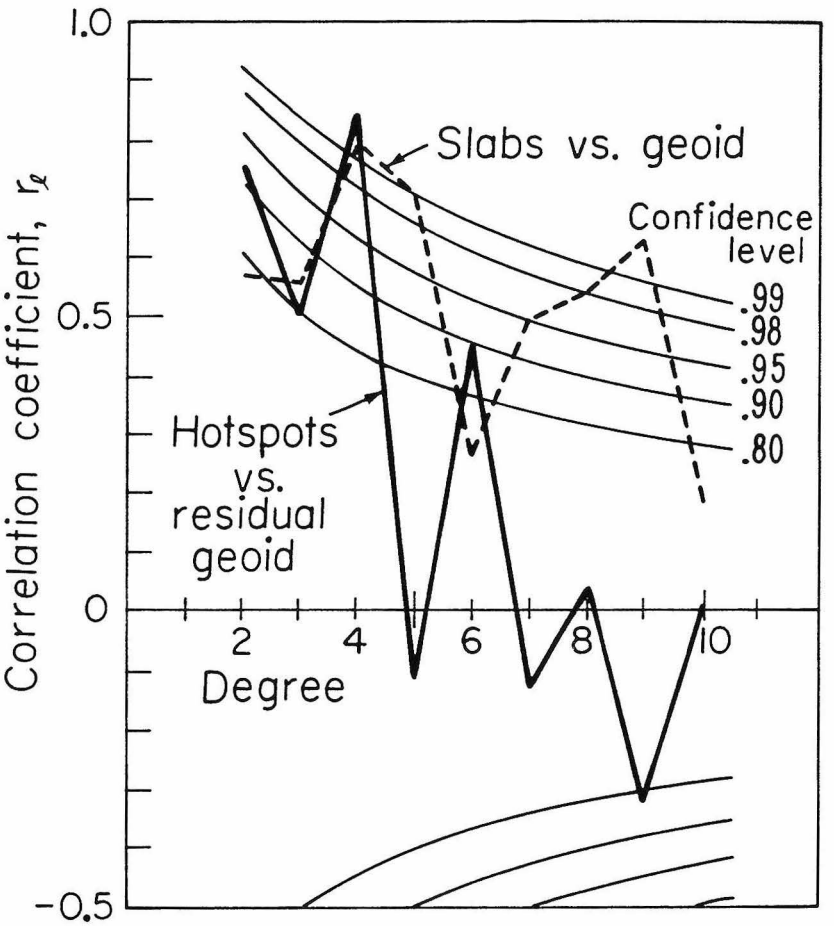
1.0
0.5
0
-0.5
Correlation coefficient, r_ℓ
Slabs vs. geoid
Confidence level
.99
.98
.95
.90
.80
Hotspots vs. residual geoid
2
4
6
8
10
Degree

Figure 4 - Degree 2 comparison of the slab residual geoid, the vertically averaged lower mantle P-wave velocity model (Clayton and Comer, 1983), and the hotspot density distribution. Geoid lows, slow velocity anomalies, and low hotspot density areas are shaded. Hotspot density contour intervals are in units of 16.5 hotspots per Earth area.

Residual Geoid: degree 2

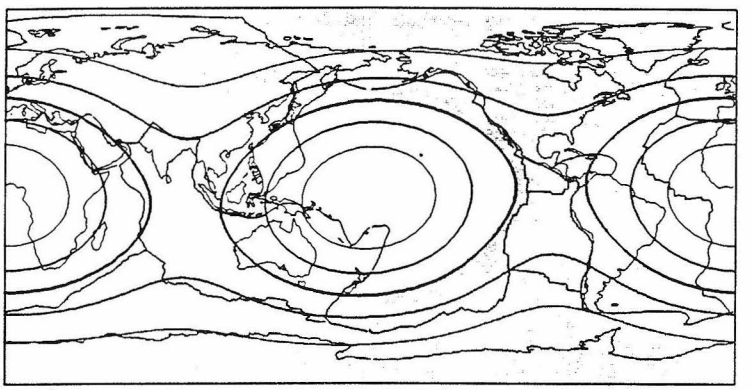

(a) contour interval: 20 m

Lower Mantle P-Wave Velocity: degree 2

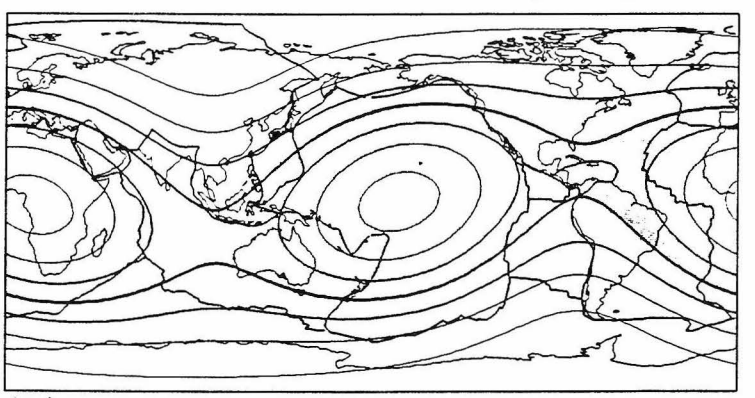

(b) contour interval: 2 m/sec

Hotspot Density: degree 2

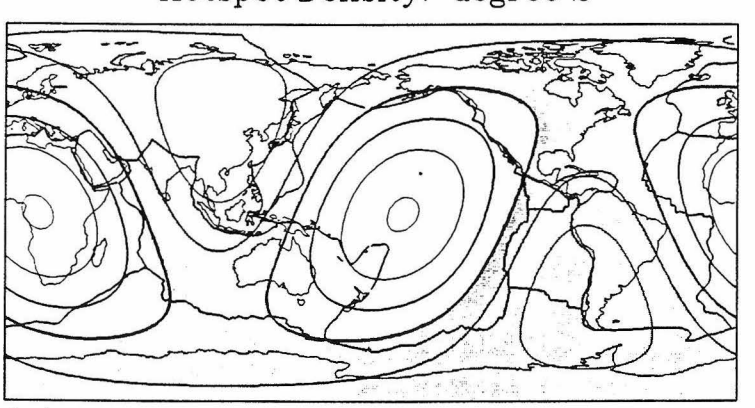

(c)

Figure 5 - Degree 6 comparison of the slab residual geoid, upper mantle shear velocity (200-500 km: Woodhouse and Dziewonski, 1984), and the hotspot density distribution. Geoid lows, slow velocity anomalies, and low hotspot density areas are shaded. Hotspot density contour intervals are in units of 33 hotspots per Earth area.

Residual Geoid: degree 6

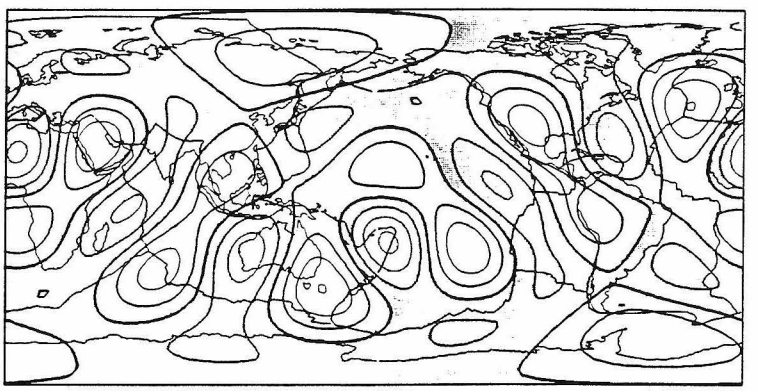

(a) contour interval: 5 m

Upper Mantle Shear Velocity: degree 6

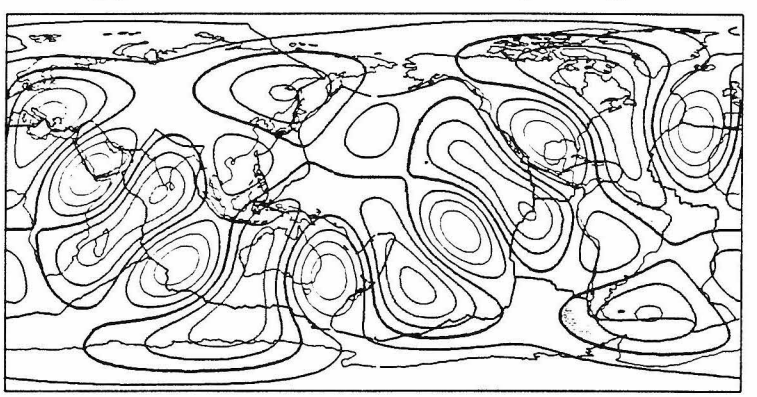

(b) contour interval: 10 m/sec

Hotspot Density: degree 6

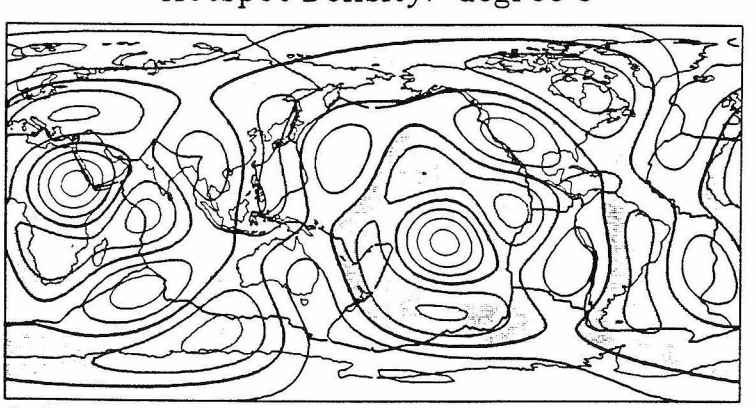

(c)

Figure 6 - Best-fitting hotspot/geoid response curve (solid dots) according to equation 3 of text. Error bars (2σ) indicate the uncertainty of fit. Open circles give best-fitting curve under the assumption of equal noise in both the slab residual geoid and the hotspot distribution (error bars not shown).

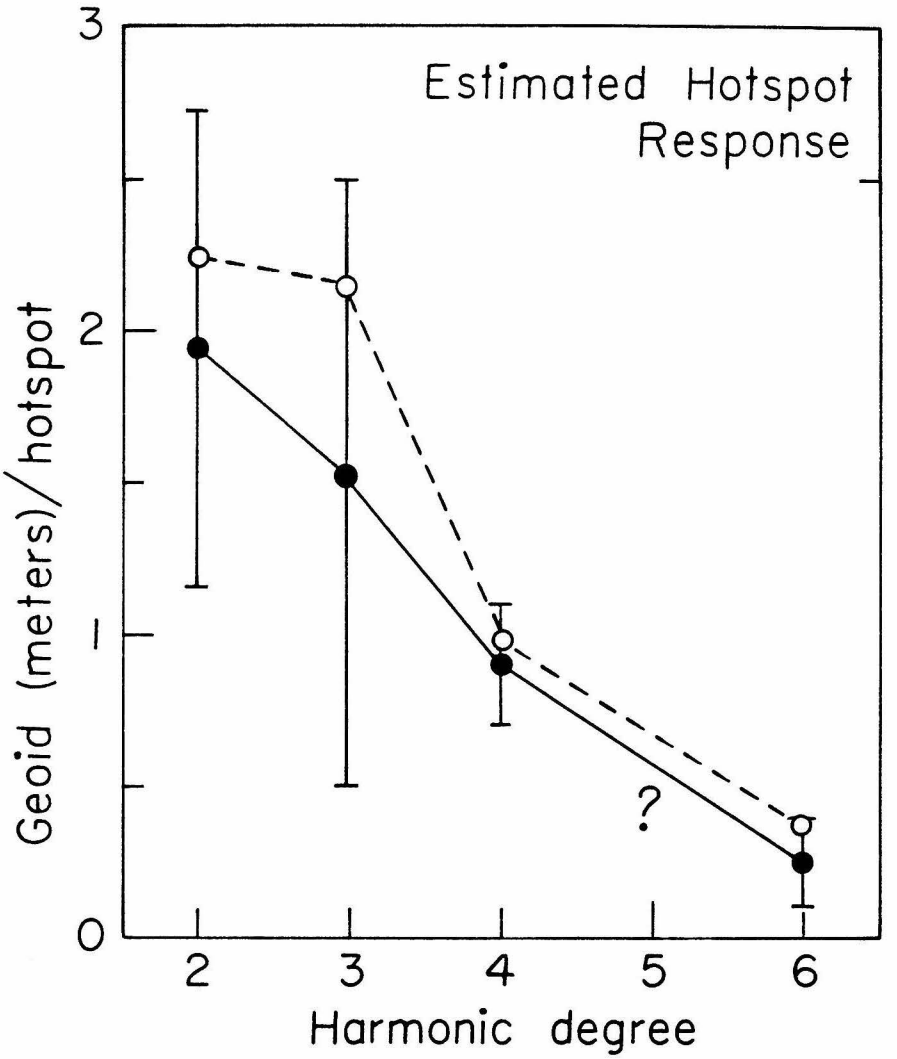
Estimated Hotspot
Response
Geoid (meters)/ hotspot
3
2
1
0
2
3
4
5
6
Harmonic degree
?

Figure 7 - Slab residual geoid in harmonic degree bands 4-6, 7-12, and 10-20. Hotspot locations are shown by black dots.

Residual Geoid: degree 4-6

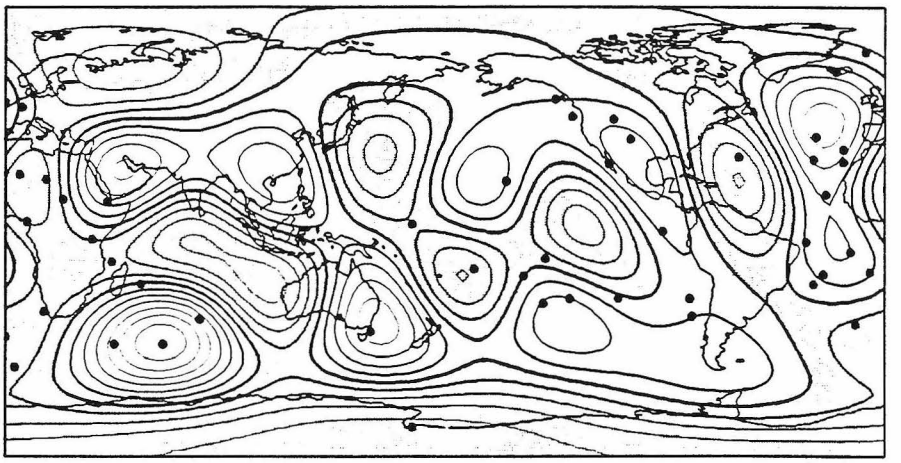

contour interval: 5 m (a)

Residual Geoid: degree 7-12

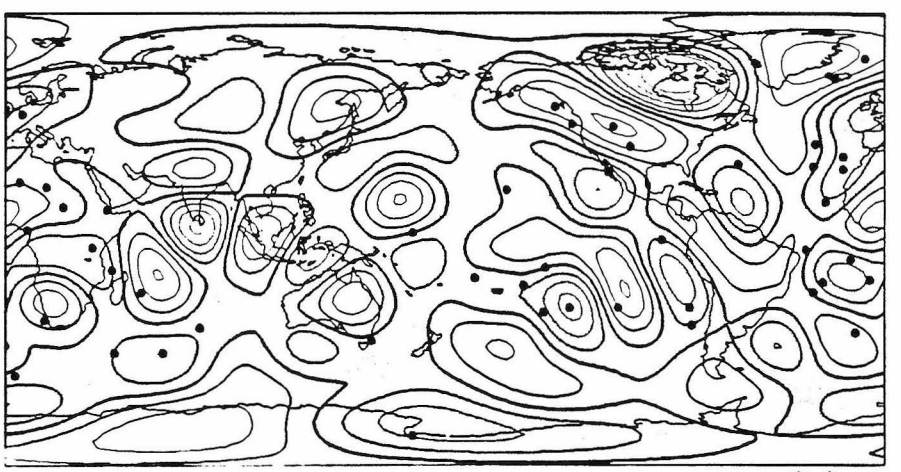

contour interval: 5 m (b)

Residual Geoid: degree 10-20

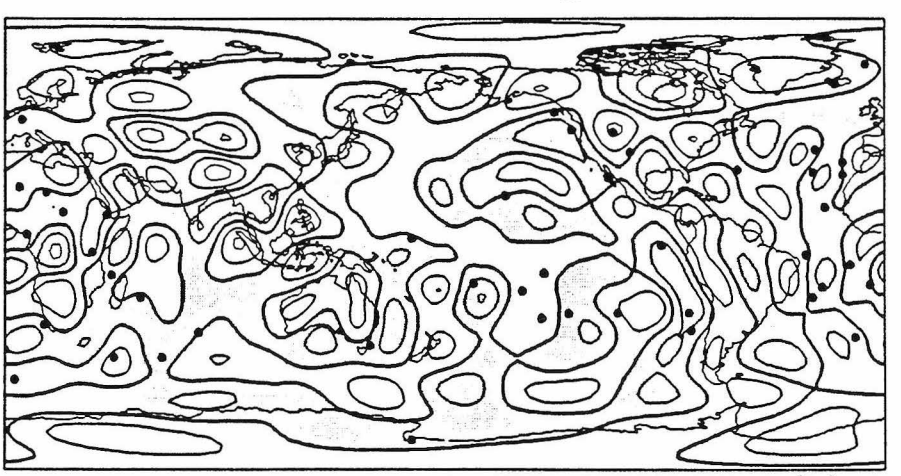

contour interval: 5 m (c)

Figure 8 - Dynamic response function, $G_l(r)$, for surface density contrasts of spherical harmonic degrees 2, 4, 6, and 8 plotted against radius, r, for six Earth models. Models U, left, permit mantle-wide flow; models C, right, have a (chemical) barrier at 670 km depth, causing stratification into separate upper and lower mantle flow systems. Models U1 and C1 have uniform viscosity; models U10 and C10 have a factor of 10 viscosity increase below 670 km; models U100 and C100 have a factor of 100 increase. The geoid responses are normalized to the geoid which would be obtained if the harmonic density contrasts were placed at the top surface with no dynamic compensation allowed.

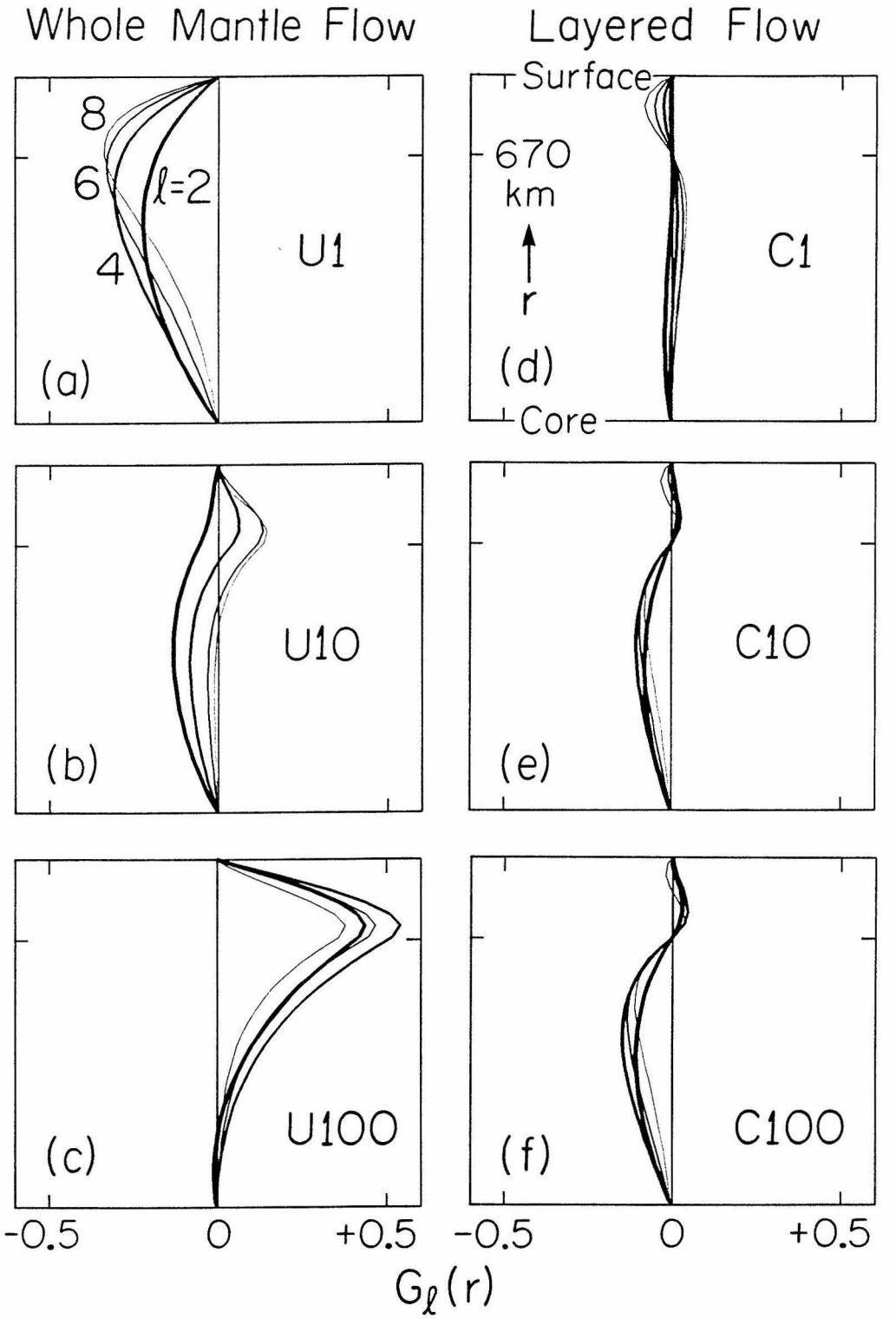
Whole Mantle Flow
Layered Flow
Surface
670
km
r
Core
8
6
4
ℓ=2
U1
C1
(a)
(d)
U10
C10
(b)
(e)
U100
C100
(c)
(f)
-0.5
0
+0.5
-0.5
0
+0.5
$G_\ell(r)$

Figure 9 - Residual depth anomaly map of the Hawaiian swell (adapted from Schroeder, 1984). Latitudes and longitudes are indicated, respectively, along the vertical and horizontal borders. Flow stagnation contours for 300^0K and 1000^0K kinematic plume models are shown by bold lines.

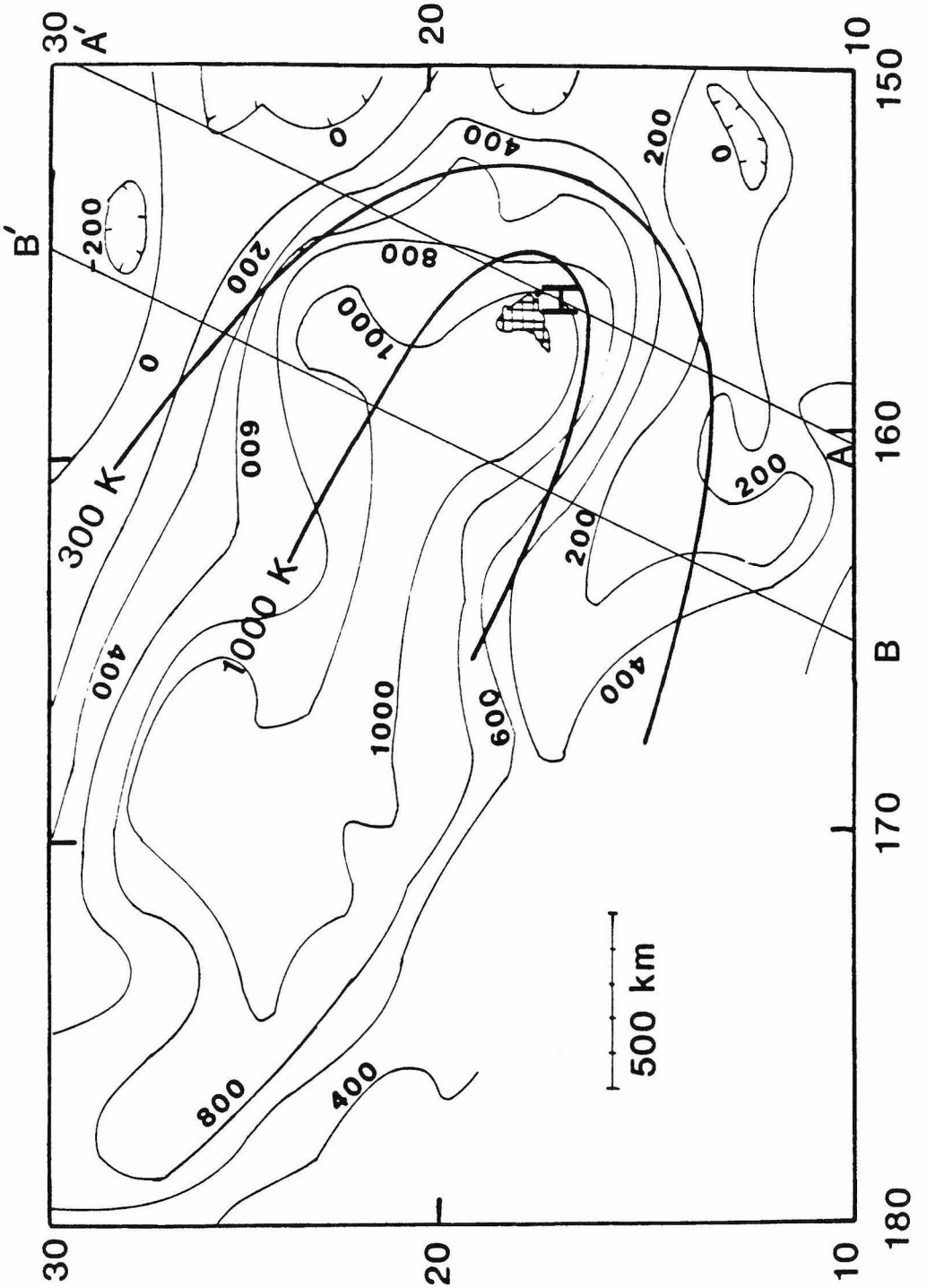
30
A'
20
10
150
B'
-200
0
200
400
600
800
1000
300 K
1000 K
H
A
B
160
170
180
500 km

Figure 10 - Example finite element grid used in plume and slab models.

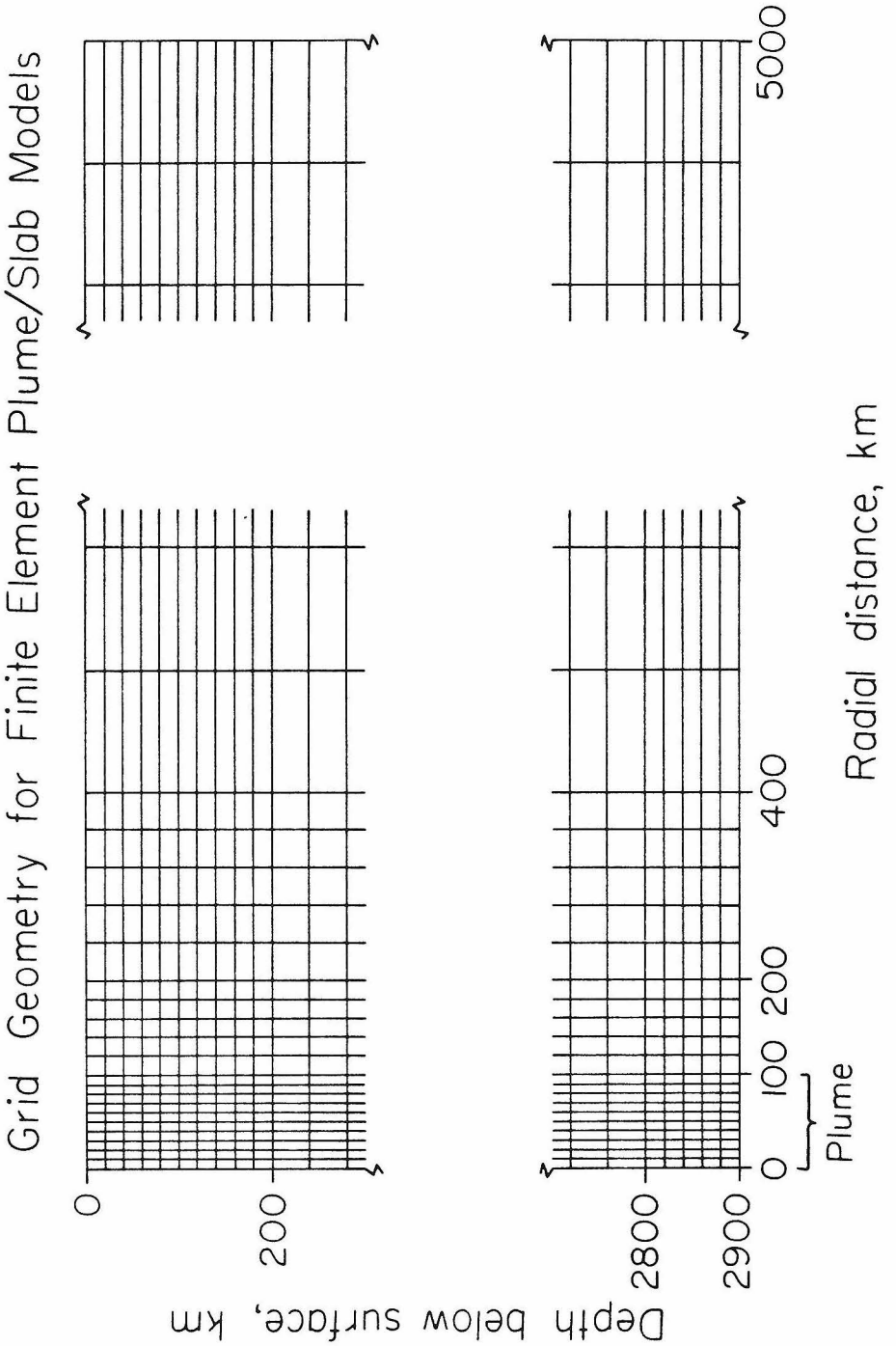
Grid Geometry for Finite Element Plume/Slab Models
Depth below surface, km
0
200
2800
2900
0
100
200
400
5000
Plume
Radial distance, km

Figure 11 - Pseudo geoid response functions (see text) for the first three harmonics (wavelengths corresponding to degrees 4,8,12) of the cylinder (or box) for the finite element model A plume (solid line) and the high viscosity slab (dashed line). The dotted line gives the analytical solution for uniform mantle viscosity.

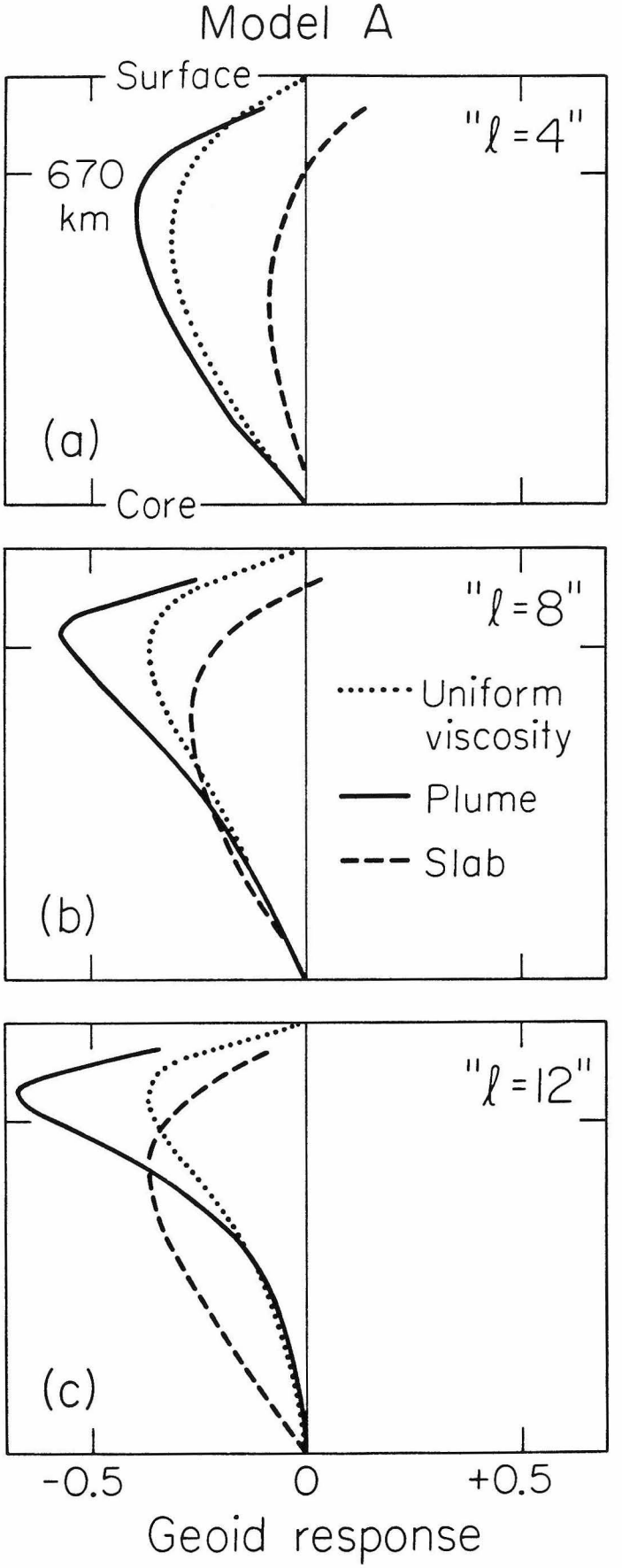
Model A
Surface
670 km
Core
"ℓ=4"
(a)
"ℓ=8"
Uniform viscosity
Plume
Slab
(b)
"ℓ=12"
(c)
-0.5
0
+0.5
Geoid response

Figure 12 - Illustration of the A, B, and C plume models. Horizontal and vertical scales are equal. η_0 is the reference viscosity.

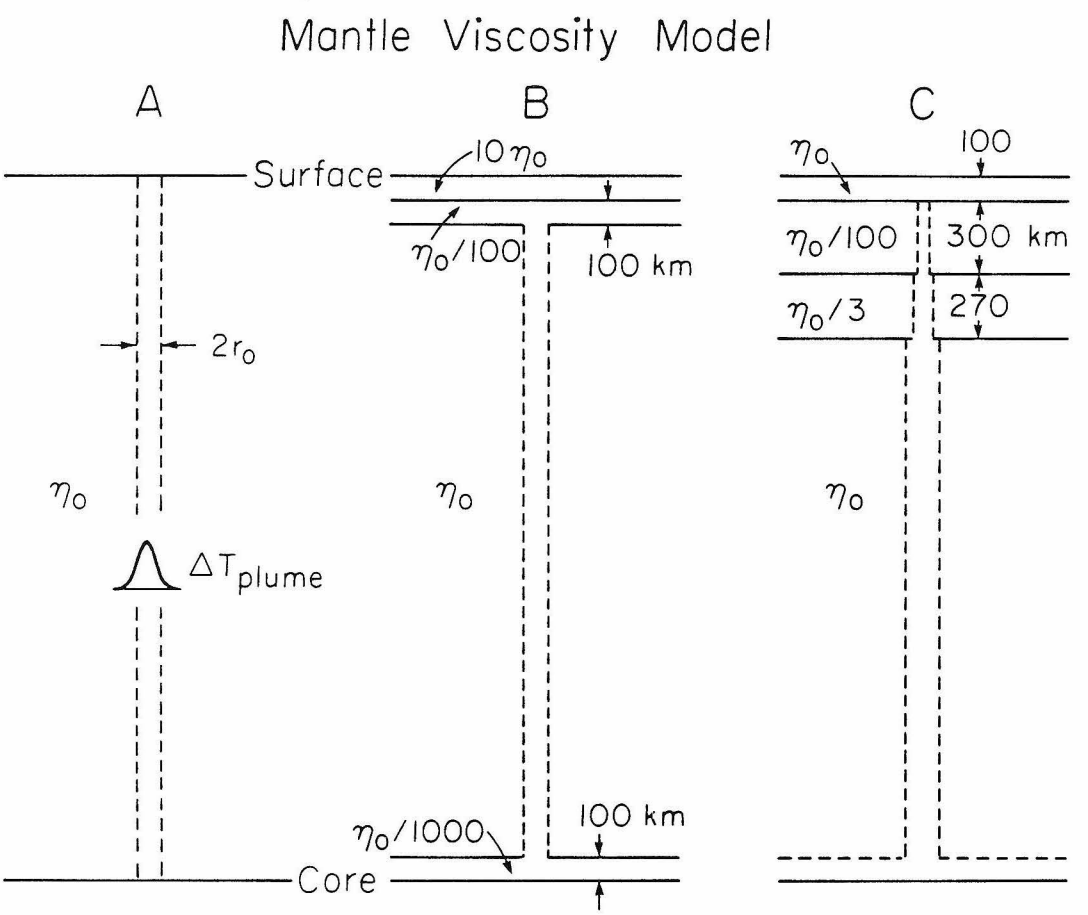
Mantle Viscosity Model
A
B
C
Surface
$10\eta_o$
$\eta_o/100$
100 km
$2r_o$
η_o
ΔT_{plume}
$\eta_o/1000$
100 km
Core
η_o
100
$\eta_o/100$
300 km
$\eta_o/3$
270
η_o

Figure 13 - Geoid signal perturbation (excess), relative to the isoviscous geoid, for the range of excess plume temperatures and viscosity exponents, β, tested at plume radius r_0=70 km. The l=4, 8, and 12 curves are for the first three harmonics of the cylinder for halo model A.

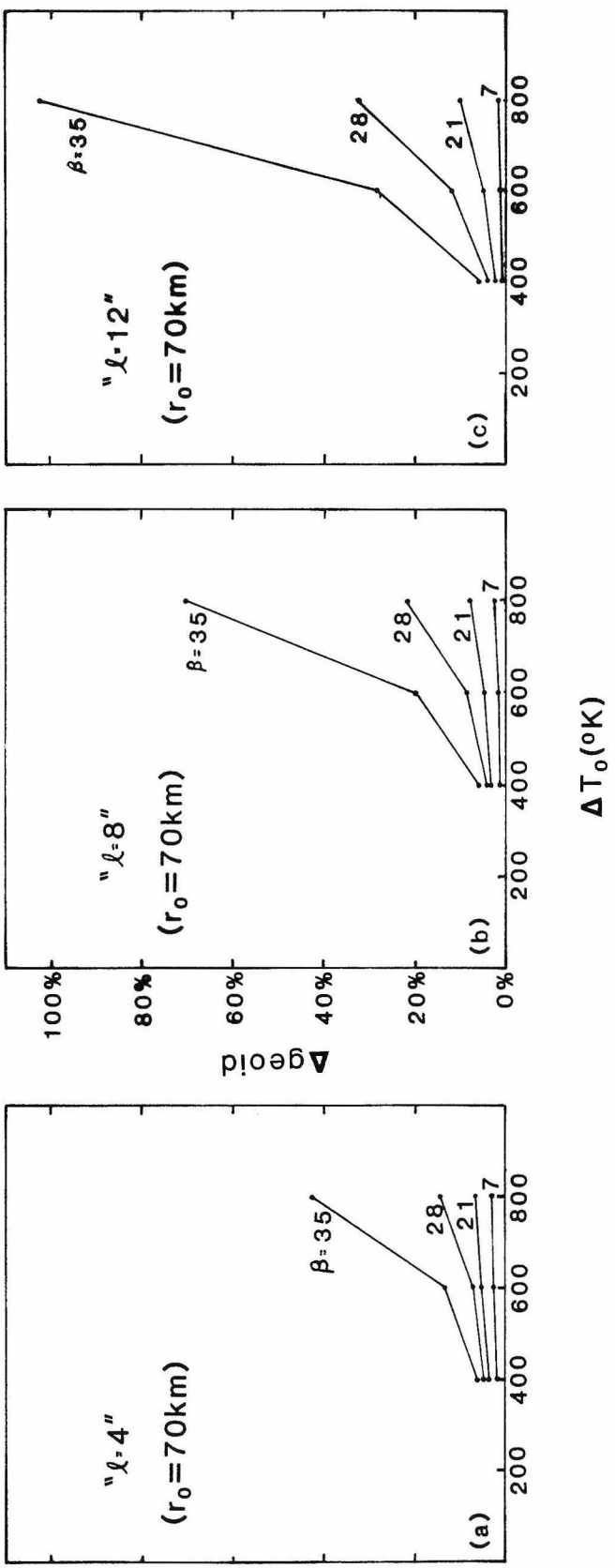
"ℓ=4"
(r0=70km)
(a)
"ℓ=8"
(r0=70km)
(b)
"ℓ=12"
(r0=70km)
(c)
β=35
28
21
7
Δgeoid
100%
80%
60%
40%
20%
0%
200
400
600
800
ΔT0(°K)

Figure 14 - Buoyancy flux (r_0=70 km) as a function of excess plume temperature and β for halo model A.

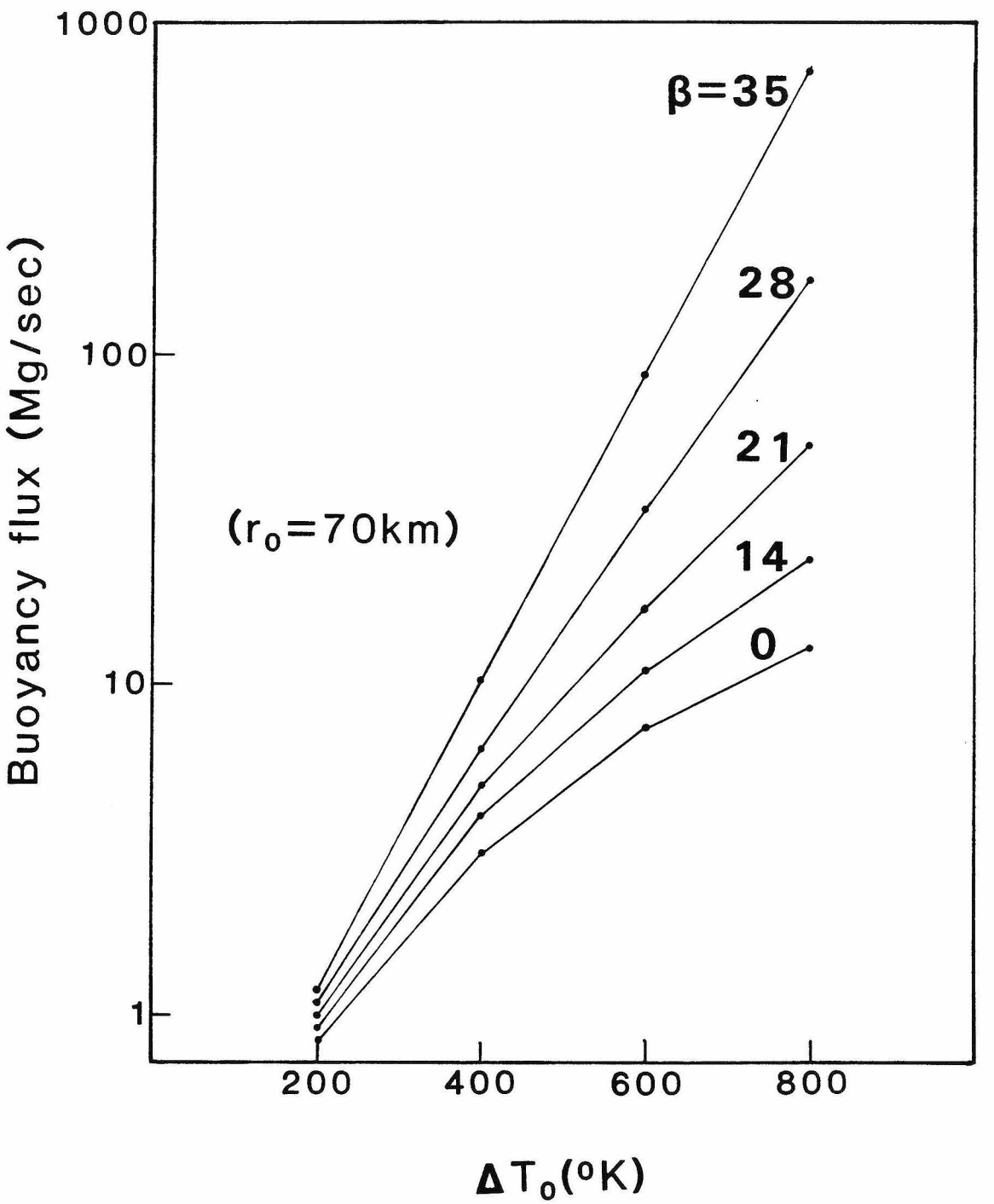
1000
100
10
1
Buoyancy flux (Mg/sec)
β=35
28
21
14
0
(r0=70km)
200
400
600
800
ΔT0(°K)

Figure 15 - Buoyancy flux as a function of plume radius for halo model A. The right-hand vertical scale is linear and gives the fourth root of the flux. Solid lines are for excess temperatures of 400^0K and 800^0K with β=28. Dashed lines are for the isoviscous models (β=0).

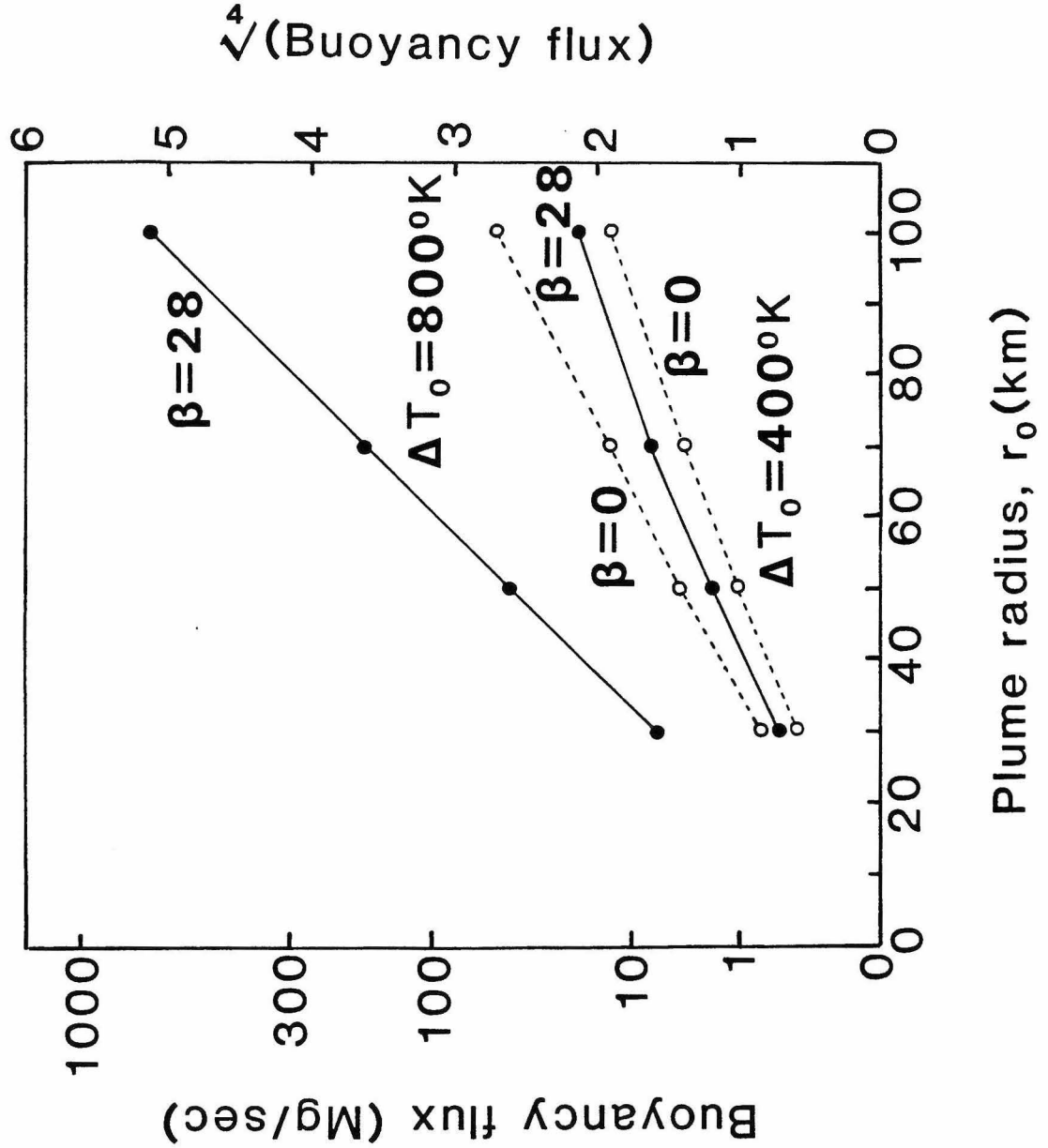
$\sqrt[4]{}$(Buoyancy flux)
Buoyancy flux (Mg/sec)
Plume radius, r_o(km)
β=28
ΔT_o=800°K
β=0
β=28
β=0
ΔT_o=400°K
1000
300
100
10
1
0
6
5
4
3
2
1
0
0
20
40
60
80
100

Figure 16 - Geoid signal perturbation (excess), relative to the isoviscous geoid, as a function of radius and viscosity contrast. The l=4, 8, and 12 curves are for the first three harmonics of the cylinder for the pipe model.

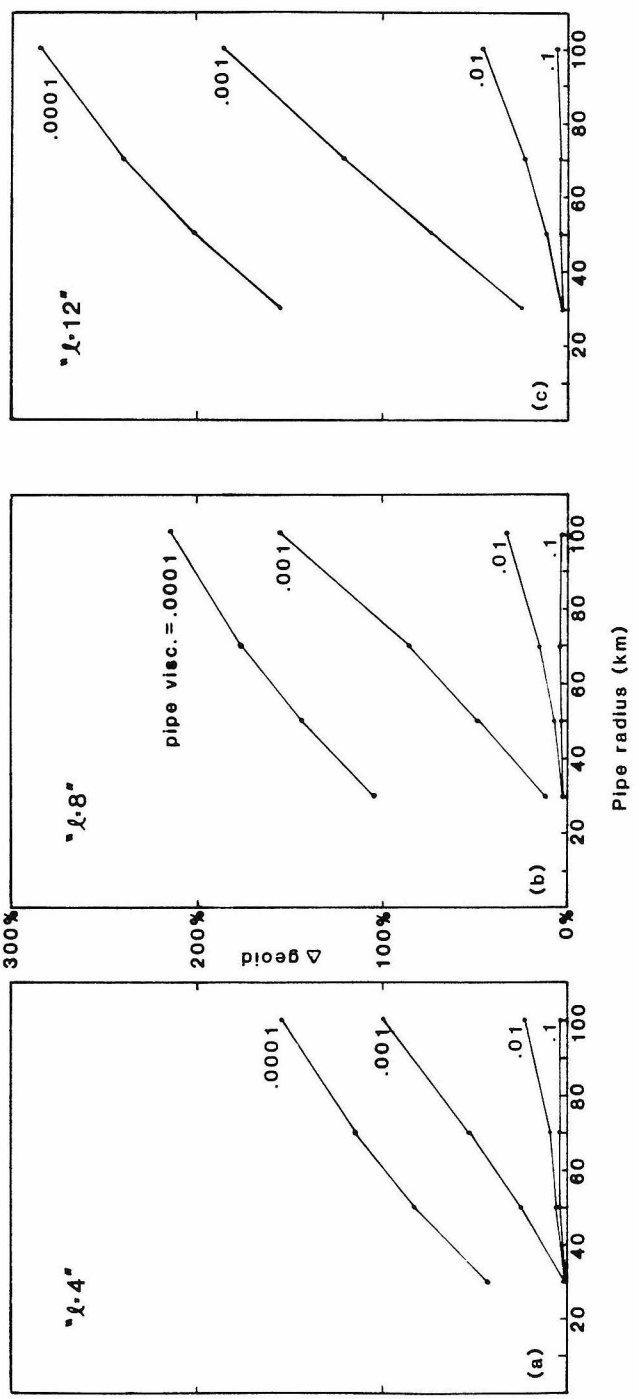
"ℓ·4"
"ℓ·8"
"ℓ·12"
(a)
(b)
(c)
.0001
.001
.01
.1
pipe visc. = .0001
300%
200%
100%
0%
Δ geoid
20
40
60
80
100
Pipe radius (km)

Figure 17 - Buoyancy flux as a function of radius and viscosity contrast for the pipe model. The flux is normalized to the square of the excess temperature for density ρ_0=5.14 and volume coefficient of thermal expansion $3x\,10^5/^0$K. The right-hand scale is linear and gives the fourth root of the flux. Dashed lines give the theoretical flux for an infinite rigid pipe (mantle) for the same interior pipe viscosities and buoyancy forces (see text).

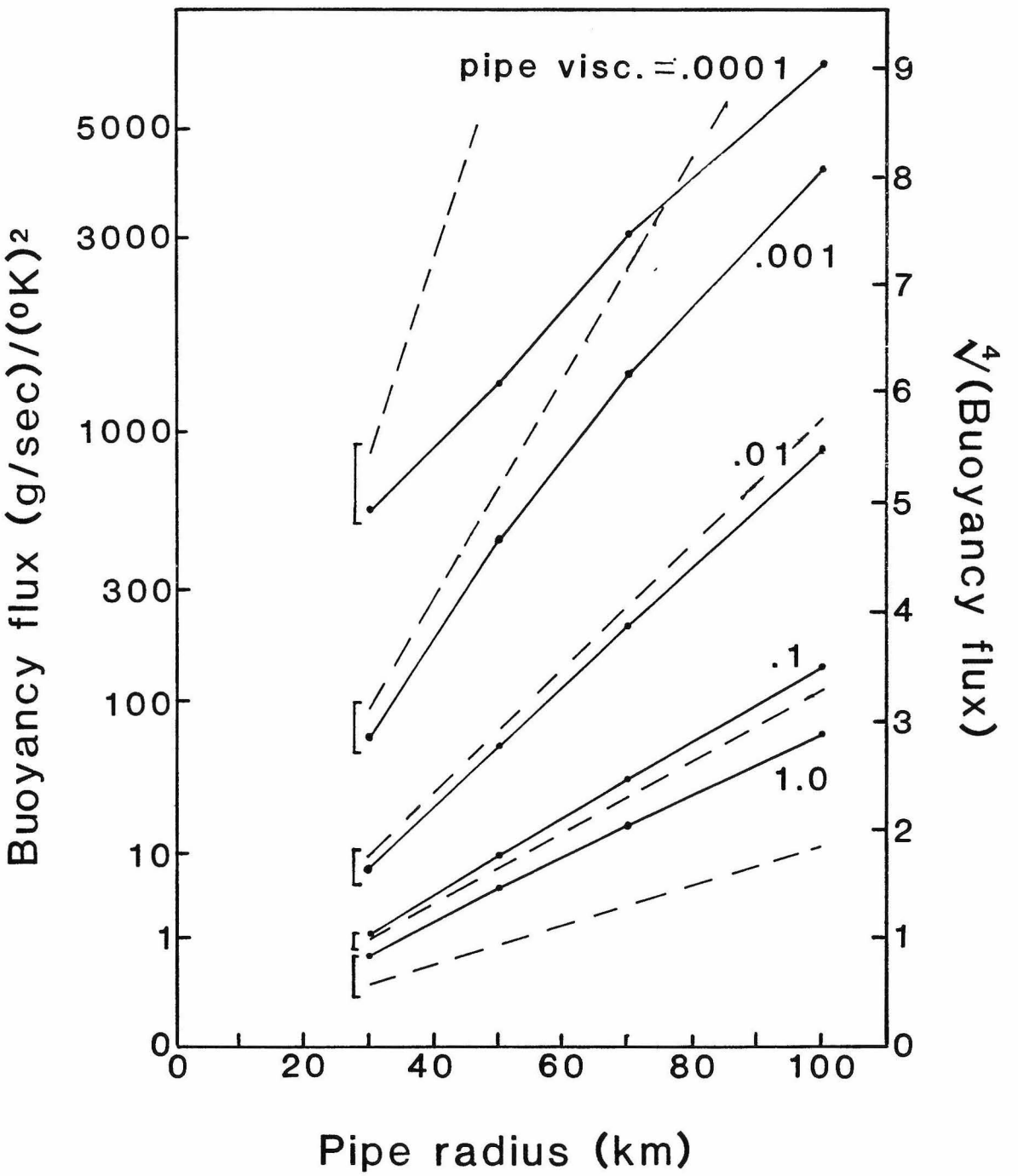
pipe visc. =.0001
.001
.01
.1
1.0
Buoyancy flux (g/sec)/(°K)²
∜(Buoyancy flux)
Pipe radius (km)
0
1
10
100
300
1000
3000
5000
0
1
2
3
4
5
6
7
8
9
0
20
40
60
80
100

Figure 18 - Comparison of global hotspot response curve (solid line with error bars) and several dynamic models. Solid triangles give the l=4,8 geoid signal, divided by 4, for plume model B (β=35). Solid diamonds are for model C (β=35), also divided by 4 to account for smearing of the signal over a range of $\sim$4 harmonic degrees in a spherical Earth. Model C$'$ (β=0), indicated by open diamonds, has no viscosity contrast between the mantle and the plume. The "spherical Earth" model (dashed lines) was calculated analytically using the method of Richards and Hager (1984; Chapter 1) with a 200 km radius plume, average temperature contrast 300^0K, and no viscosity contrast. The dotted line gives the (spherical) analytical calculation for the geoid spectrum from lithospheric delamination.

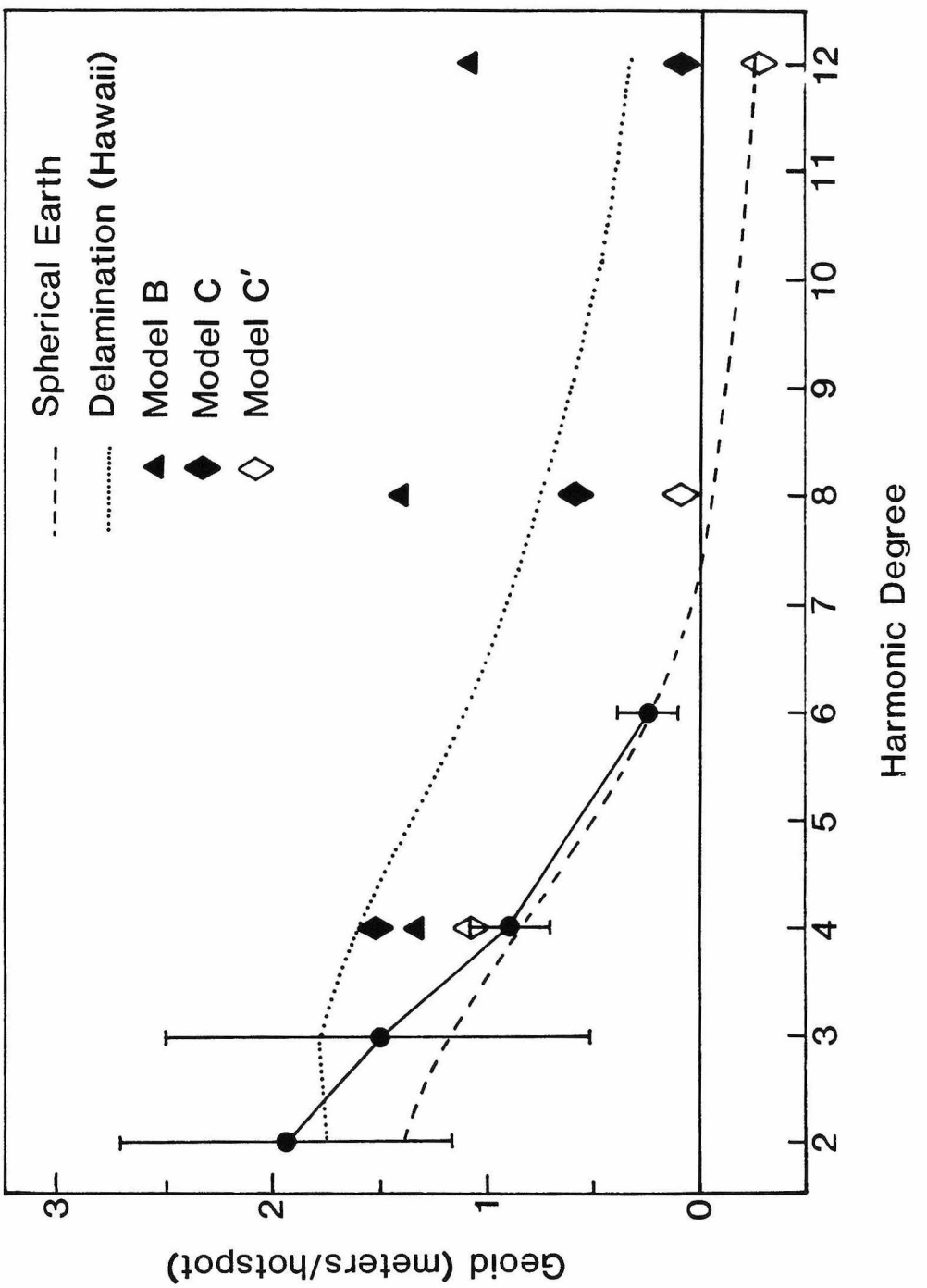
Spherical Earth
Delamination (Hawaii)
Model B
Model C
Model C'
Geoid (meters/hotspot)
Harmonic Degree
0
1
2
3
2
3
4
5
6
7
8
9
10
11
12

Figure 19 - Pseudo geoid response functions (see text) for the model C plume (solid line), subducted slab (dashed line), and slab with weakened lithosphere (dash-dot line). The dotted line gives the analytical solution for the purely layered response.

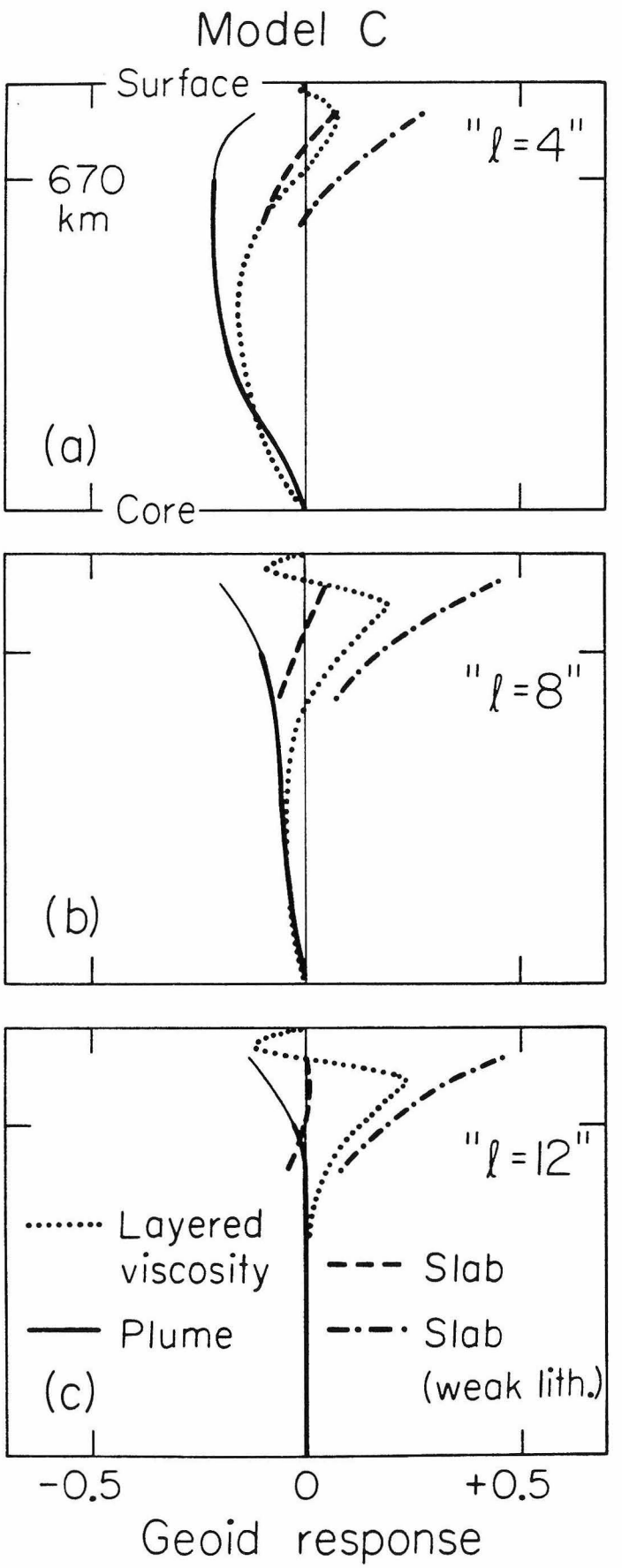
Model C
Surface
670
km
"ℓ=4"
(a)
Core
"ℓ=8"
(b)
"ℓ=12"
Layered
viscosity
Plume
Slab
Slab
(weak lith.)
(c)
-0.5
0
+0.5
Geoid response

Figure 20 - Comparison of dynamic topography from Models B and C with the observed Hawaiian swell topography. The heavy dotted line is from section A-A′ of Figure 9, and the lighter dotted line is from section B-B′ 500 km WNW of Hawaii ("anomalous" bathymetry adapted from Schroeder, 1984). Light and heavy solid curves are for strongly temperature dependent viscosity (β=35) in models B and C, respectively. Light and heavy dashed curves are for no viscosity contrast between plume and mantle (β=0) in models B and C, respectively. Deformation profiles for the theoretical models decay toward the zero level out to 5000 km from the plume axis, but are truncated in this figure in order to emphasize deformation near the swell itself.

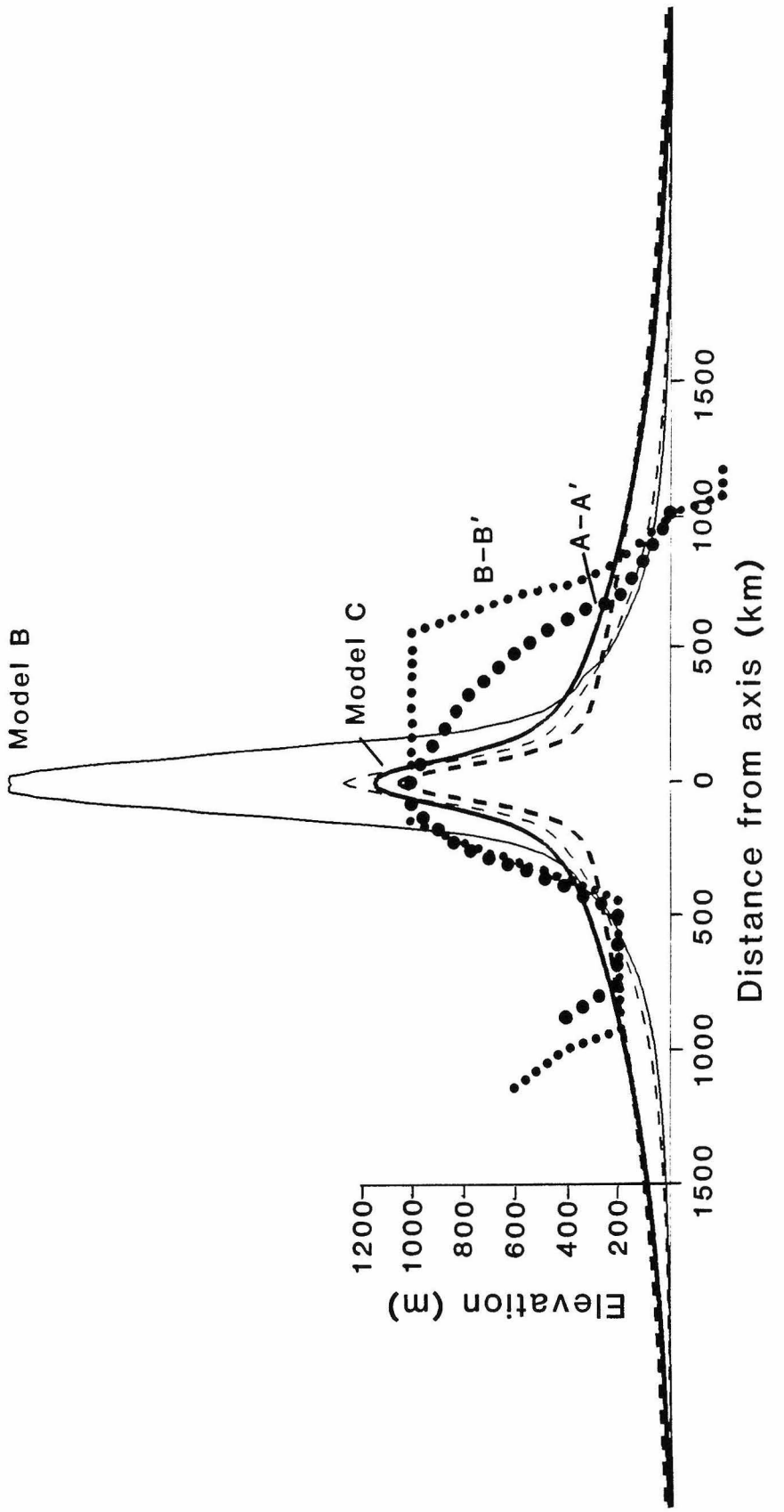
Model B
Model C
B-B'
A-A'
A
Elevation (m)
1200
1000
800
600
400
200
1500
1000
500
0
500
1000
1500
Distance from axis (km)

Figure B1 - Illustration of the geometry for the high viscosity slab calculations. Horizontal and vertical scales are equal.

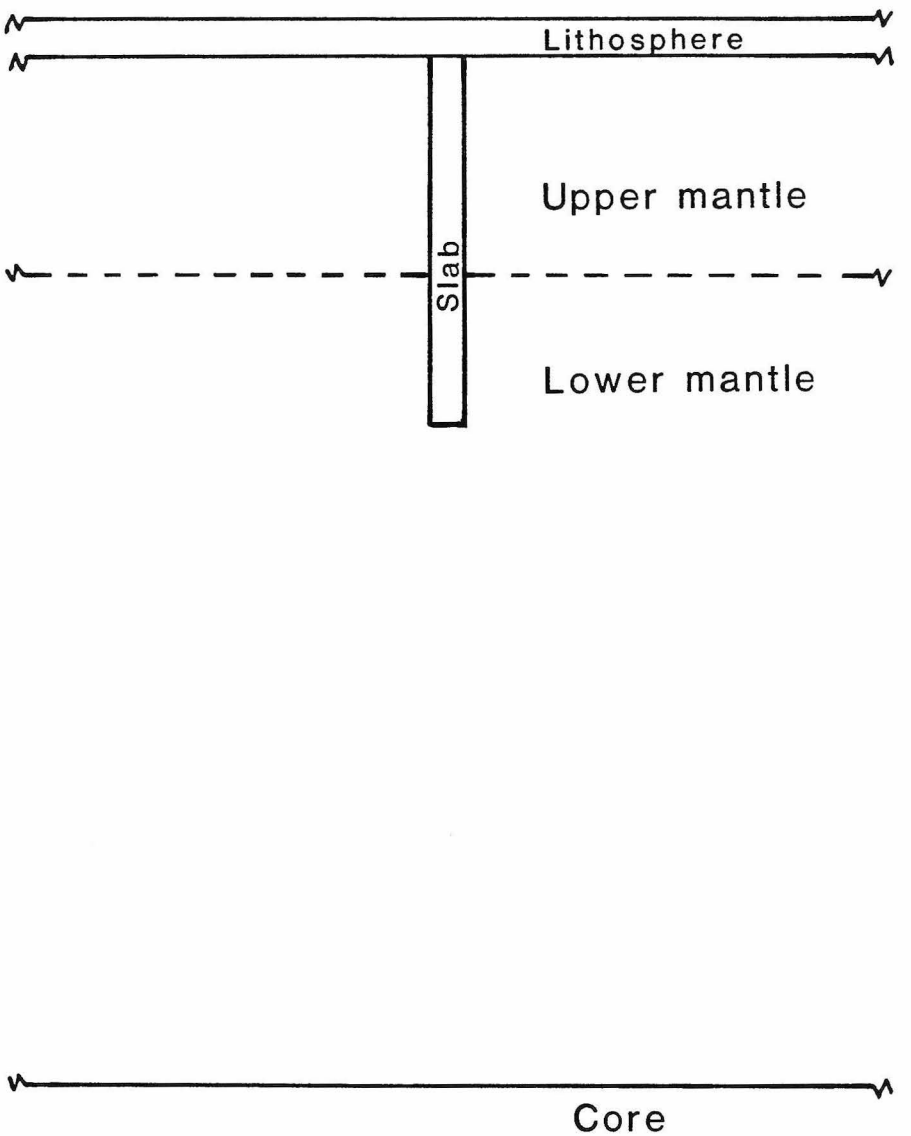
Lithosphere
Upper mantle
Slab
Lower mantle
Core

Figure B2 - Pseudo response curves (l=5,10) for models L100.u (dotted line), L100.slab (solid line), L100.slab200 (long dashes), and L100.slab400 (short dashes).

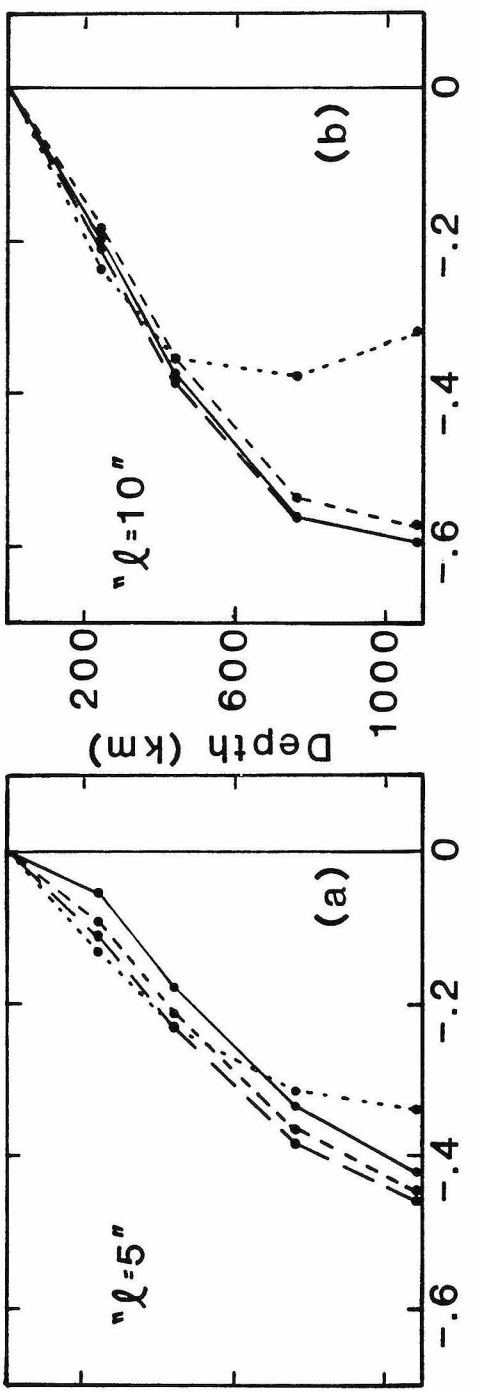
(a)
(b)
"ℓ=5"
"ℓ=10"
Depth (km)
200
600
1000
-.6
-.4
-.2
0
Dynamic geoid response

Figure B3 - Pseudo response curves (l=5,10) for models LU100.u (dotted line), LU100.slab (solid line), LU100.slab200 (long dashes), and LU100.slab400 (short dashes).

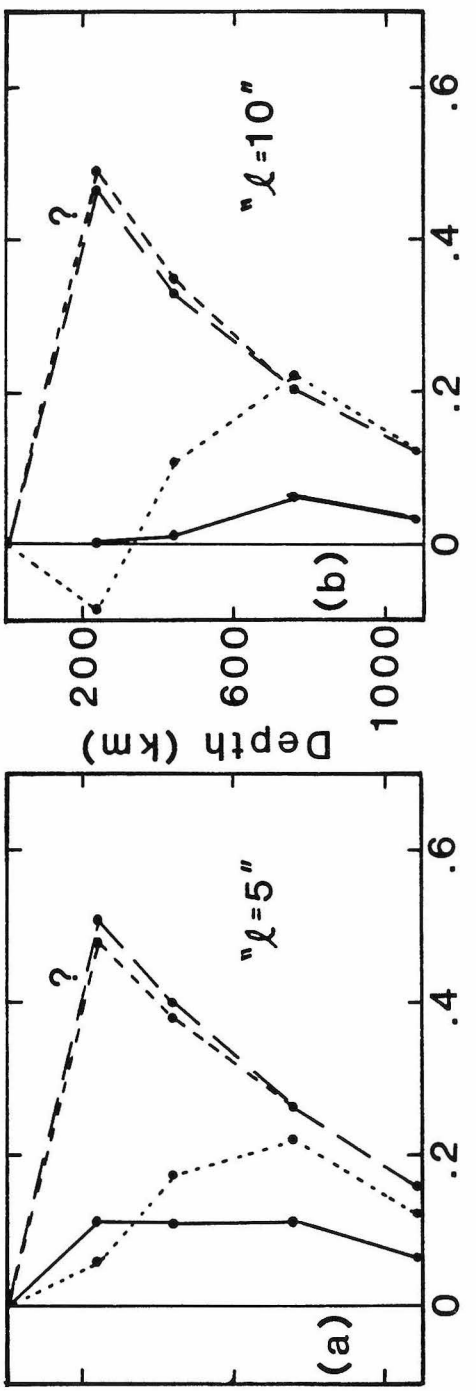
"ℓ=5"
"ℓ=10"
?
?
(a)
(b)
0
.2
.4
.6
200
600
1000
Depth (km)
Dynamic geoid response